DOCTOR OF PHILOSOPHY

The coastal transition zone of the Galician Region: Upper layer response to wind forcing and circulation.

Torres, Ricardo

Award date:
2003

Awarding institution:
University of Wales, Bangor

THE COASTAL TRANSITION ZONE

OF THE GALICIAN REGION:

UPPER LAYER RESPONSE TO WIND FORCING AND CIRCULATION

A Thesis

Submitted in accordance with the requirements of the

University of Wales for the degree of Doctor of Philosophy

by

Ricardo Torres

University of Wales Bangor

School of Ocean Sciences

Menai Bridge, Anglesey

United Kingdom

December 2003

ABSTRACT

Torres, Ricardo. Ph.D., University of Wales, Bangor, August, 2003. The Coastal Transition Zone of the Galician Region: Upper Layer Response to Wind Forcing and Circulation.

The Galician shelf response to the varying seasonal forcing has been characterised through a set of observations including satellite, cruise and mooring data encompassing the period 1997-2001. The typical spatial variability of wind and its effect on the shelf circulation has been investigated. The seasonality of the large scale wind during July 1999- May 2001 was masked by upwelling/downwelling patterns throughout the year. However, upwelling winds were found to be more consistent during summer and the system showed clear seasonality with upwelling during summer and downwelling during winter mediated by a meridional density gradient. Despite its spatial complexity, the mesoscale wind variability was reduced to a finite number of spatial patterns. These favoured upwelling north or south of Cape Finisterre or downwelling along the west coast of Galicia. Their relative abundance influenced the interannual variability during both upwelling and downwelling regimes.

Slope poleward flow characteristic of the downwelling regime was measured at all times, suggesting it is a permanent feature in the Galician CTZ system. Its winter variability was related to unusual periods of upwelling winds. It has a surface signature in winter, autumn and during spring. The shelf was effectively isolated from the ocean due to a shelf-edge front, as indicated by the lagrangian horizontal diffusivity although some exchange still occurred via a bottom Ekman layer. In the

summer it formed a subsurface poleward flow.

The weakening of the meridional density gradient initiated decay of the poleward slope current. The warm tongue broadened, and the organised flow of the poleward current broke down as eddies were generated and the flow branched into separate streams, one along the shelf break and one along the outer slope.

During persistent upwelling on the west coast, the upper column structure becomes dominated by coastal upwelling and filaments while the poleward flow is restricted to subsurface layers. A detailed survey of a filament showed limited export capabilities, although the lagrangian diffusivity was enhanced during the summer upwelling regime. Interannual variability during the upwelling regime is characterised by either presence/absence of filaments or whether the main filament is at Cape Finisterre or at 42°N latitude.

Towards the end of the upwelling regime, when upwelling winds weaken, the poleward flow returns to the upper slope. However, it is not until the meridional density strengthens that the poleward flow surfaces again. If filaments are still present, the slope poleward flow cuts their water supply and they slowly mix away.

ACKNOWLEDGMENTS

I would like to express my gratitude to my supervisor Dr. Des Barton for the invaluable guidance and support during the entire gestation of this thesis.

Part of this work was written during a stay in the CICESE station of La Paz, Mexico, and useful discussions with Dr. A. Trasviña and Dr. G. Gutierrez helped in the development of the work.

Many of the data presented here were collected during four cruises carried out under the OMEX II-II EU project and the crew, officers and scientific personnel made it both possible and highly enjoyable. My gratitude also to everybody in BODC for their fantastic work in the quality control of the cruise data.

Thanks to the RSDAS team, Plymouth Marine Laboratory for supplying the remote sensing data.

These years in Menai Bridge have been shared and enjoyed with a great bunch of friends who supported, helped and made life so much better; my brother Nacho, Maria, Teri, Consuelo, Maite, Nuno, Maria Manel, Adriana, Fernando, Jose, Mark, Lolo, John, Jonathan and many more. Thanks for the constant source of support and distraction!

I owe immense gratitude to my parents for their constant encouragement and support throughout.

My deepest and warmest thanks go to Olivia, for her constant support, comments and help, and for making me believe the end was ever nearer!.

TABLE OF CONTENTS

CHAPTER

1 Introduction

1.1 Galicia an Eastern Boundary System

This thesis investigates the seasonality of the Galician shelf (North-West of Spain). The region forms part of the wider East Atlantic Boundary System, which includes the Portugal and Canary Island systems. Like most eastern regions, Galicia experiences a marked seasonality mainly driven by the wind regime, but also by an oceanic density gradient resulting in summer upwelling and winter slope poleward flow. The Galician shelf is the northernmost limit of the Atlantic Eastern Boundary upwelling system and is characterised by the abrupt change in coast orientation at Cape Finisterre, where the coast changes from a N-S to E-W direction. The relatively narrow shelf is populated by ridges and canyons. The coastline also has abrupt indentations, the "Rias", which together with the Minho River, provide the freshwater input onto the shelf. It has not been recognised previously that the coastline complexity directly affects the wind, inducing spatial and temporal variability which transfers to the shelf. During the upwelling regime, the region is also the site of at least three filaments while during the downwelling regime, eddies are shed from the poleward flow, preferentially at capes. It is the unique combination of these features that generate this highly complex and dynamic system.

Current understanding of Galician shelf circulation and its relation to wind forcing is poor. The Ekman index has been used as a first approximation for the shelf circulation and dynamic state. However, coastline complexity renders the assumption of single point geostrophic wind measurements representative of the wider shelf region difficult to maintain. Resolving the detailed dynamics of the region is of particular importance given its status as one of the main marine shipping corridors in Europe and the relevance of associated "Rias" to the global shellfish industry. Maritime accidents like the recent oil spill from the "Prestige" are not uncommon; the last 30 years has seen seven serious oil spills ("Polycommander", "Urquiola", "Erkowit", "Andros Patria", "Casón" and "Mar Exeo"), making it the world's oil spill hot spot. The "Rias Bajas" (the three southernmost "Rias") represent one of the largest mussel production regions in the world, furthermore shelf dynamics dictates their behaviour. Much of the recent research has focused on circulation and biochemical fluxes inside the Rias suggesting a strong link between the Rias and the shelf, e.g. upwelling takes place inside the Rias in response to equatorward winds and moreover a nearshore poleward coastal current has been related to the generation of Harmful Algal Blooms (HAB). This highlights the urgent need to characterize shelf circulation in order to further our knowledge of the whole system.

1.2 Aims of the thesis

This thesis describes in unprecedented detail the main features of the Galician region at different stages of its seasonal cycle. Three main data groups have been collected for that purpose:

Cruise data Data from four cruises during the spring spin up, summer upwelling, autumn transition and winter downwelling are presented. They include meteorological data, hydrographic data (CTD, Conductivity, Temperature and Depth), current data (ADCP, Acoustic Doppler Current Profiler) and turbulence data (FLY, Fast, Light, Yo-Yo profiler).

Remotely sensed data Data from Advanced Very High Resolution Radiometer (AVHRR) and Scatterometer wind data are used extensively. Eight mixed layer drifters were released in the region and tracked through the ARGOS system.

Long-term measurements Data from meteorological coastal stations and shelf moored oceanographic buoys are used when possible, namely hourly winds and surface currents.

The main objective of the thesis is to identify and describe the key oceanographic features of the Galician coast at the different seasonal stages. To do so, the aims of the research were to:

- Identify typical wind patterns at the largest spatial and temporal resolution and characterise wind variability.

- Describe the transitional periods between upwelling and downwelling and identify their driving mechanisms.

- Describe for the first time the 3-D structure of a filament in the Galician region, and establish its possible role in shelf/ocean exchange.

- Describe the winter poleward flow and investigate the possible forcing mechanisms involved in its generation.

- Obtain novel insights into seasonal differences in mesoscale circulation and horizontal diffusion through Lagrangian drifter releases.

1.3 Thesis structure

This thesis describes the work and results from four multidisciplinary oceanographic cruises in the Galician region at different stages of the general seasonal regimes. It has been divided into eight Chapters.

Chapter 2 Current understanding of the hydrography and circulation of the region at the seasonal scale is given, and the main mesoscale structures present identified. An introduction to the physical theory behind upwelling and downwelling dynamics is given.

Chapter 3 For the first time, spatial distribution of winds around the Galician region is investigated with the first two years of daily QuikScat scatterometer winds. Typical wind spatial patterns are characterized for the different wind regimes.

Chapter 4 The response of the system at the beginning of the upwelling season to sudden changes between downwelling and upwelling favourable winds is described on the basis of results from cruise CD105.

Chapter 5 Data from cruise CD114 is used to provide a novel description of filaments during a mature stage of the upwelling regime. The effect of upwelling relaxation on the upwelling system both over the shelf and in filaments is studied.

Chapter 6 The onset of the downwelling regime is described. Hydrography and velocity data from cruise THALASSA1099 showed the structure of the poleward slope flow along the Galician shelf.

Chapter 7 The behaviour of Lagrangian surface drifters launched during cruises CD114 and METEOR 46/2 during both upwelling and downwelling regimes is described and horizontal mixing coefficients are estimated.

Chapter 8 Results from all chapters are integrated and discussed providing a comprehensive insight into the complex circulation patterns of the Galician system and their seasonal variability.

CHAPTER

2 Background and Literature review

2.1 Regional Settings And Area Characteristics

The general bathymetry and coastal morphology of the west coast of the Iberian Peninsula extends between latitudes 36° and 44°N (Fig 2.1. It includes the typical physiographic aspects of the continental shelf, the slope and the rise. The margin is cut in several places by submarine canyons which generally define boundaries between regions with relatively similar bathymetry conditions. North of the Nazaré canyon the shelf is wide and very flat, with the exception of the Porto and Aveiro canyons,

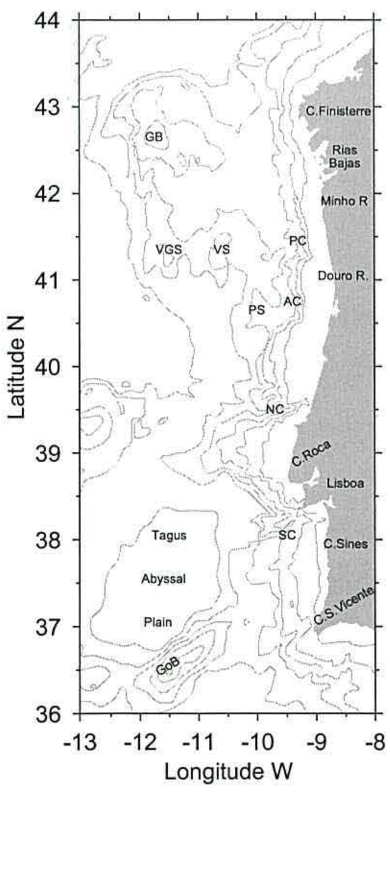

Figure 2.1.: Bathymetry and coastal morphology from GEBCO database showing the main features off the coast of Iberia from 44°N to 36°N and between 13°W and 8°W. Bathymetric contours at 200m and multiples of 1000m are shown. GB-Galician Bank, PC-Porto Canyon, AC-Aveiro Canyon, NC-Nazare Canyon, SC-Setúbal Canyon, VGS-Vasco de Gama Seamount, VS-Vigo Seamount, PS-Porto Seamount, GoB-Gorringe Bank.

as far as Cape Finisterre. Offshore of the shelf edge, indicated by the isobath of 200m, the bottom topography is quite complex. Between latitudes 43.5° and 41°N the bathymetry is characterised by a deep meridional valley with a maximum depth of 2800m separating the continental slope from the Galicia Bank (minimum depth of 560m) to its west. The shoreline extends almost meridionally up to about 42°N and then the coast presents strong indentations (the 'Rias Bajas') as far as Cape Finisterre. Further south at 41°N latitude, the Vigo, Porto and Vasco de Gama seamounts are found. Between Nazaré and the Lisbon region, the shelf is more irregular and is dominated by a well pronounced zonal ridge. South of the Setúbal canyon, the shelf is fairly flat as far as Cape Sines, beyond which it becomes very steep until Cape São Vicente, practically without a shelf break. The coastline is again orientated very nearly in the meridional direction. At the latitude of Cape São Vicente a large ridge extends offshore. Freshwater input to the Galician shelf from the Rias (four in the west coast and 3 in the north coast) and the Minho river is small during summer ($204 m^3 s^{-1}$ from mid May to mid October) [*Huthnance et al.*, 2002] but increases in winter.

2.1.1 General circulation in the North Atlantic

The general circulation in the North Atlantic (Fig. 2.2) is characterised by the presence of two large wind-driven gyres: the cyclonic subpolar gyre and the anticyclonic subtropical gyre. The subtropical gyre has its northwest boundary defined by the Gulf Stream (GS) which is responsible for the recirculation of the gyre [*Dietrich et al.*, 1975]. Southeast of the Grand Banks the GS separates into two branches: the North Atlantic current, flowing to the northeast and feeding the subpolar gyre [*Clarke et al.*, 1980; *Sy*, 1988]; and the Azores Current (AC), which crosses the North Atlantic to the east coast between 35°N and 30°N, the exact position being subjected to seasonal displacements [*Tokmakian and Challenor*, 1993]. *Stramma* [1984], on the basis of geostrophic calculations on the historical archive of hydrographic data, found that the eastward flowing AC separates into three branches as it turns southward on approaching the eastern boundary. Two branches separate

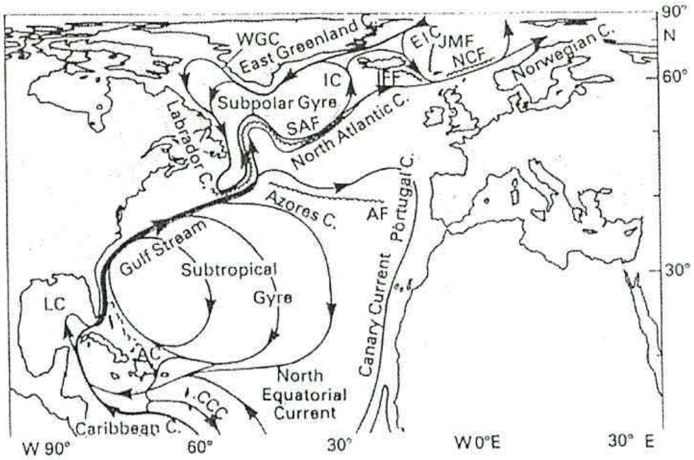

Figure 2.2.: General surface circulation of the North Atlantic (after *Tomczak and Godfrey,* 1994). Abbreviations are used for the West Greenland Current (WGC), Irminger Current(IC), East Iceland Current(EIC), Loop (LC) and Antilles Currents(AC) and the Caribbean Countercurrent (CCC). Other Abbreviations refer to fronts: Jan Mayen Front (JMF), Norwegian Current Front (NCF), Iceland-Faroe Front (IFF), Subartic Front (SAF) and Azores Front (AF).

west of Madeira to make up an interior southward recirculation of the subtropical gyre while the third passes north and around Madeira to feed into the Canary Current.

A consistent weak eastward flow of Eastern North Atlantic Central Waters (ENAW) appears to exist off the Iberian Coast from north of the Azores Current at depths of 200-300m corresponding to densities lower than 27.25 [*Saunders*, 1982; *Pollard and Pu*, 1985; *Arhan et al.*, 1994; *Mazé et al.*, 1997] consistent with a poleward shoaling of isopycnals [*Barton et al.*, 2002]. Part of that flow is later diverted off the south coast of Portugal towards the gulf of Cadiz [*Mazé et al.*, 1997]. This zonal flow is associated with a northward flow and downward entrainment with 40% of the ENAW entering the Mediterranean Intermediate Water (MIW) layer [*Mazé et al.*, 1997] although seasonal variability can be expected in its dynamics [*Saunders*, 1982; *Arhan et al.*, 1994].

The Mediterranean outflow at the Strait of Gibraltar forms MIW and travels along the Algarve continental slope to spread out ultimately into the Atlantic at depths between 600 and 1500m. The MIW is evident as two maxima of temperature and salinity cores [*Daniault et al.*, 1994] and its flow is characterized by a westward advection (mainly raised by mesoscale features as shedding eddies, MEDDIES [*Armi and Zenk*, 1984; *Kase et al.*, 1989; *Bower et al.*, 1997]) and turbulent diffusion of MIW together with a well defined northward jet along the Iberian shelf break and slope (Fig 2.3) [*Meincke et al.*, 1975; *Arhan et al.*, 1994]. The northward flow of MIW enters the Iberian slope by the Tagus Bank between Cape São Vicente and the Gorringe Bank [*Zenk and Armi*, 1990] and was named the Portugal Slope Undercurrent (PSU) by *Ambar and Fiúza* [1994]. Part of the flow separates there from the slope and flows back southwestward to the west of the Gorringe Bank (Fig. 2.3) while the rest of the flow proceeds northward in the form of a slope undercurrent [*Daniault et al.*, 1994] with a characteristic transport of 7.6 10^6 m^3s^{-1} [*Mazé et al.*, 1997]. The MIW slope current divides later into two branches between 41°N and 42°N, a western branch flowing to the west of the Galician bank and a coastal branch following the shelf break in response to the steering effect of bottom topography. A further effect of the bottom topography-flow interaction of the PSU is the existence of a bottom boundary Ekman layer enhancing downslope Ekman transport.

In the same region the Central Waters flow strongly resembles that of the MIW, suggesting a vertical coupling of both water masses.

2.1.2 Weather Regime

Upwelling occurs all along the east coast of the central North Atlantic from the northern tip of the Iberian peninsula to south of Dakar at almost 10°N, as a result of the characteristics of the wind. During the summer months, when the Azores high-pressure cell is located in the central Atlantic and the Greenland low has diminished in intensity, the resulting pressure gradient forces the air to flow southward along the coast of Iberia inducing upwelling and associated southward circulation. In contrast, in winter the Azores high-pressure cell is located further south, off the northwestern African coast, and a deep low is located off the southeastern coast of Greenland. The pressure gradient between the two pressure systems results in an onshore wind with a component of wind stress northward off Iberia.

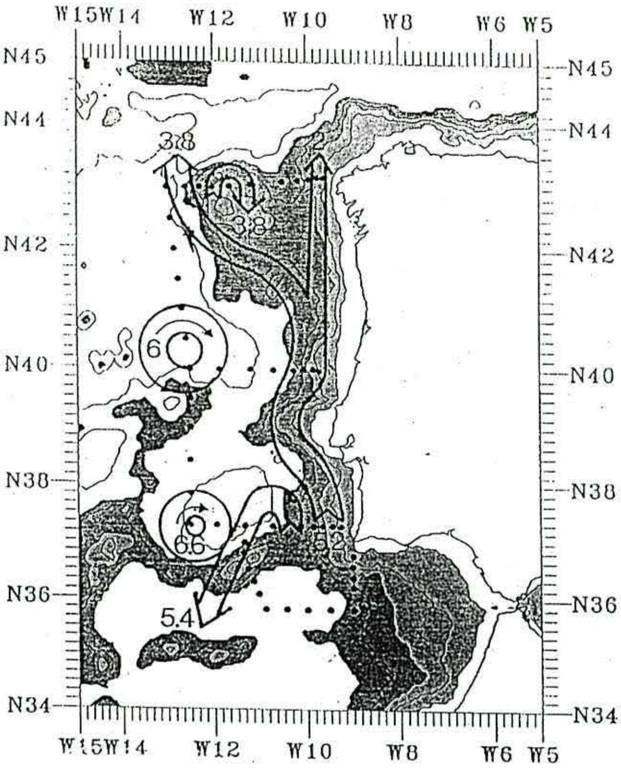

Figure 2.3.: Schematic circulation of MW in May 1989 in the Iberian coast. Black dots represent CTD stations. Reported numbers are volume transports in 10^6 m^{3}s^{-1} [from *Mazé et al.*, 1997].

Blanton et al. [1987] showed that there are large interannual variations in upwelling in response to the large-scale meteorology variations in the North Atlantic. The continuously varying strength and position of the Azores High and the Greenland Low lead to variations in the strength and direction of upwelling favourable winds at these latitudes.

2.1.3 Coastal circulation

The general structure of the Portugal Current System off the west Iberian coast is formed by the following basic components [*Fiúza*, 1996]:

1. a large scale southward surface flow in the open ocean, seaward of the continental margin related to the N. Atlantic subtropical gyre, the Portugal Current,

2. an equatorward surface flow over the slope, in the vicinity of the shelfbreak during the upwelling season (June-July until late September), the Portugal Coastal Current,
3. a poleward surface flow along the upper slope from mid-autumn until late spring, the Portugal Coastal Countercurrent,
4. the semi-permanent poleward Portugal Slope Undercurrent.

Bearing in mind that none of the above currents are restricted to the Portuguese margin they would be better named the Iberian currents.

Winter regime

The meteorological conditions offshore from the Iberian Peninsula, governed by the meridional displacements of the Azores High as mentioned before, show distinct winter and summer regimes. In winter, the weakening and southward migration of the anticyclone places the north of the region under the influence of southwesterly winds. The upper layer circulation in this season is characterised by the presence of a narrow northward slope current which settles in November and disappears around May [*Frouin et al.*, 1990; *Haynes and Barton*, 1990; *Pingree and LeCann*, 1992a]. This structure (Fig. 2.4) appears as a warm and saline intrusion (temperature 1-3°C and salinity 0.2-0.3psu higher than surrounding values), trapped within about 50km of the shelf break, about 200-600m deep. It flows along the slope with characteristic velocities of 0.2-0.3ms^{-1}, and extends more than 1500km and with transport increasing in the flow direction [*Frouin et al.*, 1990; *Haynes and Barton*, 1990]. Drifter experiments (Fig. 2.5) have revealed a meandering surface flow with eddies of different scales superimposed on the poleward mean flow [*Haynes and Barton*, 1991; *Sena*, 1996]. This Portugal Coastal Countercurrent (PCC),[*Fiúza et al.*, 1998], flows along a semi-permanent front separating the fresher shelf waters influenced by the winter river runoff from rivers of northern Portugal particularly from the Douro, from the open ocean [*Hamann et al.*, 1996]. That convoluted front was observed to contribute to the shelf-ocean exchange via mesoscale cyclonic eddies

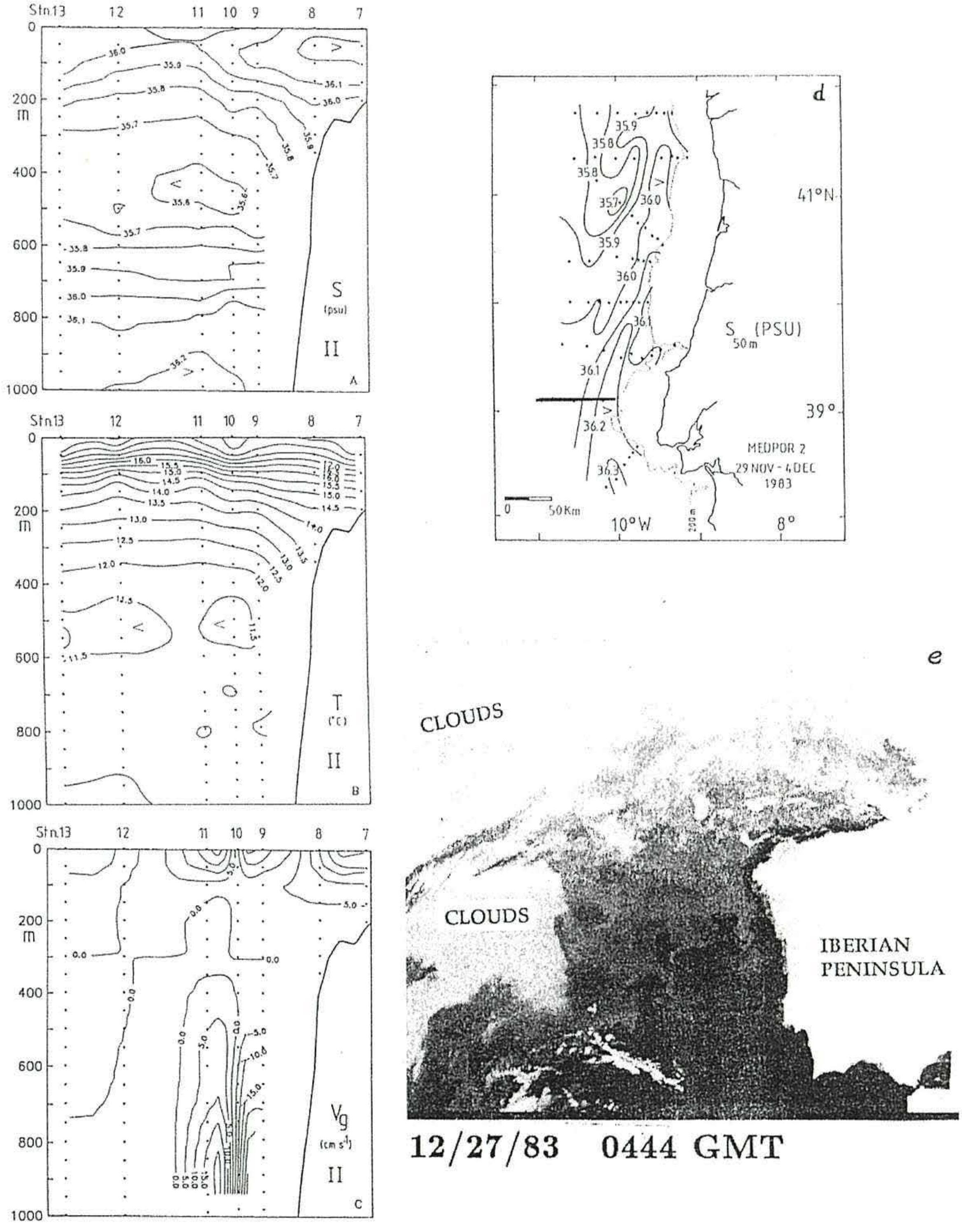

Figure 2.4.: Different signatures of the PCC from winter 1983. Vertical distribution of (a) salinity, (b) temperature, and (c) meridional component of geostrophic velocity relative to 300 dbar along section II (thick line in d). Salinity distribution at 50m (d) showing the PCC (saline intrusion) along the slope. Thermal infrared picture (e) from the NOAA 7 satellite where darker tones corresponds to warmer temperatures [from *Frouin et al.*, 1990].

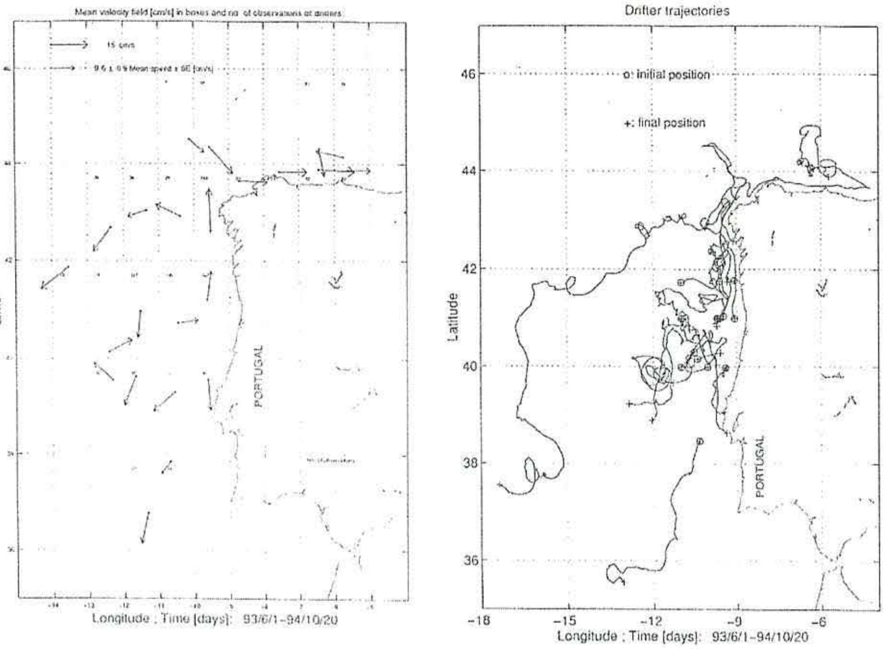

Figure 2.5.: Mixed layer drifter tracks (right) and derived surface velocities (left) for 16 drifters used in the MORENA project during June 1993-October 1994. 11 drifters were released during November 1993 and their trajectories correspond to the period November 1993-May 1994 [*Sena,* 1996].

(10-20km in diameter) which are shed into the open ocean from the Countercurrent [*Fiúza*, 1996; *Pérez et al.*, 2001]. Other active exchange processes are mixing and entrainment into the poleward Countercurrent of shelf waters which are advected alongshore for hundred of kilometres before dispersing into the open ocean with an estimated residence time on the shelf of 1-2 months[*Fiúza*, 1996]. Those fronts are common features of the shelf breaks as a result of buoyancy inputs and their "anchorage" at the shelf break is a response to potential-vorticity conservation and geostrophy [*Condie*, 1993]. As mentioned above, the slope current extends downwards including the MIW to a depth of 1500m and more, as reported by *Huthnance et al.* [2002] at various moorings along the Iberian Atlantic coast outside the shelf break.

Pollard and Pu [1985] described a meridional density gradient in the upper 200-300m associated with the poleward cooling of the sea surface which can force a poleward current that becomes intensified over the slope and which increases along the flow [*Huthnance*, 1984]. The winter wind circulation could also generate a poleward slope current and the two mechanisms were found to actively drive the PCC [*Frouin et al.*, 1990].

Large and persistent anticyclonic warm slope-water eddies (SWODDIES) have been associated with the PSU in winter if the warm flow is strong [*Pingree*, 1994] in relation with the instability of the slope current in the Bay of Biscay (Fig. 2.6) although no consistent seasonal variability has been established. They have characteristic radii of 50-60km, a signature discernible in the upper 1500m, and a lifetime of about a year. *Pingree and LeCann* [1993] also identified eddies shed from the slope at Cape St. Vincent, Setubal canyon and Lisbon canyon in response to the complex topography (Fig. 2.6b and c) and the persistence of a topographic eddy is suspected over the Galician Bank [*Hill et al.*, 1998].

There has been reported evidence of poleward flow south of 35°N [i.e. off NW Africa *Barton*, 1990; *Mittelstaedt*, 1991] which shows seasonal persistence, although its connection with the PCC is not yet established.

Summer regime

In the North Atlantic the summer Trade winds have a strong alongshore component which drives upwelling off Iberia from May to October as described in the early works of *Wooster et al.* [1976] and *Fiúza et al.* [1982]. A more detailed study of the wind regime along the coasts of the Iberian Peninsula was made by *Bakun and Nelson* [1991] who calculated wind stress and curl of wind stress on a 1x1° grid from historical merchant ship records. Their results showed that the near shore region from Iberia to 15°N is characterised generally by cyclonic wind-stress curl (positive) during the upwelling season, which causes in turn a divergence and consequent Ekman pumping enhancing the coastal upwelling. However, local wind patterns near the coast may be significantly affected by orographic influences due to the presence of capes and Rias locally enhancing upwelling [*McClain et al.*, 1986].

The upwelling favourable winds during the summer have a marked oscillatory pattern from March till October as revealed by harmonic analysis of 9 years of daily averaged

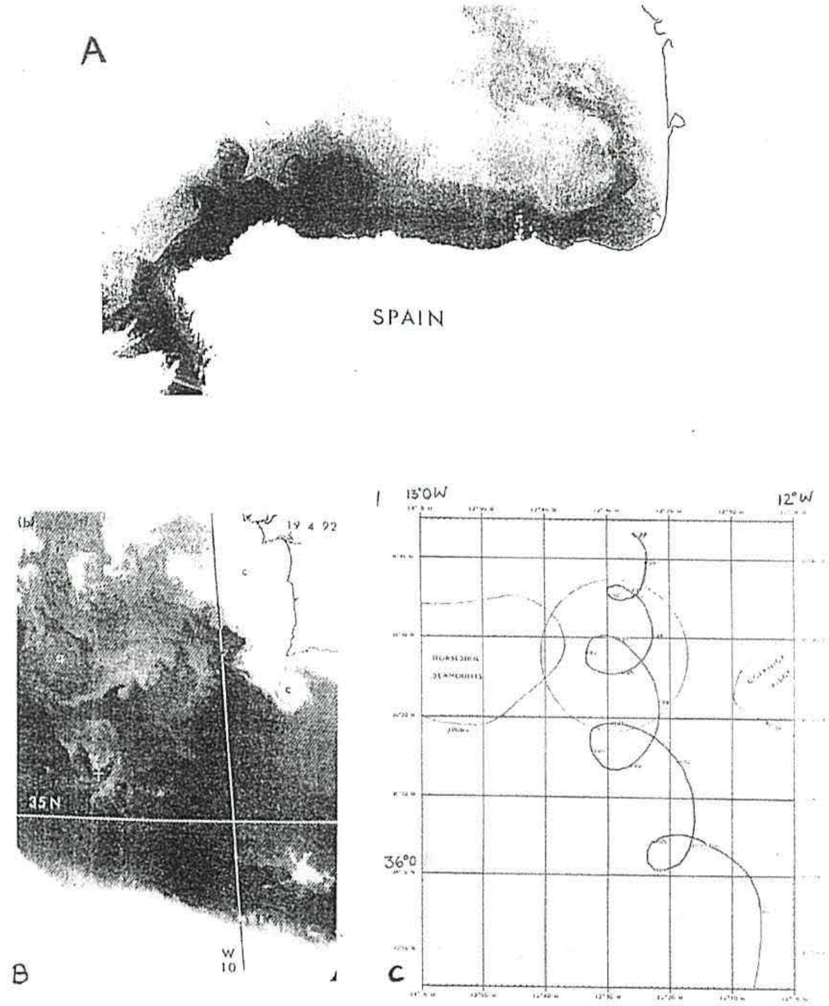

Figure 2.6.: Eddy signatures along the Iberian coast. (a) Infrared image (NOAA 10, 28 Dec. 1989) showing warm surface water flowing along the west and northern Spanish slopes and swoddy formation. (b) Infrared image (NOAA 12, May 5, 1992) showing the development of a cyclonic eddy off Cape St. Vincent (labelled c). (c) Track of buoy 3906 (drogued at 800m) with daily positions marked, showing typical 4-day period and southward translation (5km/d). A circle of 35km is shown to indicate the scale of the eddy core. ((a) from *Pingree and LeCann* 1990, (b,c) from *Pingree and LeCann* 1993).

upwelling indices deduced from geostrophic winds estimated for a cell centred at 43°N 11°W, 150km off Cape Finisterre [*Nogueira et al.*, 1997]. The wind displays a quasi-periodic component of T=15±5 days during the upwelling season. This time structuring is imposed on the shelf ecosystem and is in part responsible for the high productivity of the area. *Nogueira et al.* [1997] also concluded that the downwelling season has a less regular pattern, with the dominant mode of variation being T~ 30±20 days.

Continental shelf and slope waters off the western and southern Iberian Peninsula are dominated during the summer months by strong coastal upwelling. The associated baroclinic equatorward jet (Fig. 2.7), the Portugal Coastal Current (PCoC) [*Ambar and Fiúza*, 1994], attains velocities of 15-20cms^{-1} [*Fiúza*, 1984; *McClain et al.*, 1986]. A strong temperature front, separating the cold recently upwelled water from the offshore oceanic water (Fig. 2.7), develops in close relation to the bathymetry of the continental shelf and slope and to the coastal morphology [*Fiúza*, 1983]. The time response of the system to local wind forcing was estimated by *Sousa* [1986] to be less than 24hrs in the Portuguese coast, as expected from such a dynamic system, although *McClain et al.* [1986] give values of 3 days for the Galician coast. The time evolution of the system includes further distortion of the front and development of meanders, eddies and filaments following a seasonal pattern [*Haynes et al.*, 1993].

During the upwelling period, the wind forcing is opposite to the poleward density gradient but the PCoC equatorward geostrophic jet is enough to counter the poleward slope current at and near the surface so that southward flow is established. However, below 100-200m the flow is still poleward [*Haynes and Barton*, 1990; *Huthnance et al.*, 2002]. Spectral analysis of long-term moored current-meters have shown the presence of signals in the period range of 40-70hrs, which match the characteristics of the second mode of continental shelf waves compatible with the local stratification and bottom topography [*Fiúza et al.*, 1996]. These waves could play a significant role in accommodating the eastward flow of ENAW [*Huthnance*, 1995] and in driving part of the poleward undercurrent as suggested in the Californian upwelling system [e.g.

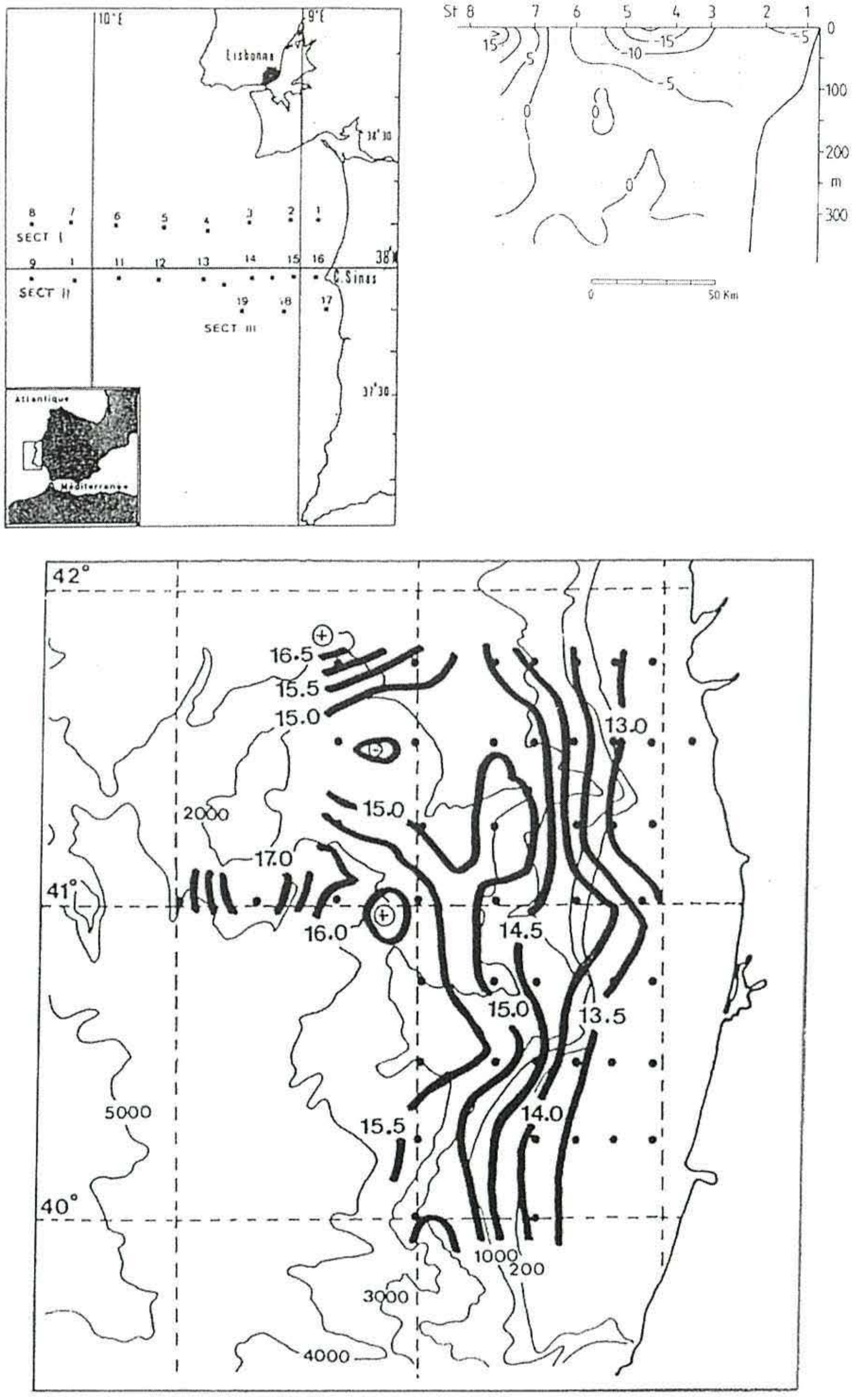

Figure 2.7.: (a) Location of stations sampled in August September 1981. (b) Section showing the meridional component of geostrophic velocity (computed relative to 300 dbar and expressed in cms^{-1}); negative values represent southward flow [*Fiuza* 1983]. (c)Temperature distribution at 50dbar in September 1994 showing the anchorage of the upwelling front to the shelf break [*Fiuza* 1996].

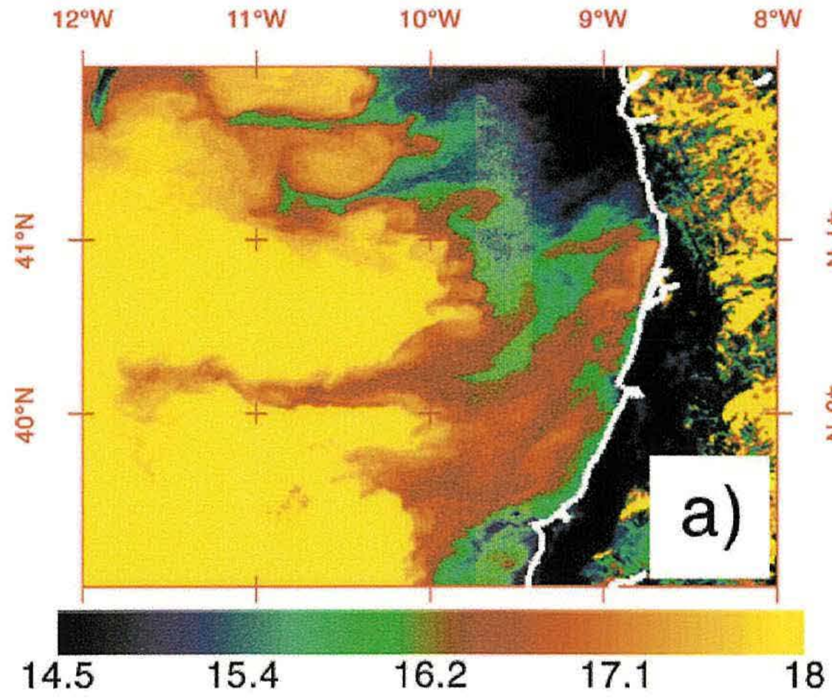

Figure 2.8.: AVHRR Channel 4 brightness temperatures of the Western Iberian coast. NOAA-14 in 24/08/98 at 03:58 UTM. The HRPT data were received at the Dundee Satellite Receiving Station and processed at IPIMAR [*Peliz et al.*, 2002]

Wang, 1997]. Their relevance in the Iberian system is yet to be established.

Patterns of mesoscale variability

Early in the eighties, *Fiúza* [1983] suggested the strong 3-dimensionality of the Iberian Upwelling system identifying an upwelling front strongly deformed by meanders, mesoscale eddies and filaments (Fig. 2.8), cold tongues of recently upwelled waters extending offshore some hundreds of km. Capes such as Cape St. Vincent [*Sousa*, 1986; *Relvas de Almeida*, 1999], or Cape Finisterre [*Blanton et al.*, 1984] are also involved in the promotion of localized or intensified coastal upwelling introducing an important component of spatial variability into the system.

The large mesoscale features of the region, in particular the filaments, follow a strong seasonal fluctuation similar to the California Upwelling System, in strong relation to the seasonal wind pattern. At the beginning of the upwelling season, May-June, a narrow band of colder water of quite uniform width develops along the coast, often consisting of many narrow "fingers" of cool water extending 20-30km offshore [*Haynes et al.*, 1993]. Those features have been successfully modelled in a $1\,^1/_2$ layer model by *Røed* [1996] for the Iberian region including realistic topography and coastline geometry. Linear stability analysis has also suggested that front waves of wavelengths about 20km appear first [*Barth*, 1994] in response to frontal instability [e.g. *Washburn and Armi*, 1988; *McCreary et al.*, 1991] which feeds from potential energy stored in the lateral density gradient.

The narrow band might temporarily disappear after relaxation or poleward wind events and is not until July or August that the fingers merge in preferred locations to form filament structures. Statistical analysis from *Haynes et al.* [1993] spanning over 9 years (1982-1990) showed filaments reached a mean length of 80km (30km seaward of the upwelling coastal band) in July and then continued growing until reaching a maximum mean length of 130km in late September (Fig. 2.9). Similar growth rates were found for the largest filaments which can reach over 250km in late September. Filaments seem to weaken towards the end of October and to disappear on a time scale of the order of a week once upwelling stops [*Haynes et al.*, 1993]. Similar seasonal increase in the strength of mesoscale meanders, filaments and eddies was observed for the Californian System during one year GEOSAT altimeter data by *Flament et al.* [1989]. The expected lifetime of the filaments ranges from 1 to 3 months [*Haynes et al.*, 1993; *Mendes de Sousa*, 1995].

Strub et al. [1991] suggested three possible mechanisms for filament formation, namely "squirts", meandering jet and pre-existent eddy field. Only the first two were identified as possible generating processes in the Iberian System [*Haynes et al.*, 1993]. "Squirts" respond to nearshore convergences while the meandering jet has been identified as a consequence of baroclinic instability and both are affected by the coastline and bathymetry as suggested by *Sousa and Bricaud* [1992] and *Haynes et al.* [1993] for the Iberian filaments. The pre-existent eddy field implies that eddy pairs interact to drag cold water seaward but the deterministic nature of the filaments

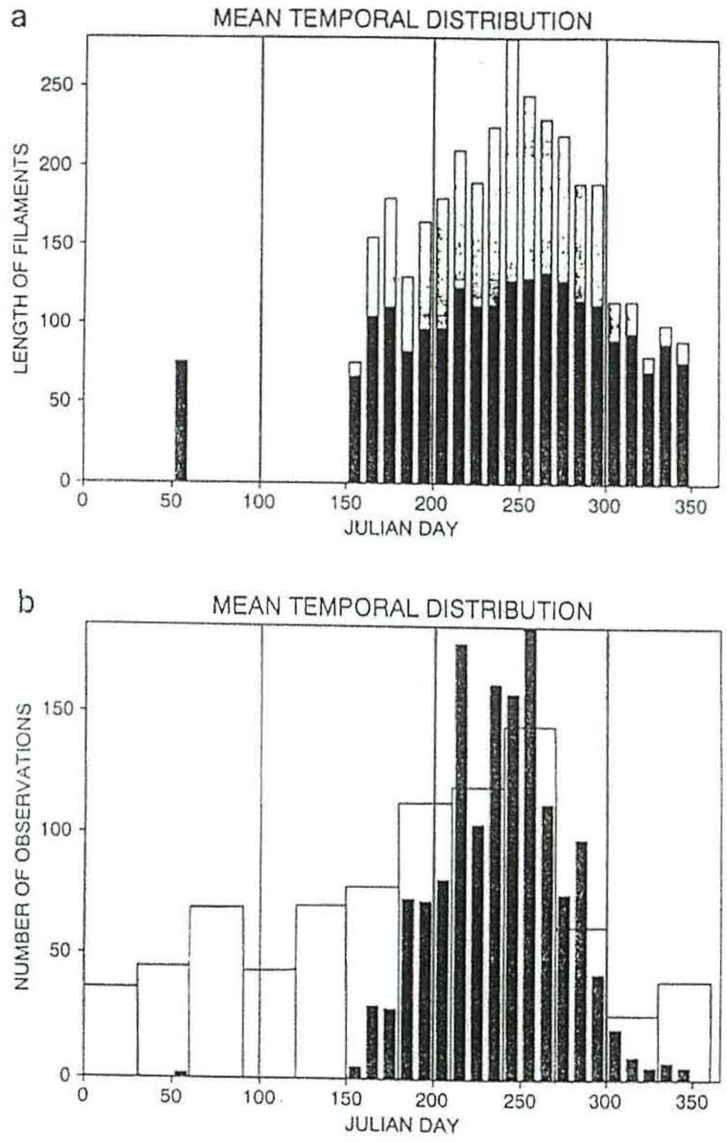

Figure 2.9.: (a) Temporal evolution of the mean length (solid bars) and greatest observed lengths (grey bars) of filaments from the brightness temperature scene archive (1982-1990). (b) Temporal evolution of the number of observed filaments per 10 day interval (solid bars). Open bars indicate the number of images available for 30-day periods [*Haynes et al.*, 1993].

means that a truly random interaction of oceanic eddies with the coastal transition zone is not possible.

Haynes et al. [1993] identified 5 major filaments in the Iberian coast which recur every year in the same position. They are associated with topographic features of the region, mainly capes such as Cape Finisterre and Cape Ortegal in the Galician coast of Iberia and Cape Roca, Cape Sines and Cape São Vicente in the Portuguese coast. Their results were later confirmed by *Mendes de Sousa* [1995] in a similar analysis of 11 years of AVHRR data (1979-1989) in which filaments were consistently associated with submarine ridges. Laboratory experiments in a rotating tank [*Narimousa and Maxworthy*, 1989] have successfully reproduced a meandering upwelling jet and filaments in the presence of ridges owing to the topographic effect and potential vorticity conservation. Modelling work done by *Røed* [1996] also reproduced the observed distribution of the Iberian filaments and their time persistence. Energy consideration within the model identified frontal instability as the baroclinic instability responsible for the generation and growth of eddies and filaments, while potential vorticity considerations suggested that coastline and topography irregularities provide sufficient background perturbation for the frontal instability mechanism.

Few in situ surveys have been carried out to determine the 3-d structure of filaments, the recent MORENA project being one of the best examples [*Fiúza*, 1996]. Hydrography and ADCP surveys showed filaments extended 100-200km offshore. They were 30-50km wide and penetrated to 250m deep near their shelf-edge "root", but diminished offshore to 20-30km in width and 50m in depth. The classical view of strong offshore baroclinic flow was supported by the geostrophic velocities calculated from the hydrographic data which displayed a surface core velocity of $0.5ms^{-1}$ decreasing to about $0.05ms^{-1}$ at depths of 150-200m (Fig. 2.10). Some irreversible mixing of filament and ocean waters is expected and filaments would play an important role in the exchange between the shelf and ocean [*Huthnance*, 1995].

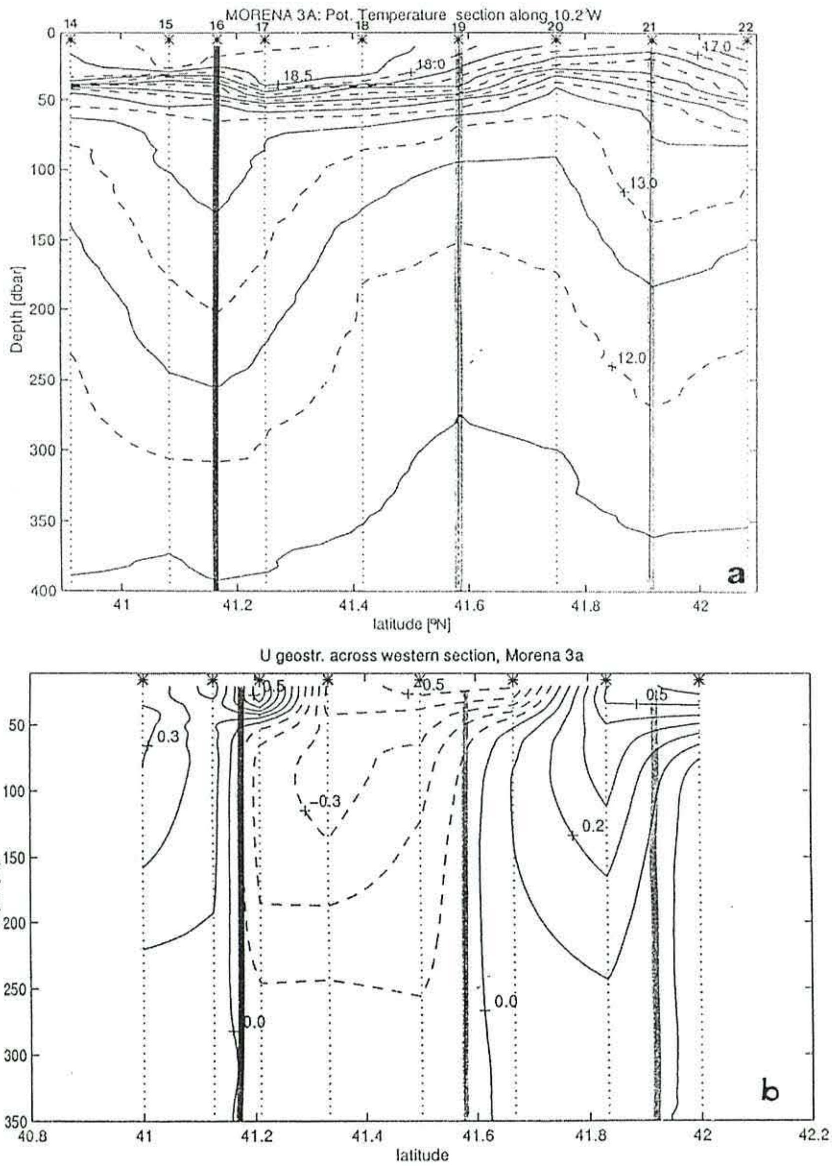

Figure 2.10.: (a) Meridional temperature section along 10.2 W carried out in the 6-7 August 1994 and (b) geostrophic velocity section along the same line calculated relative to 350dbar. Positive values indicate offshore velocities [*Fiúza* 1996].

Dynamic features of the upwelling system off the Western Iberian coast, like the 'event' scale variability, the existence of a frontal alongshore jet, and the omnipresent poleward slope undercurrent have parallels in all the major upwelling regions [*Barton et al.*, 1998]. A summary of the main characteristic of the Iberian upwelling can be seen in Table 2.1.

Principal climatic influence	**Principal Oceanic influence**	**Topography**	**Freshwater influence**	**Winds**
Azores High	Portugal Current	Narrow shelf	Small, Spanish Rias in the north	NE trades (summer)
Tides	**Poleward flow**	**Equatorward flow**	**Upwelling**	**Filaments**
Internal tide generations, solitons	Along shelf edge, turn 90°to flow along North Spanish slope	Portugal Coastal Current	37°-43°N	130km mean, 270km maximum, 5 main sites
Fronts	**Eddies**	**Quasi-permanent eddies**	**Coastal Trapped Waves**	**Short-term variability**
Upwelling fronts	Generated off Cape St Vincent	Over offshore banks?	Not known	Not known
Seasonal variability	**Interannual variability**	**Special features**		
Upwelling in summer, Poleward flow in winter	Not reported	Divided from NW Africa eastern boundary by Strait of Gibraltar		

Table 2.1: Summary of Phenomena and Processes in the Iberian Eastern boundary.

2.1.4 Water-Masses in the Iberian coast

The NW Iberian upwelling region is the least productive of the oceanic eastern boundaries [*Castro et al.*, 2000]. Pacific and Indian oceans present considerably higher nutrients and lower oxygen levels than the Atlantic ocean [*Levitus et al.*, 1993]. The Galician coast is situated in the region of the ventilated thermocline where ENAW

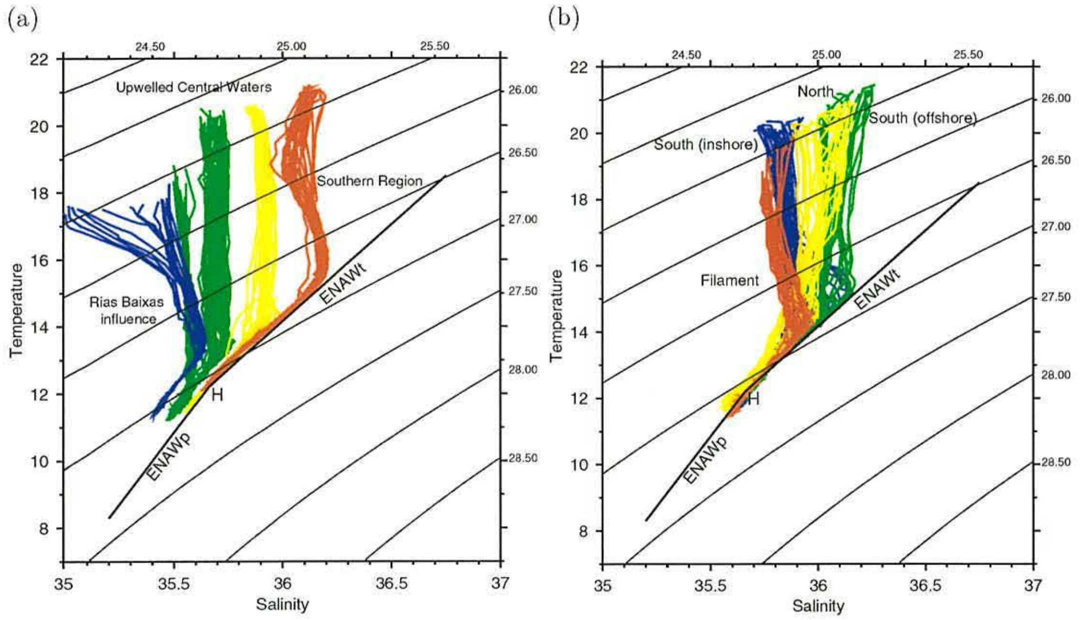

Figure 2.11.: T/S curves for selected groups of SeaSoar profiles between Rias Baixas and southern Portugal revealing the wide range of variation alongshore. (a) Characteristic T/S profiles of the different upper-layer sub-ambiences likely to be found in the Iberian Atlantic coast, (b) strong contrast of the Cape Roca filament with respect to surrounding waters. Also shown are the characteristic lines of $ENAW_P$ and $ENAW_T$ [*Barton et al.*, 2002, in preparation].

forms [*Ríos et al.*, 1992], and consequently, ENAW upwelled along the Galician coast exhibits low nutrient enrichment by oceanic ageing compared to ENAW that upwells off the African coast [*Castro et al.*, 2000].

Different water masses can be identified off the Iberian Atlantic coast where the water column can be divided into upper (first 100-200m), intermediate (to a depth of 1300) and deep (from 1300m to the bottom) layers.

The upper layer during winter months corresponds to a mixed layer, produced by wind stress mixing, of surface fresh water from precipitation and river runoff, while during summer months it displays a seasonal thermocline. Below the thermocline, ENAW can be identified. Recently the ENAW has been subdivided by various authors depending on its provenance. North of 46°N, the formation of the subpolar mode of $ENAW_P$ takes place during the winter ventilation in the Atlantic subpolar gyre and it is characterised by temperatures and salinity between 4°C, 34.96 psu and 12°C, 35.66psu [*Ríos et al.*, 1992]. The warm and salty subtropical mode $ENAW_T$ forms near the Azores front at about 34°N as a result of evaporation and deep winter convection [*Fiúza*, 1984]. It is carried eastward by the Azores current until the northern vicinity of Madeira where it splits into an anticyclonic branch constituting the southward Canary Current and a cyclonic branch flowing poleward along the western Iberian slope, the PCC [*Fiúza et al.*, 1998]. The characteristics of the $ENAW_T$ are defined as 12.2-18.5°C and 35.66-36.75psu [*Fiúza and Halpern*, 1982; *Ríos et al.*, 1992], coinciding in part with the definition of North Atlantic Central Water given by *Helland-Hunsen and Nansen* [1926]. Both characteristic lines can be seen in Fig. 2.11.

The upwelled water is generally the subtropical mode of $ENAW_T$ (Fig. 2.11) but $ENAW_P$ can also be found in the north ($>$ 40°N), underlying the subtropical mode at depths between 250 and 550m (Fig. 2.12). The southward jet-like surface flow then transports both ENAW branches towards the south along the upper slope/outer shelf zone. The poleward extent of the subtropical ENAW is strongly related with the PCC but its northernmost limit constitutes the subsurface front (Galicia Front) in the region of Cape Finisterre (43°30'N) between $ENAW_T$ and $ENAW_P$ [*Fraga et al.*, 1982; *Fiúza*, 1984]. The Galicia front has recently been identified by a strong pigment signal in CZCS images suggesting localized phytoplankton blooms [*Peliz and Fiúza*, 1996].

The upper layer along the Portuguese coast exhibits significant variability particularly in its salinity signature (Fig. 2.11), ranging from 35.0psu to 36.2psu due to a combination of surface warming, upwelling of central waters (both $ENAW_T$ and $ENAW_P$) and mixing with river runoff [*Barton et al.*, 2002, in preparation].

The MIW occupies most of the intermediate layer in the Portuguese coast and is defined by two cores (MW_U and MW_L in Fig. 2.12). The upper core (800m) is characterized by a relative temperature maximum, 13°C, and salinity of 36.4psu, [*Ambar and Howe*, 1979; *Fiúza et al.*, 1998] concentrated against the slope in close relation with the poleward PSU. The MIW lower core (at 1200m) is better characterized by its salinity maximum, 36.6psu and temperature of 12.2°C [*Ambar and Howe*, 1979].

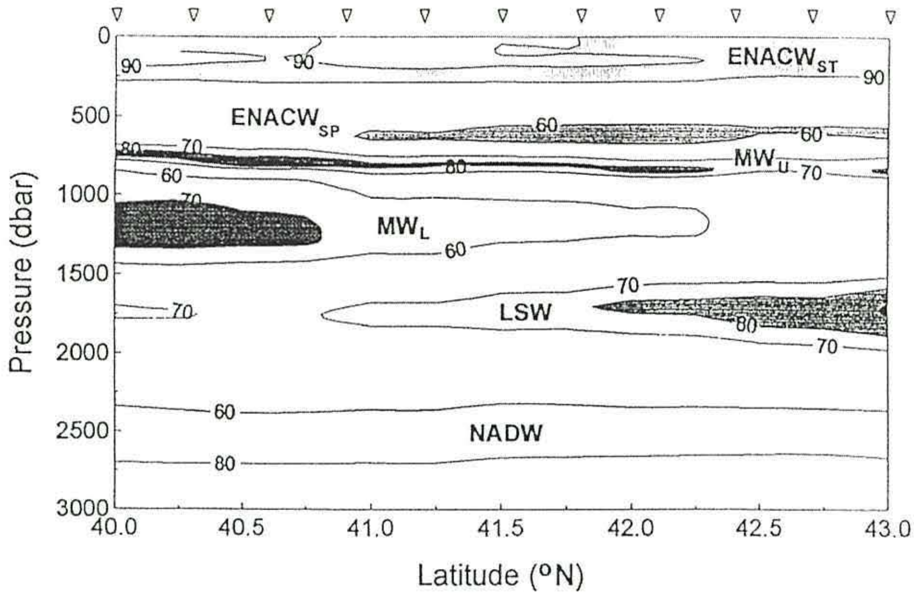

Figure 2.12.: Percentages of the different water masses as indicated by their abbreviated designations (st and sp meaning subtropical and subpolar respectively), calculated using θ/S mixing triangles along a meridional section at 10°W. The positions of the CTD stations collected during May 1993 are indicated by small triangles along the top of the figure [*Fiúza et al.*, 1997].

The lower core is generally broader and more variable, but on the mid-slope is strong and persistent [*Hamann et al.*, 1996]. The MIW is modified along the Portuguese coast by mixing with the overlying ENAW and so loses its original characteristics as it progresses northwards (becoming colder and less saline) until it reaches Cape Finisterre (43°N). There *Ríos et al.* [1992] found a strong salinity front, beyond which the MIW presence was significantly decreased.

In the bottom layer, below 1300m, an isopycnic layer of low temperature and salinity is commonly found as a result of strong mixing between the MIW and North Atlantic Deep Water (NADW) on its way to the south [*Ambar and Fiúza*, 1994].

2.2 Eastern Boundary Dynamics

Wind-driven currents are a common feature of the continental shelves and together with tides they constitute the most energetic, best-observed and best-modelled form of variability over the continental margins [*Brink*, 1998]. In eastern boundaries, equatorward winds induce net offshore surface Ekman transport which brings about transport divergence near the coast and upwelling of subsurface waters to maintain continuity in the cross-shelf section. The basic mechanisms of wind-driven coastal upwelling are well understood and there are several excellent reviews of upwelling systems [e.g. *Allen*, 1980; *Brink*, 1998]. Other features associated with forcing of finite extent [e.g. opposing undercurrent and propagation of upwelling by coastal trapped waves) were reviewed by *Huthnance* [1981] or *Brink* [1991]. The Californian upwelling system has been the subject of the most comprehensive and extensive studies such as CalCOFI, California Cooperative Fisheries Investigations [*Lynn and Simpson*, 1987], CODE, Coastal Ocean Dynamics Experiment [e.g. *Kosro and Huyer*, 1986], OPUS, Organization of Persistent Upwelling Structures, [e.g. *Atkinson et al.*, 1986] and CTZ, Coastal Transition Zone [*Strub et al.*, 1991], while other Eastern Boundaries Systems have raised less international attention, e.g. Peru [*Smith*, 1981], NW Africa [*Mittelstaedt*, 1983], Benguela Upwelling System [*Andrews and Hutchings*, 1980] and West Iberian Peninsula with the MORENA, Multidisciplinary Oceanographic Research in the Eastern boundary of the North Atlantic [*Fiúza et al.*, 1996] and the recently concluded OMEX II, Ocean Margin Exchanges [*Huthnance et al.*, 2002].

2.2.1 Surface Ekman layer

Currents varying on time-scales of days or longer tend to be constrained by geostrophy to flow along depth contours. However, frictional Ekman layers together with local, non-linear and time dependent flows may relax the geostrophic constraint and contribute to the ageostrophy of the flow.

The actual contact between wind forcing and the ocean occurs within the turbulent surface boundary layer, generally called the Ekman layer. The depth of this layer, typically 10-100m, is determined by competition between the stabilising effect of surface heating and the destabilising effects of turbulence generation by wind input, but also from surface cooling, breaking waves, or unstable shears in the water column [*Brink*, 1998].

Within the surface boundary Ekman layer, the solution to the governing equations of motion can be found to be a function of the vertical coordinate only (see *Pedlosky*, 1987, for a full description of the equations of motion):

$$u = u(z); v = v(z); w = w(z), \tag{2.1}$$

so that from the continuity equation

$$\frac{\partial u}{\partial x} + \frac{\partial v}{\partial y} + \frac{\partial w}{\partial z} = 0, \tag{2.2}$$

we obtained that $\frac{\partial w}{\partial z} = 0$. From the surface boundary condition of $w(0) = 0$, it follows that w must be zero at all depths. The coordinate system adopted is that in which x is the cross-shelf coordinate (positive onshore), y is the alongshore coordinate (positive poleward), and z is the vertical coordinate (positive upward).

Since the fluid is homogeneous, from the hydrostatic approximation it follows that the horizontal pressure gradient must be independent of z, and it is therefore entirely determined by any geostrophic velocity far from the boundary. Ignoring any flows associated with horizontal pressure gradients is reasonable as long as the pressure related flow is not too strong; that is, the (interior) Rossby number

$$R_o = \frac{v^*}{fL}, \tag{2.3}$$

(where v^* is a typical interior velocity, f is the Coriolis parameter and L a representative horizontal length scale) is small.

The basic force balance is then reduced to the local acceleration, Coriolis and the vertical gradient of turbulent stress. If the turbulent stress vanishes at some depth below the mixed layer, then the equations of motion can be vertically integrated to describe the Ekman transport (U_E,V_E):

$$\frac{\partial U_E}{\partial t} - fV_E = \frac{1}{\rho}\tau_0^x, \tag{2.4}$$

$$\frac{\partial V_E}{\partial t} - fU_E = \frac{1}{\rho}\tau_0^y, \tag{2.5}$$

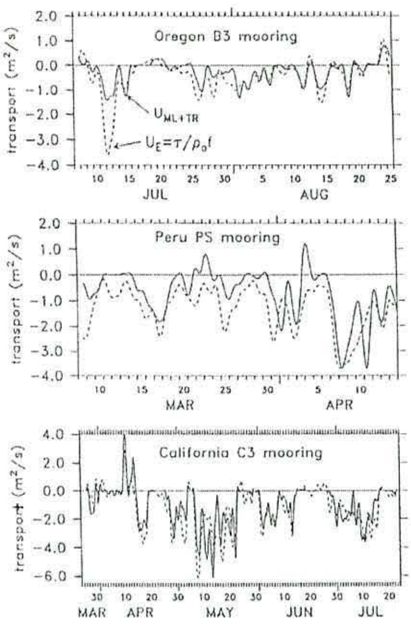

Figure 2.13.: Time series of cross-shelf transport in the surface boundary layer $U(ML{+}TL)$ (Mixed + Transitional Layer, solid line) and the Ekman transport $U_E = \frac{\tau}{(\rho f)}$ (dashed line) from three locations during the upwelling season of 1982 [*Lentz* 1992].

where U_E,V_E are the vertically averaged velocities in the Ekman layer, ρ is the density in the mixed layer and τ_0^x, τ_0^y are the wind stress applied at the surface in the x and y directions. Assuming a wind stress of the form

$$\tau_0^y = T \cos \omega t, \tag{2.6}$$

with no component in the across-shelf (x) direction yields a solution

$$U_E = \frac{fT}{\rho}(f^2 - \omega^2)^{-1} \cos \omega t, \tag{2.7}$$

$$V_E = \frac{-\omega T}{\rho}(f^2 - \omega^2)^{-1} \sin \omega t, \tag{2.8}$$

where T and ω are the amplitude and frequency of the wind stress. In the low frequency limit ($f \gg \omega$), rotational effects dominate and the Ekman transport is perpendicular to the wind stress. In the high frequency limit ($f \ll \omega$), the transport is downwind but lags by a quarter cycle. When $f = \omega$ resonance takes place.

In most cases, the low frequency limit is an adequate description which basically

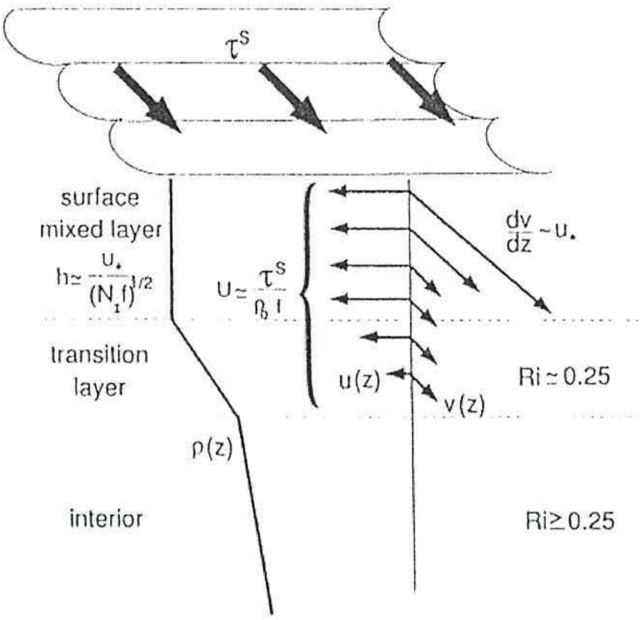

Figure 2.14.: Schematic summarizing some of the characteristics of the surface boundary layer in a coastal upwelling region: $u^* = (\frac{\tau^s}{\rho_0})^{\frac{1}{2}}$ is the shear velocity and U is the cross-shelf transport in the surface mixed layer plus the transition layer [*Lentz* 1992].

reduces eq. 2.7, 2.8 to the theoretical Ekman transport $(\rho f)^{-1}\tau_0^y$, which is completely determined in terms of the local value of the y-component of the wind stress. Substantial effort has been directed towards the verification of the theoretical Ekman transport [*Smith*, 1981; *Brink*, 1983], especially in coastal upwelling regions. *Lentz* [1992] reported experiments in 4 coastal upwelling regions which demonstrated good agreement in magnitude and variability between the observed cross-shelf Ekman transport and the theoretical value (Fig. 2.13) but only when he allowed for the surface Ekman layer being about 25-50% deeper than the surface mixed layer including a transitional stratified layer of near critical Richardson number (~0.25). The subtidal surface mixed layer depth was found to be well described in terms of the wind-induced shear velocity ($u_* = (\frac{\tau_0^y}{\rho_0})$) , the Coriolis parameter (f) and the buoyancy frequency below the mixed layer (N_I) in the form

$$\delta_E = \frac{u_*}{(N_I f)^{\frac{1}{2}}}. \tag{2.9}$$

It was found no account need be made for the surface heat flux and heat advection as they tend to balance each other in the coastal upwelling regions studied. Fig. 2.14

shows an schematic of the upper water column geometry in coastal upwelling systems.

Secondary pressure related flows can become important and influence Ekman layer processes. Vorticity of the background flow allows convergences and divergences in the Ekman transport even under the effects of a uniform wind [*Niiler*, 1969].

Coastal wind-driven upwelling

In a coastal context, wind-driven flows can be described by depth-integrated equations of motion where nonlinearities and density variations are not allowed:

$$\frac{\partial U}{\partial t} - fV = -\frac{1}{\rho}h\frac{\partial p}{\partial x} + \frac{1}{\rho}(\tau_0^x - \tau_B^x), \tag{2.10}$$

$$\frac{\partial V}{\partial t} - fU = -\frac{1}{\rho}h\frac{\partial p}{\partial y} + \frac{1}{\rho}(\tau_0^y - \tau_B^y), \tag{2.11}$$

$$\frac{\partial U}{\partial x} + \frac{\partial V}{\partial y} = 0, \tag{2.12}$$

where U, V are the cross-shore and along-shore depth-integrated transports, $h(x)$ is the water depth and p is the pressure. A rigid lid is assumed for the surface boundary because interest is confined to relatively short spatial scales compared to the barotropic radius of deformation (natural horizontal scale for upwelling and expected distance from the coast of the upwelling front). The bottom stress will be assumed to be proportional to the depth-averaged current,

$$\tau_B^x = \rho r h^{-1} U, \tag{2.13}$$

$$\tau_B^y = \rho r h^{-1} V, \tag{2.14}$$

where r is the drag coefficient.

Solving eq. 2.10, 2.11 and 2.12 is easier if the long-wave approximation is made. This assumes that alongshore scales are large relative to cross-shelf scales, $(Ly \gg Lx)$, time scales of interest are long relative to the inertial period, $(f \gg \omega)$(more specifically, longer than the sum of the inertial period and the frictional e-folding time dependent on the depth [*Dalu and Pielke*, 1990]) and finally that frictional effects are not too large ($f \gg rh^{-1}$). This approximation is justifiable as the major upwelling systems are induced by large scale wind patterns characterised by alongshore spatial scales larger than the shelf-slope width and weather changes do occur at time scales longer than several days.

The long-wave approximation has as a main consequence that alongshore flows are stronger than cross-shelf flows which is a common characteristic of upwelling systems [e.g. *Batteen*, 1997], and that the alongshore flow is in geostrophic balance due to the scaling of eq. 2.10 (cross-shelf wind and bottom stress and local cross-shelf acceleration can be neglected relative to the Coriolis and pressure terms):

$$-fV = -\frac{1h}{\rho}\frac{\partial p}{\partial x}. \tag{2.15}$$

The main failure of the scaling approximation resides in the alongshore uniformity of the wind and topography. It is well established that coastal irregularities such as capes or bays may induce wind stress variations (Fig. 2.15) which are of major importance in the evolution and final equilibrium state of upwelling systems [e.g. *Haynes et al.*, 1993; *Enriquez and Friehe*, 1995]. Furthermore, lateral wind stress gradients can induce Ekman pumping and enhance the baroclinicity of the alongshore flow [*Brink et al.*, 1987; *Batteen et al.*, 1992].

Nevertheless the above simplified model can be solved for a spatially uniform constant alongshore wind $\tau_0^y = T$, with no alongshore variations allowed, $\frac{\partial}{\partial y} = 0$ so that continuity reduces to

$$\frac{\partial U}{\partial x} = 0. \tag{2.16}$$

On the coastal boundary the no cross-shelf flow must applied so that the depth-integrated cross-shelf transport must vanish everywhere, which reduces eq. 2.11 to

$$\begin{aligned} U &= -\tfrac{1}{f}\tfrac{\partial V}{\partial t} + \tfrac{1}{\rho f}\tau_0^y - \tfrac{rV}{fh} = 0 \qquad (2.17)\\ &\equiv U_I + U_{E0} + U_{EB} = 0, \end{aligned}$$

where U_I is the interior transport, U_{E0} is the surface Ekman transport and U_{EB} is the bottom Ekman transport. Basically, the surface Ekman flow is compensated by

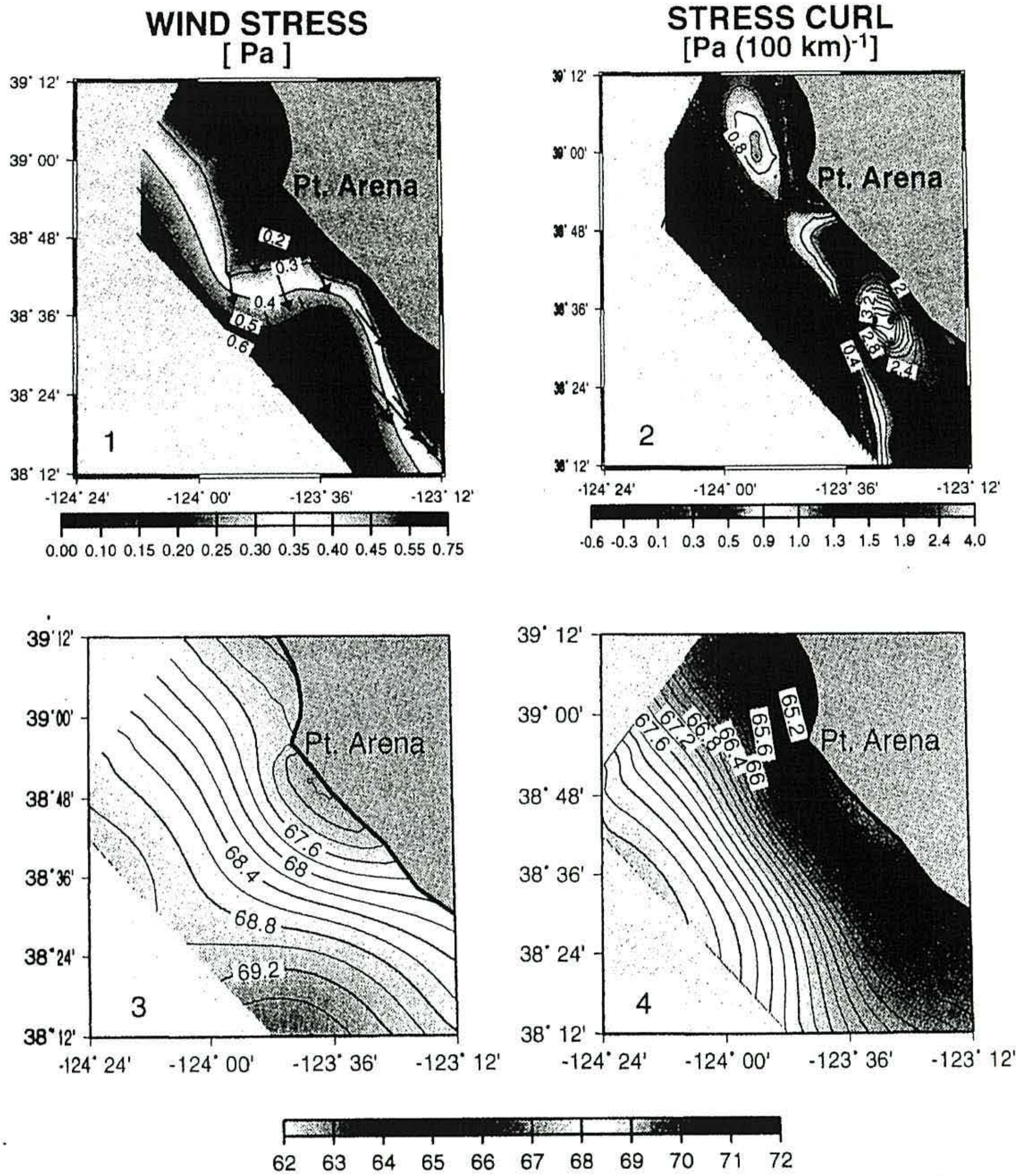

Figure 2.15.: Aircraft wind measurements acquired during CODE 2 experiment (summer 1982) from which (1) wind stress (Pa) and (2) wind stress curl (Pa/100km) were computed. (3) and (4) show simulations from a simple, two layer, vertically integrated model of coastal upwelling. They represent the upper-layer thickness (in m) after 24 hours of simulation using observed wind stresses, (3) without curl and (4) with curl. Note how the nonzero stress curl enhanced coastal upwelling, the greatest effects being around the areas of largest observed curl values [*Enriquez and Friehe*, 1995].

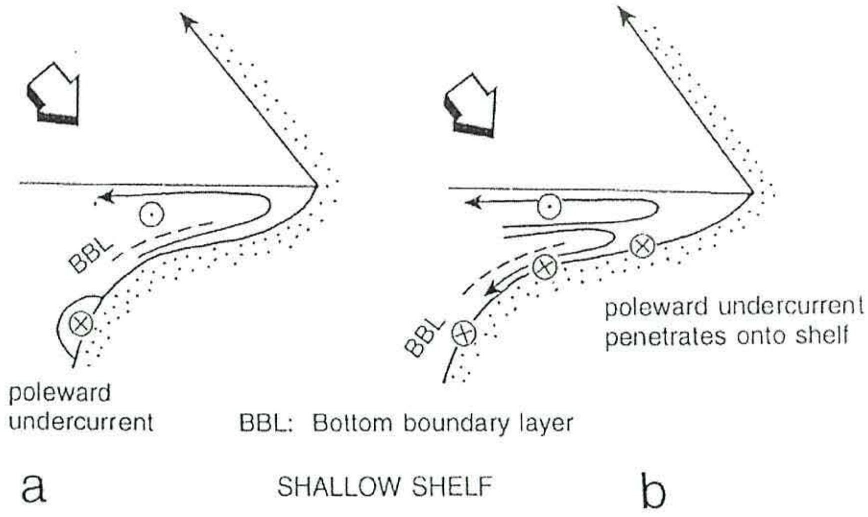

Figure 2.16.: Schematic of coastal upwelling: (a) upwelling over a shallow frictional shelf where the equatorward flow on the shelf penetrates to the bottom and bottom Ekman transport is onshore, supplying the upwelling waters; (b) upwelling over a shallow frictional shelf when the poleward undercurrent penetrates the shelf and the bottom Ekman layer transport is offshore and upwelling water are supplied from middepth [*Hill et al.*,, 1998].

flows deeper in the water column sufficiently far from the coastal boundary where lateral friction and vertical velocities can not be neglected. Solving eq. 2.17 for V is straightforward in a system starting from the rest, i.e. $V = 0$ at $t = 0$:

$$V = \frac{hT}{r\rho}[1 - \exp(-rh^{-1}t)]. \tag{2.18}$$

It can be seen that for $t \ll rh^{-1}$ the alongshore flow accelerates steadily at a rate,

$$V \approx \frac{T}{\rho}t, \tag{2.19}$$

so that the surface Ekman flow is compensated mainly from the interior flow. At larger times, $t \gg rh^{-1}$, the interior flow disappears ($\frac{\partial V}{\partial t} = 0$) reaching a steady state and the surface Ekman flow is now compensated entirely by the bottom Ekman flow, i.e. the flow is entirely frictional determined (Fig. 2.16). More generally, however, this equilibrium is not reached; acceleration, stratification and the ignored along-shore pressure gradients also distribute the stress and upwelling through the water column [*Huthnance*, 1995].

Upwelling systems are generally highly time-dependent and respond rapidly to wind stress fluctuations. Initially the upwelling favourable winds drive an offshore Ekman flow which forces the interface (seasonal thermocline) beneath the upper layer to rise near the coast at a distance defined by the Rossby radius of deformation,$R' = \frac{HN}{f}$ where H is the depth of the mixed surface layer, usually taken to be the same as the surface Ekman layer, and N is the buoyancy frequency below the mixed layer, generating geostrophically balanced alongshore currents, namely an equatorward coastal jet and a poleward undercurrent. The upwelled water band width,R', will be also governed by the time integrated offshore Ekman transport , so that the band tends to be narrower where the upwelling-favourable winds are intermittent (e.g. Oregon) and broader where winds are steadier and stronger (e.g. California) [*De Szoeke and Richman*, 1984]. Sufficiently far ($> \frac{HN}{f}$) from the coast the inflow is uniform through depth without a vertical component, as described by eq. 2.17. In the presence of stratification, an upper layer of characteristics H_1N_1 over a 2^{nd} layer of $H_2N_2(H_1N_1 > H_2N_2)$ gives a majority of upwelling inflow in the upper layer within ($> \frac{H_1N_1}{f}$) of the coast. The magnitude of the alongshore current in the coastal jet and the horizontal scale of the coastal jet also depend on stratification increasing as N^2 increases, whereas weaker stratification enables the front to develop faster [*Allen et al.*, 1995].

The time evolution of the system will also be affected by diffusive processes induced by upwelling and mixing, which reduce the coastal layer depth and density stratification (H_1N_1) and hence the offshore scale [*De Szoeke and Richman*, 1984]. One non-linear aspect of the system is that the front and surface jet are advected offshore by Ekman drift although they will be generally limited to the shelf, stopping at any shelf break [*Huthnance*, 1995]. The absence of a front over the shelf has been related to sustained favourable upwelling winds, for example in Peru (15°S) or off central California [*Smith*, 1981; *Brink*, 1983].

The front itself is characterised by relatively large horizontal density and alongshore velocity (v) gradient near surface and large vertical gradients in v at mid-depth.

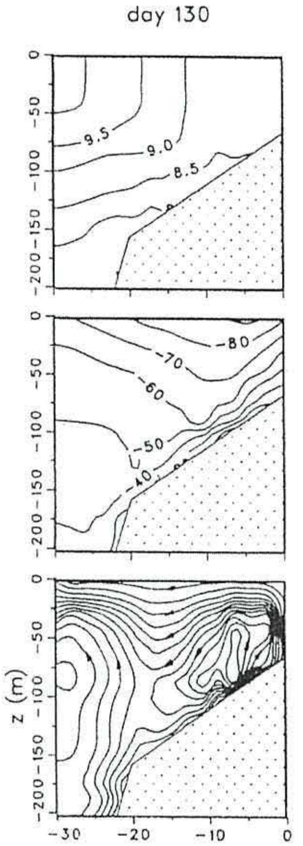

Figure 2.17.: Prediction from a combined two-dimensional circulation model and one dimensional mixed-layer model of cross-shelf structures of Temperature (C)(top), alongshore velocity (cms^{-1})(middle), and stream function (cm^2s^{-1})(bottom). On day 130 the equatorward wind stress is the strongest and the upwelling front moves to the outer shelf. Upwelling takes place in two narrow areas, one at the coast and the other on the seaward side of the front. In association with the convergence and divergence of the upper layer transport, a prominent double-cell circulation is formed [*Chen and Wang,*, 1990].

There is occasionally a convergence of near-surface offshore flow at the front that results in a general increase in depth of the surface turbulent boundary layer across the front [*Allen et al.*, 1995] and that has been suggested to constitute a two cell pattern (Fig. 2.17) [*Chen and Wang*, 1990]. In response to strong winds the front would display a tendency for the surface isotherms to parallel the bottom topography as a result of advection by a nearly uniform Ekman transport while weaker winds produce a complex contouring front [*Brink*, 1983].

A large variety of studies acknowledges the important role of shelf/slope topography in upwelling, a factor which has been neglected to this point in the review. Complex coastal features such as capes, ridges, submarine canyons and submarine banks, which have along-shelf scales that are comparable to or smaller than cross-shelf scales produce flow structures that differ fundamentally from those addressed by the classical theory and are often the site of significant cross-isobath flows [*Trowbridge et al.*, 1998].

The classical assumption of an along-shelf length scale much larger than the cross-shelf length scale leads to an along-shelf flow which is nearly geostrophic even when the Rossby (R_0) and vertical Ekman numbers ($E_v = \frac{A_v}{fH^2}$ where A_v is the vertical mixing coefficient assumed independent of z, and H is a typical vertical scale) approach unity as shown by the scaling of the momentum equations [*Trowbridge et al.*, 1998]. The geostrophic balance is only slightly altered by changes in the cross-shelf velocity caused by ageostrophic processes (mixing and local acceleration). On the other hand, the cross-shelf velocity is likely to be ageostrophic even when the Rossby and Ekman numbers are small, so that small changes in the along-shelf velocity have a major impact on the cross-shelf flow.

Another source of time dependence in upwelling systems is brought about by propagation of disturbances from remote locations by coastally trapped waves (see later) which induce variability on time scales of from 3 to 10 days [*Denbo and Allen*, 1987]. Fig. 2.18 shows an schematic of the common features that can be expected in a coastal upwelling system.

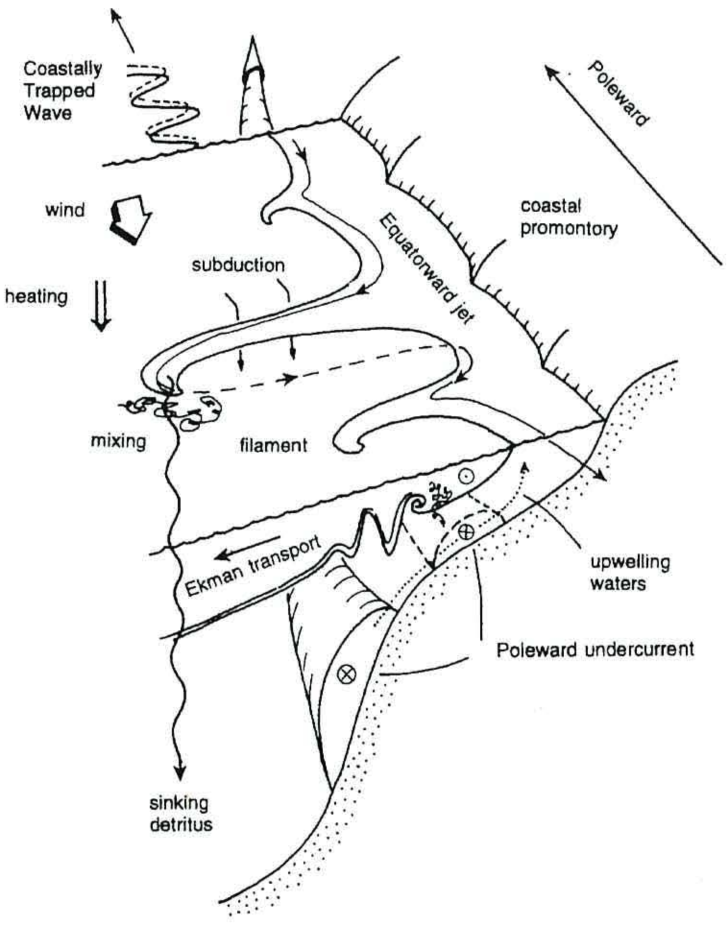

Figure 2.18.: Schematic of an upwelling system showing the varied range of possible physical processes and the complex 3 dimensionality of the system [*Hill et al.,*, 1998].

Most coastal upwelling is produced by along-shelf wind stresses and may be altered greatly by short along-shelf scales in the coastline [*Crépon and Richez*, 1982; *Crepon et al.*, 1984; *Haynes et al.*, 1993; *Wang*, 1997] in turn altering the local direction of the wind relative to the coastline and reducing or enhancing upwelling/downwelling locally. Consequently, along-shelf variations in the pressure gradient will be introduced, which may then propagate along the coast as CTW's [*Crépon and Richez*, 1982] and give rise to a countercurrent below the thermocline opposing the prevailing winds [*Suginohara*, 1982].

Enriquez and Friehe [1995] showed that the wind small-scale spatial variability near Pt. Arena (California) had characteristic scales much smaller than the scales of synoptic atmospheric pressure patterns and calculated local wind stress curl five times larger than those obtained from long-term ship data using bulk aerodynamic formulas. The local coastline (cape) was responsible for a sustained curl pattern which modified the dynamical response of the coastal water to the applied wind stress and resulted in local enhancement of upwelling downwind of the cape during favourable winds (Fig. 2.15). The theoretical study of *Crepon et al.* [1984] also supports upwelling enhancement downwind of a cape relating the intensity to the offshore scale of the cape while the geometry of the cape does not change the process qualitatively. The cape, like the alongshore variability in the wind-stress, generates an undercurrent in the opposite direction to the wind.

The shelf geometry itself also influences the upwelling system. Shallow wide shelves without poleward undercurrent generate large bottom friction and larger Ekman onshore transport which in turn limits the acceleration of the jet so weaker surface jets are expected. The front is wider and occurs further offshore [*Allen et al.*, 1995]. The concentration of depth contours tends to guide and strengthen currents along the continental slope where the sea floor slope exerts an stabilising effect [*Huthnance*, 1981]. In those steep shelves, the vertical gradients of v tend to be more geostrophically balanced so that the frictional bottom boundary layer is weaker and carries less fraction of onshore flow. Near-surface density gradients tend to occur near the coast so that offshore-displaced upwelling fronts may not be observed. [*Allen et al.*, 1995].

2.2.2 Instabilities

Mathematical models investigating the dynamics of upwelling, filaments, squirts and eddies suggest that the phenomena result from instability of alongshore currents, and they all point toward baroclinic instability as being an important process. Several of this models also developed small-scale disturbances along fronts and indicated that other instability mechanisms are involved in their generation as well [*McCreary et al.*, 1991]. In those mathematical models, meanders and eddies increased in scale as the system adjusted toward equilibrium, apparently for different dynamical reasons in each case.

McCreary et al. [1991] reviewed previous stability models and experimented with simpler models to infer two types of instability, as also found by *Barth* [1994] with continuous forms of stratification and coastal current. These two instabilities are: shorter-scale frontal instability depending on gradients of sea-surface temperature, trapped to the front and upper column and extracting potential energy; a larger-scale "traditional" baroclinic instability manifested later in filament development. The vertical shear between an equatorward upwelling front jet and the poleward undercurrent give a mechanism for the generation of baroclinic instabilities as shown by model experiments in the Californian shelf by *Batteen* [1989].

2.2.3 Coastal trapped waves

The sudden change in bathymetry at the shelf-edge imply a large potential vorticity gradient and provide conditions that lead to the trapping of certain wave motions called continental shelf waves or coastal trapped waves [*Huthnance*, 1981]. These waves are commonly generated by transient winds [*Adams and Buchwald*, 1969] and propagate along the shelf-edge, cyclonically around the ocean at sub-inertial frequencies [*Huthnance et al.*, 1986]. They arise from the conservation of potential vorticity as water passes over uneven bottom topography:

$$\frac{d(\frac{f+\xi}{h})}{dt} = 0. \tag{2.20}$$

According to eq. 2.20, if a fluid column is displaced up or down a slope, vortex stretching or compression will tend to move the water back to where it was originally. This results in long, sub-inertial wave forms which propagate cyclonically in the northern hemisphere, with the shallow water on their right. They tend to decay off-shelf but some may be at their most energetic over the slope [*Huthnance*, 1995].

A numerical investigation by *Suginohara* [1974, 1982] of a coastal ocean with cross-shelf topography and vertical stratification underlies the importance of coastal trapped waves in the development of an upwelling circulation including that of a poleward flow of about 2cms^{-1}. *Denbo and Allen* [1987] and others, have shown the importance of Coastal trapped waves in wind-driven currents in the CODE area.

2.2.4 Poleward slope flow

Current along the continental slope can and do occur with non-zero time-average and velocities exceeding or opposing those to either side of the adjacent shelf and ocean [*Huthnance*, 1995]. Poleward slope currents are in fact widespread in Eastern boundaries, and often flow against prevailing equatorward winds as in seasonal upwelling systems (e.g. California) , which suggests a large-scale, non-local forcing of the current. The precise cross-shelf distribution of the flow depends upon the character of the forcing balanced by alongshore pressure gradient, friction and acceleration.

The steep topography of the slope and the influence of Earth's rotation are the primary factors aligning barotropic currents along the depth contours and both continuity arguments and potential vorticity conservation can explain the anchorage of the slope current along the slope region. Usually the poleward flow is located at the shelf break or over the continental slope with a width of the order of 20-100km and current speeds of order of 10cms^{-1}.

The several potential forcing forces are:

- Freshwater runoff resulting in a baroclinic coastal current [*Hill et al.*, 1998] which can include the shelf edge for sufficient runoff and narrow shelf.
- Alongshore pressure gradients imposed by the ocean and incorporating density forcing combined with the slope bathymetry to drive the slope poleward current.

The latter one is of most general ubiquity and was described by *Huthnance* [1984]. It was termed JEBAR, Joint Effect of Baroclinicity And Relief, and refers to the dynamical adjustment of the density-induced pressure gradient to the bottom slope when the zonally orientated density surfaces intersects a meridional sloping boundary (Fig. 2.19). Under no net cross-shore transport and assuming the same meridional density gradient is affecting both the shelf and the ocean, the alongshore sea-level slope is proportional to the bottom depth. On the shelf the sea-level drop is less than in the ocean then generating an offshore pressure gradient which drives the poleward flow along the slope. This pressure gradient increases along-slope therefore accelerating the flow until friction becomes important and a steady state is reached.

In upwelling systems, there also exist local terms forcing the poleward undercurrent which are highly influenced by alongshore variability [*Hill et al.*, 1998]. Some of these possible forcings for undercurrent poleward flow in the face of equatorward wind stress are: remote forcing, relaxation of equatorward wind, the positive curl of equatorward wind stress or thermohaline forcing [*McCreary et al.*, 1987]. Along-slope variations in topography could allow the necessary alongshore pressure gradient to drive the undercurrent as alongshore variations in the wind stress field would do too [*Hill et al.*, 1998]. There are multiple observational evidences of the poleward undercurrent in the Oregon upwelling system but only scattered ones in the Eastern Atlantic coast like N.West Africa where the poleward undercurrent flows below the shelf break [*Mittelstaedt et al.*, 1975; *Barton*, 1990] and on the Portuguese slope where six month long measurements of poleward flow were recorded by *Ambar* [1984, 1985] at levels below 200m in bottom depth less than 1000m. Off Oregon the shelf break

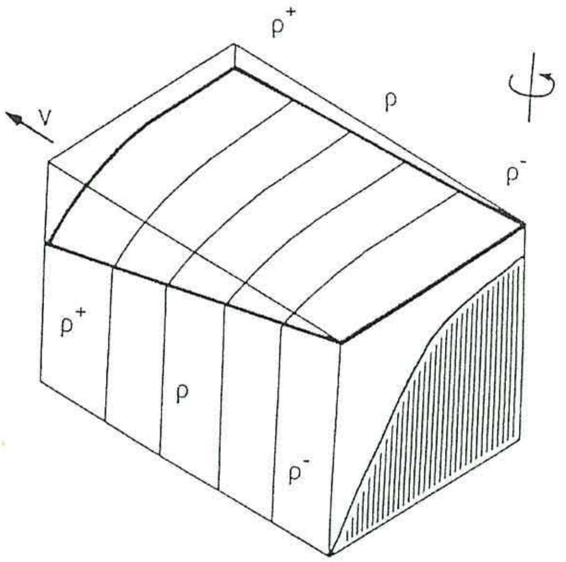

Figure 2.19.: A simple JEBAR model. The sea surface over a shelf-slope region is shown as a thick line. Density increases alongshore and continuity is maintained by a condition of no net cross-slope transport. Sea level declines more gently over shallow water than over deep water hence a steepening cross-slope sea level difference develops which drives a strengthening along-slope current [*Hill,*, 1998].

is less sharp and so the undercurrent is partly on the shelf [*Huyer*, 1976].

CHAPTER

3 The wind regime

3.1 Introduction

In eastern upwelling systems, coastal winds are the major forcing in the residual circulation and largely determine the seasonality of the region. The time scales of the wind forcing are typically of the order of a few days to weeks superimposed on a slowly varying seasonal signal. The seasonal signal influences the residual circulation and thereby the basin scale response.

The coast of Galicia (Spain, Iberia peninsula) constitutes the northern limit of the North Atlantic upwelling regime, which extends from 44° to almost 10°N south of Dakar. During the summer months, when the Azores high-pressure cell is in the central North Atlantic and the Greenland low is weak, the resulting pressure gradient drives the trade wind southward along the coast of Iberia inducing upwelling and associated southward currents. In the winter months, when the Azores high is located further south off NW Africa, and the Greenland low is deep and located off southeastern Greenland, the pressure gradient between the two pressure systems results in an onshore and slightly northward wind off Iberia, and downwelling.

The summer upwelling regime in the Galician coast is highly variable in time and spatially complex; the upper layer responds to rapid wind stress changes in 3 or fewer days [*McClain et al.*, 1986; *Huthnance et al.*, 2002]. Some of the complexity can be related to the irregular coastline, where Cape Finisterre marks the abrupt change between the meridional west and the zonal north coasts of Galicia. Capes or bays may induce important wind stress variations [*Enriquez and Friehe*, 1995], sometimes accelerating the flow to become supercritical [*Winant et al.*, 1988]. Its kinetic energy is then trapped to produce localized upwelling maxima and upwelling filaments e.g. Pt. Conception, California [*Barth and Brink*, 1987].

Finisterre is frequently the site of a stationary upwelling maximum [*Blanton et al.*, 1984; *Castro et al.*, 1994] and a recurrent upwelling filament [*Haynes et al.*, 1993]. The authors found good agreement between the laboratory results of *Narimousa and Maxworthy* [1989] and spatial structure of filaments in the Portuguese and Spanish Atlantic coast and concluded that major capes in the region played an important role in filament formation. They suggested however that the filament near Finisterre was an "overshoot" of the coastal jet when upwelling occurs along the northern coast. *McClain et al.* [1986] noted that different wind directions resulted in upwelling either north or south of Finisterre but not usually both.

The winter onshore wind regime is marked by the formation of a narrow, warm and salty surface poleward current along the Iberian Atlantic continental slope [*Frouin et al.*, 1990; *Haynes and Barton*, 1990], which settles in November and disappears around May. Two main mechanisms have been proposed to drive the poleward flow: wind-stress and thermohaline forcing. *Frouin et al.* [1990] concluded that wind stress could account for only one fifth of the total poleward transport and considered the thermohaline forcing to be the main driving mechanism. The latter is associated with the large scale meridional pressure gradient in the upper 200-300m caused by the poleward temperature decrease and the slope bathymetry [*Huthnance*, 1995]. The large scale pressure gradient is a consistent feature and interannual variations of the poleward flow could be related to anomalous winds.

Although the wind field plays a major role in the Galician region, it has largely been studied superficially in terms of upwelling indices estimated from geostrophic winds calculated for a cell centered offshore Finisterre. Large scale studies by *Bakun and Nelson* [1991] and *Wooster et al.* [1976] have demonstrated the important seasonal variability of wind stress and wind stress curl, but were based on seasonally averaged winds at wide spacing. Only the temporal variability at a few coastal sites has been related with upwelling processes. For example, *Fiúza et al.* [1982] showed the seasonal and interannual dependence of coastal upwelling on coastal winds at Portuguese sites. In the present chapter, 2 years of wind data from the QuikScat mission are analysed, supplemented by *in situ* observations at near-shore buoys, in relation to AVHRR sea-surface temperatures. First, seasonal differences and typical wind patterns are described. Different coherent wind patterns lead to formation of the Finisterre filament and cause the differences in the upwelling north and south of the cape seen in SST images. Spatial wind patterns related to the larger scale pressure fields are used to explain variations between different upwelling years. The winter wind regime is described during both an "anomalous" and a "typical" year and the implications of the wind patterns in the evolution of the upwelling and non-upwelling regimes are discussed.

3.2 Methods

The SeaWinds instrument on the QuikScat satellite is a specialized microwave radar that, since 21 July 1999, has measured near surface wind speed and direction twice daily in 1,800 km swath bands. Wind speed measurements range from 3 to 20 m/s, with an accuracy of 2 m/s and 20° in direction. Spatial resolution of 25 km enables identification of fine scale features poorly sampled with previous scatterometers. The small coast mask makes the data suitable for studying near-shore wind patterns and processes.

Wind data were retrieved from the Jet Propulsion Laboratory web site [*http://podaac.jpl.nasa.gov/quikscat/qscat_data.html*] as Level 3 Scientific product. The data set consists of global gridded values of meridional and zonal components of wind velocity on an approximately 0.25 x 0.25 degree grid. The data were obtained from the Direction Interval Retrieval with Threshold Nudging (DIRTH) wind vector solutions contained in the QuikScat Level 2B data.

The data from either the ascending pass (6AM LST equator crossing) or the

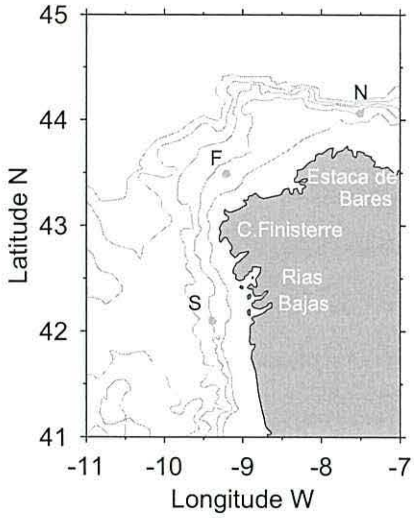

Figure 3.1.: Map of the region of study with the position of the main coastline features and instruments.

descending pass (6PM LST equator crossing) were selected each day from 19 July 1999 to 16 May 2001, depending on which had the higher data density. The data cover the Coastal Transition Zone off Galicia, 40.5°N to 45.5°N and 6.5°W to 13°W. Gaps in the data were dealt with by objectively interpolating the data. This method is equivalent to applying a spatial filter with smoothing scales 0.25° (0.55°) in longitude (latitude).

The remotely sensed wind data were complemented with a set of *in situ* wind observations collected between 1 May and 15 August 1999 by 3 buoys from the Spanish agency *Puertos del Estado* Deep Water Network (DWN), moored near the Galician shelf break (Fig. 3.1). They were located at 44° 3.9'N, 7° 31.1'W in 382m north of Finisterre (Estaca de Bares); at 43° 29.4'N, 9° 12.6'W in 382m off Cape Finisterre (Villano-Sisargas) and at 42° 6'N, 9° 23.2'W in 323m (Silleiro). In the text we refer to them as N, F and S buoys, respectively. The DWN buoys also measured currents at 3m depth by an UCM60 acoustic currentmeter. The data were measured hourly and filtered with a moving average filter A24A24A25 [*Godin*, 1991] with a cutoff frequency of 30 hours to remove tides and inertial components.

SST from Advanced Very High Resolution Radiometer (AVHRR) for the same period and location were processed at Plymouth Marine Laboratory using the Panorama software [*Miller et al.*, 1997] .

Wind data were further processed by calculating Complex Empirical Orthogonal functions (CEOFs) similar to *Münchow* [2000a]. CEOFs provide an objective means to summarize the wind measurements and to establish the dominant mesoscale features coherent within the data set.

The wind data are expressed in a two dimensional complex vector where the u component is the real part and v the imaginary part (Eq. 3.1) and $X_i (i = 1 \ldots N)$ denote the location and $t_k (k = 1 \ldots M)$ time.

$$W(X_i, t_k) = u(X_i, t_k) + \hat{\imath} v(X_i, t_k) \tag{3.1}$$

In matrix form it is,

$$W = \begin{pmatrix} W_1(1) & \ldots & W_1(N) \\ \vdots & \ddots & \vdots \\ W_M(1) & \ldots & W_M(N) \end{pmatrix}.$$

For each data series the temporal mean was subtracted and the modified covariance matrix R calculated,

$$R = W \times W^* / (M - 1), \tag{3.2}$$

where the * denotes the complex conjugate and results in a $M \times M$ matrix. We have normally dealt with matrices containing more locations than points in time (N>M),which results in a smaller matrix than the true covariance matrix. The CEOFs are obtained by solving,

$$R \times D = D \times \Lambda, \tag{3.3}$$

where Λ are the real eigenvalues of the covariance matrix, which are identical irrespective of which way the covariance is calculated [*Kelly*, 1988]. D are the complex eigenvectors which are different from the results we would have obtained using an $N \times N$ covariance matrix but they can be calculated from,

$$E = W^* \times D, \tag{3.4}$$

by which we obtained E, an $N \times M$ matrix. Therefore we calculate a smaller number of eigenvectors than the N eigenvectors that are defined for the problem but, because only the first few are significant, the lost ones are irrelevant.

The time varying amplitudes are obtained as shown in Eq. 3.5,

$$A = W \times E, \tag{3.5}$$

where A is complex, having magnitude and orientation, and represents the amplification factors for the spatial patterns. The original data can be reconstructed from,

$$F = A \times E^*. \tag{3.6}$$

The orientation of the temporal amplitudes and spatial patterns are relative to an arbitrary reference [*Kundu and Allen*, 1976]. To facilitate their interpretation the spatial patterns and temporal amplitudes are rotated along the direction of the semimajor principal axis of the corresponding amplitude time series [*Merrifield and Winant*, 1989]. Furthermore, the amplitude and spatial modes are normalized in such a way that amplitude series have uniform variance, and the spatial modes have units of m/s and correspond to a vertical amplitude of value 1.

Two important properties of EOFs are that the spatial distributions are orthogonal and that their time series are uncorrelated over the data set. Thus the EOFs are uncorrelated modes of variability. Usually a large portion of the variance can be explained by a small number of modes. To decide which modes are significant the sampling error associated with the EOF analysis was estimated following the method described by *North et al.* [1982],

$$\delta\lambda_i = \lambda_i \left(\frac{2}{n}\right)^{1/2}, \tag{3.7}$$

where $\delta\lambda_i$ refers to the sampling error of the ith mode, λ_i is the ith eigenvalue, and n, the number of independent measurements or degrees of freedom, is calculated after *Davies* [1976], according to

$$n = \frac{N\Delta t}{\tau}. \tag{3.8}$$

Here, Δt is the sampling interval, N is the number of records, and τ a de-correlation timescale,

$$\tau = \sum_{i=-\infty}^{\infty} C_{uu}(i\Delta t) C_{vv}(i\Delta t) \Delta t. \tag{3.9}$$

$C_{uu}(t)$ and $C_{vv}(t)$ are the lagged autocorrelation functions of $U(t)$ and $V(t)$ series. The sampling errors associated with each eigenvalue of the first 6 eigenfunctions are computed using equations 3.7 to 3.9. Only those eigenmodes whose errors do not overlap are distinct.

3.3 Seasonal evolution of the Galician region

The seasonal wind regime in the Iberian peninsula can be broadly divided into summer upwelling and winter downwelling regimes. The median of the wind field for summers 1999 and 2000 in Fig 3.2a and c, shows typical upwelling favourable winds along the Atlantic coast of Galicia strengthening to the south. North of Cape Finisterre the winds are locally downwelling favourable flowing to the south-west. The typical downwelling winter regime is characterized by onshore winds on the Atlantic coast as in winter 2000-2001 (Fig 3.2d). This picture is however complicated by interannual variations in the location of the pressure systems (Fig 3.2b), as occurred in winter 1999-2000. The Azores high remained in a more northern location than winter 2000-2001 and the median of the winds show a large scale circulation like the summers of 1999 and 2000 (Fig 3.2a and 1c) albeit with weaker winds.

Partly in response to the annual winds the coastal regime typically changes from upwelling in summer to downwelling and slope poleward flow in winter, as in the period of study, 1999-2001, (Fig 3.3). During both summers upwelling took place from June-October. The first sign of upwelling in 1999 started to appear in early June as a cold thin strip next to the Atlantic coast off Galicia. By mid June (Fig 3.3a), the upwelling was stronger in the north coast and the Finisterre filament was starting to develop. The Finisterre filament was present for most of June and July and disappeared in August (Fig 3.3b). No other filament developed during this season. This is not exceptional in the Galician region. Years 1995 and 1996 (not shown)

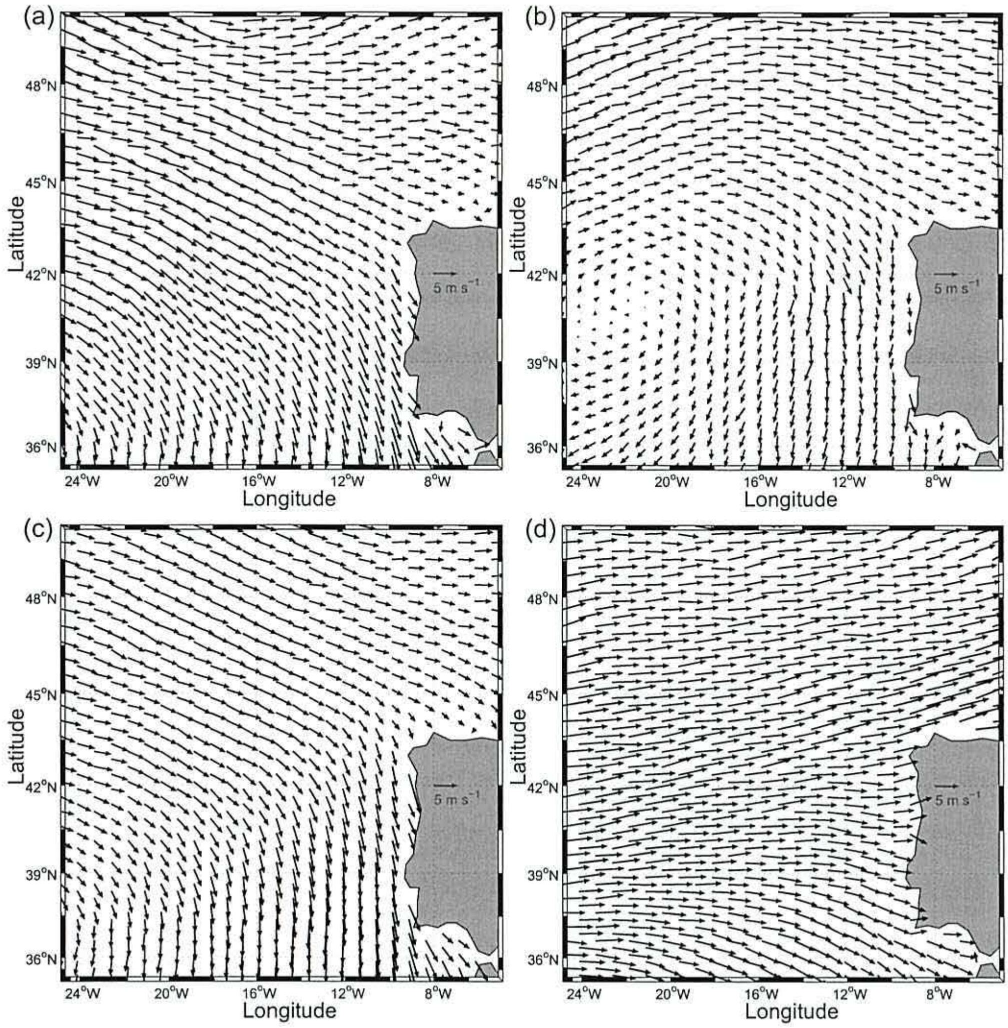

Figure 3.2.: Median wind fields from (a) summer 1999 (July-October), (b) winter 1999 (November-April), (c) summer 2000 (May-October) and (d) winter 2000 (November-April)

also saw a predominance of north coast upwelling and the Finisterre filament over other filaments. Examination of weekly composites of SST imagery for the period 1993-2000 suggests that the Finisterre filament is normally the first one to appear and is accompanied by north coast upwelling.

Poleward flow, suggested in SST by a warm tongue extending along the shelf break (Fig 3.3c), started to develop from the 20 October and persisted till early May. Several periods of weakened (end November) or absent (March) warm anomaly suggest suppression of the poleward flow.

Upwelling in 2000 started earlier, the first signs appearing in mid-May north of Cape

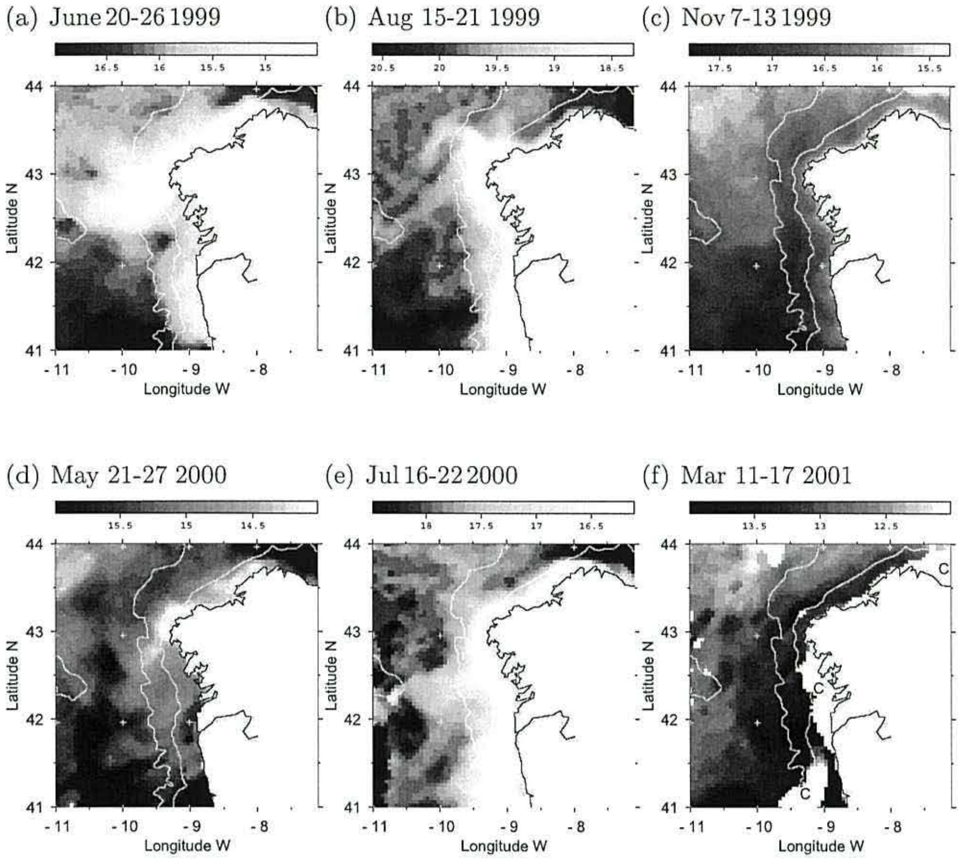

Figure 3.3.: Samples of weekly SST average images for the period of study. Note the different temperature scales.

Finisterre. At the same time the Finisterre filament started to develop (Fig 3.3d) although it disappeared at the end of May, and never reached the size of the previous year. Upwelling occurred intermittently until mid-July (Fig 3.3e), then almost continuously for the rest of the season but no clear filament developed at the cape. Moreover, north of Finisterre upwelling was very weak while to the south, upwelling extended beyond the 200m isobath with intermittent filament formation. The insignificant filament activity was compensated by an upwelling season extending to mid-November.

Poleward flow in the following season was first seen in early December 2000 and lasted until late April. Its SST signal in March (Fig. 3.3f) shows a narrow extension of warmer water turning east around Cape Finisterre along the northern coast.

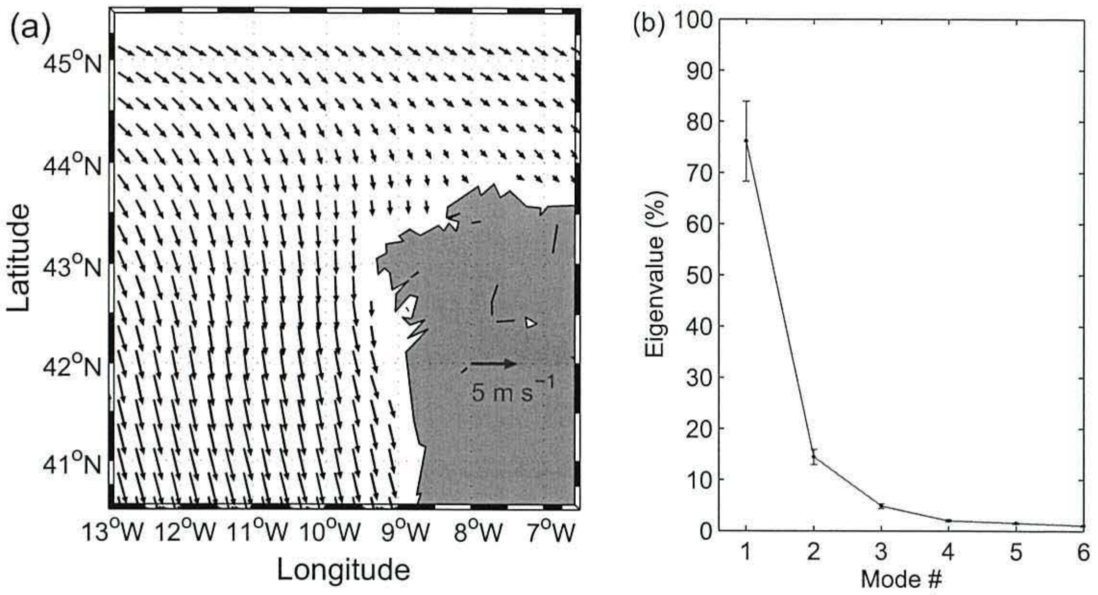

Figure 3.4.: Mean and variance distribution from the seasonal EOF analysis, 13 October 1999 to 28 October 2000

3.4 Common spatial wind patterns

A CEOF analysis was performed on the 2 year record comprising both upwelling and non-upwelling regimes. Further CEOF analysis of shorter data periods to investigate regime or interannual differences showed a high consistency in the spatial modes and variance distribution with the full record analysis. Figures 3.4 and 3.5 show the overall representative results. The mean wind field (Fig 3.4a), subtracted from the data prior to the EOF calculations, resembles the median (Fig 3.2a and b). The first two modes account for 88% of the total variance (Fig 3.4b) and are statistically distinct since the uncertainty of the eigenvalues do not overlap with any of the other eigenvalues [*North et al.*, 1982]. The de-correlation time scale for all QuikScat data was shorter than 2 days and a conservative value of 3 days was used in all uncertainty estimates.

Figure 3.5 depicts the spatial pattern of the largest 2 modes. The first mode (Fig 3.5a), corresponding to a spatially coherent wind field, represented 74% of the total variance. The second mode (14% of total variance), where the wind field is opposed in direction north and south of Finisterre, adds wind curl to the first mode

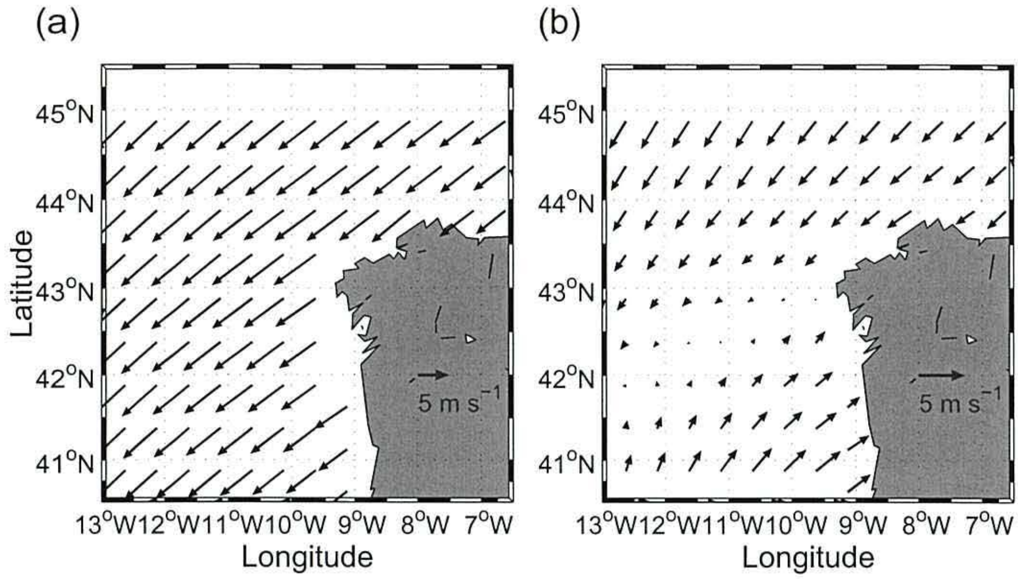

Figure 3.5.: EOF wind distinctive modes from the seasonal analysis (13 October 1999 to 28 October 2000), First a), Second a).

(Fig 3.5b). The mode shows a minimum of wind speed and maximum wind curl along a line running south-west from Finisterre with a uniform intensification to the north and strengthening near the coast to the south. This mode would contribute to Ekman pumping along the line of minimum wind intensity.

3.4.1 The 1999-2000 season

The instantaneous orientation depends on the direction of the complex amplitudes. The patterns shown in Fig 3.5 correspond to a unit amplitude vector in the direction of the principal axis which is represented in Fig 3.6 by a unit vector pointing vertically upwards. A unit vector to the right represents the same pattern rotated 90° clockwise. For clarity, the direction of southerly winds is represented by the arrow to the right of Fig 3.6a. The amplitude time series for mode 1(Fig 3.6a) is highly variable for the period 13 Oct 1999 to 28 Oct 2000 comprising one upwelling/non-upwelling cycle as identified from SST imagery. The large scale wind is far from unidirectional and changes occur very rapidly, as the short de-correlation time suggests. For this year, the expected seasonal signal is absent although both upwelling and downwelling events were stronger in winter than in summer, in particular from October to January.

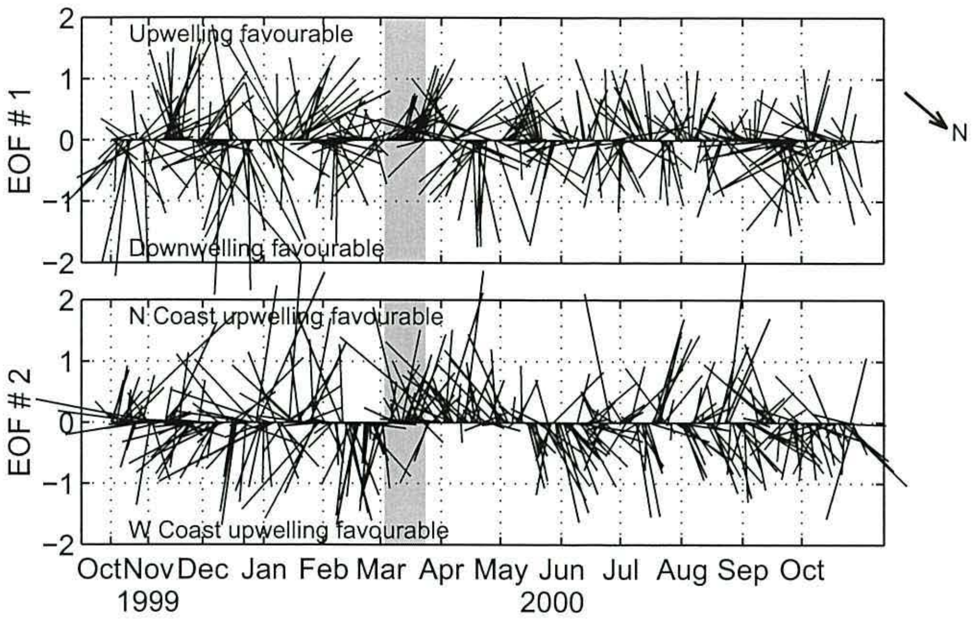

Figure 3.6.: Amplitude Time series for the seasonal analysis (13 October 1999 to 28 October 2000). The shaded intervals are referred to in the text. The arrow on the left points at the geographical north for the largely coherent wind field of Mode 1.

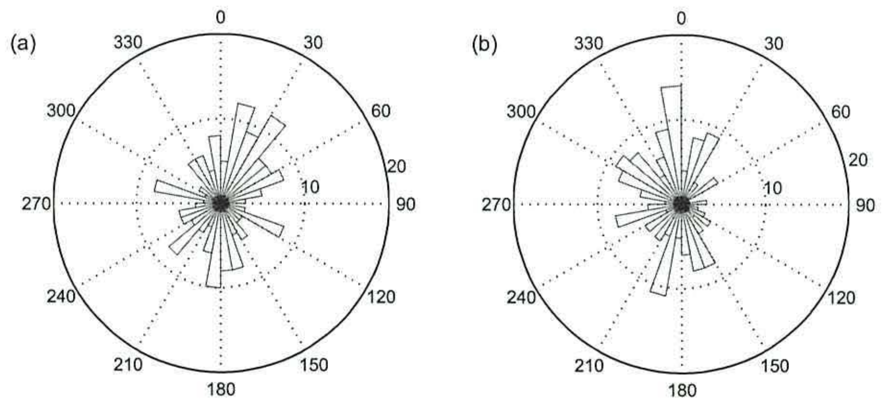

Figure 3.7.: Rose plot of EOF #1 amplitude directions for winter (Oct-April) and summer (May-Oct) 1999-2000. 0°corresponds to the direction of the semimajor principal axis of the amplitude time series.

The downwelling events, lasting for about 4-5 days, alternated with longer and more consistent upwelling events. Nonetheless, downwelling was predominant during October, December and April.

Directional differences in the wind occur between summer and winter. During

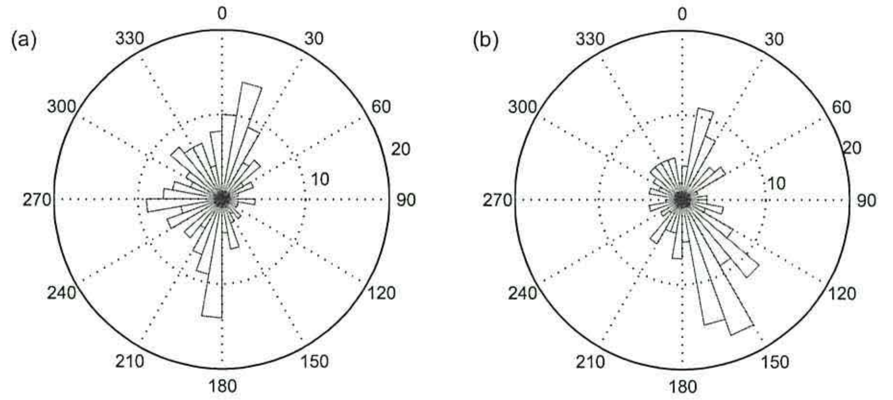

Figure 3.8.: Rose plot of EOF #2 amplitude directions for winter (Oct-April) and summer (May-Oct) 1999-2000. 0°corresponds to the direction of the semimajor principal axis of the amplitude time series.

winter (Fig 3.7a) there are two main orientations, the first corresponds to that shown in Fig 3.5a, rotated 10-40° clockwise. Adding the mean field makes the wind south of Finisterre more aligned with the coast. The second preferred orientation corresponds to the less common downwelling winds, i.e., rotated 160-190° to the pattern of Fig. 3.5a. In summer (Fig 3.7b) the preferred orientation corresponds to the pattern shown in Fig 3.5a (i.e. no rotation), while other maxima correspond to the orientations already discussed for the winter period and 290-320°, an enhancement of the mean field.

In winter, mode 2 (Fig 3.8a) shows similar orientations to mode 1 (between 0-30° and 180-210°). During summer, orientations between 130-170° were dominant with a small contribution from 10-30° (Fig 3.8b).

Combining the mean field with the first two modes for the preferred orientations (Fig 3.9) produces winds fields that typify the entire 2 year record. Figure 3.9a represents a combination of unit amplitude vectors directed at 30° for mode 1 and 2 (but is representative of a wider range of orientations ±10°). This wind field, dominant during March (shaded window in Fig 3.6), shows intensified southwestward winds parallel to the coast of Finisterre, slightly onshore on the north coast and weaker and slightly offshore south of the cape. This pattern favours upwelling along the north

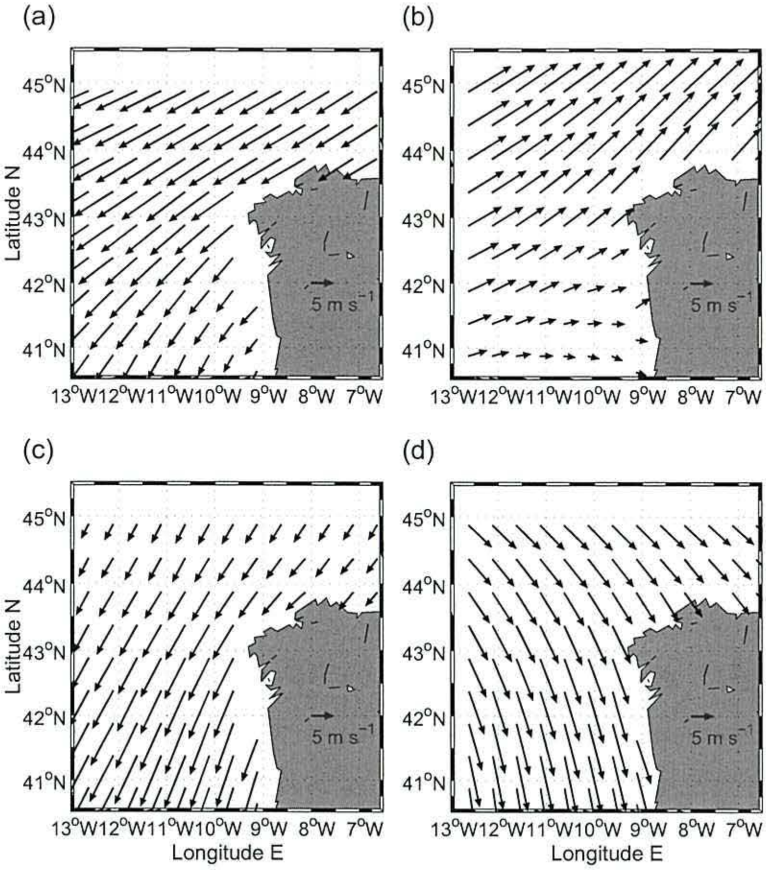

Figure 3.9.: Typical reconstructed wind patterns found in 1999-2000 showing combination of unit vectors for mode 1 and 2 directed, a) 30° and 30°, b) 180° and 180°, c) 0° and 150° and d) 300° and 150°

coast between Cape Finisterre and Estaca de Bares, and especially off Finisterre and will be referred to here as the PUNC (Predominant Upwelling on North Coast).

Figure 3.9b is a combination of unit amplitude vectors directed towards 180° for both modes and shows a typical pattern of downwelling winds. This situation with northeastward winds stronger north of Finisterre, is found in December and February. Varying the orientation of mode 2 produces different downwelling intensifications north and south of Finisterre. They will generically be referred to as DOWN (Downwelling off West and North coast).

Figures. 3.9c and 3.9d correspond to orientations 0° (300°) and 150° (300°) for mode 1 (mode 2) respectively and typify the dominant upwelling patterns for summer 2000. Both wind fields are more intense along the west coast and favour upwelling along the

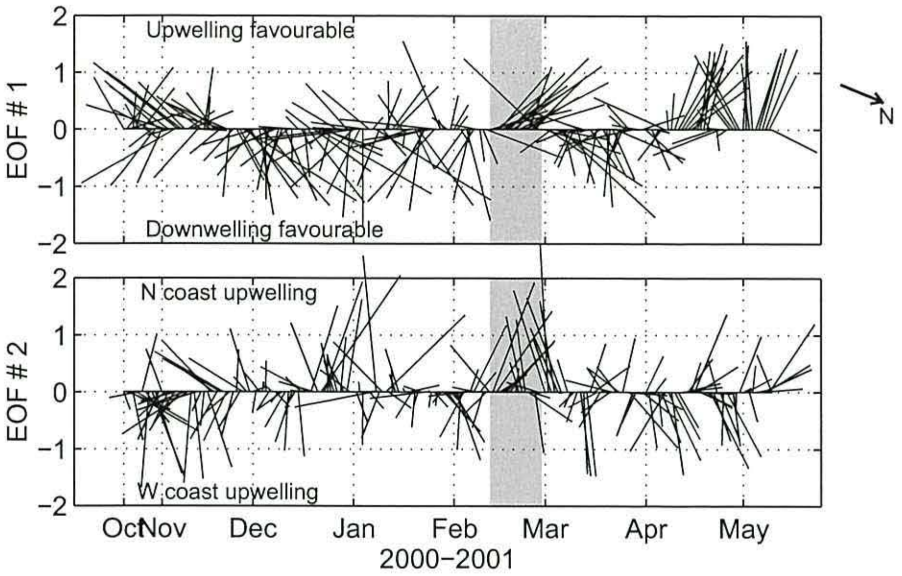

Figure 3.10.: Amplitude time series for the winter 2001 analysis (20 Oct 2000-10 May 2001). The shaded intervals are referred to in the text. The arrow on the left points at the geographical north for the largely coherent wind field of Mode 1.

west coast over the Finisterre and northern coasts (PUWC - Predominant Upwelling on West Coast).

3.4.2 The winter season of 2000-2001

Unlike the winter wind regime of 1999-2000, which in many respects, was similar to the summers 1999 and 2000, the winter of 2000-2001 was more "typical". The median for November to April (Fig 3.2d) showed a spatially coherent wind field of $5ms^{-1}$ with an E-SE direction near coast south of 43°N rotating to a E-NE orientation further north. The CEOF analysis (20 Oct 2000-10 May 2001) yielded two modes (80% and 10% of the total variance respectively) similar to the ones presented in the seasonal analysis of Fig 3.5. Mode 1 represents a stronger wind field ($\sim 9ms^{1}$) directed more parallel to the coast than that depicted in Fig 3.5a, while mode 2 is directed more in the offshore direction when compared to Fig 3.5b. The mode 2 wind intensity is similar in both analyses; however, the channel of maximum curl is orientated more perpendicular to the west coast in winter 2000-1 so that the winter modes are more perpendicular to each other.

The amplitude series (Fig 3.10) show that sustained if variable DOWN wind fields were dominant, particularly from late November until early April. From 12-28 February a PUNC wind field,like March 2000 (Fig 3.8a) occurred. Mode 2 contributes less overall to the wind field than in the seasonal analysis with relatively few strong events. Upwelling winds were more directionally consistent than downwelling winds. The former can be grouped in two preferred orientations: 310-340° and 0-40°, similar to Fig 3.8d and c; downwelling winds fall into two wider ranges: 270-280° and 150-210°, westerlies and southwesterlies similar to Fig 3.2d. Downwelling patterns persisted for <6 days, while upwelling wind periods of <14 days occurred in February and April to May.

The narrow, warm tongue indicative of poleward flow first appeared over the slope in weekly SST average images in early December after a week of downwelling favourable winds. Short upwelling events like 11-15 January temporarily detached the poleward current from the shelf but did not disrupt its SST signal. Subsequent downwelling winds intensified the SST poleward flow signal, which returned to its original position along the slope. However the tongue disappeared from the north coast following 5 days of PUNC winds up to $12 ms^{-1}$. The SST signal of the flow was not re-established until 11 March (Fig 3.3f), 10 days after the return to DOWN winds. Winds changed to PUWC on the 6 April and remained predominantly so until the end of the record on 10 May. The upwelling response in this season appears slow. Although first signs of weakening poleward flow occurred during 8-14 April, when the SST differences between the warm tongue and oceanic waters reduced, west coast upwelling did not appear until 29 April-5 May after 14 days of continuous upwelling winds.

3.5 PUNC wind pattern effects on upwelling

Spatial variability of coastal upwelling can be explained largely by the dominant wind patterns of Fig 3.9. Winds on the 21 July 1999 (Fig 3.11a) were PUWC upwelling favourable similar to Fig 3.9c. Winds of speeds up to $10 ms^{-1}$ parallel to shore forced strong upwelling both at Finisterre and the west coast. The SST image for the 21 July

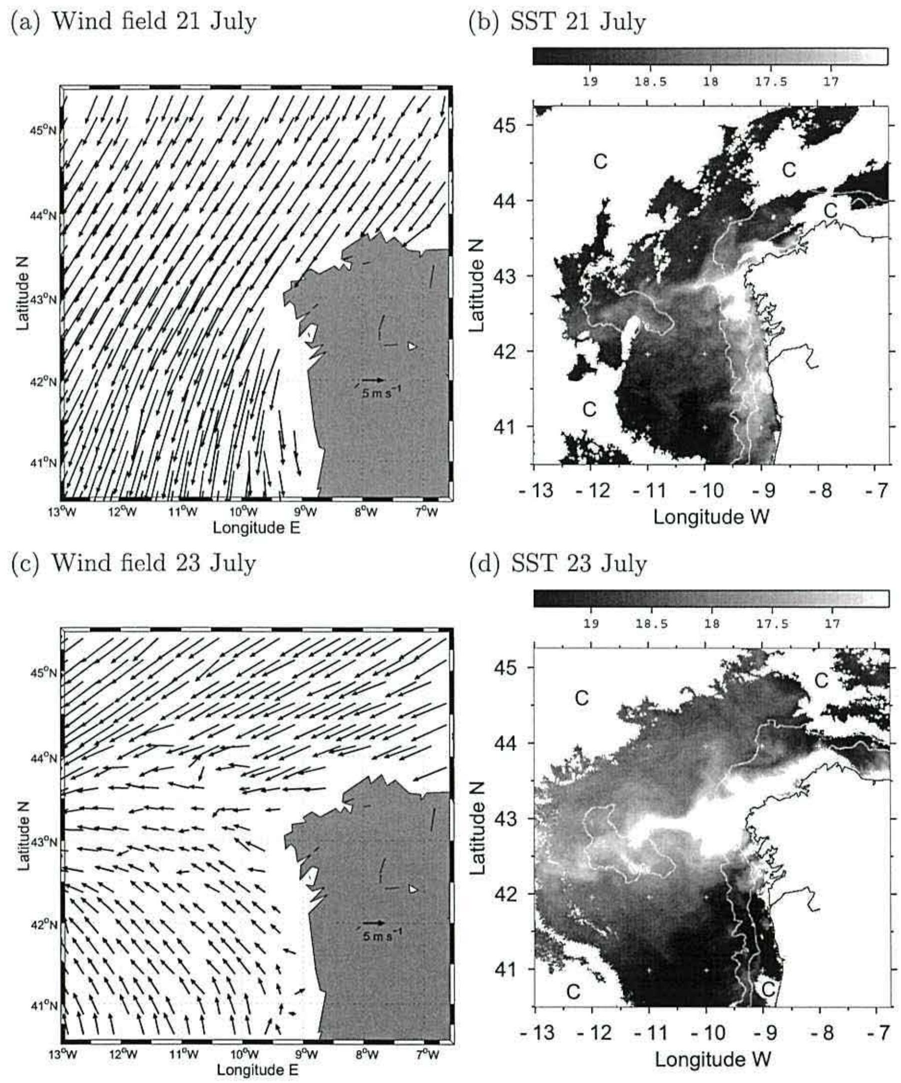

Figure 3.11.: Wind fields and SST images from 21 and 23 July 1999.

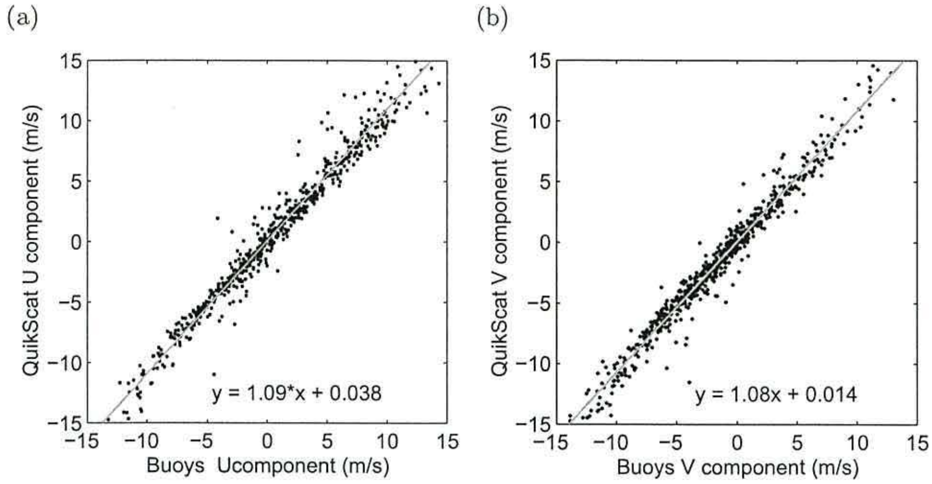

Figure 3.12.: Comparison between QuikScat and coastal Buoys during the period of study for (a) U and (b) V wind components. The resulting linear fit is included.

(Fig 3.11b) shows minimum temperatures around Finisterre and a clearly identifiable Finisterre filament. West coast upwelling extended south to 41°N and offshore to the 1000m isobath. Weak north coast upwelling persisted despite onshore winds north of the Cape. However the wind rotated clockwise through a PUNC pattern to that of 23 July (Fig 3.11c), dominated by mode 2 as in Fig 3.5b. This enhanced upwelling in the north coast, strengthened the Finisterre filament, but was downwelling favourable on the west coast (Fig 3.11d). Although this particular pattern with northward winds south of Finisterre is infrequent, strong development of the Finisterre filament to the exclusion of those further south in e.g. 1995 and 1996, suggests similar PUNC wind fields can predominate over part of the upwelling season.

3.5.1 Coastal Wind Buoy measurements

The DWN buoy observations allow extension of the analysis to the period when the Finisterre filament was starting to develop but before QuiKSCAT data are available. Both data are compared in Fig 3.12 for the common periods and are simultaneous in time to the closest hour. The data agreed well with correlations $r^2 = 0.96, 0.97$ (their coefficients significant at 99% level of confidence, F=24893, 31423, df=1023, $p<0.001$) for the U and V components respectively. Linear regression model for both

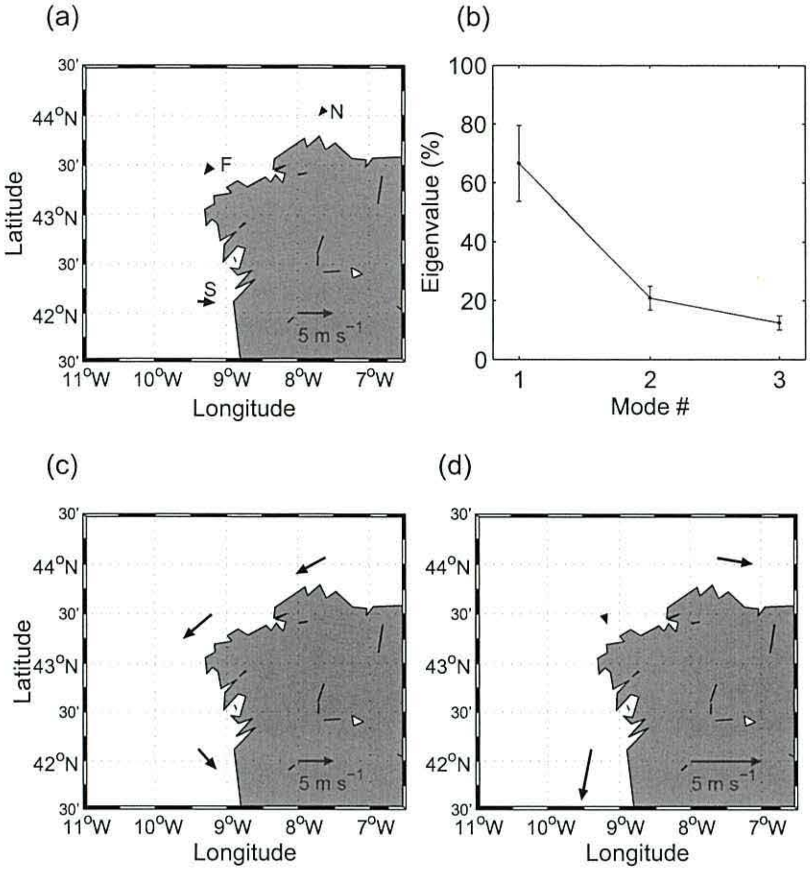

Figure 3.13.: Mean field (a), the variance (b), and Eofs #1 (c) and #2 (d) of the wind data available during the upwelling season of 1999, 1-May to 15-August for the offshore buoys.

components were,

$$QU = 1.09\,(\pm 0.00044) \times BU + 0.038\,(\pm 0.0024), \tag{3.10}$$

$$QV = 1.08\,(\pm 0.00038) \times BV + 0.014\,(\pm 0.0021), \tag{3.11}$$

in which Q and B stand for QuikScat and Buoys data for each the U and V components. The QuikScat data is consistently larger than the Buoys data by less than 10% which could be explained by the more offshore position of the QuikScat grid locations.

The daily median of the hourly winds was used to calculate the CEOFs for the period 1-May-1999/15-August-1999 (Fig 3.13). No data were recorded afterwards due to instrumental failure. The first two modes explained 87% of the total variance of the 107 days record and are statistically distinct (Fig 3.13b). The mean winds

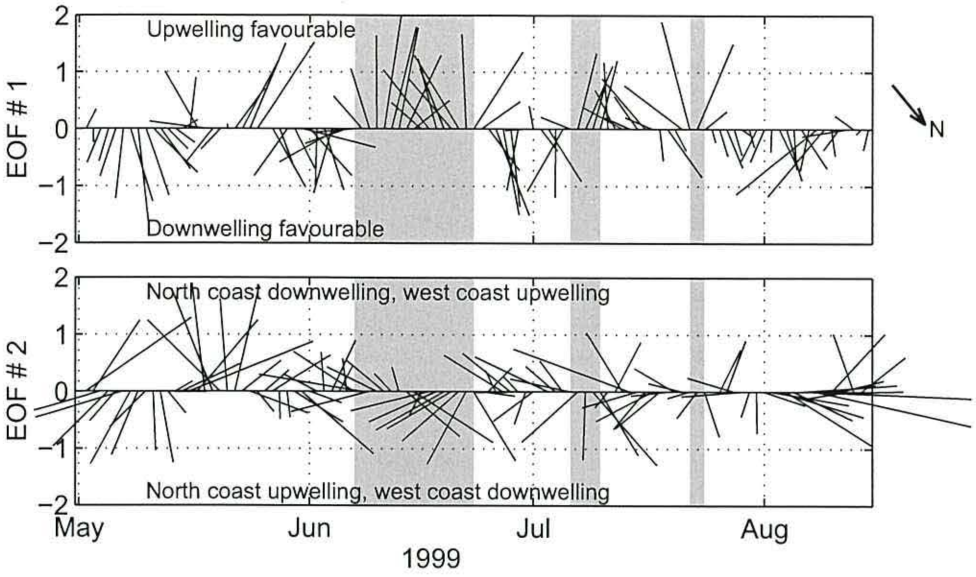

Figure 3.14.: Amplitude Time series of the wind analysis in 1999. The shaded intervals are referred to in the text. The arrow on the left points at the geographical north for the largely coherent wind field of Mode 1.

(Fig 3.13a) are very small reflecting the averaging over non-upwelling and upwelling periods. Mode 1 (Fig 3.13c) represents stronger north coast upwelling. Mode 2 (Fig 3.13d) represents opposing winds at the S and N buoy and null near Finisterre, strongly similar to the corresponding QuikScat mode. This similarity is remarkable considering the difference in record length and timing. When both modes are positive the wind becomes less upwelling favourable off the north coast (N buoy), and more so off the west coast (S buoy). When only mode 2 is negative the wind is more upwelling favourable along the north coast and less so off the west coast.

The amplitude time series (Fig 3.14) show periods of alternating upwelling and downwelling favourable conditions. The first consistent upwelling favourable period was 7 to 23-June (Fig 3.14a)when the first signs of upwelling were seen in SST images. The period was structured into two pulses; each started with northerly winds that gradually strengthened and rotated to north-easterly, then weakened and rotated to easterly winds. During this development mode 2 became more negative, particularly during the second pulse, favouring north coast upwelling and west coast downwelling. The SST images for the same period show the development of strong upwelling in the north coast, weaker upwelling along the west coast, and the progressive advection of

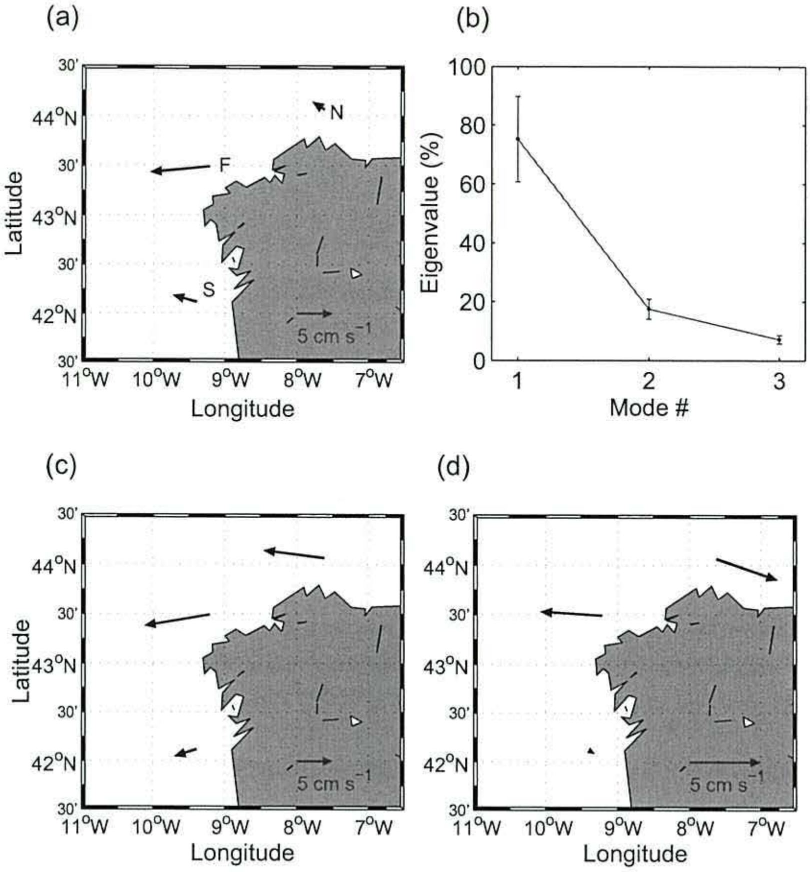

Figure 3.15.: Mean field (a), the variance (b), and Eofs #1 (c) and #2 (d) of the current data available during the upwelling season of 1999, 1-May to 15-August for the offshore buoys.

the cold upwelled coastal waters directly offshore at Cape Finisterre. From 24 June till 6 July, downwelling winds weakened the Finisterre filament, then renewed upwelling winds strengthened it again. This time, mode 2 was strongly negative producing the same wind pattern identified for 22-23 July in the QuikScat observations (Fig. 3.11c).

3.5.2 Coastal Current Buoy measurements

The CEOFs for the buoy current data at 3m depth (1 May-15 August 1999) were calculated as for the wind data. The mean current Fig 3.15a is significantly different from zero (F, 8.3cms^{-1}) only off Finisterre where it is directed westward i.e. alongshore equatorward and slightly offshore. Mode 1 (Fig 3.15c) accounted for 75% of the variance and shows stronger variability off Finisterre and the north coast (F and N,

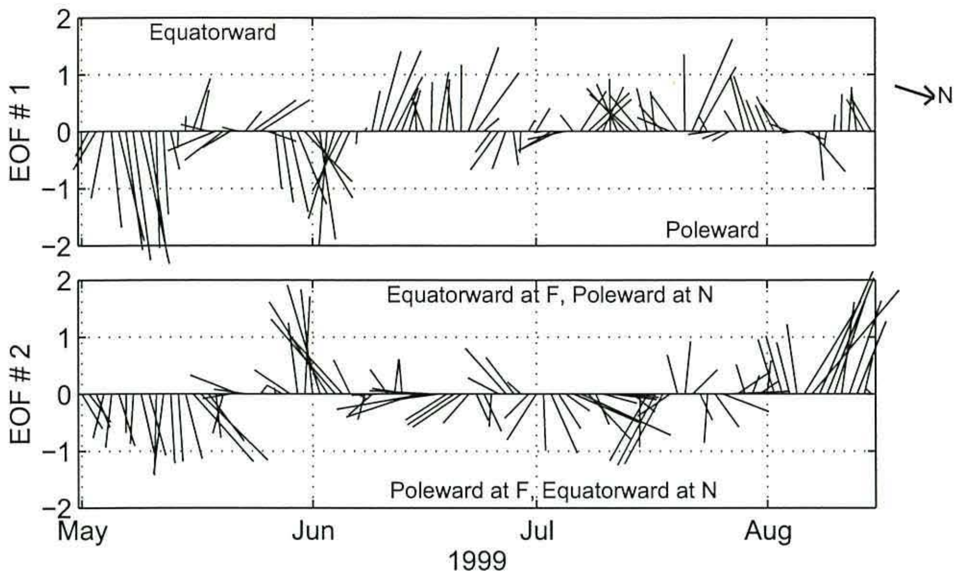

Figure 3.16.: Amplitude Time series of the current analysis in 1999. The arrow on the left points at the geographical north for the largely coherent field of Mode 1.

~8.5cms^{-1}) than off the west coast (S, ~3cms^{-1}). Mode 2 (Fig 3.15d) accounted for 15% of the variance and represents diverging vectors at the northern buoys (N and F) and negligible contribution from site S. This contrasts with wind mode 2, which showed opposed north and west coast winds. For both modes, the axes of maximum variability are directed such that flow is in the equatorward and offshore or poleward and onshore sense, as expected for the local wind driven regime.

The amplitude time series of Fig 3.16 show the expected poleward flow for the downwelling regime during the first half of May. The change to the upwelling regime is seen in mode 1 on the 9-June, two days after the onset of the upwelling winds. Thereafter, the circulation corresponds mostly to upwelling but wind reversals produced short lived current reversals (e.g. end of June) or weakening of the upwelling (e.g. end of July). Peak offshore velocities at buoy F coincide with wind peaks, which favour the Finisterre filament, reaching values of 22cms^{-1}. In the first half of May, the mode 2 contribution enhanced the poleward tendency at F but weakened it at N, partly compensating for the more equatorward mean at F. From June on, it opposed the equatorward flow at F and enhanced it at N, again tending to reduce the difference in actual flow at both.

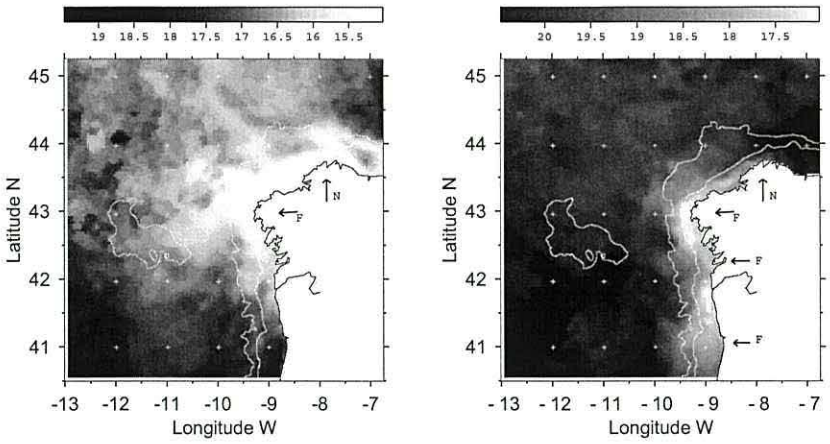

(a) June 18-24 (b) August 06-12

Figure 3.17.: SST weekly averaged images from 1995. Arrows labelled F mark known locations for filaments. Arrows labelled N mark the north coast site with largest upwelling differences.

3.5.3 Comparison with other years

The Finisterre filament followed similar development in 1995 and 1999. Coastal upwelling first appeared in SST imagery at the end of May along both coasts but a week later upwelling was mainly north of Finisterre. By 11 June 1995 a filament extended 125km from the cape and upwelling on the west coast had disappeared (Fig 3.17a). This situation persisted through July but by August, north coast upwelling had weakened. The lowest temperatures were located on the west coast, where upwelling extended to the 1000m isobath. After 6 August frontal instabilities started to develop (Fig 3.17b) at 43.25°N (off Finisterre) and at 42.25°N and 41.25°N, other well known locations for filaments [*Haynes et al.*, 1993]. They continued to grow until 27 August when upwelling was re-established north of Finisterre. The Finisterre filament continued to grow as the west coast upwelling weakened. After 17 September, the situation of August was repeated, i.e. the Finisterre filament retreated, upwelling weakened north of the cape while it intensified further south, and the instabilities developed again. This evolution can be explained by alternation of the typical PUNC and PUWC wind patterns of Fig 3.9a and d, favouring upwelling on one or other of the coasts.

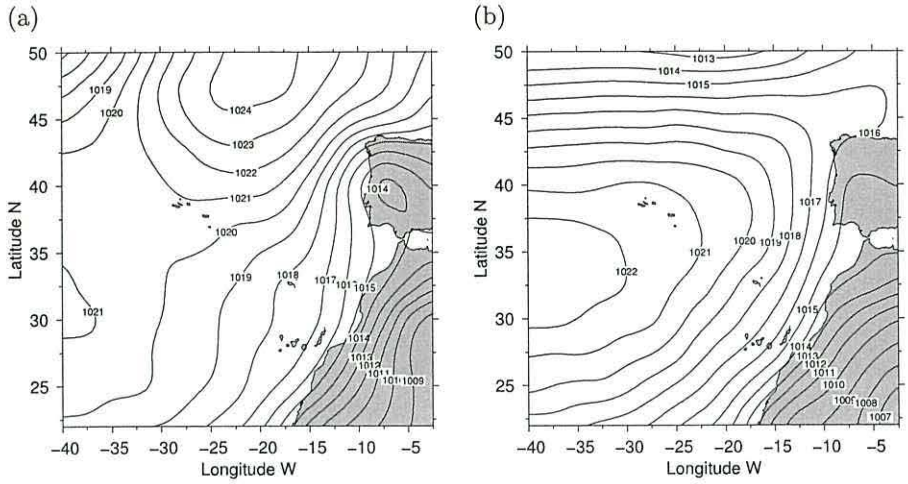

Figure 3.18.: Monthly averages of Sea Level Pressure for a) June and b) July 1995

Though no *in situ* wind observations are available for 1995 this interpretation is supported by Sea Level Pressure (SLP) data from the National Centers for Environmental Prediction (NCEP) Reanalysis project at the Climatic Diagnostics Center web site [*http://www.cdc.noaa.gov/cdc/reanalysis/*]. The SLP field in June 1995 (Fig 3.18a) indicates winds parallel to the north Iberian coast and offshore on the west coast, as in the PUNC pattern of Fig. 3.9a, with tight packing of the isobars indicating strong winds at Finisterre. During July 1995 the SLP field (Fig 3.18b) shows the Azores High well to the south (33°N, 40°W), producing a PUWC wind pattern similar to Fig 3.9c that favoured west coast upwelling and weakening of the Finisterre filament, as was observed (Fig. 3.17b).

3.6 PUWC wind pattern effects on upwelling

In some years, the Finisterre filament does not develop and west coast upwelling with (e.g. 1998) or without (e.g. 2000) filament development dominates. The CEOF mode 1 amplitude time series for summers 1999 (19 Jul-30 Sep) and 2000 (1 May-31 Oct) accounted for 76% and 72% of the variance respectively. The mean fields were similar in both summers (Fig 3.2a and c) to the typical PUWC pattern (Fig 3.9d) and in both the first two modes (not shown) were like the overall modes (Fig 3.5a and b). However,

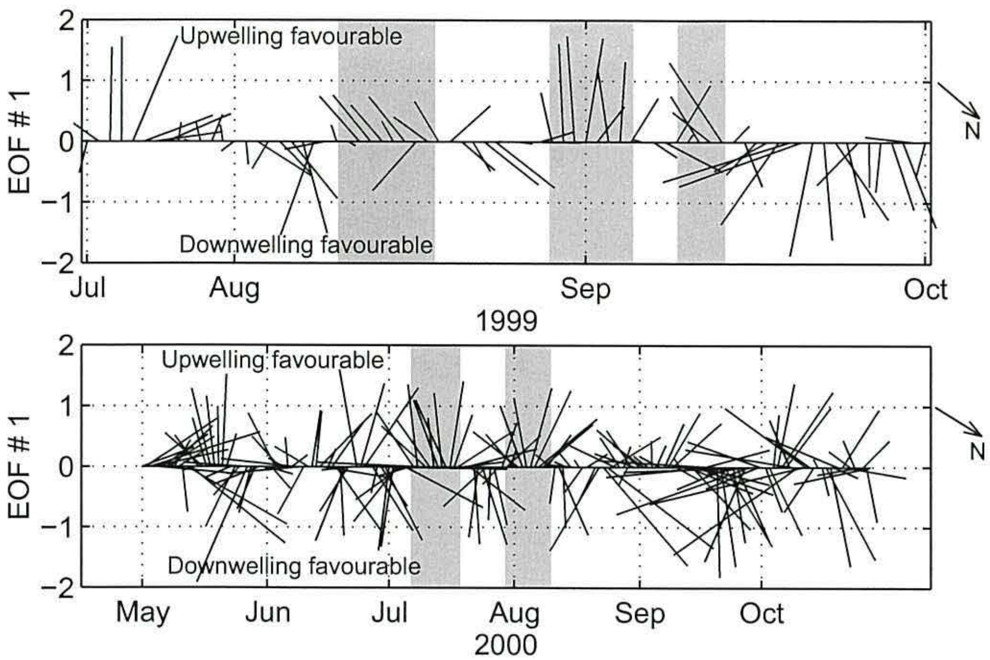

Figure 3.19.: Amplitude Time series for the summers 1999 (19 Jul-30 Sep) and 2000 (1 May-31 Oct). The shaded intervals are referred to in the text. The arrow on the left points at the geographical north for the largely coherent wind field of Mode 1.

during summer 1999 few wind events lasted long enough to produce significant west coast upwelling (shaded in Fig 3.19a) and filaments. During summer 2000, repeated short west coast upwelling events of various intensities again alternated with shorter downwelling periods. Even the two most persistent upwelling events (6-19 July and 31 July-10 August) generated only short 80 km filaments at 42.25°N and 41.25°N (Fig 3.3e) that weakened after each event.

In contrast, west coast upwelling and full filament formation dominated during July 1998, when sustained upwelling favourable winds occurred from June [*Smyth et al.*, 2001]. During June-August a series of filaments formed, grew and merged near 41.25°N, 42°N and 43°N. During August both Finisterre and west coast upwelling coexisted although the former did not develop a filament and west coast upwelling persisted until September [*Barton et al.*, 2001]. Fig 3.20a-b show the monthly SLP field for July and SST image for 29 July, 1998. During July, the mean field shows the well defined Azores high with strong winds parallel to the west coast of Iberia producing the west coast upwelling and development of the 42°N filament (Fig 3.20b).

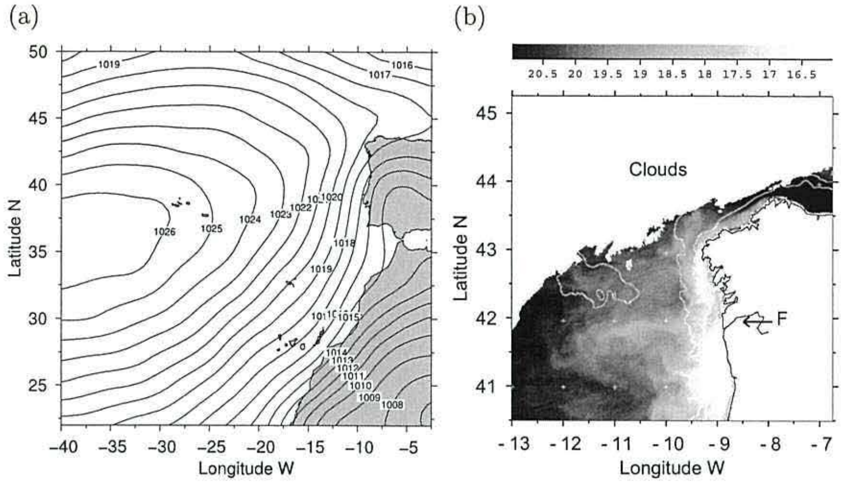

Figure 3.20.: (a) Monthly average of Sea Level Pressure July 1998 and (b) SST image of 29 July 1998.

3.7 Discussion

The period under study, July 1999 through to May 2001, showed no clear seasonal wind signal with upwelling and downwelling winds distributed year-around. Similar results were obtained by *Nogueira* [1998], who found that only 20% the variability in daily Ekman transport off Cape Finisterre over 9 years was associated with the seasonal cycle, while 70% concentrated at frequencies <30 days. *Nogueira et al.* [1997] showed from harmonic analysis that the average upwelling event length was $T = 15 \pm 5$ days, close to our estimate of 14 ± 2 days. Comparing our data with those of *Kosro et al.* [1991] off California, we observe that although cycles of upwelling-winds/relaxation take place in both regions, Galicia is more variable in wind speed, direction and persistence. Much of the summer variability relates to anticyclones moving northeastward over the bay of Biscay.

Differing patterns of upwelling favourable wind fields force different responses in the system favouring either north or west coast upwelling (PUNC and PUWC, respectively). Summer 1999 experienced winds favourable to north coast upwelling and Cape Finisterre filament development while summer 2000 was more typified by

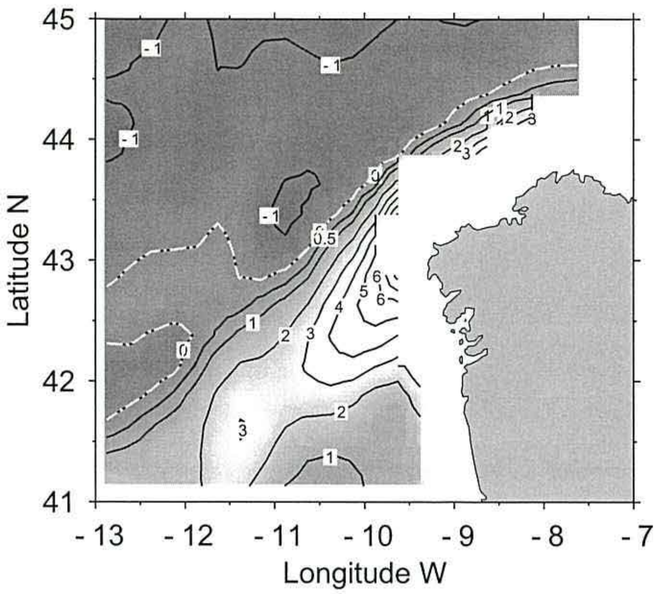

Figure 3.21.: Vertical Ekman pumping velocities on 22 July 1999 in m/day, positive upwards.

west coast upwelling. Both years experienced highly variable winds that did not persist long enough for upwelling filaments to develop on the west coast. The strongest development of west coast filaments in recent years occurred in 1998, when west coast upwelling-favourable winds lasted from June to early August with few interruptions. These sustained upwelling favourable winds maintained a sharp upwelling front that allowed the development and growth of the west coast instabilities into upwelling filaments.

Much has been hypothesized about the generation of upwelling filaments. *Roed and Shi* [1999] and *Haynes et al.* [1993] reported a clear link between bottom topography and filament formation in the Galician region on the basis of models and observations, respectively. However, in the case presented here, the Cape Finisterre filament is clearly dependent on particular wind conditions for its development. The mere presence of upwelling at Finisterre is not sufficient. Although small scale instabilities sometimes develop off the cape (see Figs 3.11b,d and 3.17a), it requires a well developed north coast upwelling for them to grow into a full sized filament. At these times the wind field is like that of Fig 3.9a and the filament extends offshore along the line of maximum wind curl identified in mode 2 in Fig 3.5.

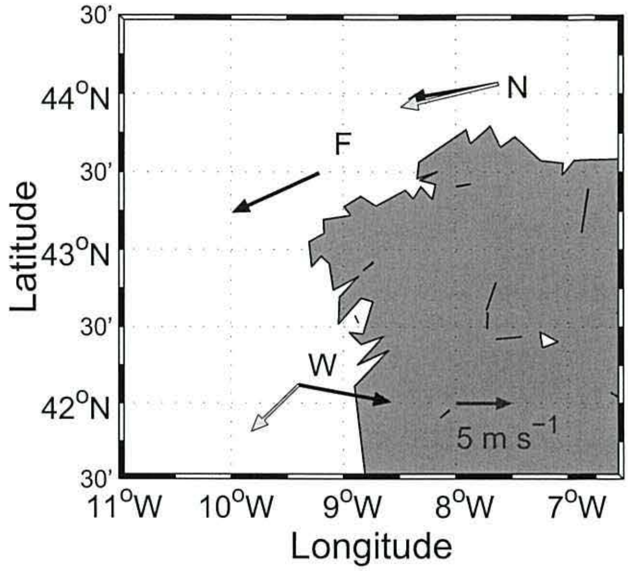

Figure 3.22.: Example of measured winds from the offshore buoys on 7 July 1999 (black) and 20 March 2000 (light grey).

This maximum wind curl produces upwelling velocities given by $w = k \cdot (\nabla \times \frac{\tau}{f\rho})$, where k, τ, f and ρ are vertical unit vector, wind stress, Coriolis parameter and density of water. This Ekman pumping is caused solely by the divergent Ekman fluxes in the presence of spatially variable wind and is unrelated to the coastal upwelling. An example is shown in Fig 3.21 for measured winds on 22 July 1999 corresponding to a wind field similar to Fig 3.9a. Positive Ekman pumping velocities indicative of upwelling can be seen south of the maximum wind curl northern limit in Fig 3.5b and towards the west coast. Maximum vertical velocities coincided with the axis of maximum curl and decreased from $6md^{-1}$ near Cape Finisterre to $1md^{-1}$ farthest offshore. Calculations on a similar day in March 2000 yielded a similar pattern except vertical velocities were smaller by a factor of 2 and decreased rapidly on the west coast. The strong winds in June 1995 (Figs 3.18a and b) were again like the 1999 case. We conclude that summer occurrences of this wind pattern lead to upwelling velocities of 5-$6md^{-1}$ off Cape Finisterre. These are smaller than the ones (up to $20md^{-1}$) reported by *Münchow* [2000a] off Point Conception, California. His finer sampling covered a much smaller area which defined a maxima wind curl ridge 80km long and 10km wide. In our case, the ridge extends 320km in length and 90km in width and vertical velocities are likely to reach higher values nearer to the shore at Cape Finisterre.

Münchow [2000a] reported flow separation in the wind field at Point Conception in the presence of upwelling. He argued that the lower sea surface temperatures enhanced the vertical stability of the marine layer, which is capped by a temperature inversion. Coastal upwelling can modify air temperatures by as much as 1-5°C over timescales of 12-24 hours [*Samelson et al.*, 2002]. As in *Enriquez and Friehe* [1995], the marine layer flow becomes supercritical and separates from the coast causing the wind curl and Ekman pumping velocities. We see some evidence of wind flow separation in the lee of Cape Finisterre during the summer upwelling regime. For example the buoy wind data for 7 July 1999 (Fig 3.22) show north coast and Finisterre winds flowing nearly opposite to west coast winds, suggestive of strong flow separation at the cape. Similar north coast winds were common throughout March 2000 and after 14 June 1999, but flow separation only occurred in the presence of cold upwelled water around Cape Finisterre during the 1999 examples. Hence, there is some evidence that the PUNC strengthens both near the coast and after the start of the coastal upwelling, generating larger wind curl and associated Ekman pumping velocities increasing shorewards. The positive wind curl would cause a poleward alongshore pressure gradient as indicated by model studies of *Wang* [1997]. However, finer scale wind observations near Finisterre and atmospheric observations would be needed to reach a definitive conclusion.

The existence of recurring wind curl west of Cape Finisterre will influence the vertical water structure to cause doming of the isopycnals. *Münchow* [2000a] showed that a similar wind curl influenced the vertical water structure to cause doming of the isopycnals off Point Conception. A similar local effect on the shelf circulation may be expected around Cape Finisterre. The systematically weaker southward velocities observed at the west coast buoy (S) compared to the Finisterre buoy (F) are consistent with such a cyclonic tendency but we presently have no hydrographic evidence to verify it. Doming could help explain the persistence of the Finisterre filament following cessation of favourable wind patterns, but again, observational evidence of the detailed hydrographic and current structure near the cape is lacking. Capes also have a significant impact on the alongshore variability of the upwelling flow field [*Crepon et al.*, 1984; *Dale and Barth*, 2001; *Rosenfeld et al.*, 1994], producing nonlinear effects accompanying the acceleration of the flow around the capes, and a cyclonic tendency downstream.

Winter winds in general showed larger variability than summer winds during both "typical" (2000-2001) and "atypical" (1999-2000) seasonal years. Downwelling wind patterns emerged from CEOF analysis during both the 1999-2000 and winter 2001 analyses. E,NE and N winds were predominant during both winters reaching speeds in the range 15-20 ms^{-1}, higher than the 10-15 ms^{-1} range of summer winds. However their persistence was far less (4-6 days) than during summer ($\sim$12 days). Both winters saw the PUNC wind field predominate during sustained periods in March and February respectively. Its effect on the SST field was the disappearance on the north coast, but not the west coast, of the warm temperature anomaly indicative of poleward flow only.

It is difficult to define transitional regimes, non-upwelling to upwelling and vice versa in terms of the wind forcing because of the absence of any clear seasonal cycle. Extension of the analyses to a longer period will provide better information, but it appears that as long as the meridional sea surface temperature gradient is present, (nearly until July) upwelling favourable winds do not fully set up upwelling; and even sustained winds provoking upwelling early in the season do not develop filaments, e.g. April-May 2001.

3.8 Conclusions

Investigation of the QuikSCAT and in situ wind fields in the Galician upwelling region around Cape Finisterre has shown:

- The wind field is far from homogeneous in the region so that wind observations at a single point, coastal or offshore, will not necessarily be representative of coastal conditions over any significant distance.
- The wind field's long-term mean summer and winter patterns are not necessarily representative of particular years when, as we have seen, summer-like patterns may

dominate in winter also.

- Similar Wind Modes were obtained in all CEOF analysis, of both satellite derived and *in situ* buoy measurements.
- Summertime wind fields have a small number of dominant patterns, discernible in complex empirical orthogonal analysis, that are responsible for the typical distributions of upwelling in and off the Galician coast.
- One pattern produces north coast, but no west coast, upwelling. In years when this pattern dominates, the Cape Finisterre filament is strong but no others develop. The filament is partly supplied by cold water from the north coast but also, importantly, by local open ocean upwelling produced by the wind stress curl, whose maximum extends SW from the cape.
- Another pattern produces west coast upwelling, but no north coast upwelling. When this pattern persists, west coast filaments develop at favoured locations other than Finisterre and may extend up to 200km offshore.
- These patterns may alternate producing brief episodes of north or west coast upwelling with little filament development, or a combined pattern may occur that produces weak upwelling on both coasts with a localized maximum at Finisterre, where the wind lies parallel to the coast.
- Winter time wind patterns show strong similarities to those of summer, symptomatic of frequent short occurrences of winter upwelling during our study years of 1999 and 2000.
- The onset of the winter poleward flow regime as indicated by presence of the warm water anomaly along the continental slope is delayed after the cessation of summer upwelling winds. Likewise the spring onset of upwelling lags significantly the commencement of favourable winds, though subsequent upwelling events respond rapidly to wind changes.
- North coast currents are more variable in all records and showed the largest velocities.

CHAPTER

4 Spring transition

4.1 Introduction

The spring transition is here taken to be the period during which the winter regime of predominant downwelling and poleward flow over the slope is replaced by a regime of sustained coastal upwelling. In Chapter 3 it was shown that transitions between regimes are largely determined by the seasonal cycle in the meridional density gradient inferred from SST. Initial stages of this transition are characterised by large variability in both circulation and property distribution on the shelf and offshore. In the absence of the steady sea level gradient and stratification, the response of the Galician system to upwelling favourable wind is stronger than in summer [*Castro et al.*, 2000]. During the transition, there can be short periods during which poleward flow offshore and upwelling nearshore coexist.

The spring transition between downwelling and upwelling regimes can be found in all major eastern upwelling systems with a seasonal cycle. The transition is fast in the California system [*Huyer*, 1983] with a time scale of a few days. Equally the response of the Galician system to upwelling winds during the spring transition has been estimated to be fast. In other regions like the Canary Current upwelling system, no transition is reported though there is a lack of systematic year round observations.

The Rias Bajas have recently started to be regarded as an intrinsic component of the "shelf system" that respond to similar forcings, i.e. large scale and local winds can drive their circulation pattern, more so during summer when freshwater input is at its minimum. The downwelling winds and the presence of the poleward flow over the shelf prevents the "outwelling" or water discharge from the Rias Bajas, detaining it at the inner shelf stations [*Castro et al.*, 1997] and even forcing shelfwater into the Rias Bajas at times [e.g. *Prego et al.*, 2001; *Sordo et al.*, 2001]. During upwelling winds, the Rias Bajas behave like an extension of the shelf [*Doval et al.*, 1998] and upwelling takes place inside the Rias [*Álvarez-Salgado et al.*, 2000] enhancing the flushing of the Rias.

In the next sections data from a cruise in June 1997 coincident with the spring transition are analysed. The cruise is put into a broader temporal context by using SST images before and after the cruise. The sampling strategy is presented first, followed by the data description and analysis techniques. Horizontal and vertical distribution of properties and velocity vectors are then described and particular attention will be placed on the interaction of the outflow from the Rias and the offshore circulation. The Chapter finishes with discussion and main conclusions.

4.2 Cruise description

The RRS *Charles Darwin* Cruise 105 took place in the Galician Coastal Transition Zone from 29 May to 20 June 1997 as part of the European Ocean Margin EXchange (OMEX) II-II project. The cruise was divided into two legs: leg A ran from 29 May to 8 June while leg B ran from 10 to 20 June. The main objectives of the cruise were:

- to make a detailed swath bathymetry of the slope topography of the region during leg A.
- to deploy a bottom-mounted acoustic Doppler current profiler at 156m depth and a mooring of four current meter in 686m, both near 42°40'N,
- to sample a grid of CTD stations typically 10km apart on cross slope sections ranging from 43°N to 41°25' every 10' of latitude and covering depths from 100m on the shelf to 3000m offshore,
- to record underway ADCP, temperature, salinity, fluorescence, transmittance and

irradiance.

The sampling of the slope bottom topography was carried out during leg A and only underway temperature and salinity were recorded for that period. The CTD grid sampling took place during leg B. The grid stations were roughly separated 10 to 18 km, smaller than the local internal Rossby radius of 20-30km and provided enough detail to resolve mesoscale structures. However, the 10 days it took to complete the survey compromised its synopticity. Besides the standard measurements of temperature, salinity and pressure, the CTD was also equipped with a fluorescence sensor.

Downwelling favourable wind conditions were typical for the first 4 days of Leg B with increasing northerly winds thereafter until the end of the cruise on 20 June. The moorings were deployed on the first day (10 June) and the CTD grid started on the following day. The 3 northernmost grid lines (Transects N,O and P, Fig 4.1) were done first during downwelling wind conditions, while the remainder of the grid was completed northwards from the southernmost deep station in the order V-Q under upwelling conditions.

4.3 Data and Methods

4.3.1 CTD

A total of 82 CTD stations were sampled with a Neil Brown Systems Mk IIIB CTD including a pressure sensor, a conductivity cell, a platinum resistance thermometer and a Beckmann dissolved oxygen sensor. The CTD unit was mounted vertically in the centre of a protective cage approximately $1.5m^2$. A Chelsea Instruments Aquatracka configured as a fluorometer was also attached to the system.

A General Oceanics 12-bottle tone-fire rosette pylon was fitted to the top of the CTD frame. 10-litre Niskin bottles were used throughout the cruise.

On each cast, the CTD was lowered continuously at 0.5 to $1.0ms^{-1}$ to about 20-30m

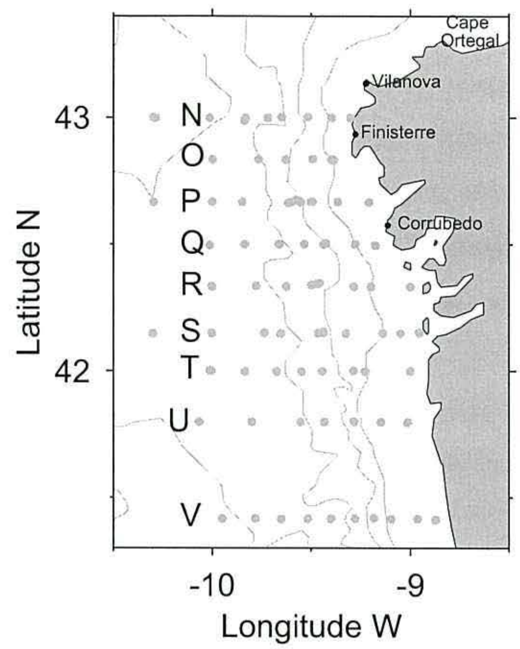

Figure 4.1.: Location of Coastal weather and CTD stations and Transect names for CD105 cruise

from the sea floor. The data were logged by the NERC Research Vessel Services (RVS) ABC data logging system. Output channels from the deck unit were logged at 32 Hz by a microprocessor interface (the Level A) which passed time-stamped averaged cycles at 1 Hz to a Sun workstation (the Level C) via a buffering system (the Level B).

The data were subsequently transferred to the British Oceanographic Data Centre (BODC) where it was converted to specific BODC data format. The data were separated into downcast and upcast and edited for spikes or spurious data. The downcasts were logged into the BODC system, calibrated and binned to 2dbar prior to their release to the OMEX II community.

The temperature sensor was calibrated against on board measurements from a digital reversing thermometer at depths greater than 1000m. Agreement was found within the manufacturers specifications and no correction was applied.

The salinity sensor was calibrated against 47 bottle samples analysed on a Guildline Autosal bench salinometer and a constant offset of 0.024psu ($\pm$0.005psu) was applied.

4.3.2 Underway measurements

The ship was fitted with a non-toxic pumped sea water supply with water drawn from an inlet approximately 5m below the surface, amidships on the starboard side. All ship's discharges were to port to minimise risk of contamination. Water from the non-toxic pump was fed into the thermosalinograph and the tank containing the fluorometer and transmissometer.

Continuous data from the Falmouth Scientific Instruments thermosalinograph were recorded every minute during both legs of the cruise. During leg A only temperature and salinity were recorded. In leg B, chlorophyll data were measured by a Chelsea Instruments Aquatracka fluorometer.

Where possible, data collected from underway sensors were calibrated against CTD data and/or discrete samples from the non-toxic supply or CTD rosette bottles. A constant offset of -0.024°C (N=77,±0.0305°C) and -0.081psu (N=85,±0.0109psu) were found for the temperature and salinity sensors.

The data were also logged by the RVS ABC data logging system as were the position data from GPS, primarily an Ashtech 3-D GPS system.

4.3.3 ADCP data collection and calibration

Instrumentation and acquisition

A RDI Acoustic Doppler Profiler (ADCP) 150 kHz instrument was used during the cruise. The ADCP transducer transmitted sound pulses every few seconds in four separate beams. Each beam was oriented at a 30 degree angle from the ship's vertical axis. The transducer was mounted roughly amidships at 5m below the water. The data acquisition system consisted of an IBM-PC compatible computer running the RDI TRANSECT program. The navigational data and the ADCP raw data were merged at the RVS ABC system level C. The instrument was set up with a pulse length of 4m, a band width of 4m, a blanking interval of 4m, and an ensemble averaging of 5min. The number of processed and recorded bins had been set to 100, about twice the actual number of good bins. Because of the additional processing time, the number of pings per ensemble was greatly reduced and the quality of the final data set degraded. The error velocity threshold for raw pings during acquisition was $1ms^{-1}$ and bins with less than 25% of percentage good (PG) were automatically flagged. No correction for pitch and roll were made; errors associated with these are likely to be small [*Kosro*, 1985]. The data were recorded continuously from 10 June 08:39 to 20 June 16:47. The sampling track and the longitude and latitude time series estimated

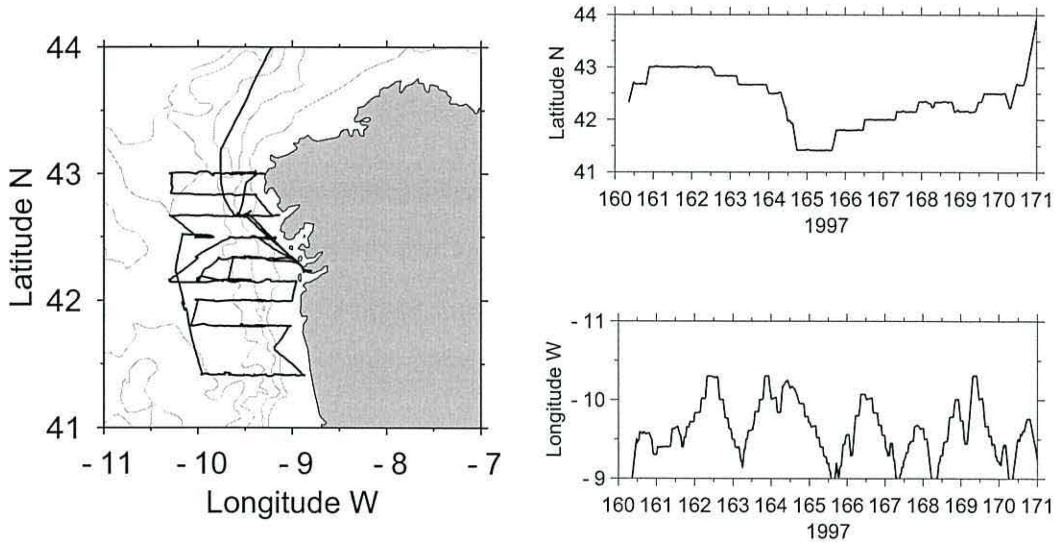

Figure 4.2.: Cruise track and longitude and latitude displacement from ADCP during CD105 cruise

from the edited GPS record are shown in Fig 4.2. The Percentage-good (PG) pings against time and depth (bin number) during CD105 decreased towards the bottom (Fig 4.3, darker colours indicate lower PG). The black region of low PG can generally be related to interference with the seafloor. The echo intensity from a hard surface such as the bottom is much stronger than the echo from scatterers in the water and for an ADCP with 30° beam angle, the echo from the side lobes facing the bottom will return to the ADCP at the same time as the echo from the main lobe at 85% of the distance to the bottom. This means that data from the last 15% are usually contaminated and were therefore removed. The bulk of the water column recorded values higher than 80%, however the first 1-2 bins appeared contaminated with values between 40-80% and were carefully inspected and dropped when necessary. The last good record that had been used for plotting later in the chapter was on 20 June 07:12 after which data degraded considerably due to worsening of weather conditions.

ADCP data processing

ADCP processing was done with the Common Oceanographic Data Access System (CODAS), which includes MATLAB routines, developed at the University of Hawaii by Eric Firing and Ramon Cabrera with subsequent updates by Julie Ranada [*Firing et al.*, 1995]. The system consists of several iterative programs to carry out editing, calibration, navigational correction and plotting of the ADCP database.

Editing The principal objectives of the editing stage are to identify when and at what depth the acoustic beams reflect off the bottom (in shallow water), to set the top bin at which a profile contains good data, and to flag bins contaminated by interference from physical objects, such as the winch wire during a CTD cast, or by other random occurrences such as instrument failure. The main editing steps are:

- Set thresholds for the quality control test. These are specific to the data set and depend upon some basic statistics from the cruise long record. First the error velocity is used which comes from the redundancy in the 3-dimensional velocity estimates u,v,w and allows the four beam RDI system to calculate two different estimates of the vertical velocity. Large discrepancies between the two indicate an inconsistency among the oceanic velocities sampled by each beam. Individual bins with an error velocity larger than 14cms^{-1} were rejected. Other quality parameters used were the second differences with respect to depth of the horizontal (*d2uv*) and vertical (*d2w*) velocities for each profile. If *d2uv* or *d2w* exceeded global 2 standard deviation thresholds, the bin was rejected. Entire profiles were also flagged if the standard deviation of w exceeded a global 3 standard deviation threshold.
- Employ the CODAS/MATLAB editing system to view various parameters such as

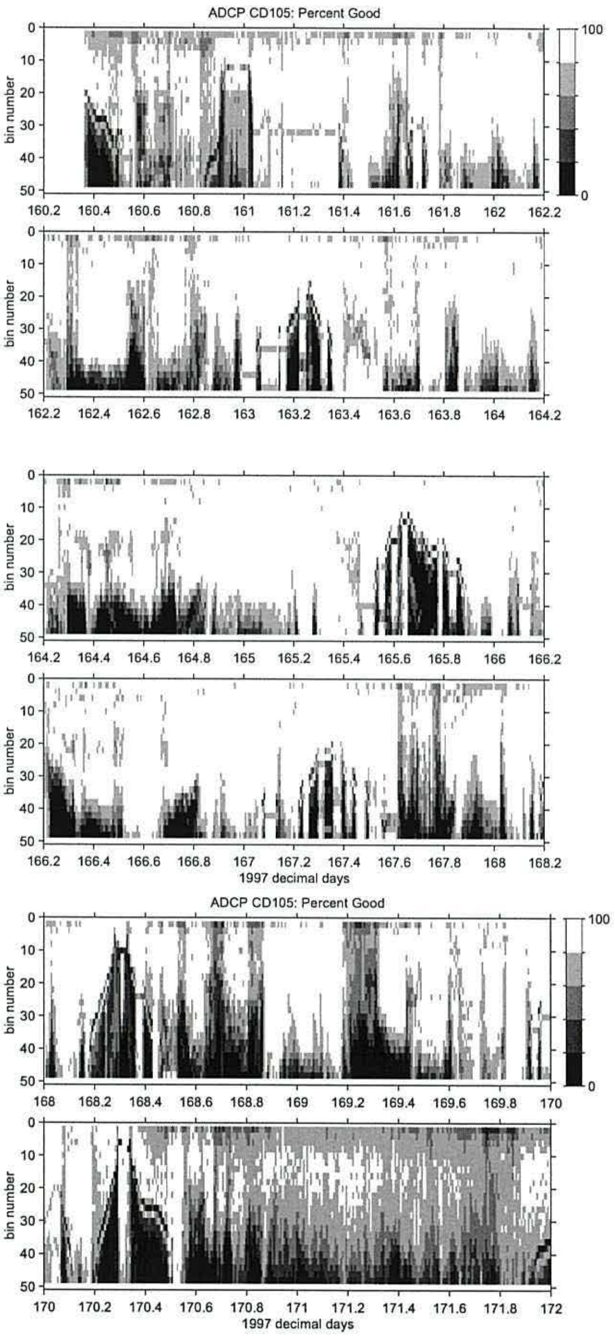

Figure 4.3.: Percentage-good pings vs. time and bin number during CD105.

relative velocities, return signal amplitude, error velocity and percentage good. At this stage the quality thresholds from above were applied and careful inspection of each individual profile determined whether the automatic flagging was accepted. The signal from the bottom was determined by jumps in the Automatic Gain Control (AGC, which gives an indication of the echo return signal strength; 1AGC count correspond to about 0.45dB change in signal power) larger than 20. The deepest subsequent bin was taken as the bottom depth and 15% of the profile depth was flagged to account for interference from the reflected signal.

- Reject or accept the flagged bins and profiles which are automatically placed in output files based on the type of error.
- Update the ADCP database by setting the maximum depth (bottom), setting the top good bin, and flagging suspicious bins for each of the profiles.

An indication of the data set quality can be inferred by looking at cruise-long averages of key variables like the PG, AGC and error velocity profiles both underway (UW) and on station (ST) shown in Fig 4.4. The variables were plotted to the maximum depth of usable data, 200m, below which no ADCP data will be discussed. From the set of variables, some indicate a certain degradation in the data quality while underway like the PG and Error velocity. The return signal amplitude was larger at shallow depths as expected, gradually decreasing with depth, never reaching a constant noise level. No significant differences can be observed between ST and UW data in either the mean or standard deviation statistics. The PG mean profiles showed the same shape with depth in ST and UW data, however UW recorded values smaller by 10-20%. Overall, no bins recorded 100% of PG, with the maximum 85-90% (70%) in ST (UW) data situated around 40m and decreasing either side. The PG threshold for 'good data' was set to 30% which corresponds to 175m (160m) in ST (UW) records. The low PG return at the shallowest bins might be related to the physical installation of the ADCP transducer in the *Charles Darwin* and similar problems were experienced in a later cruise on the same ship (see Chapter 5). The mean vertical difference of the horizontal components of velocity were relatively small over the depth range, generally less than 2.5cms^{-1}, but very variable. However no significant changes were noticeable between ST and UW data. Nonetheless, the spikiness of the profiles suggest that a larger vertical averaging is required in order to reduce the variability and indeed the ADCP data later shown in this chapter correspond to 10m or larger vertical means and at least 10min temporal averages. Vertical velocity values were relatively small as expected and discrepancies between ST and UW profiles were restricted to the shallowest bins. The larger values found below 160m are another indication of decreased data quality. The error velocity profiles showed the largest and most consistent differences between ST and UW data. Maximum values of 0.2cms^{-1} were measured while in station while values of 1cms^{-1} were typical of UW profiles.

Calibration Velocities relative to the ship must be adjusted for orientation of the transducer relative to the gyro compass and for any inaccuracy in the relative geometry of the four beams. With accurate navigation information available during large changes in ship's velocity, amplitude and angle errors can be computed from the ADCP velocities during post processing [*Pollard and Read*, 1989]. The method used was water track, which compares the acceleration relative to the water, measured with the ADCP, to the acceleration over the ground, calculated from navigation. The calibration consists in the calculation of the amplitude (β) and phase (α) correction factor to the water track velocities to be used subsequently in the Gyro correction,

$$U_c = \beta e^{i(\alpha\pi/180)} U_u, \tag{4.1}$$

where suffix c and u stand for corrected and uncorrected velocity in their complex form $U_c = u_c + iv_c$. The angle is specified counterclockwise from the gyro compass forward axis (which should be aligned with the ship's keel) to the transducer forward axis. In the case of CD105 cruise, the amplitude and angle values used to correct the raw ADCP data with their respective standard deviations are shown in Table 4.1. The raw values were edited following a simple median criterion to exclude outliers among β and α estimates. Their time evolution and frequency distribution are shown

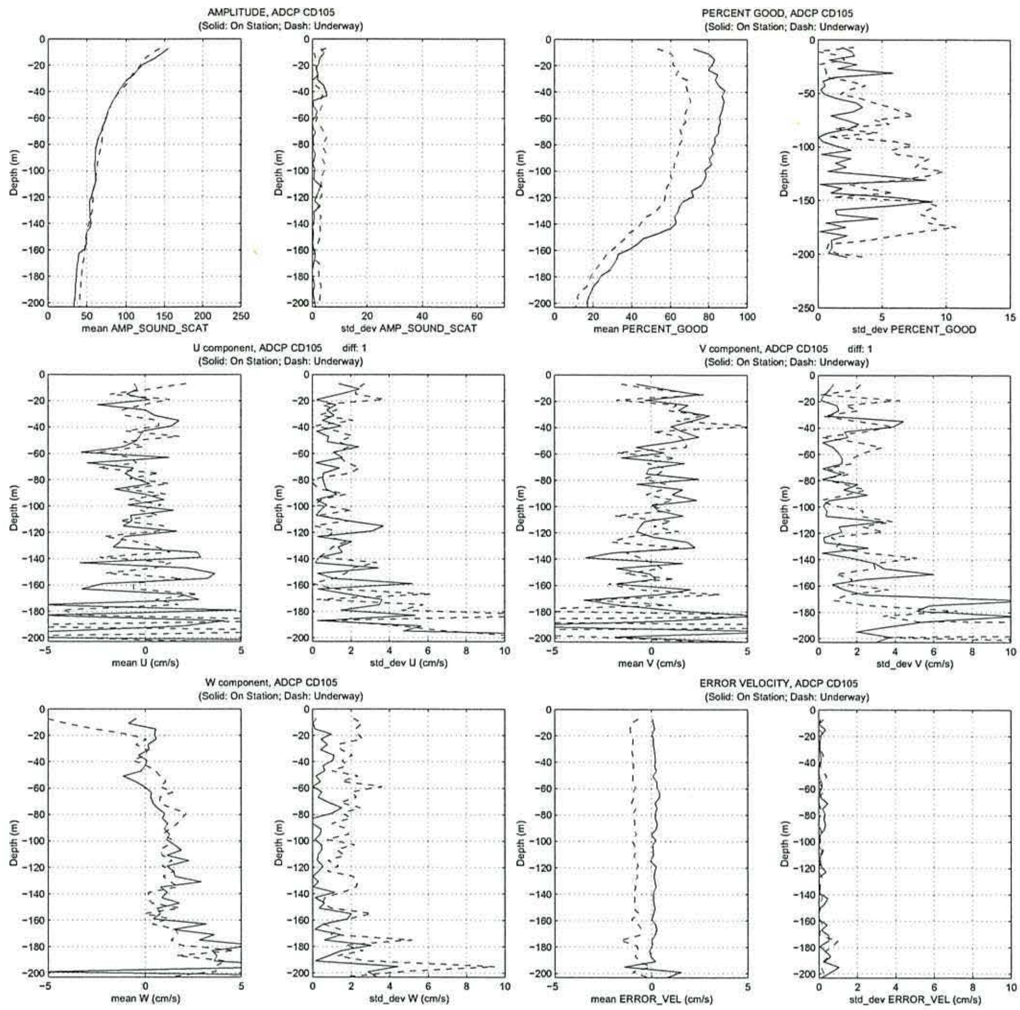

Figure 4.4.: Plots of average value and standard deviation among the 5 minutes ensembles for underway and on station profiles of AGC, PG, first vertical difference of horizontal components U and V, vertical component of velocity and error velocity against depth. For each plot the solid line represents on station data and the dashed line, the underway data.

in Fig 4.5. At worst (at highest ship speed of $\sim$ 5ms^{-1}), the β and α uncertainties imply an unknown bias of 5cms^{-1} in velocity measurements.

$\beta \pm \sigma$		$\alpha \pm \sigma$	
1.02	$\pm$0.01	-7.2	$\pm$0.5

Table 4.1: Calibration parameters for CD105

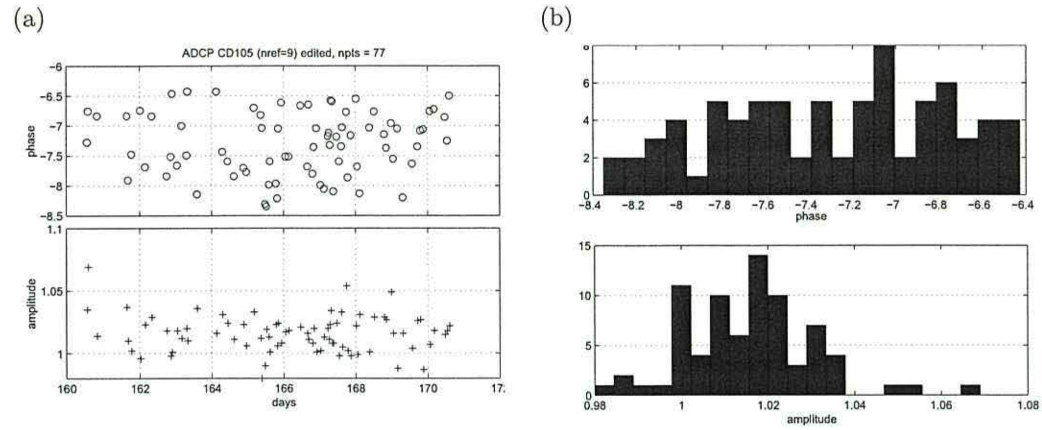

Figure 4.5.: Calibration parameters for CD105 cruise ADCP data.

Navigation The final step in processing ADCP data is the introduction of navigation data, which are used to calculate the ship's velocity and absolute water velocities. The absolute reference layer velocity is the sum of the ship's speed over the ground obtained from the navigation data, and the average relative water velocity in the reference layer, measured by the ADCP. This layer is calculated with reference bins between 5 to 30. The data used in this interval have a percentage good over 30. Once the reference layer is obtained the data are interpolated and smoothed with a Blackman window and a filter width of 30min as recommended in *Firing et al.* [1995]. Profile positions are also calculated from the smoothed velocities. The final estimate of absolute velocities is made by adding the shear profile for each ensemble to the reference layer velocity. The steps followed in this process were: 1) obtain the ship velocity relative to the reference layer, 2) calculate the absolute ship velocity, 3) smooth and interpolate the data to the ADCP ensemble times and 4) update the database. An example of smoothed reference layer velocity can be seen in Fig 4.6

Streamfunction Estimates of non-divergent flow

In order to minimize the described limitations of the ADCP data set due to instrumental errors, and the aliasing effects of tidal and inertial signals, the

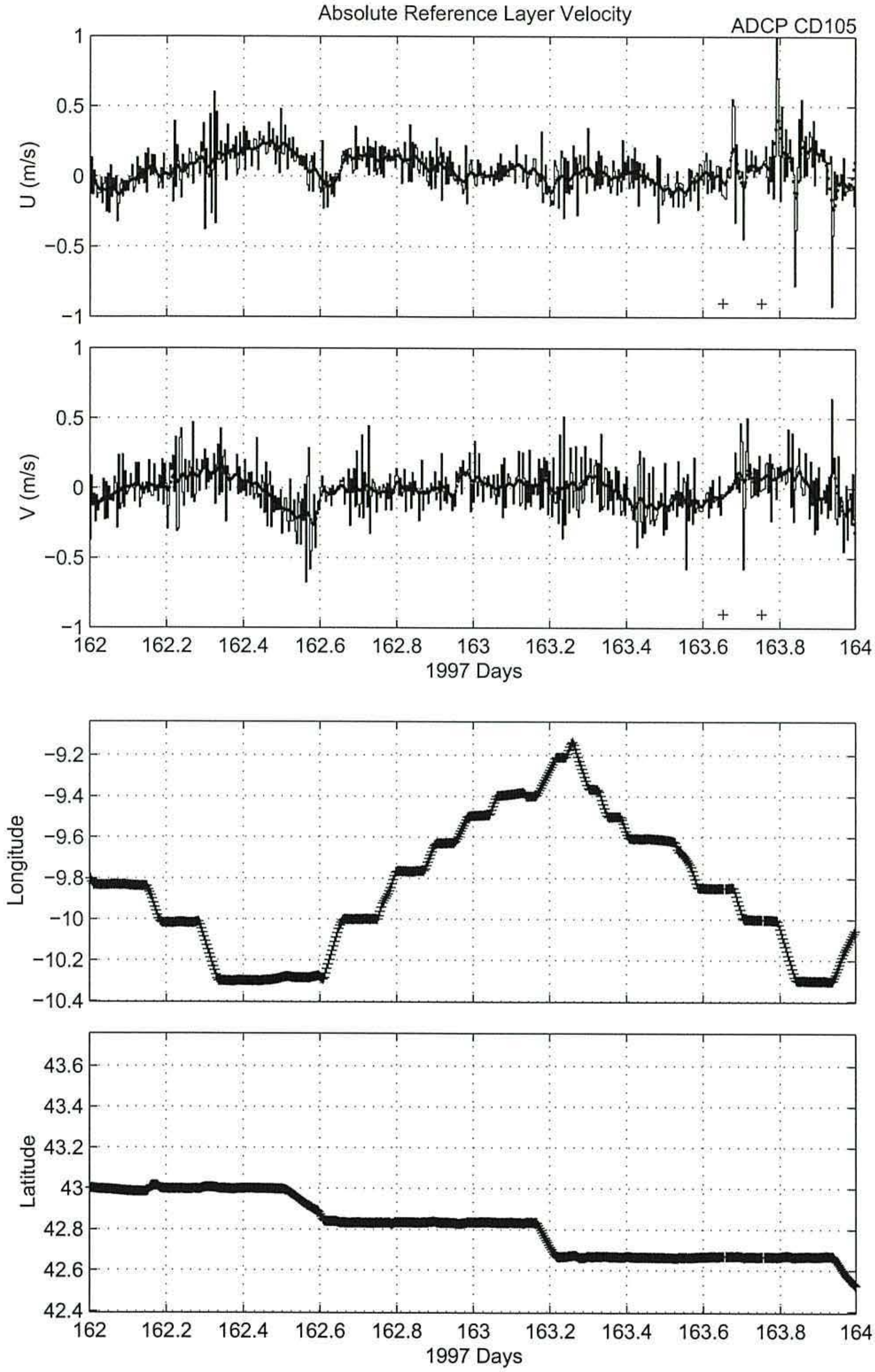

Figure 4.6.: Smoothed reference layer velocity calculated over bins 5-30, and latitude and longitude time series from days 162-164. The data were filtered to remove motions with time scales of less than 30min and rotated with the calibration parameters. Crosses at the bottom of the velocity panels indicate gaps in the GPS record.

streamfunction for the ADCP velocities is derived (Eq. 4.2).

$$\nabla^2\psi = \frac{\partial v}{\partial x} - \frac{\partial u}{\partial y}. \tag{4.2}$$

The processing was similar to that reported in *Barth et al.* [2000] and *Pierce et al.* [2000]. Gridded fields of U and V components at selected depths were built using a four-pass Barnes objective analysis (OA) scheme [*Barnes*, 1994; *Koch et al.*, 1983]. The gridded field is estimated by iteratively applying a Gaussian-weighted average converging towards the observed points. To account for the larger uncertainties in the UW ADCP data, ship velocity weights were used together with the distance-based weighting. Although related to the statistical optimal interpolation, this method does not required prior specification of a covariance model for the observed field. The Barnes radii corresponded to 7km and 11km in the X and Y directions so that scales larger than these were not smoothed. The streamfunction was then calculated for the gridded levels using the version III method of *Hawkins and Rosenthal* [1965], also described by *Carter and Robinson* [1987], which represents an alternative way of estimating the streamfunction values at the boundaries. The method derives from the Helmholtz theorem (Eq. 4.3) which allows the separation of a velocity field into a non-divergent part and an irrotational component. $\overline{V}$ is the horizontal velocity, K is the unit vertical vector, ψ is the horizontal streamfunction (the non-divergent part) and η is the horizontal velocity potential (the irrotational part).

$$\overline{V} = K \times \nabla\psi + \nabla\eta. \tag{4.3}$$

Taking the scalar product of Eq. 4.3 with n, the unit outward normal vector, we get,

$$\frac{\partial\psi}{\partial s} = -\overline{V}_n + \frac{\partial\eta}{\partial n}, \tag{4.4}$$

where s is the distance along the boundary in a counterclockwise direction, and $\overline{V}_n$ is the velocity normal to the boundary. By integrating equation 4.4 around the boundary, we get ψ values at the boundary that will be used in the streamfunction calculations, rather than using the observed velocity field, which need not be non-divergent given the measurement noise. However, the boundary values of η

need to be calculated first by solving Eq. 4.5, for the velocity potential forced by the observed field of divergence.

$$\nabla^2 \eta = \nabla \cdot \overline{V}. \tag{4.5}$$

Boundary conditions of $\eta = 0$ were imposed. In this way, the total kinetic energy of the ψ field is maximized while minimizing the amount of energy in the η field [*Carter and Robinson*, 1987].

The Poisson solver developed by *Cummins and Vallis* [1994] was used to solve Poisson equations Eq. 4.2-4.5. The solver uses the capacitance matrix method and handles Dirichlet boundary conditions in an irregular domain. Non-divergent vectors are derived from the gridded streamfunction and then interpolated back to their original locations using improved Akima bivariate interpolation [*Akima*, 1996] The Barnes OA and the streamfunction derivation together amount to a method of systematically applying conservation of mass throughout a region [*Pierce et al.*, 2000]. The derivatives were calculated with central differences in the interior points while forward difference was used at the boundaries. Trapezoidal numerical integration was used in all integral calculations.

An example of the vectorised ADCP data and non-divergent current vectors centred at 51m is shown in Fig. 4.7. ADCP current vectors (Fig 4.7a) were averaged in cells of 0.05x0.05°. The non-divergent field clearly reproduces the large scale features seen in the raw field. The offshore poleward flow, coastal southward jet and the two eddies are all well defined in the non-divergent field. It is important to bear in mind that strong wind changes took place during the cruise, mostly affecting the nearshore region, and the non-divergent field is a smoothed version of the raw field.

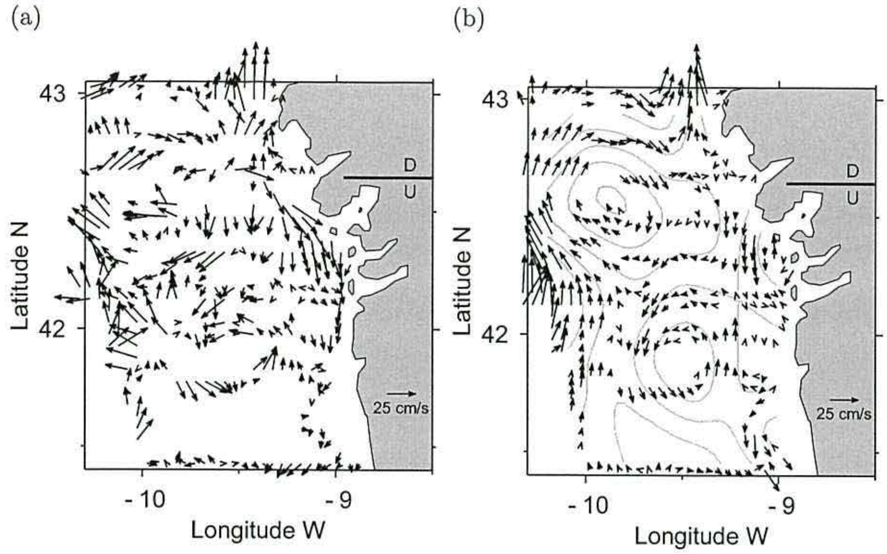

Figure 4.7.: Example of (a) vectorised ADCP data with minimum averaging of 10min and 12m in the vertical centred at 51m and (b) non-divergent ADCP current vectors superimposed on transport streamfunction contours with a $0.01 \times 10^6 m^3 s^{-1}$ contour interval over 12m. The line on land indicates the area sampled under upwelling (U) and downwelling (D) conditions.

4.4 Results

4.4.1 SST and wind conditions prior, during and after the cruise

The CD105 cruise took place during the Galician transition from the poleward flow dominated winter regime to the upwelling summer regime. The weekly SST composite images in Fig 4.8 correspond to 1-7 June, coincident with leg A, and 29-05 July, nine days after the completion of the cruise. Their resolution is about 4km and they are the median, pixel by pixel, of all early morning satellite passes over the week. Spurious structures and patchiness may have been introduced by the merging process due to clouds and transient structures and so the figures have to be considered cautiously. In Fig 4.8a the coastal warm waters extend to the 200m isobath, with temperature decreasing northwards, while a second warm tongue of similar temperature lies offshore of the 1000m isobath. The two tongues appear to converge south of 41°N. Eddy like structures with scales of 30km are evident in the offshore tongue (E1-E3) but were no longer visible in subsequent images, possibly due to the storm on 6-8 June (e.g. Fig 4.9). In the following two weeks, the offshore

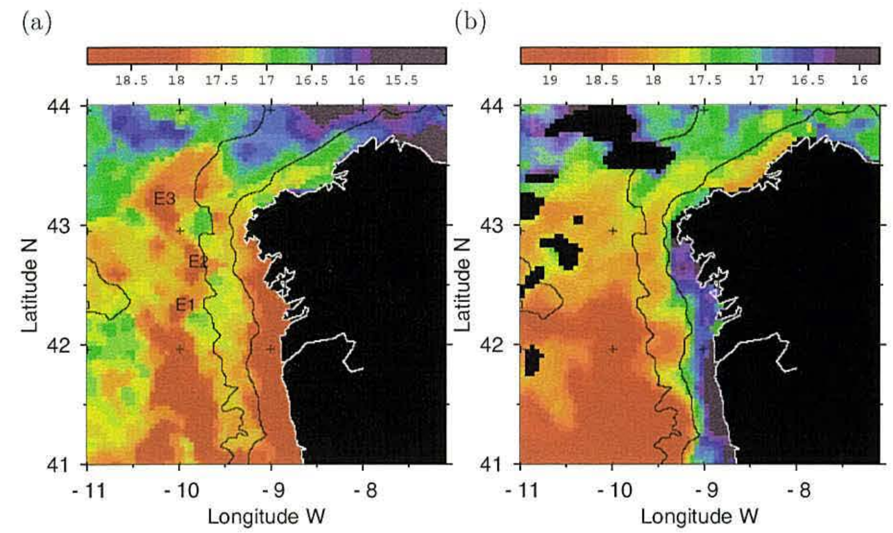

Figure 4.8.: SST weekly averaged images from a)1-7 and b)29-05 July 1997 corresponding to leg A and 9 days after the end of cruise CD105. Eddies have been numbered with an E prefix. The 200 and 1000m isobath are included. Note the different temperature scale.

branch of the warm tongue weakened and receded, and on the third week it did not extend beyond 42.5°N Fig 4.8b. The coastal tongue disappeared and was replaced by a coastal band of upwelled water extending to 200m Fig 4.8b.

Coastal winds (Fig 4.9) were recorded at three locations along the Galician coast at Vilanova, Finisterre and Corrubedo (Fig 4.1) for the months of June and July. The period of the cruise is indicated in the figure. The wind flows predominantly along the direction of the coast and spatial differences are expected due to the complex coastline of the region. Although these might not be representative of the more complex large scale winds (e.g. Chapter 3) they can give an indication of predominantly upwelling or downwelling favourable winds. During leg A until 13 June conditions were downwelling favourable with peak winds of $15ms^{-1}$ and $12ms^{-1}$ at Vilanova and Corrubedo respectively, on 6-8 June when a storm hit the region. Thereafter conditions were upwelling favourable with variable weak winds of $6ms^{-1}$ until 13 July, and remained strongly upwelling favourable in excess of $10ms^{-1}$ afterwards. Hence, 4 days after the start of leg B, the regime changed from a strongly downwelling scenario to a weak upwelling one, which had an impact in the nearshore stations and affected the synopticity of sampling. This will be discussed later in the chapter.

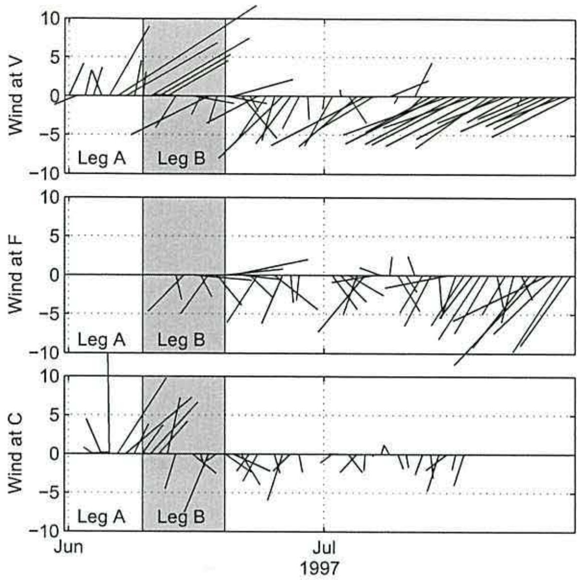

Figure 4.9.: Daily coastal winds from Corrubedo (C), Finisterre (F) and Vilanova (V). The time of the two Cruise legs is indicated in the graph. The sticks point in the direction of the wind with the north in the positive Y axis.

Six hourly estimates of upwelling index at 42°N, 9°W from May to August (Fig. 4.10) were derived from the Fleet Numerical Meteorology and Oceanography Center synoptic wind fields obtained from the NOAA Pacific Fisheries Environmental Laboratory [*http://www.pfeg.noaa.gov*]. The upwelling indices were calculated using Bakun's method [*Bakun*, 1973]. Figure 4.10 clearly shows the shift in the wind regime in agreement with the local winds. Except for brief episodes of upwelling favourable winds at the beginning of May, weak or downwelling favourable winds were common throughout the second half of May and early June. On 14 June, winds became upwelling favourable and remained so until the end of the record.

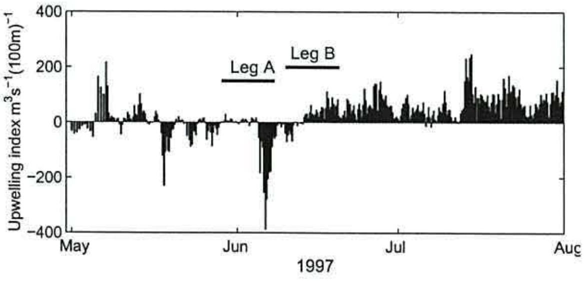

Figure 4.10.: Six hourly estimates of upwelling index at 42°N, 9°W, m^3s^{-1} $(100m)^{-1}$. Data from NOAA Pacific Fisheries Environmental Laboratory.

4.4.2 Horizontal Fields

Near-Surface (5m) fields

The near-surface salinity distribution (5m) recorded from the thermosaligraph for legs A and B are shown in Fig 4.11. Although it is difficult to consider them as true synoptic fields in the light of the wind changes occurring during the cruise they will be discussed as snapshots. The temperature fields are not discussed here as they showed a strong diurnal heating that masked any of the spatial structures. The salinity in this region can be used as a circulation tracer because the T/S characteristics in the upper layer (top 100m) are roughly perpendicular to the isopycnals (Fig 4.26a).

During leg A (Fig 4.11a) the salinity range was small over most of the area (36.08-35.70psu) with the exception of an isolated low salinity region marked as "L" in the graph where it reached values of 35.4psu. Salinity generally decreased with latitude, and meridional differences were larger than zonal ones. The SST composite image of leg A has a signature similar to the near surface salinity field, with warmer temperatures related to higher salinities. The region of highest salinity ($> 36psu$) in the SW corner of the graph corresponds to an area of high temperatures in Fig 4.8a and the warm tongue extending from it has a rough equivalent in the salinity field, both turning inshore at ~42.4°N. Near the location of E2 (Fig 4.8a) in Fig 4.11a, a local salinity maximum exists. The low salinity region "L" is part of a relatively low salinity tongue which seems to have its origin in the Rias Bajas (Fig 2.1), between 42.2° and 42.5°N, although more southern origins can not be ruled out. The tongue turns southwards at -9.5°W, rather than northwards as would have been expected from freshwater plume dynamics. Note that along that longitude a colder water band can be seen in Fig 4.8a parallel to the offshore warm tongue.

In leg B, the sampling included coastal stations at depths $< 100m$ and the salinity range widened to include lower values (36-30.5 psu). The period was characterized by weak upwelling favourable winds except for the time of the three northernmost sections. The shoreward limit of leg A decreased in salinity in leg B (Fig 4.11b), which showed even lower values nearshore, particularly south of 42.75°N. This led to the formation of a strong salinity front which was enhanced south of 42.25°N due to the presence of the high salinity tongue offshore (P in the graph) with $\triangle S > 0.4psu$. The high salinity tongue P broadened during leg B and split at 42.25°N, one branch turning offshore at that latitude, while the other progressed northwards only to turn offshore further north. The high salinity structure E is now better defined with values $>$ 38.85psu. The low salinity tongue (L in leg A), had shifted slightly northward, decreased in salinity and extended offshore to -10°W south of E.

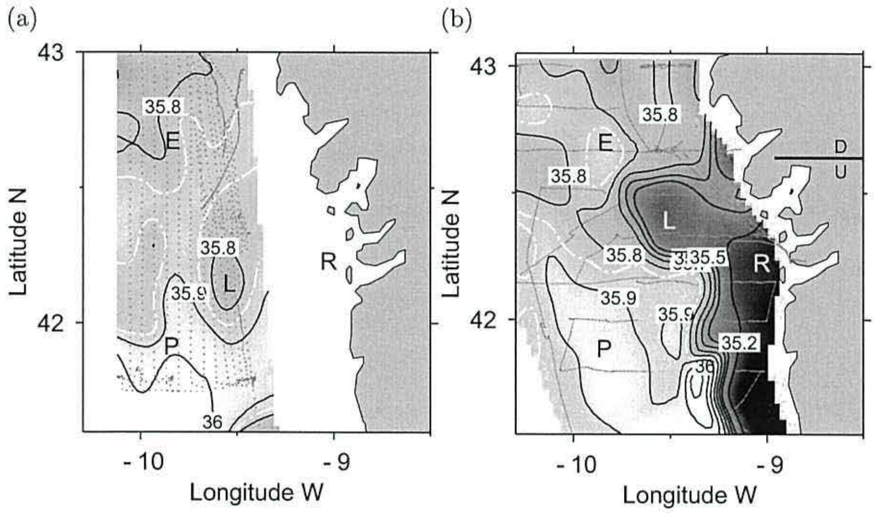

Figure 4.11.: Salinity distribution at 5m as recorded by the thermosalinograph from a)leg A and b)leg B. The isosaline of 35.85 appears as a white dashed line. The structures identified in leg B are indicated as E (eddy), P(poleward flow) and R (fresh water runoff) and are included in a) for reference. A low salinity region found in leg A is marked as L. Darker shading indicates lower salinity. The line on land indicates the area sampled under upwelling (U) and downwelling (D) conditions.

The near surface (5m) un-calibrated fluorescence data from leg B (Fig 4.12a) resembles the salinity field with high fluorescence values related to low salinity. The salty tongue P is associated with low fluorescence values ($<$ 0.5V), as are the northern offshore waters. Values are higher close to the mouth of the Rias and the Miño River, where the highest values were measured ($>$ 1V), but decrease rapidly offshore on scales of $<$ 20km. The previously identified low salinity tongue L can be seen in Fig 4.12 as a region of fluorescence in the range 0.55-65V extending offshore near

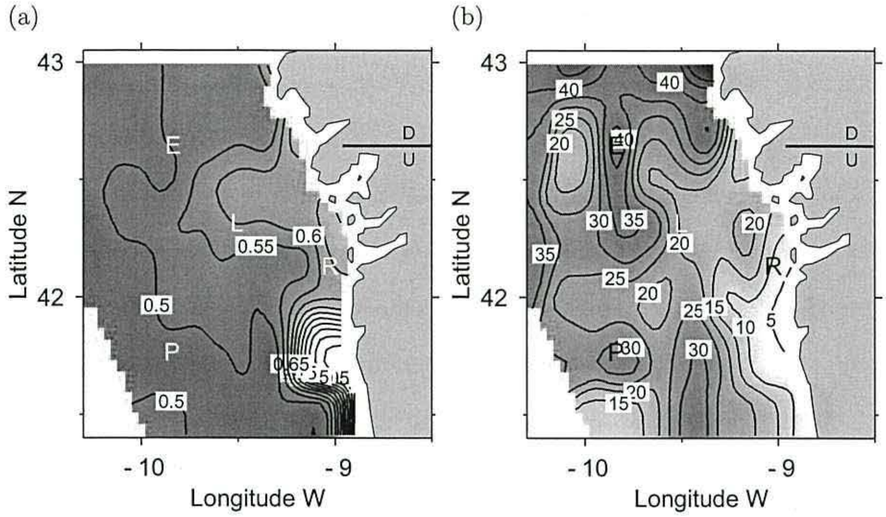

Figure 4.12.: a) Fluorescence distribution (in Volts) at 5m as measured by the CTD from leg B. Darker shading correspond to lower fluorescence values. b) Distribution of surface mixed layer depth using criteria of $\Delta\sigma_t = 0.1\text{kgm}^{-3}$. The line on land indicates the area sampled under upwelling (U) and downwelling (D) conditions.

42.4°N.

The mixed layer distribution (Fig 4.12b) was calculated using the density difference with the surface, with the criteria $\Delta\sigma_t = 0.1\text{kgm}^{-3}$, which represents a measure of the layer that has been recently mixed [*Brainerd and Gregg*, 1995]. Maximum depths ($> 40m$) were measured in the northern limit in association with the poleward flow while minimum values were encountered nearshore south of 42.25°N. The latter corresponds to the region influenced by the freshwater runoff from the Miño river. The low salinity plume L has typical mixed layer depths of 20m. The centre of the eddy E is characterized by deeper mixed layer depths than surrounding waters by as much as 20m.

Near-Surface (15m) fields

Horizontal fields at the level of the shallowest reliable ADCP bin (12m bin centred at 15m depth) are shown in Fig 4.13. The salinity and fluorescence contours (4.13a-b) show some fundamental differences when compared to the 5m fields. The freshwater coastal band south of 42.15° N has now disappeared although a narrow band of high fluorescence is still visible 15km off the coast. The salty tongue P at this depth shows

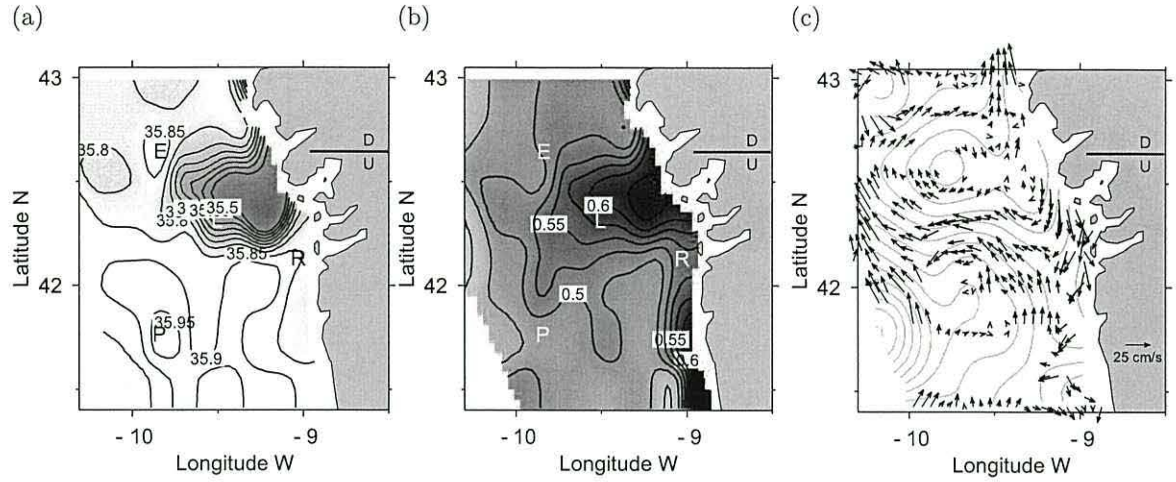

Figure 4.13.: Near-surface (15m) properties during Leg B 10-20 June 1997. (a) Salinity; darker shading corresponds to lower salinity. (b) Fluorescence in Volts; darker shading correspond to higher values. (c) Non-divergent ADCP current vectors with minimum averaging of 10min and 12m in the vertical centred at 15m superimposed on transport streamfunction contours with a $0.01 \times 10^6 m^3 s^{-1}$ contour interval over 12m. The line on land indicates the area sampled under upwelling (U) and downwelling (D) conditions.

two branches, the offshore branch, which was clearly present at 5m in Fig 4.11a and b, and a coastal branch, only slightly evident at 5m, running along the slope as far as 42.15° N. The low salinity region L still extends offshore but at a more northern position and with minimum values (< 35.5) now closer to shore than at the surface. The eddy E is again identifiable by its salinity maximum. The fluorescence field shows a similar pattern to the 5m level, however high values extend further offshore. Part of the high fluorescence plume turns southwards at 9.75°W 42°N, while a smaller tongue turns northward offshore the high salinity eddy E. The poleward branching is also noticeable in the fluorescence data south of 42°N.

The non-divergent current field and overlaid contours of streamfunction transport for that level are shown in Fig 4.13c. The main structure is the broad contorted poleward flow with maximum velocities of $>25 cms^{-1}$. Much of its transport appears to enter the region west of 10°W where no measurements were available at this level. Observations at deeper levels (Fig. 4.7a) show this inflow clearly. The inflow fed the offshore poleward flow (0.04Sv) and only 0.02Sv came from the south to form the coastal branch with velocities up to $15 cms^{-1}$. The two branches correspond to the salinity and fluorescence distribution of Figs. 4.13a-b. The coastal poleward current meets the southward coastal current with velocities up to $25cms^{-1}$ at 42.3°N (0.03Sv) and veers offshore to merge with the offshore branch. This change in direction from a northward to southward coastal current could also be related to the shift in wind forcing and may represent a temporal change. Most of the poleward flow (0.08Sv) leaves the region westward between 42°-42.5°N but 0.03Sv proceeds northwards with lower salinity after mixing with the low salinity coastal current. Anticyclonic circulation was associated with the high salinity eddy E involving 0.01Sv. The flow further splits into the offshore and the coastal poleward current (0.02Sv) reaching velocities up to $25cms^{-1}$. At this shallow level the current field was affected by the wind reversal and so the coastal poleward flow observed in the first three northern lines might have later reversed with the wind to form part of the coastal southward jet observed in the south. A more detailed discussion on the nearshore variability during the cruise is presented later in the chapter.

Sub-surface fields

The salinity field below the mixed layer (at 50m, Fig 4.14a) shows the offshore salty tongue along the western limit of the grid more clearly. Salinity was higher ($36psu$) in the offshore branch than in the separate coastal branch (35.95-$35.90psu$). The high salinity eddy E appears shifted to the west. No sign of the coastal freshwater plume seen at shallower levels is apparent at 50m. Lower salinity ($< 35.9psu$) is found mainly north of 42.5°N at the coast, and further north offshore.

The fluorescence field (Fig 4.14b) also lacks the high coastal values seen in Fig 4.12a-4.13b. It exhibits a patchy distribution of high fluorescence centres (0.5-0.65V) which seem related to the offshore poleward flow and the eddy E. These centres were not present at shallower levels.

The non-divergent field (Fig 4.14c) shows weaker circulation at this level. Nonetheless the offshore poleward flow is still strong ($\sim$20-$25cms^{-1}$) at the western limit of the sampled region with a transport of at least 0.03Sv. The northern coastal poleward

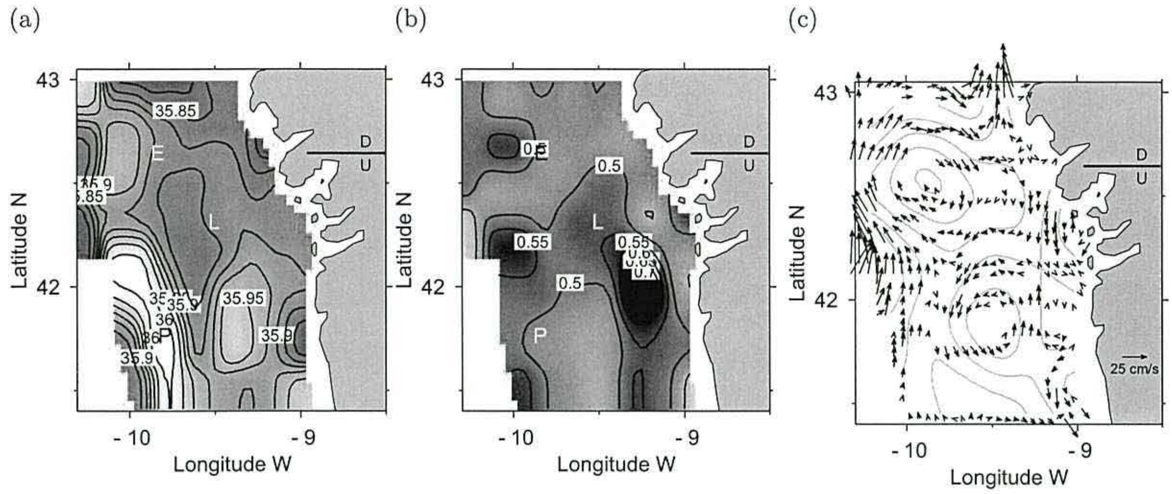

Figure 4.14.: Sub-surface (50m) properties during Leg B 10-20 June 1997. (a) Salinity; darker shading corresponds to lower salinity. (b) Fluorescence in Volts; darker shading correspond to higher values. (c) Non-divergent ADCP current vectors superimposed on transport streamfunction contours with a $0.01 \times 10^6 m^3 s^{-1}$ contour interval over 12m. The line on land indicates the area sampled under upwelling (U) and downwelling (D) conditions.

branch has similar transport to 15m (0.02Sv) and the same holds for the anticyclonic circulation of the eddy E (0.01Sv). However, some of the offshore waters return to the shelf north of the eddy, and join the weak coastal southward flow. The more inshore poleward flow in the south appears more part of a cyclonic re-circulation than a continuous current.

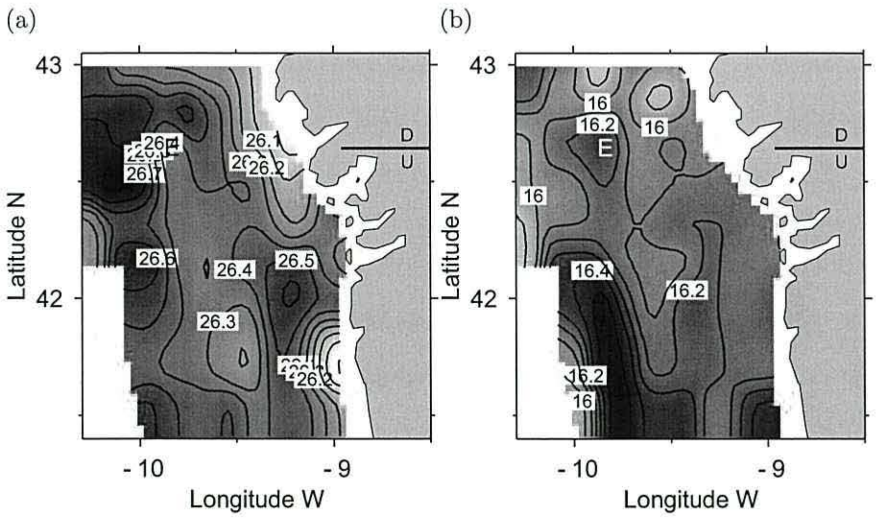

Figure 4.15.: Sub-surface (50m) contour of (a) Density and distribution of (b) Temperature at $\sigma_t = 26.4 kgm^{-3}$ isopycnal. The line on land indicates the area sampled under upwelling (U) and downwelling (D) conditions.

The density distribution at 50m (Fig 4.15a) is similar to the temperature distribution at this depth as temperature is the controlling factor over salinity. The 50m level is in or just below the thermocline for most of the off-shelf CTD stations. Small deviations in the pycnocline caused by internal tides and waves can significantly contaminate the temperature distributions near this depth level. The temperature is therefore plotted on the isopycnal surface ($26.4kgm^{-3}$) which best represents the base of the mixed layer. The resultant distribution (Fig 4.15b) resembles the salinity distribution at 50m. Higher temperatures were associated with the high salinity offshore poleward flow as expected and the centre of the eddy E is now positioned east of the high salinity anomaly in better agreement with the non-divergent current vectors.

Similar structures are present at deeper levels. The offshore salty and warm poleward flow is present down to 200m (Figs. 4.16a- 4.18a), its salinity difference with surrounding waters decreasing with depth. The more nearshore poleward flow is completely separated from the offshore branch at 100m by a low salinity-low temperature band running parallel to the coast (Fig. 4.16a-b). Remnants of the coastal branch (warm and salty pools) are found north and south of the Rias Bajas at 100m but disappear at deeper levels (Fig 4.17a,b- 4.18a,b). The eddy E is present down to 250m with highest associated anomalies 0.1psu (0.8°) salinity (temperature) at 150m (Fig 4.17a-b) suggesting it is a deep seated feature, though smaller than a typical SWODDY [*Pingree and LeCann*, 1992b].

The non-divergent current field at 100m is similar but less energetic than at shallower depths (Fig 4.16c). The offshore poleward flow, the northern coastal poleward current and the anticyclonic eddy are all present down to 150m (Fig 4.17c), at which depth the coastal equatorward flow had disappeared. The offshore flow off the Rias Bajas at 42.25°N weakens with depth and disappears below 150m. The meridional low salinity/temperature band clearly visible at 100m can be traced as a southward flowing jet down to the maximum penetration of the ADCP (Fig 4.18c), at which level a weakened poleward flow is still present offshore.

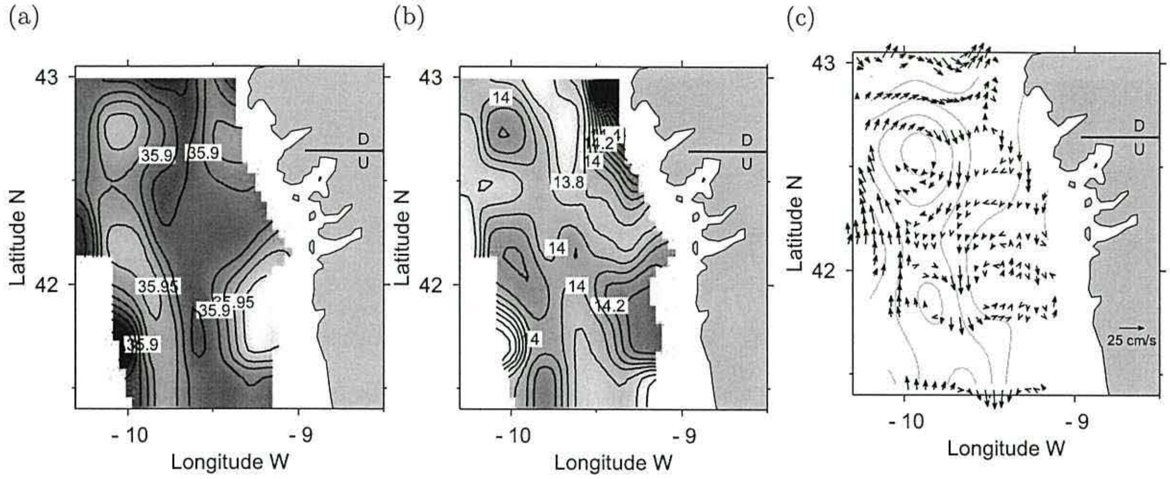

Figure 4.16.: Sub-surface (100m) properties during Leg B 10-20 June 1997. (a) Salinity; darker shading corresponds to lower salinity. (b) Temperature; darker shading correspond to warmer temperatures. (c) Non-divergent ADCP current vectors superimposed on transport streamfunction contours with a $0.01 \times 10^6 m^3 s^{-1}$ contour interval over 12m. The line on land indicates the area sampled under upwelling (U) and downwelling (D) conditions.

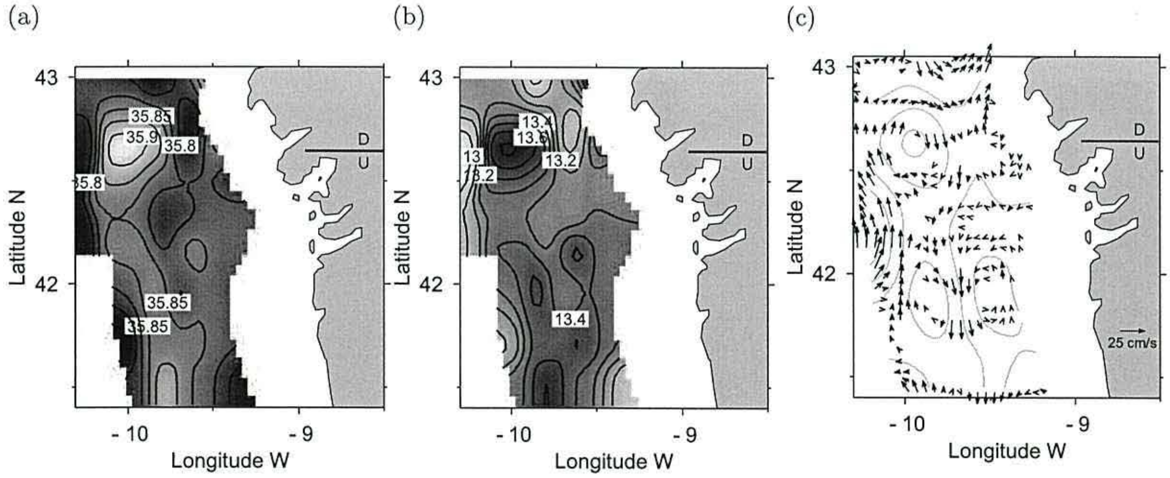

Figure 4.17.: Sub-surface (150m) properties during Leg B 10-20 June 1997. (a) Salinity; darker shading corresponds to lower salinity. (b) Temperature; darker shading correspond to warmer temperatures. (c) Non-divergent ADCP current vectors superimposed on transport streamfunction contours with a $0.01 \times 10^6 m^3 s^{-1}$ contour interval over 12m. The line on land indicates the area sampled under upwelling (U) and downwelling (D) conditions.

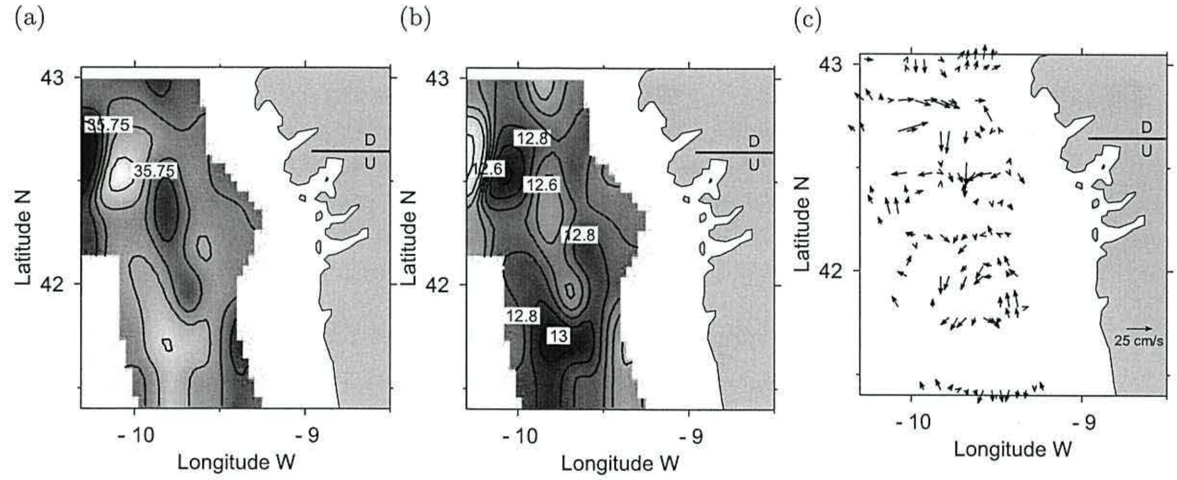

Figure 4.18.: Sub-surface (200m) properties during Leg B 10-20 June 1997. (a) Salinity; darker shading corresponds to lower salinity. (b) Temperature; darker shading correspond to warmer temperatures. (c) vectorised ADCP data with minimum averaging of 10min and 12m in the vertical centred at 195m.The line on land indicates the area sampled under upwelling (U) and downwelling (D) conditions.

4.4.3 Vertical Fields

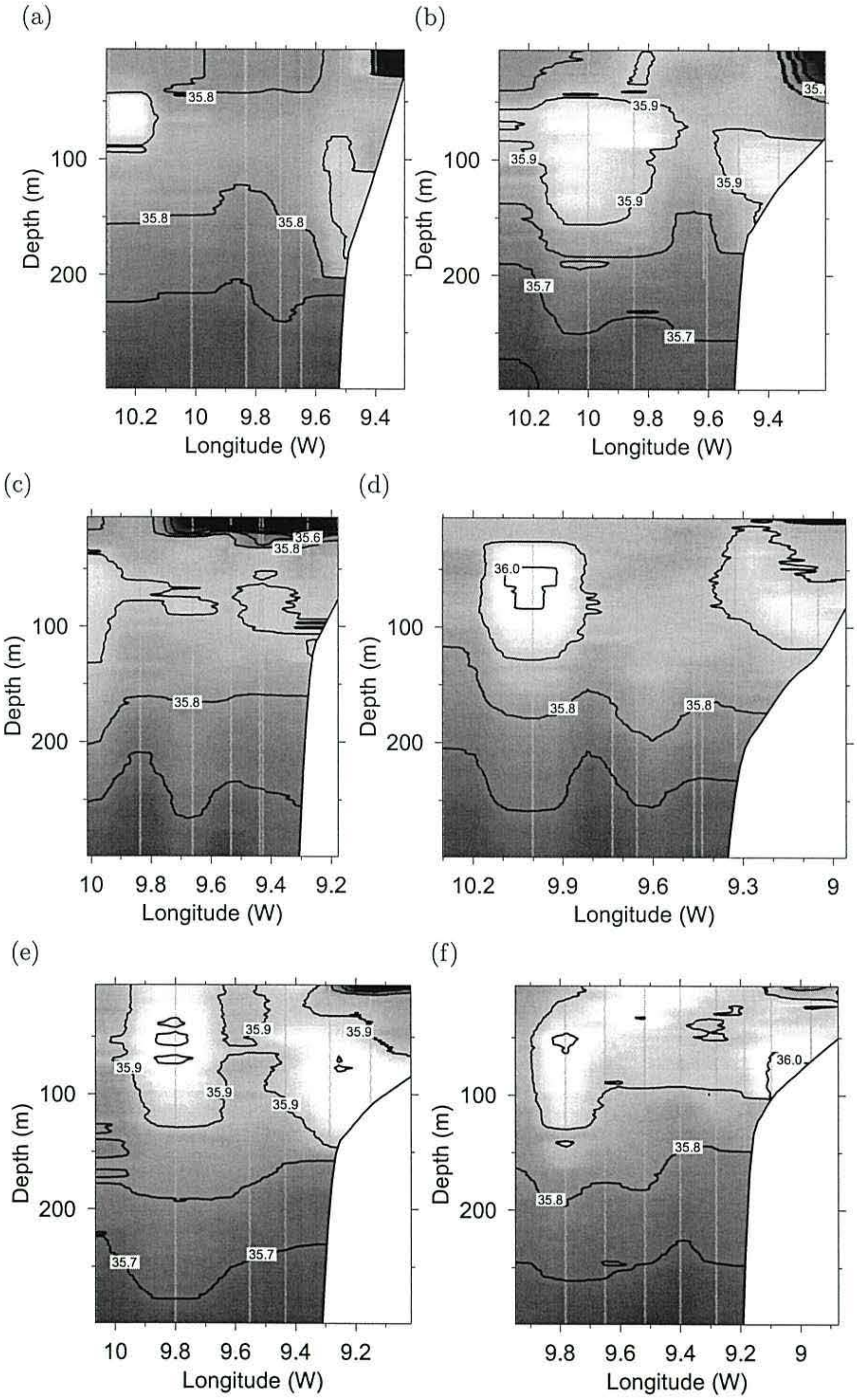

Figure 4.19.: Vertical sections of salinity for transects (a) N, (b) P, (c) Q, (d) S, (e) U and (f) V down to 300m. Contouring interval is 0.1psu.

Salinity structure

The top 300m of the salinity salinity structure is shown in Fig 4.19 for transects (a) N, (b) P, (c) Q, (d) S, (e) U and (f) V (locations in Fig 4.1). Two maximum salinity cores (>35.9psu) can be seen in the range 50-150m over the shelf and at ~70km offshore. Both are associated with the poleward flows seen in the surface contours. The offshore core is consistently shallower and has higher salinity than the shelf core. The cores are almost merged into a single feature in the southernmost section, transect V (Fig 4.19f), and are increasingly separated towards the north. Although the core maximum values are located at surface to mid-depth, local high salinities below the salinity cores extend down to 300m. At the most southern latitudes, the isohalines below 150m seem to rise shorewards.

Towards the north, the two salinity cores separate, decrease in maximum salinity, and become more sub-surface features. The cores are most widely separated in section S (Fig 4.19d). From this section northwards, the isohalines below 150m slope downwards towards the coast, possibly reflecting the dominance of poleward flow before and at the start of the upwelling favourable wind. The thin (< 20m) layer of fresher Ria waters extend most offshore in the central sections and is most strongly concentrated against the coast in the early northern sections. This again agrees with the idea of downwelling influence in the first sections sampled and increasing effect of upwelling and offshore Ekman flow in succeeding ones. Transect P (Fig 4.19b) shows the broadest and deepest offshore salinity core (50-150m), and coincides with the location of the anticyclonic eddy.

V component structure

In general poleward flow with a significant barotropic component is associated with the offshore half of the high salinity cores. Between the two salinity cores, equatorward flow is measured in a relatively narrow band at all depths. Poleward flow is measured over the shelf on all transects except Q.

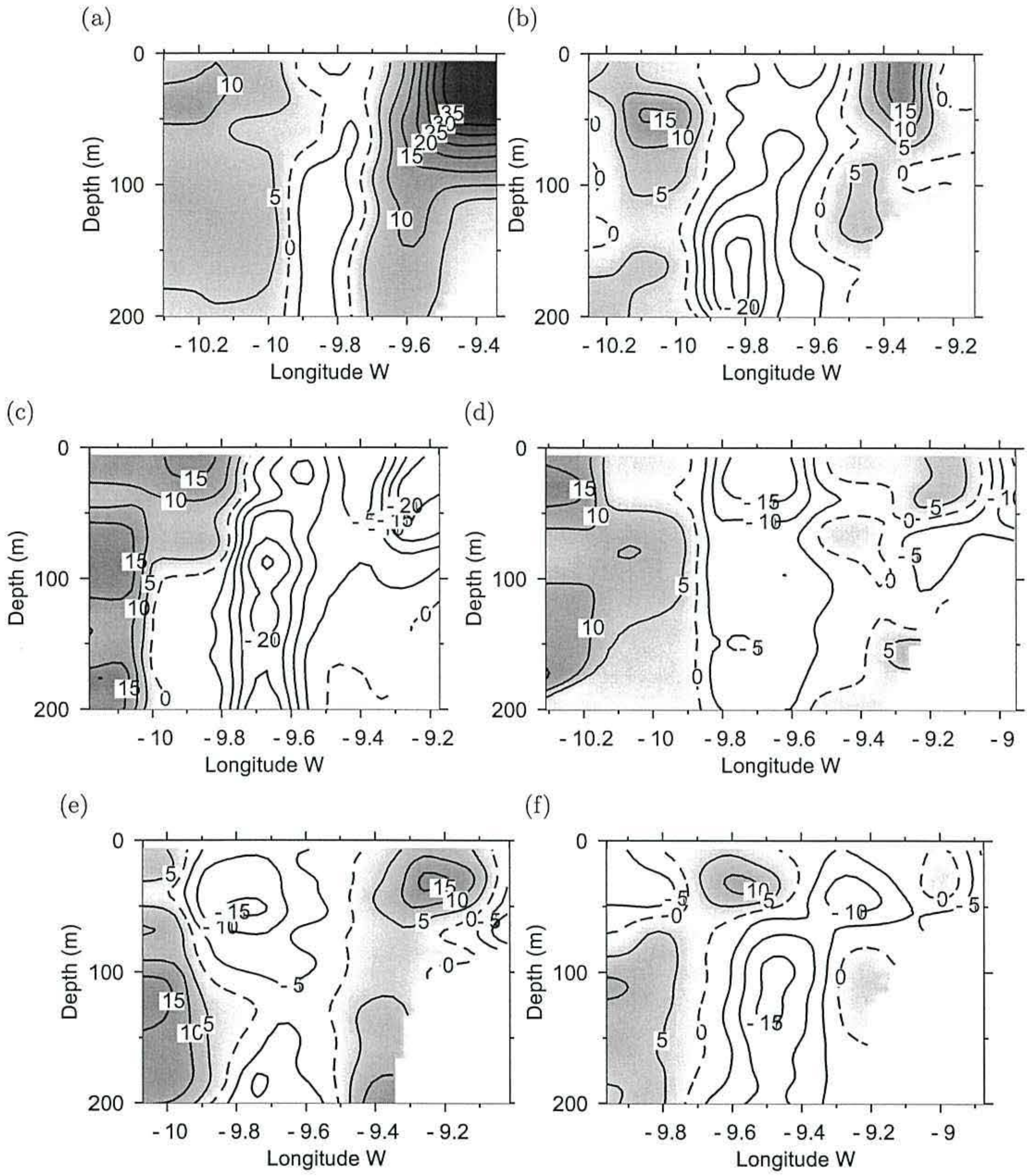

Figure 4.20.: Vertical sections of velocity component V for transects (a) N, (b) P, (c) Q, (d) S, (e) U and (f) V down to 200m. Shading correspond to northward flow. The 0 velocity contour appears as a dash line.

The correspondence of poleward flow and salinity is not simple. As stated, the offshore branch of poleward current is associated with the outer portion of the salinity maximum, while the poleward flow on the shelf is absent from section Q despite presence of a salinity core (Figs 4.19c- 4.20c). Moreover, in the southernmost section V, where a single combined salinity maximum is found, the inshore poleward flow is weak and limited in extent (Fig 4.20f). The poleward current over the outer slope

Offshore		Nearshore	
Poleward	Equatorward	Poleward	Equatorward
3.9 ± 1.5	-4.6 ± 2.2	0.8 ± 0.8	-1.0 ± 1.6

Table 4.2
: Mean and standard deviation of meridional transport estimated from all sections. Estimates have been vertically integrated to 200m from the raw V component data. Units are in $0.1 \times 10^6 m^3 s^{-1}$

has typical values 10-15cms^{-1}, and is strongest in section Q and weakest in section V. The shelf poleward flow is considerably weaker. It is most defined in the early northern sections, especially N (Fig 4.20a), where the highest poleward velocities of all are measured in a narrow band against the coast. The band of equatorward flow is also relatively barotropic with velocities up to 20cms^{-1}. In the more southern sections, weak equatorward flow appear over the shelf, and in sections Q and S (Figs 4.20c,d) some indication of an intensified coastal jet is evident. So again, the evidence suggests a shelf response to the upwelling winds after the first three sections in which initial poleward flow is replaced by an increasingly equatorward tendency. The mean meridional transport down to 200m (Table 4.2) clearly shows the four main currents seen in Fig 4.20. The offshore poleward transport is smaller than the equatorward one. However, the oceanic limit of the offshore poleward flow was not sampled during the cruise and its associated transport is underestimated.

Temperature structure

The temperature structure (Fig 4.21) shows that the thermocline is centred at 50m deepening at the stations closest to shore, and rising locally above and deepening below the sub-surface salinity cores seen in Fig 4.19. The most notable feature of the temperature sections is the general downward slope of the isotherms shorewards over the shelf. This is most pronounced in the northern sections (Figs 4.21a-b), made during downwelling favourable winds, where the isotherms are bunched near 100m over the bottom, suggestive of sinking. This is consistent with a bottom Ekman layer in the stronger poleward flow found close to shore in these sections. Despite the change to upwelling favourable winds before the remaining sections there is little sign

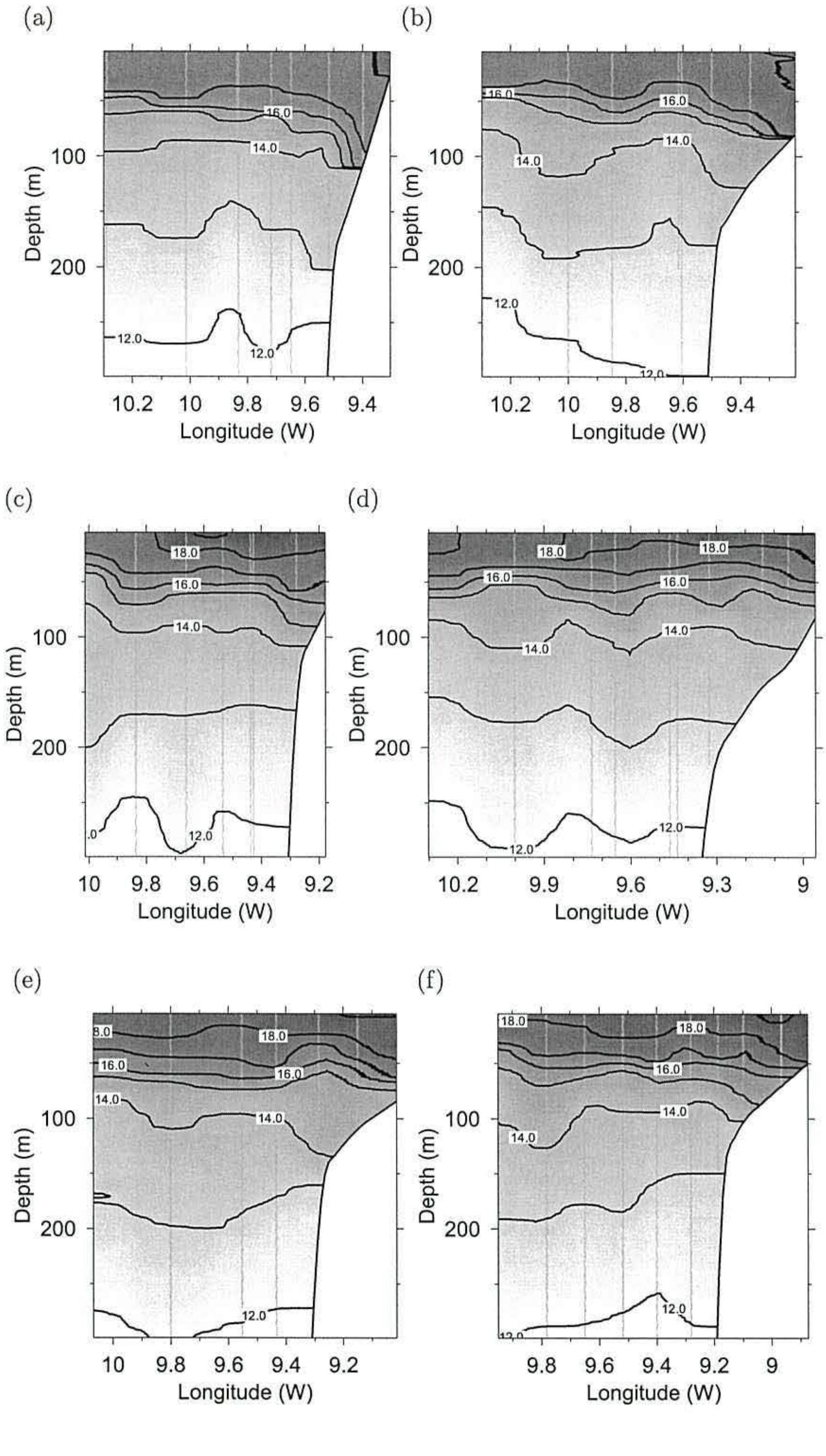

Figure 4.21.: Vertical sections of temperature for transects (a) N, (b) P, (c) Q, (d) S, (e) U and (f) V down to 300m.

of upwelled isotherms. However, the isolines are more horizontal than in the north and section Q, the last sampled, shows a slight shoreward rise in the 18°C isotherm

(Fig 4.21c).

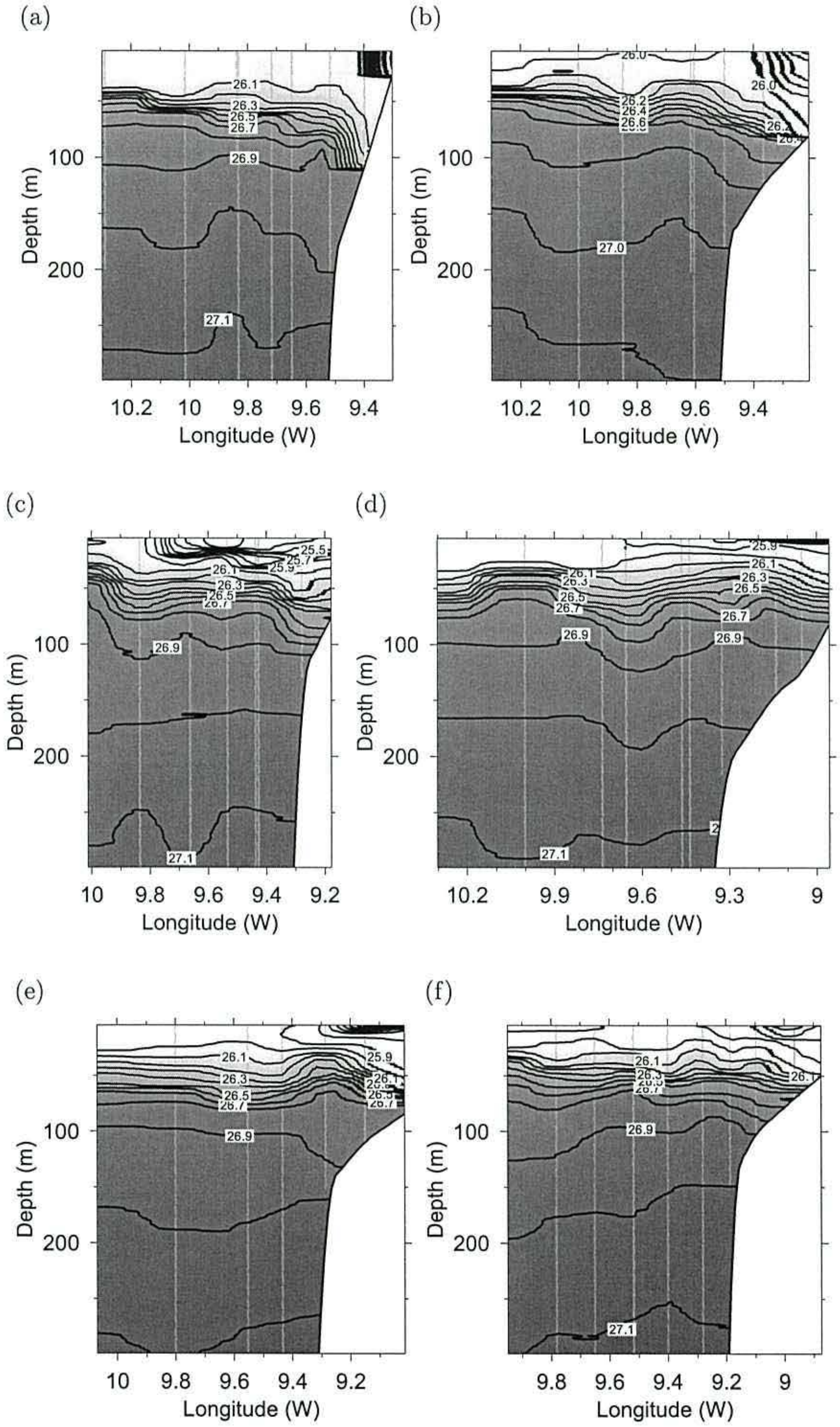

Figure 4.22.: Vertical sections of density for transects (a) N, (b) P, (c) Q, (d) S, (e) U and (f) V down to 300m.

Density structure

The density distribution is largely determined by the temperature structure. The pycnocline is centred at 50m overall, and is thicker at the southern end of the grid (50m) than at the northern end (30m). In most sections the pycnocline has a downward slope shorewards. Surface stratification is present in all transects, but is prominent in section Q, where it reaches furthest offshore. This nearsurface layer of relatively low density water may be partly responsible for the apparently weak upwelling response, although of course the winds were only moderately strong (5-10ms^{-1}) during Leg B.

The northward velocity component field showed qualitatively good agreement with the density structure at large scales. Some of the discrepancies between the velocity and density field could come from the different resolutions of the sampling. The downward sloping of isopycnals over the shelf edge corresponds to a negative lateral density gradient which translates to a positive geostrophic shear by the thermal wind equation, hence northward flow against the sloping bottom (e.g Fig 4.22- 4.20-b). In a similar way, negative geostrophic shear, (equatorward flow) would be related to positive lateral density gradient as in Fig 4.22b (100-200m; 10°-9.6°W), and when this is not the case, forces other than Coriolis and pressure are needed for dynamical balance, which is not surprising since the sampling took place during a transitional period.

Assessing the variability during CD105

To investigate the effect of the wind shift during the cruise on the hydrography of the region, 3 CTD cast pairs (Table 4.3) were selected from transect P at adjacent positions, before and after the change in wind regime. The solid lines in Fig 4.23 correspond to casts before the change in wind for both temperature (red) and salinity (blue). Most of the variability is restricted to the top 75m, above the thermocline. The three casts show the same changes, the surface salinity drops by $\sim$ 0.2psu and surface temperature increases by $\sim$ 0.7°, in response to changes from southerly to

Data for the reference CTD				
CTD cast n°	Day	Latitude N	Longitude W	Cast depth
1	10 14:24	42.6742	- 9.57720	751.0
29	13 08:44	42.6672	- 9.50000	179.0
31	13 12:22	42.6631	- 9.61580	201.0
92	20 12:21	42.6683	- 9.49440	167.0
93	20 13:50	42.6664	- 9.55220	487.0
94	20 15:04	42.6658	- 9.60190	985.0

Table 4.3: Time and location of CTD casts 1, 29, 31, 92, 93 and 94

northerly winds. The first CTD pair (Fig 4.23a) corresponds to the first and last CTD taken during the cruise and shows differences similar to the other two pairs, where the "early" CTD was taken on the last day of southerly winds, 13 June. Hence, most of the change took place after the wind shift. As changes can not be explained by vertical mixing, they are most likely a result of nearshore waters being advected offshore.

The changes measured by the ADCP (Fig 4.24) are less straightforward to explain as the velocity field responds not only to winds, tides and other oscillatory phenomena (i.e. inertial waves, coastal trapped waves), but results from the interaction of the offshore eddy and the advection of the freshwater plume off the Rias Bajas as shown previously. The profiles in Fig 4.24a correspond to 40min averages centred at the time of CTD 1 and 94 (Fig 4.23a). The standard deviation in all profiles was consistently $\leqq$ 5cms^{-1}. They show a change from poleward flow (20cms^{-1} at the surface) with constant negative vertical shear to a situation where the top 50m reversed to equatorward flow of similar magnitude while the rest of the water column flowed poleward with a smaller negative vertical shear. The largest differences in the U-component took place below the thermocline (50m), while the top 25m remained unchanged. Below 50m, the flow changed from offshore before the wind shift to onshore afterwards. Similar changes in the U-component can be seen in the other profiles (Fig 4.24b-c), except that the changes took place in the top 75m rather than at the deeper levels where the flow was close to zero. The northward component was not different from zero in Fig 4.24b while in 4.24c the flow changed from equatorward to poleward below 50m, remaining equatorward in the upper 50m.

Changes are more dramatic nearshore when comparing underway data (temperature, salinity and ADCP vector currents) from 10 June, before, and 20 June, after the wind shift of 14 June. Two short sections when the ship was leaving the port of Vigo following a similar path at roughly the same velocity ($4.5ms^{-1}$) are compared in Fig 4.25. Errors induced by the uncertainty in the ADCP calibration can be assumed to be comparable during the two lines.

The surface values (Fig 4.25a) showed a temperature increase of over a degree centigrade, the disappearance of the zonal temperature gradient and a reduction of 0.4psu in the salinity west of 9°W after the onset of northerly winds due to enhanced outwelling from the Rias. The changes are larger than the ones measured in the reference CTDs, as expected from the closer proximity to shore in this instance. A narrow tongue of low salinity/high temperature was measured east of 9°W on 20 June and it likely originated from the Ria de Arousa. A similar temperature and salinity distribution was already encountered on 18 June when the same region was occupied for the first time after the wind shift of 14 June.

The flow in the top 50m (Fig 4.25b) was northward ($\sim 20cms^{-1}$) at the time of the first line and followed roughly the orientation of the coast. At the end of cruise, the flow had reversed after the wind shift, and reached a peak velocity of $\sim 35cms^{-1}$. Both flows had a narrow jet geometry with similar zonal scales. The low salinity tongue was probably advected southwards rather than offshore by the southward coastal jet measured at the time.

4.4.4 Water mass analysis

The typical water mass distribution explained in Chapter 2 was well represented in CD105 cruise. The upper waters of the Iberian coastal ocean were divided into

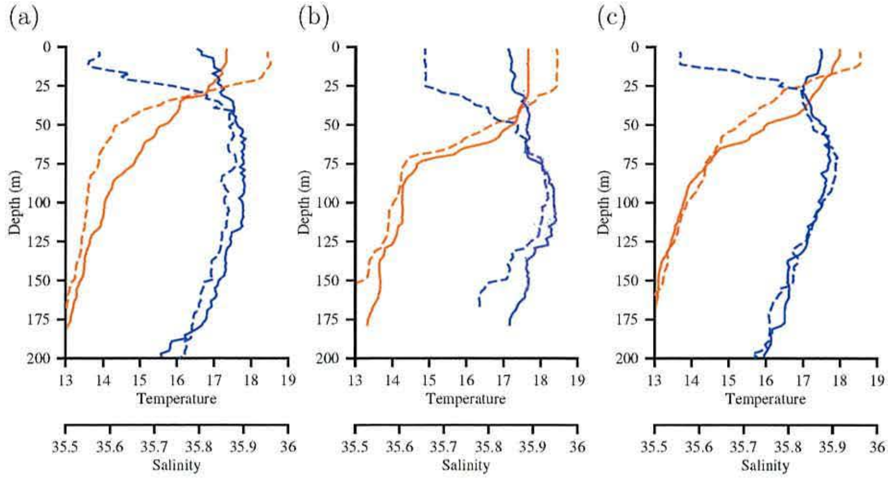

Figure 4.23.: Vertical profiles of temperature (red) and salinity (blue) for CTD casts (a) 1 (solid line) and 94 (dashed line), (b) 29 (solid) and 92 (dashed) and (c) 31 (solid) and 93 (dashed) down to 200m.

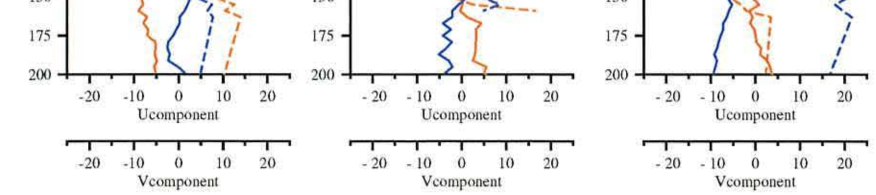

Figure 4.24.: Vertical 40min averaged profiles of U (red) and V (blue) components centred around the CTD casts (a) 1 (solid line) and 94 (dashed line), (b) 29 (solid) and 92 (dashed) and (c) 31 (solid) and 93 (dashed) down to 200m.

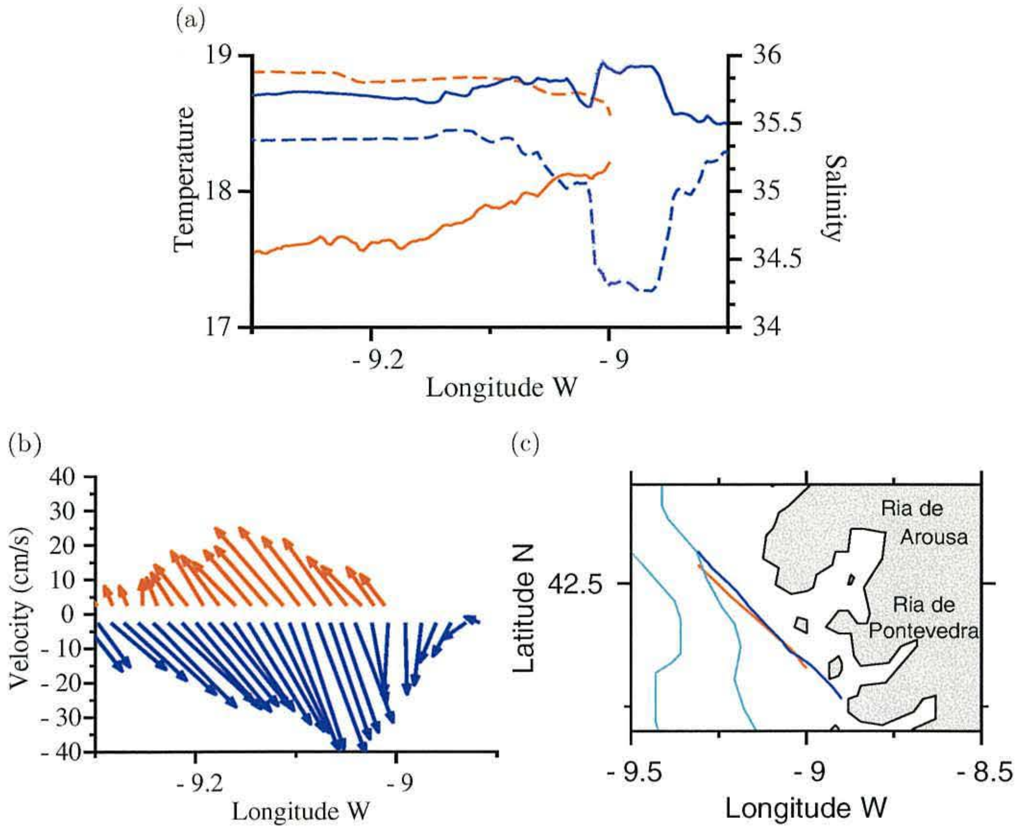

Figure 4.25.: Underway data collected at the start (10 June 08:45-10:31, red) and end (20 June 08:13-10:38, blue) of leg B of CD105 cruise; (a) temperature (solid line) and salinity (dashed line), (b) top 50m ADCP vector currents with scale on the y axis and (c) position of observations.

a surface mixed layer above a seasonal thermocline reaching down to 100m, and then the permanent thermocline, down to 500m, below which the influence of the Mediterranean outflow began. The permanent thermocline had the characteristic linear relationship between temperature and salinity typical of Eastern North Atlantic Waters.

From the CTDs collected during the cruise 6 sub-regions have been defined to investigate the T/S differences among them (Fig 4.26). The graph shows the subdivisions of the ENAW as $ENAW_T$ and $ENAW_P$, and their shared limit H defined by *Ríos et al.* [1992]. The 6 sub-regions correspond to latitudinal and zonal variations in relation to the poleward flow and the regions of influence of the Rias Bajas and the Miño river. Their influence can be seen in the top 10-25m for the regions labelled Southward Coastal Jet (SCJ) and Minho runoff (M) (see Fig 4.26b for their exact

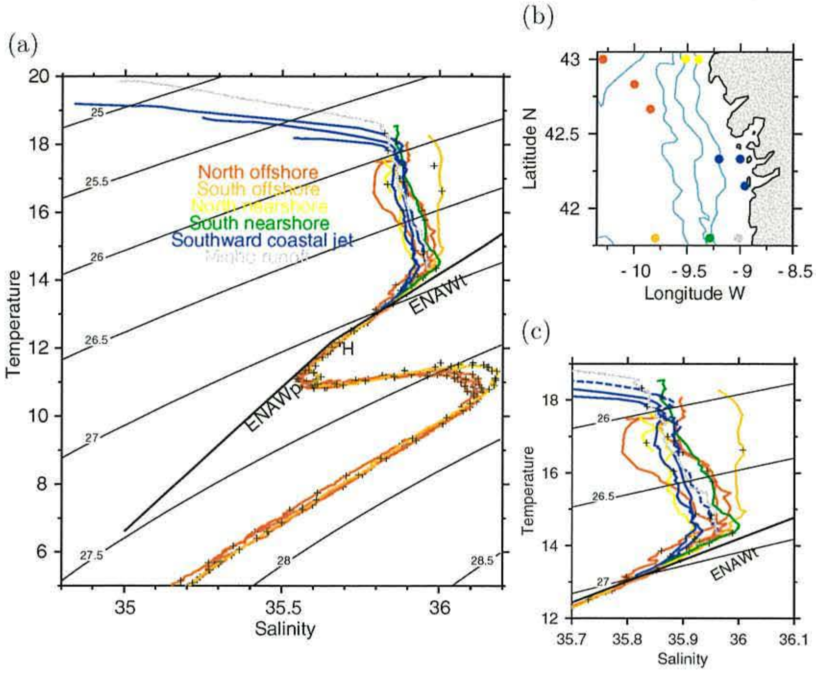

Figure 4.26.: T/S characteristics found during CD105 for selected CTD casts. (a) T/S diagram down to a maximum depth of 1800m for the colour coded sub-regions, (b) CTD casts position and (c) blow up of the T/S diagram. All share the same colour codes.

location). Their surface salinity fell below 35psu at the stations nearer to shore, and increased offshore.

The bulk of the central waters are $ENAW_T$, with only a small portion lying on the $ENAW_P$ line definition. As we move northward (Fig 4.26c), the surface salinity decreases defining a salinity maximum at the level of the $ENAW_T$ (100m) which gradually reduces with latitude. The exception is the southward coastal jet region, where the salinity maximum is of similar value to the north nearshore region suggesting southward advection of waters returned from the poleward flow.

Below the central waters we find the Mediterranean Water (MW) high salinity core, which corresponds to the vein of MW flowing northwards along the continental slope between 800-1300m. No evidence was found of the two main outflow cores of MW normally located offshore at ≈750 and ≈1250m [*Zenk and Armi*, 1990]. The MW high salinity core reduced with latitude and offshore in agreement with its northward advection along the slope.

4.5 Discussion

In mid-latitude continental shelves the net surface heat flux changes from cooling to warming in spring [*He and Weisberg*, 2002]. Near the mouth of the Ria de Vigo, such change takes place in April as estimated from bi-weekly data for the period 1987-1992 [*Nogueira et al.*, 1997]. From November to March, thermal inversion takes place, the water column becomes briefly homogeneous in early April but quickly stratifies and remains so until October, when thermal inversion develops once more. Similar trends can be expected on the shelf, considering the strong linkage between the Rias and the shelf [*Álvarez-Salgado et al.*, 2000]. However, the transition between the downwelling winter regime and the upwelling summer regime typically takes place in June, two months after the onset of the spring warming [*Nykjaer and Vancamp*, 1994]. The *Charles Darwin* CD105 cruise took place during the transition from the winter downwelling to the summer upwelling season, from 10 to 20 June.

4.5.1 General circulation

During Leg A, surface salinity hinted at the presence of a contorted poleward current, the PCC. The PCC followed the slope in the south, separated from it further north off the Rias Bajas and turned back to the slope south of Cape Finisterre. The weekly SST average from satellite images showed a similar trend, while the *in situ* data revealed a high salinity tongue associated with warmer temperatures. Scattered along the warm tongue were warm patches suggestive of anticyclonic eddies. Their SST signal suggested a spatial scale of ~30-40km. Eddies associated with the PCC have been previously reported [*Haynes and Barton*, 1991; *Sena*, 1996]. Evidence of the poleward flow SST signal separating from the slope between 41.5°-42°N are also present in May when some coastal upwelling was also measured (not shown). The SST distribution is very similar to Fig 4.8a and coincides with the absence of poleward flow north of Cape Finisterre which has been related to PUNC wind pattern in Chapter 3. A similar picture arises from Leg B, except that a southward jet was present over the inner shelf in response to northerly winds.

High salinity values are the distinctive mark of the PCC. Previous studies of the PCC in the west coast of Iberia (40°N) have also found a high salinity core at 100m close to the slope [*Frouin et al.*, 1990; *Haynes and Barton*, 1990]. The double core structure of the salinity data is however surprising but could be related to strong winter upwelling episodes and might be present only towards the end of the downwelling regime. The subsurface salinity maximum and poleward flow were better defined offshore than at the shelf edge particularly off the Rias Bajas. The weaker salinity signal over the shelf edge could correspond to a more intermittent poleward flow during the final stages of the downwelling regime. The offshore salinity maximum coincided with northward velocities up to $15cms^{-1}$ similar to the average speed of $20cms^{-1}$ measured by *Haynes and Barton* [1990]. Smaller and more discontinuous northward velocities were associated with the shelf edge salinity maximum. Between the two salinity maxima, southward flow was present in all transects in association with a wedge of low salinity and temperature at all depths. SST images implied it advected waters from north of Cape Finisterre and was present as early as May. Equatorward flow separating two poleward flow currents has been previously reported in the Galician region [*Sordo et al.*, 2001] and in the Cape Saõ Vicente, south of Portugal [*Relvas de Almeida*, 1999], but during the cessation of the upwelling regime in autumn. In both cases, the feature could be attributed to remnants of the upwelling front having been displaced offshore. However, on this occasion the front had not been established yet. One possible explanation is that it was the result of advection of colder oceanic water from off Cape Finisterre by the two eddies seen in the velocity data (Chapter 4, Figs 4.14- 4.16).

The offshore anticyclonic eddy related to the PCC was evident in the data. Its SST signal disappeared after the 6-8 June storm but it was still evident in the subsurface data. It had an estimated diameter of ~30-40km from both surface SST and *in situ* data to a depth of 150m, carrying ~$128km^3$. This eddy is distinct from SWODDIES, which form in the Bay of Biscay [*Pingree*, 1994] and have also been linked to the PCC. Their characteristic radii can be four times bigger (50-60km) and they reach depths of 1500km. However, the present data are insufficient to hypothesize about the eddy's life span or its origin. *Huthnance et al.* [2002] presented eddy statistics for a region 40.5-45.5°N out to 13°W for years 1993-1999. They had a mean diameter of $\sim 52 \pm 22$km based on their SST signal and most were found north of Cape Finisterre-Cape Ortegal a preferred eddy generation area [*Dubert*, 1998; *Paillet et al.*, 2002]. Although they constitute an active shelf exchange mechanism their small number (20 per year) makes a modest contribution to the overall exchange in the region [*Huthnance et al.*, 2002]. A cyclonic eddy-like re-circulation was apparent on the shelf slightly south of 42°N but its velocity signal was less well defined. It is located at the site of a recurrent filament [*Haynes et al.*, 1993] and might be related to the topography, as the coast and shelf orientations change.

Coexistence of the PCC and coastal upwelling has been previously reported [*Castro et al.*, 1997; *Peliz et al.*, 2002]. *Haynes and Barton* [1990] reported a resurgence of upwelling producing equatorward shelf flow while flow over the outer slope remained poleward. The PCC appeared furthest offshore off the Rias Bajas, where significant seaward flow of low salinity/ high fluorescence Rias water was measured. The offshore extension of the low salinity plume had minimum values of $\sim$35.5, although lower values could have been expected, as observed further south off the Miño estuary. It thus provides evidence that during downwelling shelf waters are piled up inside the Rias, mixed with riverine flow, and when downwelling winds relax or change to northerly the waters are flushed to the shelf. *Álvarez-Salgado et al.* [2000] have also suggested that upwelling occurs within the Rias so that flushing is enhanced. The offshore extent of the freshwater plume increases due to the enhanced stratification, suppression of turbulence and response to Ekman across-shelf mass transport forced by local winds.

The change in coast and shelf orientation off the Rias Bajas might play a significant role in the offshore flow measured there. A conceptual model similar to *Rosenfeld et al.* [1994] with an idealised representation of the coastline hints at one of the possible mechanisms favouring offshore flow off the Rias Bajas. (Fig 4.27). Two coordinate systems are defined, one with y positive northward and x positive eastward; and a

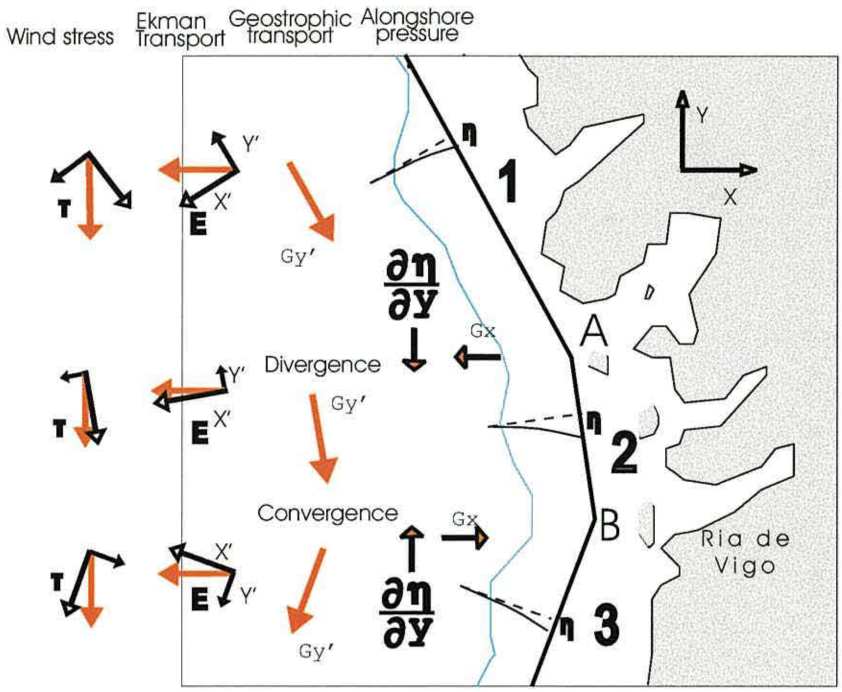

Figure 4.27.: Wind stress, τ, Ekman transport, E, geostrophic transport, G, alongshore pressure gradient, η_y and sea level at the coast, η. Two horizontal coordinate systems x,y and x', y' are defined. Coastal points A and B, and segments 1, 2 and 3 are labelled. The 200m isobath is also shown.

second with x' and y' defined locally cross-shelf and alongshelf respectively.

The depth-integrated surface Ekman layer transport, E, is to the right of the uniform wind stress, τ. This offshore transport results in a drop in sea level at the coast, η. The magnitude of the Ekman transport perpendicular to the coast, $E^{x'}$, and hence η, are functions of the coastline orientation relative to τ, and are greatest where the coast is more aligned with τ, i.e. along segment 2. Along the entire shelf, the cross-shelf pressure gradient drives an equatorward transport $G^{y'}$. The alongshore variation in η leads to convergence of the alongshore geostrophic flow, $G^{y'}$, and a poleward-directed pressure gradient force, $(\frac{\partial\eta}{\partial y})$ near point B. Near point A, the alongshore variation of η creates geostrophic transport divergence and an equatorward-directed pressure gradient force. Both the cross-shelf geostrophic, G^x, and Ekman, E^x, transports are seaward near point A, contributing to the offshore displacement of the slope poleward flow. Near point B, E^x is also seaward but G^x is shoreward, thereby reducing the offshore tendency of the flow.

4.6 Conclusions

Data from the transition between the downwelling and upwelling regimes have been presented. The picture is one of complex circulation, where poleward flow over the slope coexists with coastal upwelling and strong outflow from the Rias. The interaction generates eddies carrying PCC waters which could contribute to breakdown the PCC during the start of the upwelling regime.

In conclusion:

- The cruise sampled the area at a time of transition from winter downwelling to summer upwelling.
- Spatial patterns observed during the cruise were aliased by the change in wind conditions but can be interpreted in combination with temporal change.
- The poleward flow along the slope south of 41°N separated into a slope branch and a shelf branch, both associated with a prominent salinity maximum.
- The poleward branches were separated by a well defined equatorward flow, apparently originating north of Cape Finisterre, which spread onto the shelf with the onset of upwelling winds.
- The shelf poleward flow was strongest during the initial downwelling wind period and disappeared in the final section after several days of upwelling winds.
- A surface layer of buoyant warmer low salinity water spread out over the shelf from the Rias as water previously forced in by southerly winds was flushed out by upwelling winds.
- The associated offshore flow appeared to cause a displacement of the slope poleward current further offshore, but this could also be a coincidence of meandering flow.
- A conceptual model is proposed whereby the coast orientation with respect to the upwelling winds would enhance offshore flow opposite the Rias and push the

poleward flow offshore after several days of upwelling winds.

- The cruise captured only the onset of coastal upwelling, but the complete transition to an upwelled thermocline breaking the surface nearshore was evident in subsequent satellite images.

CHAPTER

5 Upwelling regime

5.1 Introduction

As previously stated, coastal upwelling is a major feature of the Galician region from May through to October. Short cycles of upwelling/downwelling favourable winds modulate the seasonal wind cycle and typify the summer regime [*Nogueira*, 1998]. A succession of fortnightly upwelling events has been suggested by various authors [*Castro et al.*, 1994; *McClain et al.*, 1986; *Nogueira et al.*, 1997, see also Chapter 3]. *Castro et al.* [1994] described the hydrographic changes caused by one such upwelling relaxation. The authors described the weakening of the seawards surface upwelling circulation and bottom compensating flow nearshore. Shorewards advection of surface oceanic waters took place off the shelf and a convergence front developed at mid-shelf. Although not documented for the Galician region, upwelling relaxation in other areas like the California shelf, produces a reversal of the currents and surfacing of the poleward California Undercurrent [*Send et al.*, 1987].

The Iberian region, like other coastal upwelling areas, is characterised by the presence of filaments of cool upwelled water which collectively form a coastal transition zone between shelf and open ocean waters. Filaments are associated with narrow baroclinic jets that are formed over the continental shelf and flow offshore advecting cold, upwelled water into the open ocean [*Brink and Cowles*, 1991]. They are easily identified in satellite Sea Surface Temperature images (SST) by their temperature signature [*Flament et al.*, 1985]. Many projects have focussed on filaments in recent years in Eastern Boundary Systems (i.e. California, South Africa, Canaries, Chile) because they constitute a likely candidate for enhancing exchange between the productive shelf and the oligotrophic oceanic waters. Following the May or June onset of seasonal upwelling off Iberia, filaments begin to develop in July or August and grow to lengths of 200km by September [*Haynes et al.*, 1993], and quickly disappear with the cessation of upwelling favourable winds in October. The repeatability of the filaments over many years in similar locations suggests that they are topographically controlled, although they show high variability on time scales of the order of a week. A recent modelling study [*Roed and Shi*, 1999] suggested that topography caused local differences in the frontal configuration, which then triggered instabilities and downstream meandering that anchored the filaments close to and at intervals downstream of the cause.

In the following sections, data collected during and in support of the R/V *Charles Darwin* CD114 cruise in August 1998 will be analysed. During the cruise, a "parcel of water" was tracked from the shelf until it became entrained in a recurrent upwelling filament. In situ measurements of the hydrographic, velocity and turbulent dissipation structure were obtained together with Lagrangian observations, both on the continental shelf near the filament origin and in the filament itself. In both experiments, direct observation of turbulence patches within the water column was made with a free-falling probe. Until recently, no information on the subsurface structure of filaments off Iberia was available. The measurements provide insight into some of the physical processes affecting the filament at its origin and offshore and allow an estimation of the vertical mixing rates of interest to production studies.

5.2 Data and methods

The physical sampling strategy on board RRS *Charles Darwin* cruise 114 was designed to support Lagrangian primary production experiments during Leg 1 (2-10 August 1998) on the shelf (Fig. 5.1) and Leg 2 (11-20 August) in the filament (Fig. 5.2). Further physical observations were made following the drift experiments, at a time series station on the shelf and in a spatial survey of the filament structure. In the shelf

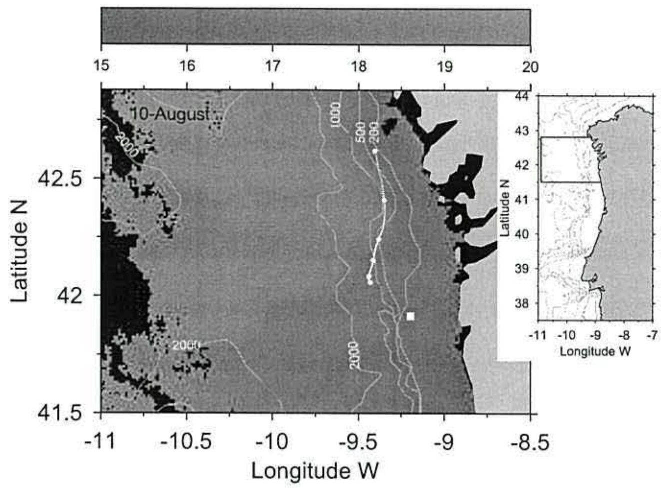

Figure 5.1.: Drifter track (dotted line) and the position of the time series observations (white square) of Leg 1 (2-10 August 1988) overlaid on the sea surface temperature image of 10 August. Colder upwelled waters are seen along the coast and extending offshore in the filament south of 42°N. The drifter was always inshore of the upwelling front, which receded towards the coast during the observations. Isobaths are shown in metres.

experiment the work was based around the drift of a primary production rig, while in the filament a primary production rig and recoverable Argos buoy were deployed at the centre of a cluster of 4 Argos drifters. The rig and their water tracking characteristics are detailed by *Joint et al.* [2001]. It comprised a small surface float, with radar reflector and radio beacon, designed to offer minimum windage. A semi-submerged toroid buoy, 1.2m in diameter was attached to the float and 3 sediment traps at 30m, 40m and 50m acted as drogues. The drifter deployment positions for the filament experiment (Fig. 5.2b) on 14 August were chosen on the basis of SST images transmitted to the ship during previous days. Horizon Marine drifters released in a 5nm side square in the core of the upwelling filament were equipped with cylindrical 'holey sock' drogues (7m length, 1.2m of diameter) at a nominal depth of 15m. The drifters had an approximate drag area ratio of 50 which restricts wind slippage to less than 1cms^{-1} for winds of 10ms^{-1} [*Niiler et al.*, 1995]. They were tracked with the ARGOS system, yielding 6-8 fixes per day. The same sampling set up as in cruise CD105, described in Chapter 4, was used again in CD114. The CTD salinity data were calibrated against 8 (leg A) and 11 (leg B) water samples analysed on a Guildline Autosal bench salinometer. A constant offset of 0.042±0.008psu (0.029±0.006psu) was found for leg A (leg B). CTD temperatures agreed well with calibrated digital

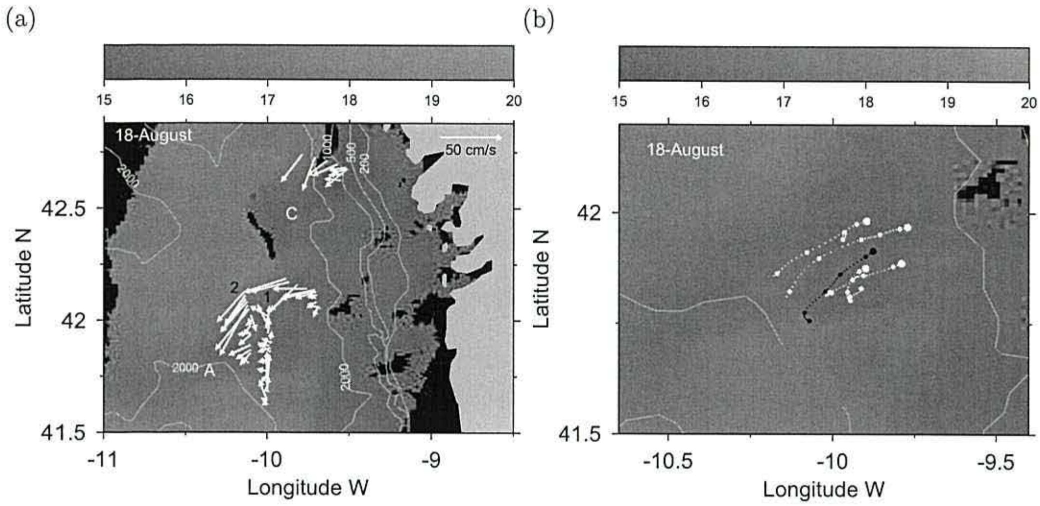

Figure 5.2.: (a) Absolute ADCP velocities at 25m along sections during Leg 2 (12-22 August 1988) overlaid on the sea surface temperature image of 18 August. Colder upwelled waters extend from the coast beyond the shelf break and offshore in filament A south of 42°N. A newly developing filament C is seen near 42.5°N. Isobaths are shown in metres. (b) Drifter tracks from 14 to 19 August superimposed on blow up of SST image of (a). Large dots mark the release point and smaller dots start of each day. The instrument rig track is shown in black. The isobath shown is 2000 m.

reversing thermometers and no correction was applied.

CTD casts were made during both legs of the cruise adjacent to the primary production rig approximately every 6 hours. Additionally, casts were made across the base of the 42°N filament and on other short sections, totalling 83 casts over the cruise. Velocity profiles along the ship track were obtained with the RD Instruments hull-mounted 153.6kHz narrow-band ADCP already described in Chapter 4. The complete Acoustic Doppler Current Profiler data set and in-depth details of processing are given by *Torres and Barton* [1999] and follow the steps described in Chapter 4. Bin size was set at 8m and data from above 25m were rejected as unreliable. ADCP data were recorded in 5 min ensembles during Phase 1, and in 2 min ensembles during Phase 2. The overall quality of Leg 1 data was good, with a typical depth range of 300m or to the sea bed on the continental shelf. Leg 2 data, recorded in 5 min ensemble averages, were of poorer quality with penetration typically to only 150 m.

A subset of the Percentage good (PG) record for Leg 1 and 2 exemplifies the differences encountered during both legs (Fig. 5.3). Good quality data were obtained during Leg

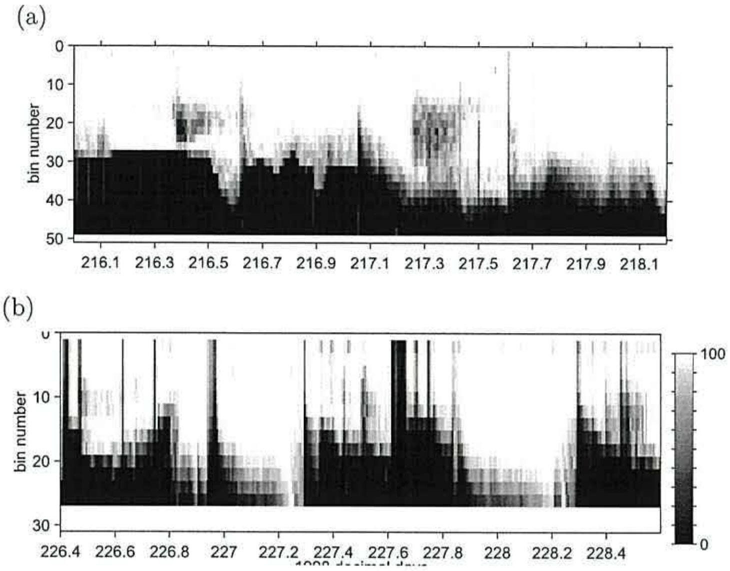

Figure 5.3.: Example of Percentage-good pings vs. time and bin number for a) Leg 1 and b) Leg 2 for the 150Khz NB ADCP.

1 (Fig. 5.3a), with PG in excess of 85% in the water column, sharply decreasing to zero at the bottom (black in the example). During Leg 2 (Fig. 5.3b), PG in the top water column was similar to Leg 1, but penetration was much more limited, at most 200m when on station. The penetration was greatly reduced at times of sailing against the prevailing sea when it was impossible to record below 50m or less (e.g. day 227.6 in Fig. 5.3b). The physical installation of the transducer is believed to account for much of its malfunctioning as bubbles are trapped beneath the ship's hull [*New*, 1992]. These problems were particularly evident during Leg 2 where the decrease in passive acoustic reflectors worsened the ADCP performance. This is supported by the rapid decrease of the Amplitude Gain in Leg 2, when, on average, it fell below 50 at 100m while in Leg 1, it reached 50 at 200m.

The data quality was further assessed by comparing underway and on station profile averages. The PG profile averages summarise the main differences between the two legs seen in all other variables checked (Fig. 5.4). Underway and on station mean and standard deviation profiles showed relatively small differences during Leg 1 (Fig. 5.4a), negligible in the top 100m and less than 10% below to 200m, increasing downwards. Differences less than 5% were found in the standard deviation with absolute values

(a)

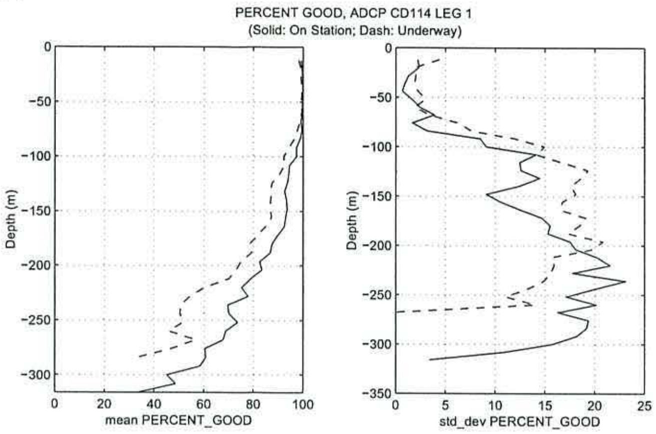

(b)

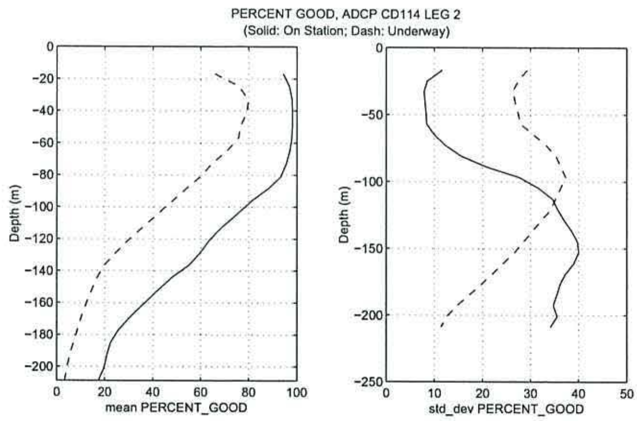

Figure 5.4.: Comparison between underway and on station averaged and standard deviation profiles of Percentage Good for a) Leg 1 and b) Leg 2.

	Leg 1		Leg 2
	Bottom Track	Water Track	Bottom Track
$\beta \pm \sigma$	1.01 $\pm$0.01	1.02 $\pm$0.01	1.04 $\pm$0.02
$\alpha \pm \sigma$	-0.1 $\pm$0.6	-0.1 $\pm$1.0	0.4 $\pm$1.0

Table 5.1: Calibration parameters for CD114

less than 20%. Differences were small (<5%) in the top 70-80m, but increased rapidly reaching 10-20% below 100m. During Leg 2 (Fig. 5.4b), a consistent 20% difference in the mean and standard deviation was evident between underway and on station data through the water column. Mean values decreased rapidly below 80m while on station (60m while underway), on average yielding unreliable data from 140-150m. The standard deviation values were larger during Leg 2, but its change with depth was similar to Leg 1.

The ADCP was checked for misalignment of the transducer with respect to the gyro compass by calibrating the data. In conjunction with the water method described in Chapter 4, the bottom track method was attempted for Leg 1, which compares acceleration relative to the water and over the ground as measured with the ADCP only. The values obtained for amplitude and angle with their respective standard deviations for all calibrations attempted are shown in Table 5.1. The calibration parameters during the Leg 1 agree very well for water and bottom track estimates although they differ with respect to the phase estimate of Leg 2. However, due to the poorer quality of the data during the last Leg only the calibration coefficients for Leg 1 were considered. Their small value suggested that no correction of the data was needed.

Direct observations of turbulent kinetic energy dissipation ϵ were made at a 1 cm resolution with the Free-falling Light Yo-yo (FLY) shear microstructure profiler (see *Dewey et al.* [1987]). A description of the instrument and data processing is detailed in Appendix A.1. During the six day Lagrangian productivity drifter experiment on the shelf (Leg 1, Phase 1), groups of dissipation profiles were made approximately every 6 hours. Each group, or series, contained about 10 profiles. Leg 1, Phase 2 comprised an Eulerian internal wave experiment lasting ~24 hours at a location 5km shoreward of the shelf break in about 170m water depth (Fig. 5.1). FLY profiled the water column with a repeat cycle of ~6 min with breaks of 20 to 30 minutes every 3 to 4 hours for battery recharging. A more in depth description of the data can be found in *Barton et al.* [2001]. During Leg 2, the filament was sampled with the FLY probe, CTD and shipborne ADCP. As the drifter array moved away from the coast, partial across-filament transects were performed. These were interspersed every 6 hours with biology stations conducted next to the primary production buoy. The detailed spatial sampling of the filament was undertaken with the FLY in ~10 min cycles of 3-5 profiles to an average depth of 250 m. Calculation of the rate of turbulent kinetic energy (TKE) dissipation from the FLY shear microstructure data followed *Dewey et al.* [1987] and *Inall* [1998] and is described in the Appendix A.1. TKE data were converted to vertical diffusion coefficient, K_z, using $K_z = 0.2\epsilon/\rho N^2$ [*Osborn*, 1980], where N is the local buoyancy frequency; and ρ is density (assuming that ϵ is in Wm^{-3}). FLY temperature and conductivity records were calibrated against the calibrated CTD data.

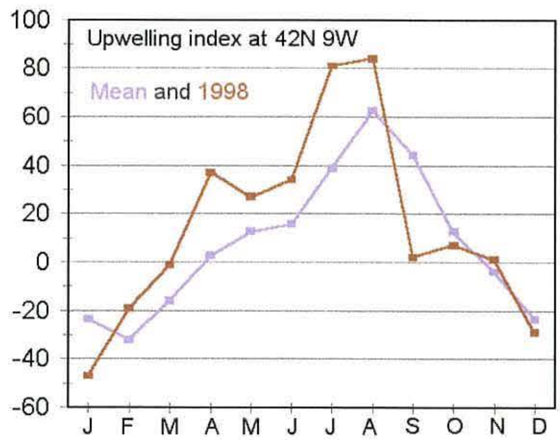

Figure 5.5.: Monthly averages of Upwelling index calculated for a cell centred at 42°N 9°W from daily ECWNF winds for years 1986-1998 (blue) and 1998 (red).

5.3 Results

5.3.1 Background and evolution

The seasonal cycle in the wind is clear in the interannual mean of derived Ekman transport (Fig. 5.5). In 1998 (Fig. 5.5), wind became upwelling favourable in April, earlier than in the average year, and was stronger than average until it reached a peak in August. Wind strength dropped quickly in September to weaker than average values, but remained weakly upwelling favourable until December. In AVHRR images a band of cold upwelled water was clearly visible next to the coast after 12 June 1998 (Fig. 5.6a). The upwelling front quickly developed short scale instabilities like the ones described by *Haynes et al.* [1993]. The sustained northerly winds drove the upwelling front steadily offshore until the upwelled water expanded across the 200m isobath late in June (Fig. 5.6b), at which time the first filament-like structure developed off Cape Finisterre. By 8 July (Fig. 5.6c), two filaments, one at 42°N and one at Cape Finisterre were fully developed. The 42°N filament (Filament A after *Smyth et al.* [2001]) was detectable until the end of the upwelling season (late September) while the Finisterre filament disappeared in mid-July when the band of upwelled water receded in the north and became wider south of 42°N (Fig. 5.6d-e). During the cruise, winds were generally upwelling favourable in direction but went through several cycles of relaxation and strengthening (Fig. 5.7). On 31 July, prior to Leg 1, winds were strong (~15ms^{-1}) towards the southwest, became more southward and weaker (5-10ms^{-1}) during 2-5 August, and then weakened to near zero at the end of the shelf drift experiment and during the internal wave observations on 8-9 August. Strong southward winds prevailed for the first days of the Leg 2 filament experiment but weakened from 10ms^{-1} on 13 August to near zero on 16 August, when the first filament section was completed. Winds of ~10ms^{-1} were re-established for the second filament section on 17-18 August and persisted until the end of the cruise. The 42°N filament A was present throughout, although it diminished in response to weakening winds and reactivated with the renewal of upwelling favourable winds. At the start of the cruise in early August upwelling immediately south of Cape Finisterre weakened

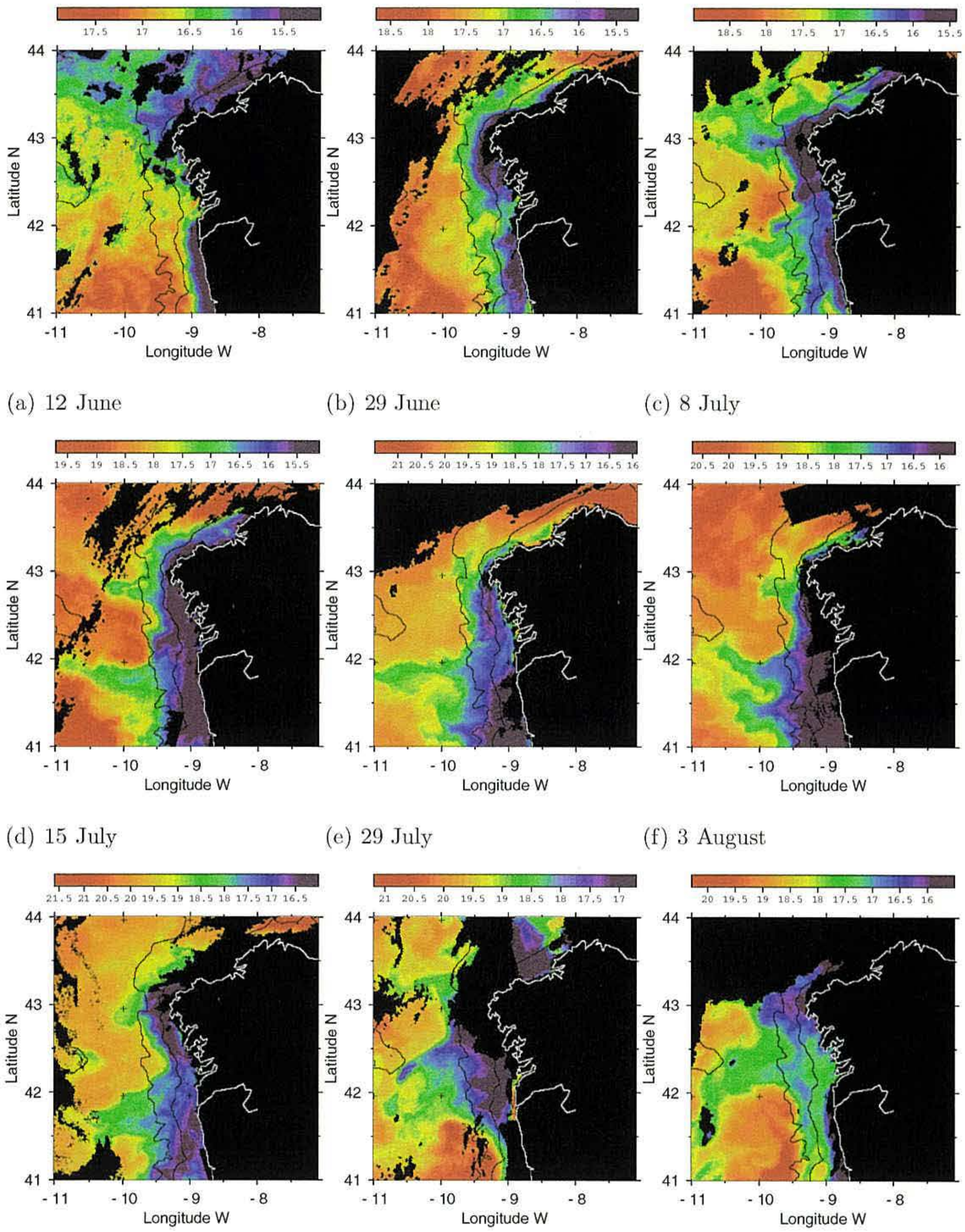

(a) 12 June (b) 29 June (c) 8 July

(d) 15 July (e) 29 July (f) 3 August

(g) 10 August (h) 5 September (i) 15 September

Figure 5.6.: SST images during the upwelling season of 1998 depicting some of the characteristics of the season evolutions. Note the different scales on each image in order to highlight frontal areas.

and another filament (Filament B after *Smyth et al.* [2001]) north of 41°N developed (Fig. 5.6e). Filament B moved north (Fig. 5.6f) and merged with filament A by 10 August (Fig. 5.6g), at the end of the first wind relaxation. With the re-establishment of strong winds by 12 August the band of coastal upwelling widened and filament definition in the SST images strengthened. Subsequent wind relaxation was evident

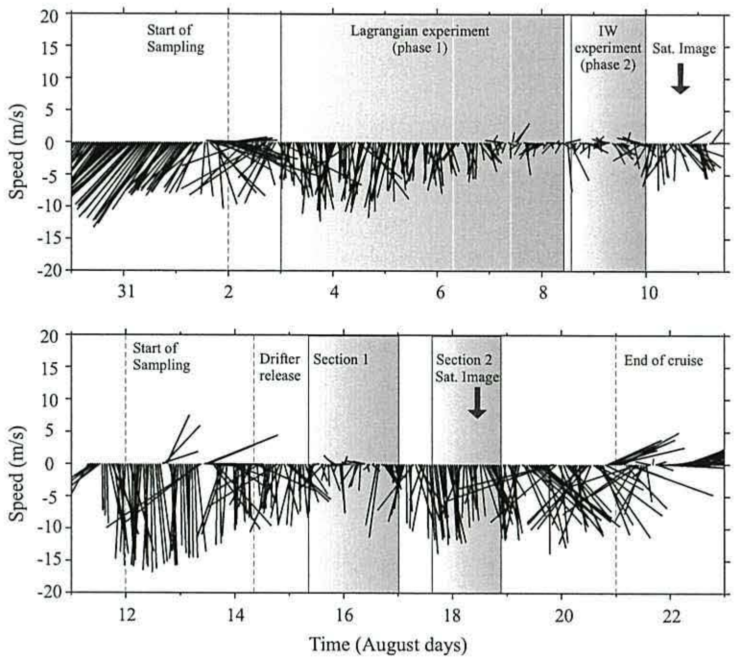

Figure 5.7.: Wind vector series for Leg 1 (upper) and Leg 2 (lower). Southward wind vectors point vertically down the page. Timing of the different experiments is shown.

in later images as a narrowing and weakening of filament A. It was 30km wide and over 200km long at the time of the spatial sampling. The final stages of the filament during September coincided with slackening in the winds as reflected by the monthly average upwelling index. The offshore extend of the coastal upwelling band south of the filament narrowed (Figs. 5.6h-i). The filament widened and was advected northwards while a warm tongue developed offshore of the upwelling front.

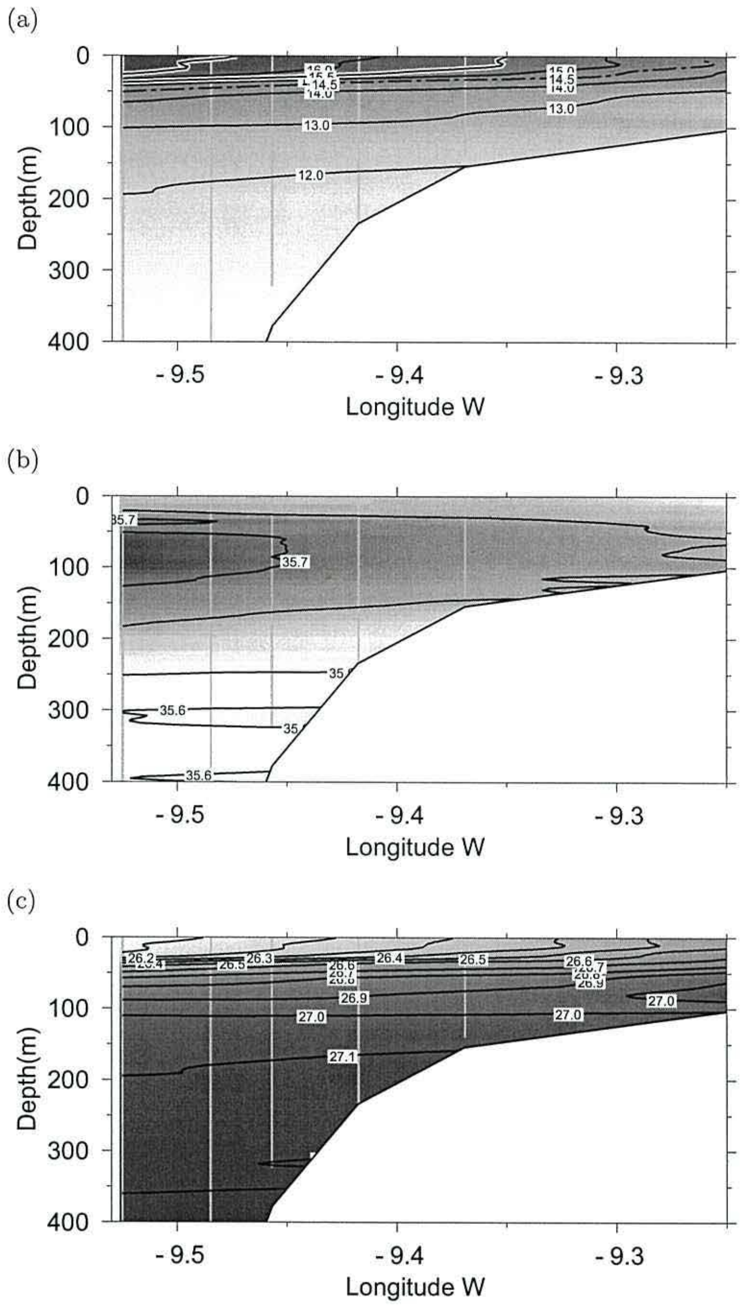

Figure 5.8.: (a) Temperature (b) Salinity and (c) Density in the across-shelf transect at the beginning of CD114 cruise.

5.3.2 The Shelf experiment Leg 1

Water column structure and fluxes during the drift

At the start of the cruise, a cross-shelf transect at 42.6°N latitude was undertaken to determine the best position for the drift experiment (Fig. 5.8). An across-shelf temperature gradient (2°C in 23km) was present in the top 50m of the water column. Isotherms and isopycnals all showed an uplifting onshore, indicative of coastal upwelling, with a vertical displacement of ~50m across the section at 100m depth. The slope of the isolines decreased with depth but was still evident at 200m and below (Fig. 5.8c). The salinity displayed a broad salinity maximum off the shelf, larger than 35.7psu between 50 and 200m depth, which became narrower and less saline onshore (Fig. 5.8c). The productivity rig was released at 9.4°W in 150m depth. As the wind relaxed during the Phase 1 drift experiment, the internal water column structure remained essentially unchanged, which suggested that the buoy remained within a single near-surface water packet (Fig. 5.9). The main features were the downward slope of the isotherms over the first ~24h, changes in the high salinity core at ~75m and warming of the upper few tens of metres towards the end of the drift experiment. The downward slope in the isolines on the first day corresponded to rapid offshore drift into deeper waters. It was the least "truly Lagrangian" stage overall, considering the strong velocity shear of the top 60m (Fig. 5.10). The range of salinity on the 26.9 isopycnal, located approximately at 80m depth, was less than 0.1psu. The data seen in T/S space conformed with the expected variability of $ENAW_T$ at these positions. The drifter moved into deeper waters during the last two days, and the daily mean surface temperature increased by ~1.5°C as the surface layers stratified in near zero wind (Fig. 5.9a). This increase occurred throughout the region [*Smyth et al.*, 2001]. The stratification reached maximum daily values after midday as suggested by the short fluctuations of up to 1.5°C in the underway surface temperature record caused by the pitching of the ship.

Shipborne ADCP records made within 1.5km of the rig during its drift show a change from initially relatively strong ($>0.3ms^{-1}$) southward flow to weak ($<0.1ms^{-1}$)

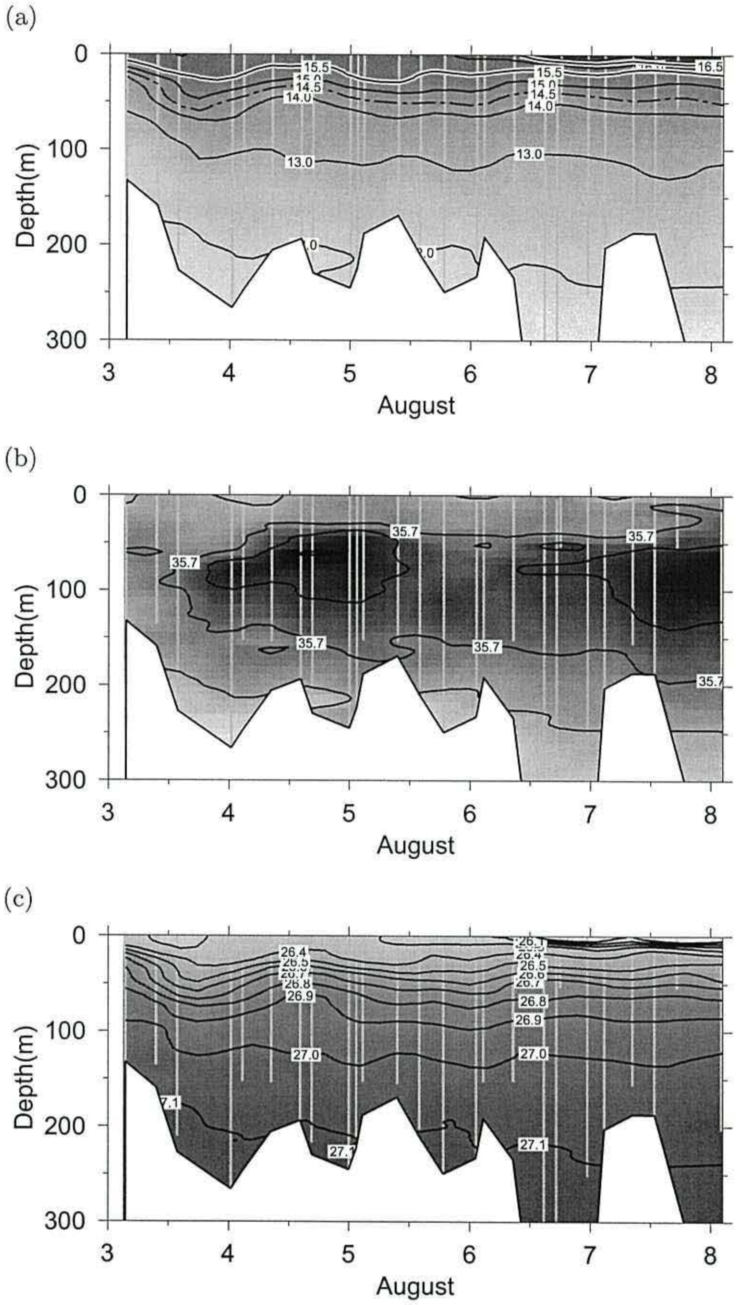

Figure 5.9.: (a) Temperature (b) Salinity and (c) Density during the shelf drift experiment. The buoy gradually moved into deeper water.

northward flow (Fig. 5.10). The drift took place between neaps (31 July) and springs (9 August). During the first day, a wind driven surface jet with strong southward and weaker eastward flow was apparent. On the next two days (4 and 5 August) the currents were characterised by a return to tidally dominated flow (mainly M2 tide), with some baroclinic structure evident (as expected for a shelf edge). From 6

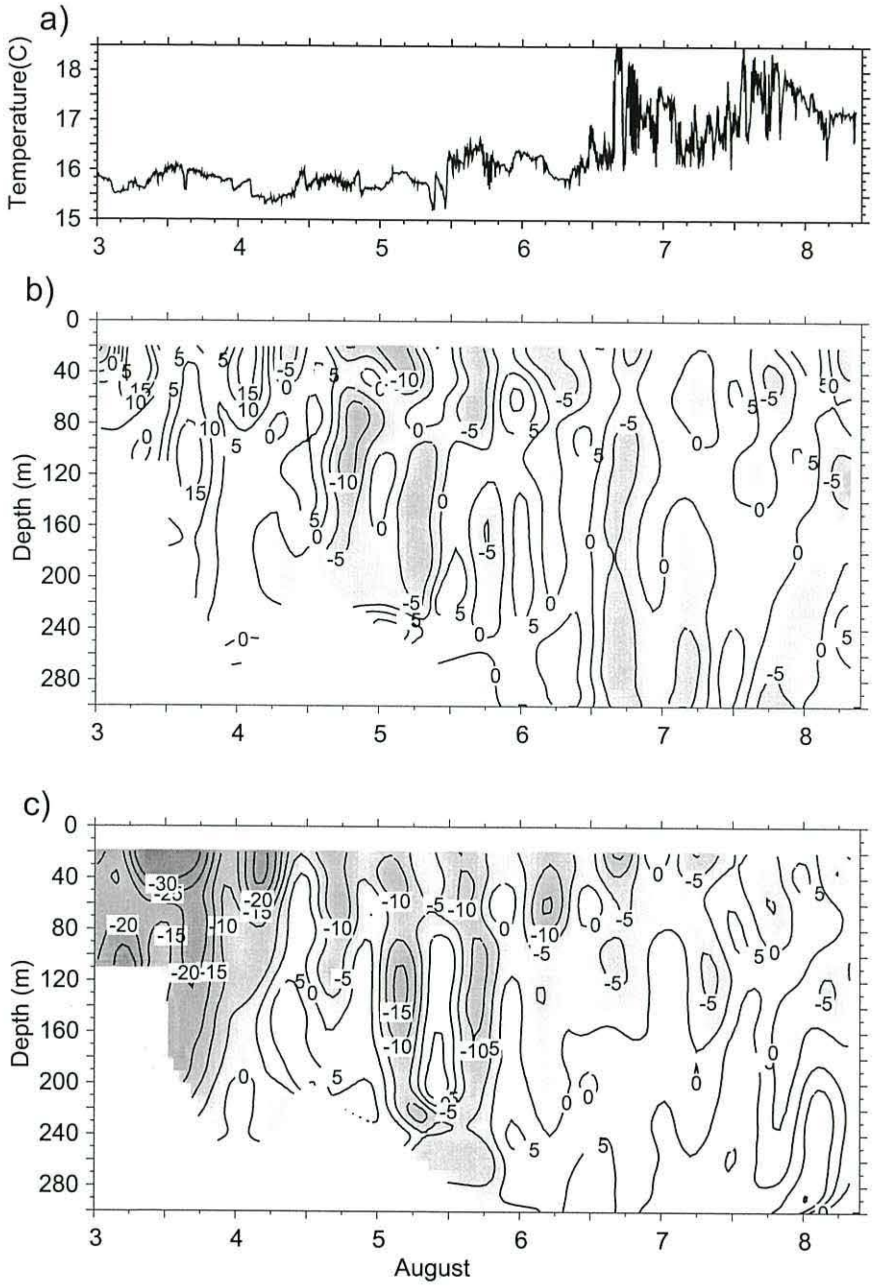

Figure 5.10.: (a) Surface temperature (b) east-west and (c) north-south components of ADCP velocity during the shelf drift experiment. The buoy gradually moved into deeper water.

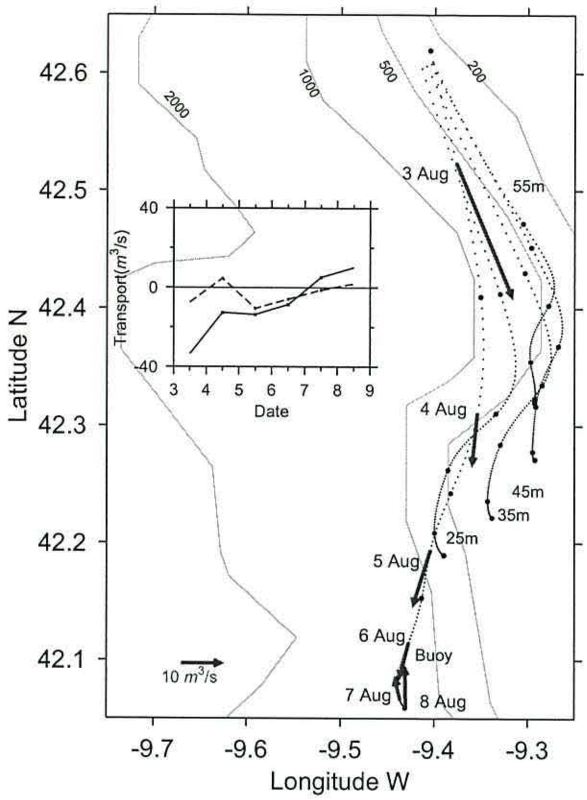

Figure 5.11.: Smoothed track of the drift buoy and pseudo-trajectories calculated from the ADCP observations during the shelf experiment, showing the flow following the isobaths (indicated in m). The dots mark each day beginning on 3 August. The black arrows indicate the direction and strength of the integrated daily transport. Shown inset are the daily transport components across (dashed) and along (solid line) local isobaths. Note the change from offshore southward transport to onshore poleward.

August, the tidal velocities weakened, which was commensurate with drift out into deeper water. At the same time there was an increase and shoaling of the northward component, implying an increase in northward transport of water throughout the entire water column measured. The east-west component indicated predominantly shoreward flow in the first days of the series, even though winds were still strongly upwelling favourable and would be expected to correspond to offshore flow. This apparent paradox of a net onshore flow component during upwelling favourable wind can be resolved by considering the volume fluxes in relation to the orientation of the bathymetry (Fig. 5.11). The buoy trajectory and pseudo-trajectories calculated from the ADCP data at different levels, all low pass filtered with a half power point at 40 h, show the overall flow to follow broadly the pattern of the isobaths. Daily average depth-integrated eastward and northward fluxes were calculated from the ADCP data and extended to the surface with the drifter velocities. When superimposed on the buoy track each mid-day, the weakening and reversal of the alongshore flux vectors with time is evident. On 3 August although the flux had a significant eastward component, relative to the local isobaths it was directed offshore, consistent with the shelf regime locally feeding water into the filament at 42°N. The flux components, rotated along and across the local isobath direction, and estimated over each day's drift (Fig. 5.11 inset), show the weakening and reversal to poleward of the along-isobath flow. At the same time there was a decrease of cross-isobath flux toward deeper water and subsequent reversal to shoreward, i.e. a cut off of water supply to the filament. The exceptional shoreward flux indicated on 4 August was associated with an abrupt change in the poorly defined bathymetry and could well be caused by an inappropriate selection of that day's "along-isobath" direction.

The drift experiment was followed by a 2-day time series station (Phase 2) at a site in 140m depth where the local bathymetry was oriented almost exactly north-south. Wind was minimal at the start of the station and the small net fluxes over the two days there were shoreward and poleward (Fig 5.12), indicative of a relaxation. Variability was dominated by the internal tides. The semidiurnal barotropic current had an amplitude of about $4 cms^{-1}$, which was smaller than the amplitude of the shear in the internal tide, about $10 cms^{-1}$ between the upper and lower layers. However, during the series, wind increased sufficiently southward to produce an average upper layer equatorward flow above deeper poleward flow. A slight decreasing trend in surface temperature was consistent with weak renewal of upwelling. Mean current profiles for both the shelf drift and time series station indicate upper layer equatorward flow over poleward flowing bottom boundary layer (Fig. 5.13). U component was zero or weak onshore.

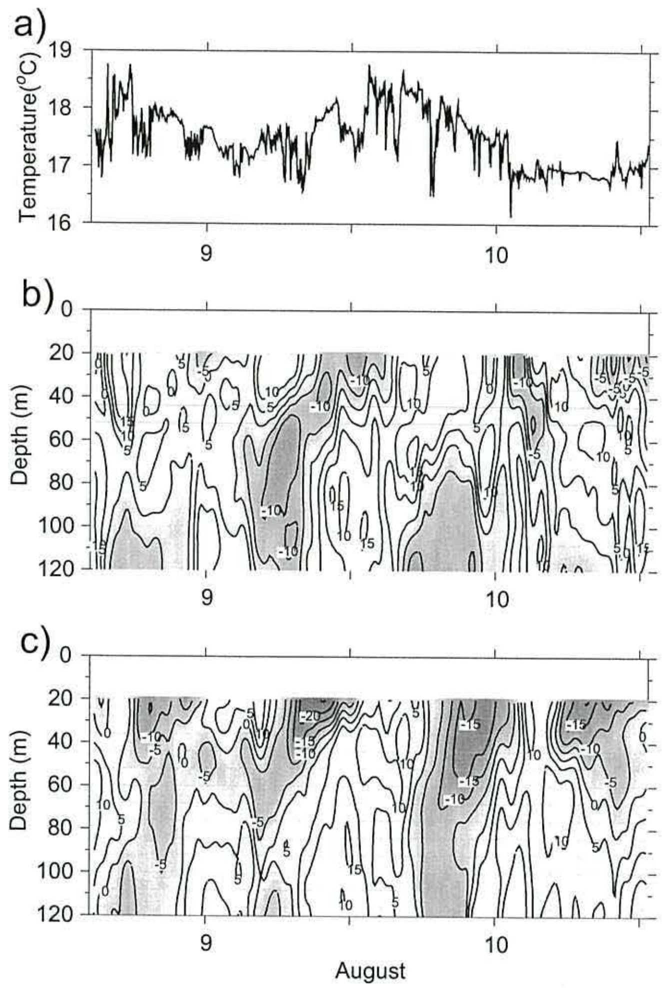

Figure 5.12.: (a) Surface temperature (b) east-west and (c) north-south components of ADCP velocity during the shelf time series experiment

5.3.3 The filament experiment Leg 2

The drifters and water column structure

Mixed-layer drifters were deployed near the southern core of the filament (Fig. 5.2b) during the weakening of the winds on 14 August. As the wind continued to decrease in strength from 10 to 3ms^{-1} during the next two days, they moved slowly offshore (0.05ms^{-1}) and converged towards the filament's southern boundary (SB). The convergence rate, calculated following *Brink et al.* [1991], was consistent with a localised sinking at the SB of about 10md^{-1}. Following the wind intensification to 10ms^{-1} on 17-18 August the northern two accelerated before the others. One northern drifter traced the offshore extent of the filament's northern boundary (NB) with mean

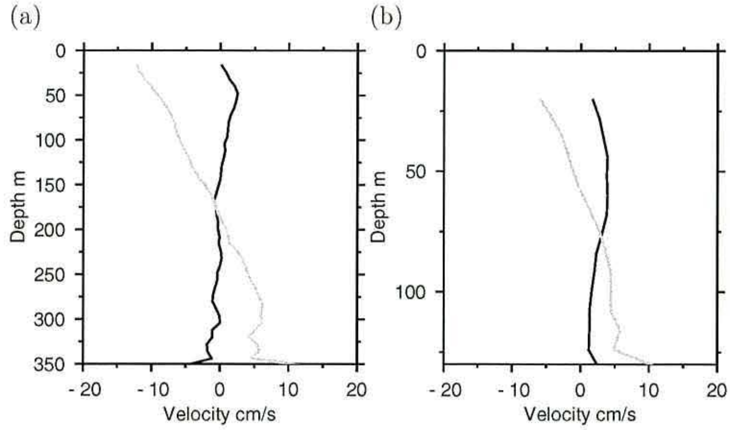

Figure 5.13.: Mean current profiles for U (black) and V (grey) components during, (a) shelf drift and (b) shelf time series experiment. Standard deviations are consistently less than 0.1 ms^{-1} below 50m.

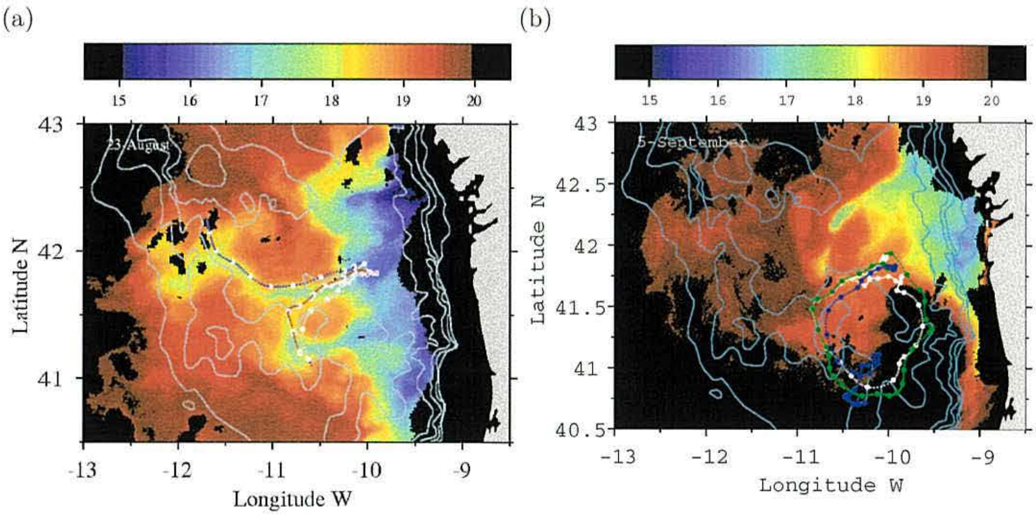

Figure 5.14.: SST images with drifters overlaid on a) 23 August 1998 with first ten days of deployment overlaid and b) 5 September 1998 with 25 days of drifter data. Dots correspond to the start of each day.

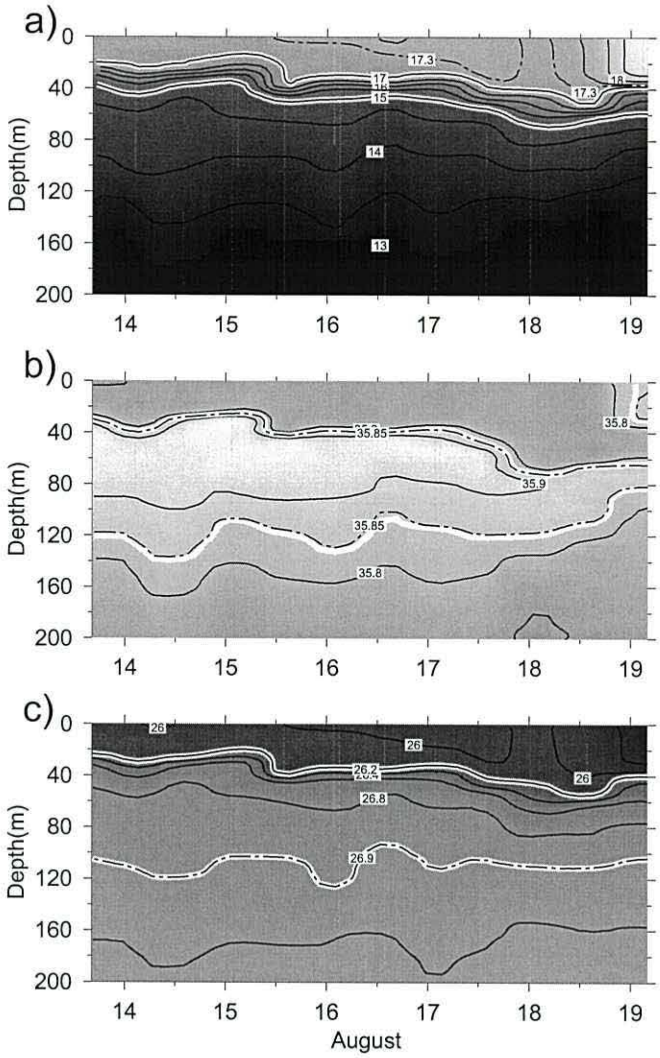

Figure 5.15.: (a) Temperature (b) salinity and (c) density from the CTD time series following the filament drifting productivity buoy.

speed $0.28ms^{-1}$ (Fig. 5.14a) while the others, which had crossed the SB, re-circulated shoreward with average speed $0.17ms^{-1}$ in an apparent return flow. It took them another 20 days to complete the gyre and return close to the launch site (Fig. 5.14b). The MLD in the centre of the buoy array was initially 25m and decreasing (Fig. 5.15), but deepened to near 50m as the array drifted towards the SB. The boundary was marked by the decrease in the salinity maxima at 50-100m, a weak surface minimum of temperature and density, and the maximum MLD.

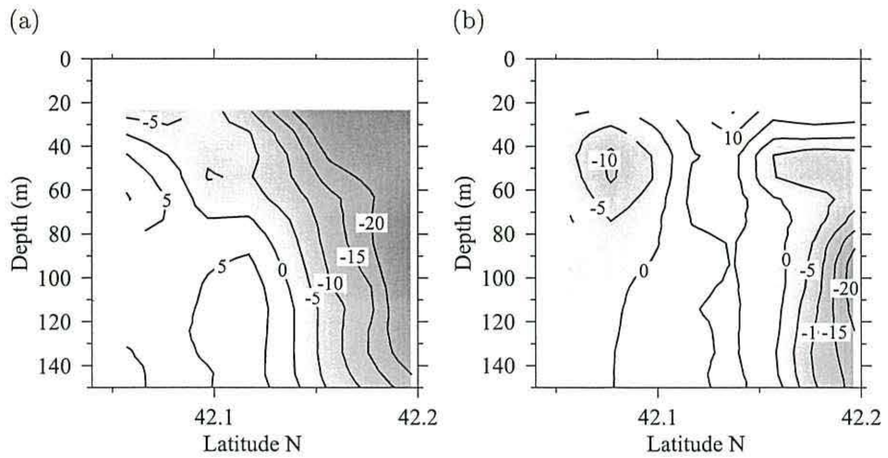

Figure 5.16.: Cross section of the north front a) along filament and b) across filament velocity structure

Filament cross sections

Several incomplete crossings of Filament A were undertaken during Leg 2 of CD114 with CTD, ADCP and FLY although not simultaneously. The first crossing (11-12 August) was done only with underway measurements following a period of slack winds (Fig. 5.7). The ADCP velocities rotated along and across filament for the north front are presented in Fig. 5.16. Offshore flowing velocities in excess of $20 cms^{-1}$ were measured on the seaward side of the filament while onshore flow occupied most of the interior of the filament. Across filament velocities (Fig. 5.16b) showed subsurface convergence, particularly below 80m. Unexpectedly, little baroclinicity was associated with the along filament component.

The first section sampled with ADCP in conjunction with the FLY (Fig. 5.17) on the 16-17 August show details of the filament interior and the southern front. The southern front had a shallow frontal structure with isotherms rising and outcropping from 20m (Fig. 5.17d), and isohalines locally deepening in what could be related with subduction processes. On the filament side of the front, the isotherms domed above 60m depth, but deepened below. Within the filament, a salinity maximum was located at this depth. Its salinity of > 35.9psu was closer to oceanic values than to those of upwelled waters. Surface salinity values <35.7 were restricted to the top 20m

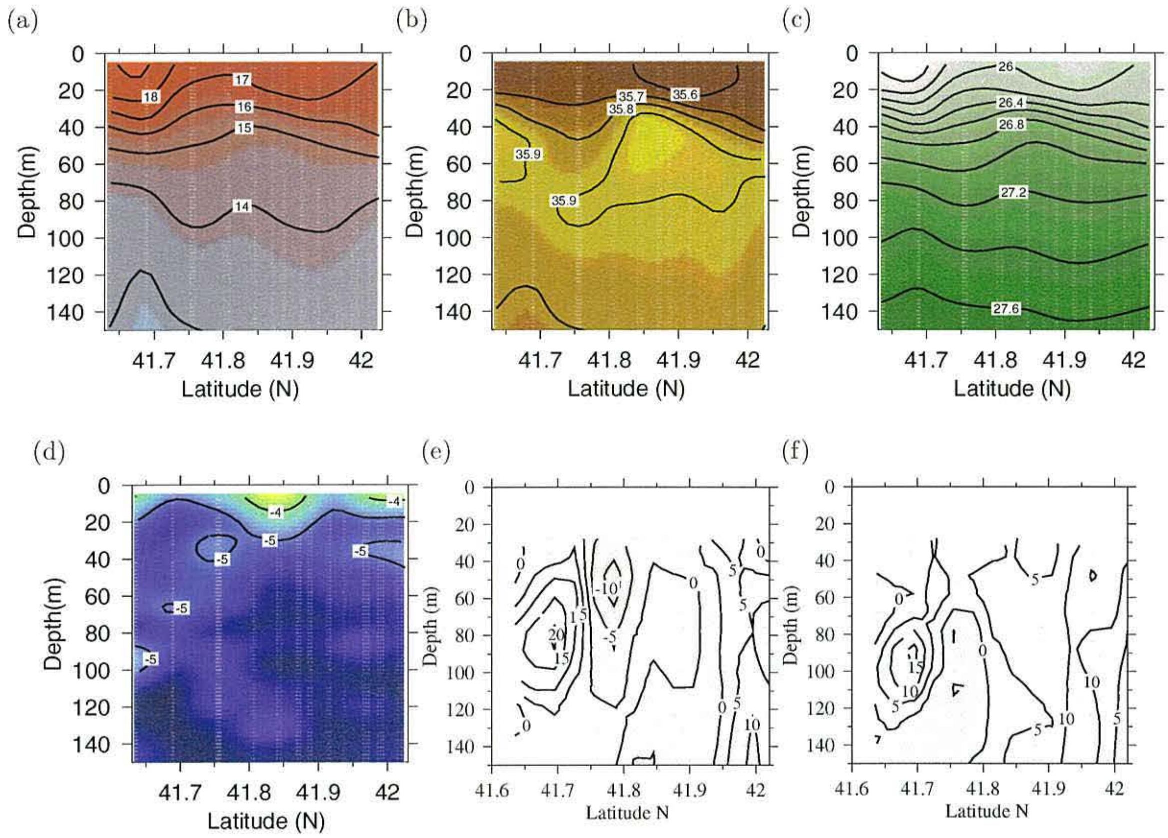

Figure 5.17.: Partial cross section of filament of a) temperature, b) salinity, c) density, d) log dissipation rate e) along filament and f) across filament velocity structure.

at the southern front deepening northwards to 40m. Enhanced mixing, as represented by the logarithm of the dissipation rate (Fig. 5.17d), was restricted to the top 30m north of the southern front and shallower than 15m everywhere else, falling to less than 10^{-5}Wm^{-2} at deeper levels. Little structure is evident in the velocity section (Fig. 5.17e-f) except for strong horizontal shear at the front but with little indication of convergence compared to Fig. 5.16b.

A complete FLY crossing of the filament was undertaken when the wind speed was increasing on 17-18 August (section 2 in Fig. 5.2a). The surface signal of both frontal boundaries was clearly seen in temperature, salinity and density (Fig. 5.18a-c). Both temperature and salinity were lowest in the filament core (<17.5°C, < 35.55psu) and increased away from the core by up to 2°C and 0.2psu in sharp (<4km) frontal boundaries. The associated temperature and density gradients were very similar in

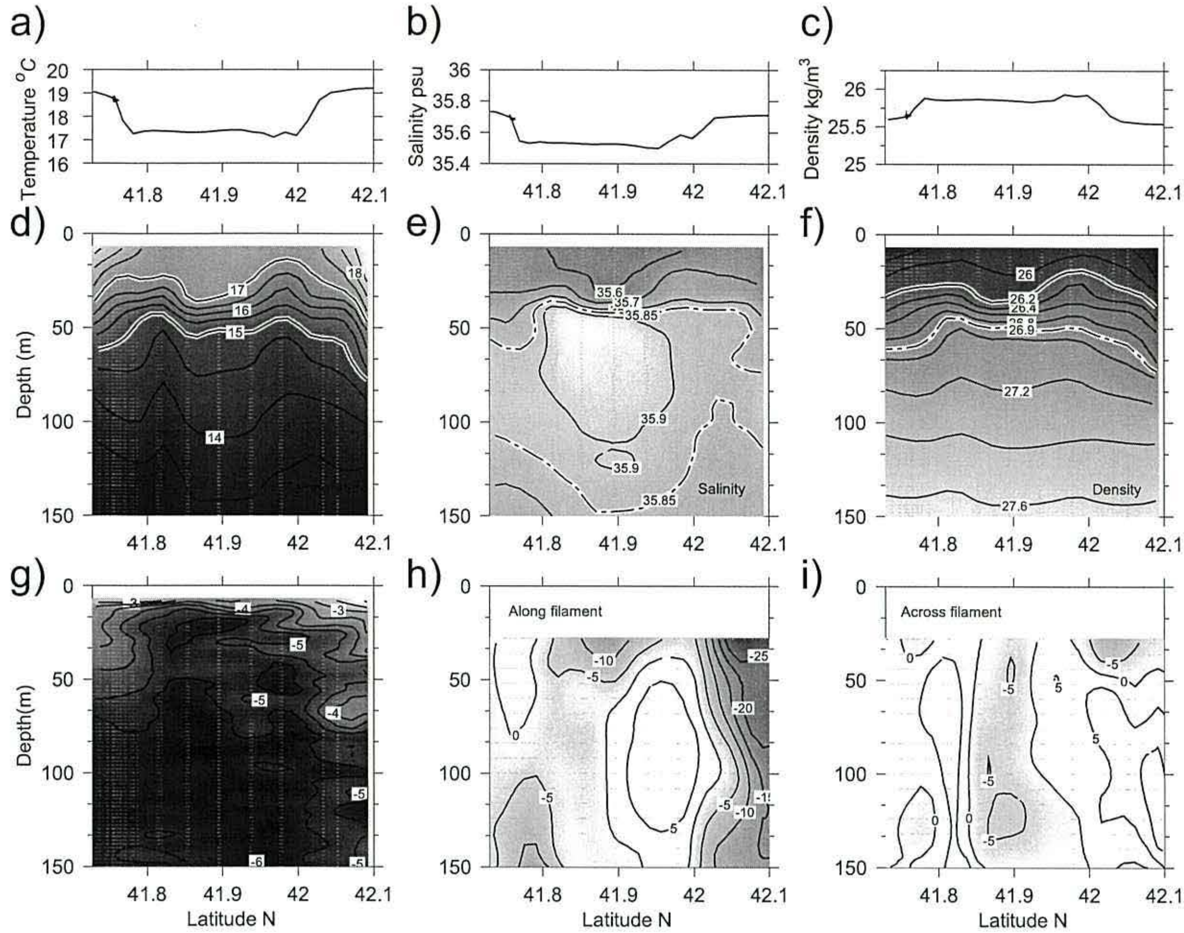

Figure 5.18.: Distribution of properties along section 2 across the filament. Sea surface profiles of (a) temperature (b) salinity and (c) density. Vertical sections of (d) temperature (e) salinity (f) density, (g) $\log_{10}$ dissipation rate , (h) along and (i) across filament velocity. Note onshore flow beneath the centre of the filament and weak convergence to its southern side.

both fronts, less than 0.7°C km^{-1} and 0.06 kgm^{-3}km^{-1}. The filament presented a double core structure resulting from its merger during Leg 1 of the cruise with the filament originating at 41.5°N, as reported by *Smyth et al.* [2001]. The temperature, salinity and density fields in Fig. 5.18d-f show the double core structure as two separate domes evident down to 200m. The section did not continue far enough to sample the full extent of the frontal regions but they seem restricted to the top 60m. The pycnocline was situated around 40m, deepening at the fronts, particularly the northern one, in relation to the stronger baroclinicity seen there in the velocity data. At the core of the filament, water below 50 m was characterised by a salinity maximum (>35.9psu) that did not extend across the fronts. Fig. 5.18h and i shows the velocity structure through the filament rotated into along and across filament components.

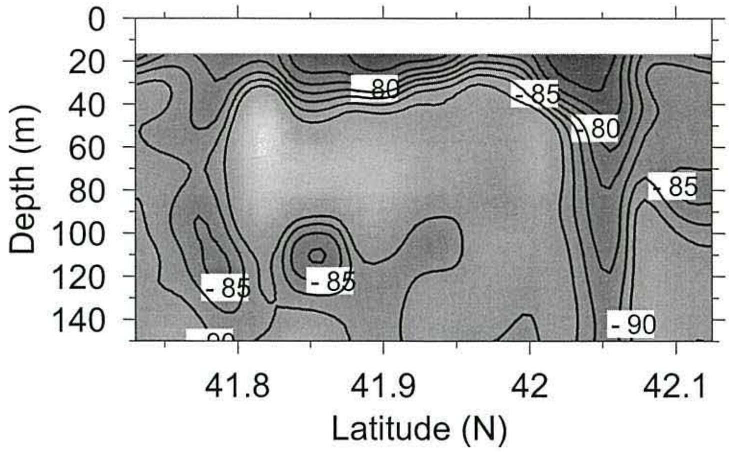

Figure 5.19.: Distribution of Acoustic Backscatter Intensity in dB across the filament as derived from the NB ADCP.

The first available ADCP bin (25m) showed intensification of offshore flow at the filament boundaries, with larger values at the northern boundary (>0.35ms^{-1}) than at the southern one (~0.1ms^{-1}). The horizontal shear associated with the fronts was also higher in the north, $0.5f$ compared to $0.15f$ for the SB ($f \sim 9.7 \times 10^{-5} s^{-1}$). Flow within the filament itself was generally very weak and, remarkably, directed offshore only in the top 50m; below there it was weak (0.05-0.1ms^{-1}) and onshore. Near the fronts, the flow was offshore down to the maximum penetration of the ADCP with a surface intensified jet showing stronger baroclinity in the north than in the south. The total offshore volume transport down to 150m calculated in the section was only 0.5Sv, less than reported for filaments in other regions, though offshore flow extended beyond the northern limit of the section and may be underestimated slightly.

Acoustic backscatter intensity (ABI) derived from the ADCP yielded further support to the property distribution within the filament (Fig. 5.19). The ABI is a by-product of the ADCP which has been successfully related to the abundance of zooplankton [*Flagg and Smith*, 1989; *Zimmerman and Biggs*, 1999]. No attempt was made to relate ABI data to zooplankton abundance for CD114 cruise although it is assumed to correlate with abundance of scatterers. ABI values were derived from the Automatic Gain Control recorded by the ADCP following *RD Instruments* [1998] as:

$$ABI = 10 \log_{10} \left[\frac{4.47 \times 10^{-20} K_2 K_s (T_x + 273)(10^{K_c(E-E_r)/10} - 1) R^2}{cPK_1 10^{-2\alpha R/10}} \right], \tag{5.1}$$

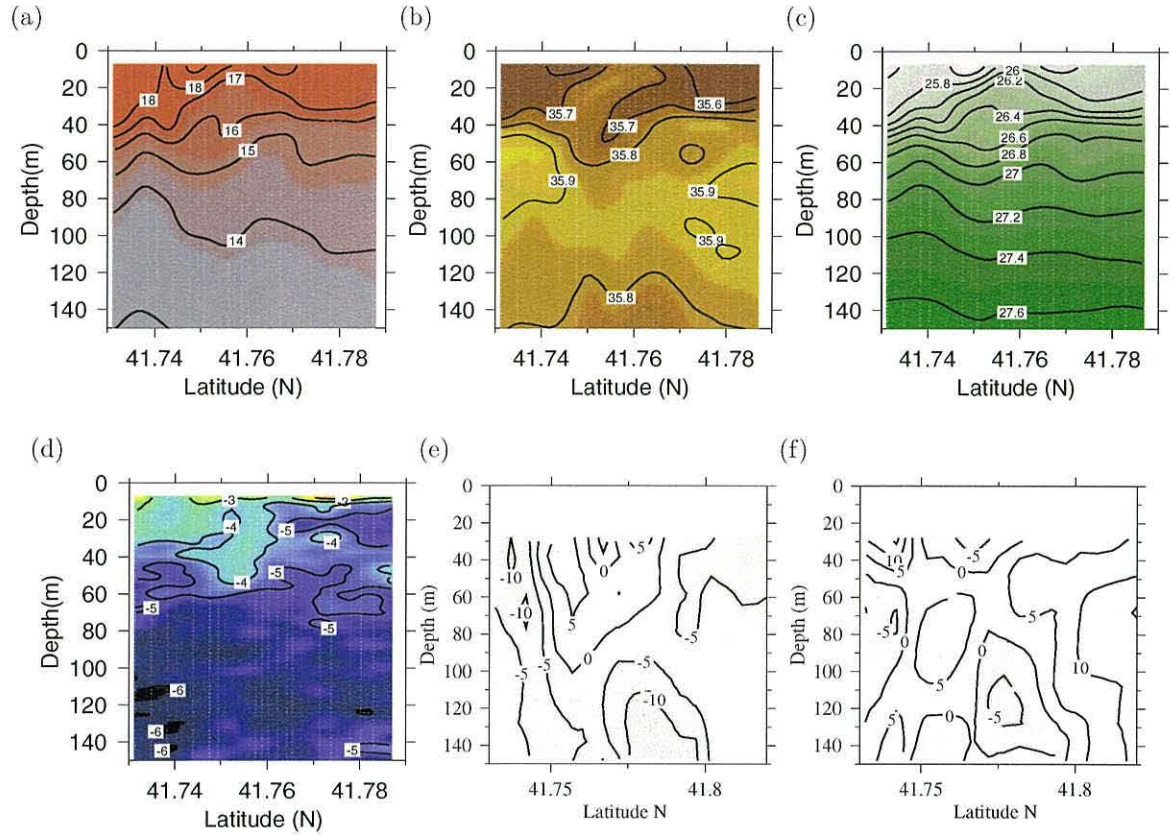

Figure 5.20.: Distribution of properties in detailed sections of the filament's south front of a) temperature, b) salinity, c) density, e) log dissipation rate f) along filament and g) across filament velocity structure

where K_2 is the system noise factor (dimensionless); K_s is a system constant (dimensionless); T_x is the temperature of the transducer in °C; K_c is the conversion factor for AGC echo intensity (dB/count); E is the AGC echo intensity (counts); E_r s the real-time reference level for AGC echo intensity (counts); R is range along beam to scatterers (m);c is sound speed (m/s); P is transmit pulse length (m); K_1 is real-time power into the water (W); and α is the absorption coefficient of water (dB/m). Higher ABI reflecting larger amounts of scatterers are clearly visible at both fronts and in the surface layer, while minimum levels were recorded in the core in the region of the salinity maximum. High ABI values penetrated deeper at the northern boundary than at the southern one reflecting the larger intensity of the first.

A blown up section of measurements within the southern front (Fig. 5.20) clearly shows indications of subduction at the front. A lower temperature, vertically mixed

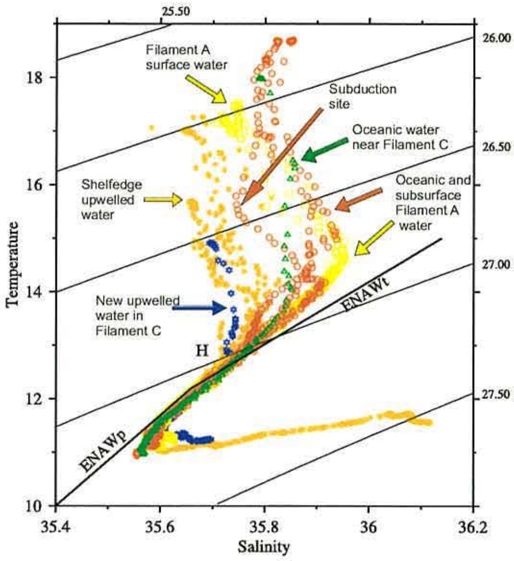

Figure 5.21.: T/S plot of selected CTD stations showing the different water masses in filaments A and C. See text for details.

lens 2km wide (Fig. 5.20a) was associated with a low salinity intrusion (Fig. 5.20b) and locally enhanced mixing (Fig. 5.20d, with values larger than 10^{-4}Wm^{-2}). Strong mixing was also measured down to 40m depth in the frontal region immediately south of the intrusion where the isotherms outcrop to the surface. The velocity structure was weak and complex. Flow was locally onshore at the intrusion but mostly offshore south and north of it (Fig. 5.20e). The across filament component was very patchy with weak convergence at the intrusion from 40m depth to the uppermost ADCP bin at 28m (Fig. 5.20f).

Water masses

The AVHRR image (Fig. 5.2) gives no indication of whether Filament A was a superficial or a substantive oceanographic feature. However, a T/S diagram of selected CTD casts during the cruise (Fig. 5.21) provides evidence that it was surprisingly shallow, and that the only part that comprised water that had upwelled on the shelf was in the surface layers. These layers had a salinity of ~35.74psu, indicating an origin at about 180m depth. Their temperature, 1-1.5°C less than that of surrounding oceanic surface waters, suggests that there had been considerable warming of the upwelled water as it was advected offshore. The mid-depth filament waters (yellow in Fig. 5.21), on the other hand, had a signature that was closer to the surrounding sub-surface oceanic water (red) than the upwelled shelf water (orange). This interpretation is consistent with the observed along-filament flow (Fig. 5.18) where oceanic water was carried shoreward beneath a superficial offshore moving filament structure. A single CTD profile made on the filament's southern boundary (red, and marked "Subduction site") had T/S characteristics that lay between those of the upwelled water and the truly oceanic stations. At and just beneath the surface its properties were oceanic, but below 20m there was a salinity minimum which had the same value as that of the upwelled water in the surface layer of the filament. This suggests subduction in the convergence zone, as indicated by the drifter tracks (Fig. 5.2). The situation in the actively growing filament C, which started developing close to Finisterre after 13 August (described in more detail by *Smyth et al.* [2001]) contrasted with that of the weakening filament A. Throughout its depth range filament C was composed of of colder, newly upwelled water (blue) moving offshore.

Turbulence observations

Only few observations of turbulent dissipation in filament structures have been made. In a 100km wide eddy-like feature off Oregon, *Moum et al.* [1988] found very low dissipation levels ($< 10^{-5}Wm^{-2}$) in the core but enhanced values in regions of high shear at the edge of the structure and in an intrusion into the core. Generally low dissipation levels were observed below the surface layer in some upwelling filaments off California [*Dewey et al.*, 1993], apart from the core of a narrow (10km wide) filament, where locally enhanced values of order $10^{-3}Wm^{-2}$ were observed.

Enhanced mixing was observed in both fronts (Fig. 5.18g) although larger integrated values were found on the northern boundary. In the filament core, active mixing was restricted to the surface 15m, while in the fronts, high values of TKE penetrated to 80m in the NB and 60m in the SB. Representative values of integrated TKE and derived K_z for the thermocline are presented in Table 5.2. Confidence intervals for the estimates were calculated using a non-parametric (bootstrap) method [*Press et al.*, 1992]. The thermocline was subjectively chosen to be 15-17°C, and total

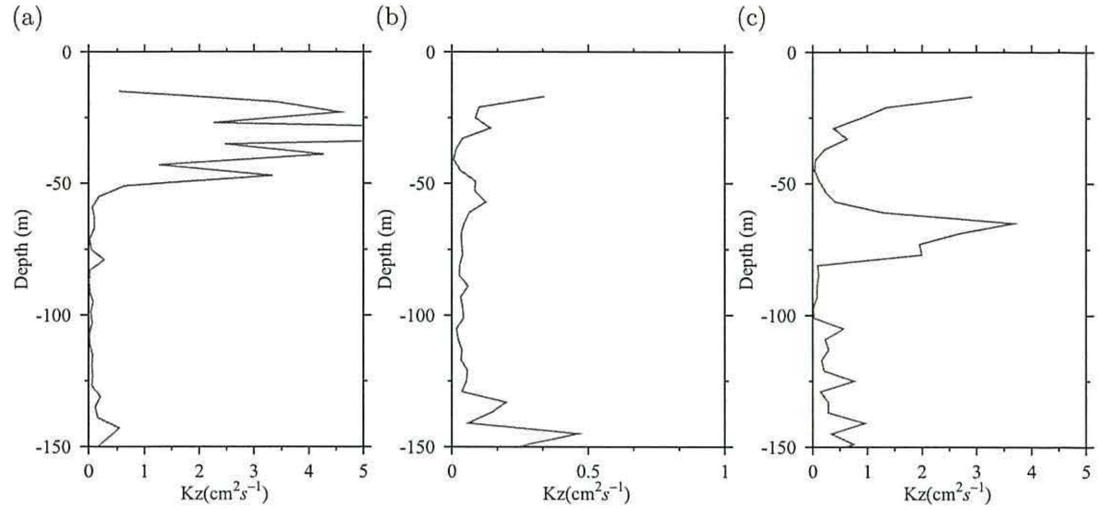

Figure 5.22.: Examples of averaged K_z profile estimates at the a) south and c) north fronts and b) the filament interior. Five consecutive FLY drops were used in the calculations.

dissipation was integrated over the depth of the dissipation profiles (typically 250 m). K_z estimates spanned three orders of magnitude across the filament. Estimated errors were similar to those for the shelf experiment, albeit with less confidence since they are based on fewer observations (typically 10 profiles). The enhanced localised mixing in the thermocline of the SB is believed to be related to the subduction processes. Selected 5 drops averaged K_z profiles (Fig. 5.22) exemplify the differences encountered in the filament. A broad layer of 30m of high diffusivity was present in the southern front at the intrusion (Fig. 5.22a). The highest diffusivities were measured there due to the weak stratification of the intrusion, rapidly falling to levels similar to the filament core, an order of magnitude smaller (Fig. 5.22b). In the northern front, diffusivities of value $\sim 3 cm^2 s^{-1}$ were measured near the surface and at the pycnocline falling to the filament core levels in between (Fig. 5.22c).

	K_z cm^2s^{-1}	75% confidence limits cm^2s^{-1}	Thermocline dissipation Wm^{-2}	Total dissipation Wm^{-2}
South Front	1.6	1.1	4 10^{-3}	8.5 10^{-3}
Core	0.015	0.01	0.3 10^{-3}	1.4 10^{-3}
North Front	0.1	0.04	1.5 10^{-3}	12.6 10^{-3}

Table 5.2
: Vertical eddy diffusivity and vertically integrated dissipation rates for the filament survey.

5.4 Discussion

Both periods of sampling took place when winds were changing from strongly upwelling favourable to near zero, but winds were never actually downwelling favourable. The experiments are therefore representative of relaxation following an upwelling event. In this respect, results seem typical in the indications of convergence at the filament boundary, as also observed by *Flament et al.* [1985] and *Flament and Armi* [2000] off California, the establishment of poleward flow on the shelf and slope, like California [*Winant et al.*, 1987], and the general decrease in extent of the filaments with weakening wind, previously noted off Iberia by *Haynes et al.* [1993]. Indications of persistent poleward undercurrent during the summer in the Galician system were seen in current-meter records of 1989 at 280m depth in 300m of water [*Huthnance et al.*, 2002], reversing briefly only during the strongest upwelling wind events. They also encountered predominant poleward flow over the slope from May to September 1999 at 430m depth. During the wind relaxation of Leg 1, the poleward undercurrent became shallower, reaching depths of 170m over the slope (Fig. 5.10), and depth-integrated transport reversed to poleward. Across-shelf transport also changed accordingly; seaward at the beginning of drift but onshore on the last day and during Phase 2. The decreasing contribution to the filament seen during the shelf experiment and the relatively small offshore filament transport - compared to 1-3 SV in active filaments off California [*Strub et al.*, 1991] and NW Africa [*Barton et al.*, 1998] - reflect the weakening system. However, both drift experiments sampled packets of water recently upwelled and represent conditions commonly found in the highly variable system off Galicia.

There was considerable spatial variability in the observations of diffusion in the filament. On its southern boundary the levels were similar to those observed at the shelf edge (about $1cm^2s^{-1}$, *Barton et al.* [2001]), whilst on its northern boundary they were an order of magnitude smaller. Very low values were observed within the core of the filament (about $0.01cm^2s^{-1}$). This distribution of vertical mixing is closer to that observed in the wide eddy like structure off Oregon, [*Moum et al.*, 1988] than the narrow filament off California [*Dewey et al.*, 1993]. It is not possible to give a specific explanation for these differences from the observations made in the filament, but it is clear that the enhanced diffusion coefficients occurred in regions of high vertical shear. Both frontal regions showed similar surface gradients and horizontal extend in contrast with previous measurements that showed consistently sharper fronts in the cyclonic boundary (our southern front) of filaments [*Washburn et al.*, 1991; *Dewey et al.*, 1991; *Flament and Armi*, 2000]. Sharp convergent shear fronts associated with upwelling filaments have been reported by several authors [e.g. *Moum et al.*, 1990; *Flament and Armi*, 2000]. In the present experiment, ADCP data showed inconclusive evidence for weak convergence in both boundaries but was supported by the observed convergence of the drifters towards the southern boundary. *Flament and Armi* [2000] found subducting layers during slack winds in a cyclonic convergence front. The authors suggested a secondary frictional flow induced by the along-front geostrophic flow as the possible cause of the convergence. The subducting layer found in the southern front was of similar size to the one sampled by *Flament and Armi* [2000] but the associated frontal shears were far weaker. No information on the along filament extend of the subducting layer was gathered but it might have been very localised, associated with the curvature of the front causing along-filament convergence rather than across-filament [*Shearman et al.*, 1999].

A vertical mixing time, τ, across a thermocline of thickness h, should approximate to $\tau = h^2/K_z$, on dimensional grounds. If h is (say) 20m then τ will increase from about 1 month to 1 year as K_z decreases from 1 to $0.1cm^2s^{-1}$. On the shelf a rate of $1cm^2s^{-1}$ would be large enough to cause the thermocline to both broaden and transport material into the lower layers over the duration of summer. However, in the lifetime of a filament (order 1 week) vertical mixing at $1cm^2s^{-1}$ makes only a small contribution to the evolution of the temperature and nutrient structure. Any observed changes must be due to other horizontally dominated factors, such as eddies. At the southern boundary, convergence appears to dominate vertical mixing, causing sinking at about $10mday^{-1}$ ($\tau = 7$ days when $h = 10$m and $K_z = 1.6cm^2s^{-1}$). Water mass characteristics within the filament will not be significantly modified by vertical mixing during its lifetime, though surface warming and horizontal exchanges will gradually change them.

The apparently anomalous double core structure of filament A may result from several factors. It was one of the "oldest" filaments, having developed at the start of the upwelling season, and had therefore been subject to several cycles of development and relaxation prior to sampling. Moreover, it had merged with a second filament (B) arising some distance to the south. The shoreward flow in its centre was probably a relic of the recirculation between the originally separate filaments A and B. Finally, it was sampled during a period of minimal wind, when the slow drifter speeds and convergence indicate relaxation of the system, so that its structure may not be typical of an active filament. In this respect, filament C may have been more representative, but it developed too late to be thoroughly sampled. The presence of shoreward flow beneath the surface signature of the merged filaments underlines the difficulty of making transport estimates solely on the basis of remotely sensed sea surface temperatures. Finally, the results show that there is not a simple one-way transport from shelf to open ocean or sub-surface to surface. Three of the four filament deployed drifters recirculated shoreward. Their trajectories suggests that at least some waters transported offshore in the filament may return to near slope on a time scale of a month. However, it must be remembered that the behaviour of surface drifters where they crossed the convergence zone on the filament boundary is not truly Lagrangian in that they cannot follow submerging water parcels. The evidence of subduction at the southern boundary of the filament implies vertical recirculation of water parcels

(a) (b)

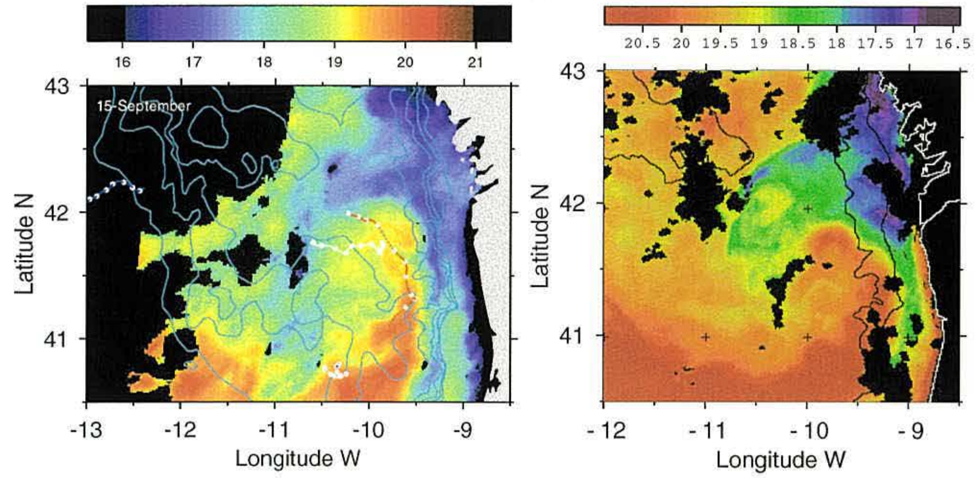

Figure 5.23.: SST images on a) 15 September 1998 overlaid with drifters positions five days either side of image date and b) 7 September 1995. White dots correspond to the start of each day. Clouds are masked black.

on a relatively short time scale. Given the typically 2 weeks cycling of wind forcing observed here, these vertical exchanges may have implications on significant biological time scales.

The disappearance of Filament A in September was brought about by the sudden weakening of the upwelling favourable winds as seen in Fig. 5.5. During that time, *Peliz et al.* [2002] measured the establishment of poleward flow off the shelf. Filament A drifted northwards (Fig. 5.6h-i) advected by a warm tongue anomaly reminiscent of the winter slope poleward flow [e.g. *Haynes and Barton*, 1990]. Filament A weakened and became narrower (Fig. 5.23a). The offshore end of the filament bent southwards and the frontal boundaries became less well defined, probably as a result of increase insulation due to the slackening of the winds. The poleward anomaly strengthened and the one drifter that was within its influence moved northwards with larger speed than the other three. A similar situation, also involving the 42°N filament, was identified in SST imagery in 1995 (Fig. 5.23b). The offshore end of the filament is broad, badly defined and bends southward while a warm anomaly develops over the slope. At the coast, another warm anomaly is clearly visible extending over 150km. It has been related to a poleward coastal countercurrent which is typical at the end of the upwelling regime [*Sordo et al.*, 2001]. In the absence of upwelling favourable winds, the meridional density gradient quickly forces the poleward flow over the slope and filaments are slowly cut off from its water source over the shelf. With time, their surface signal disappears masked by solar insulation or horizontal mixing.

5.5 Conclusions

A combination of Lagrangian and other observations has revealed complex features of the upwelling filament system on and offshore of the NW Iberian continental shelf. Observations were made during a period of upwelling favourable but weakening winds.

- On the shelf near the source of the 42°N filament, the net offshore flux to the filament decreased as upwelling favourable winds relaxed to near zero. At the same time alongshore currents reversed to slightly poleward.
- The 42°N filament had an unusual double core structure arising from the earlier merger of two separate filaments. Remnant return flow below the surface carried oceanic water shoreward between and under the two merged filament cores.
- Offshore transport in the filament was estimated at only 0.5 Sv moving offshore, which is small compared to filament transports reported elsewhere. This low level of transport is compatible with measurements made during a weakening of the upwelling and almost certainly underestimates transport in a developing filament.
- Enhanced turbulence was found in the filament boundaries, and probably results from stronger baroclinic shear at the northern boundary (K_z=0.1cm^{2}s^{-1}) and possible subduction at the southern boundary (K_z=1.6cm^{2}s^{-1}). Overall vertical mixing in the filament itself appeared to be small (K_z=0.01cm^{2}s^{-1}).
- Drifters showed some water transported off shelf in the filament was carried far out to sea, but some could recirculate on a time scale of a month back to the shelf edge. This has strong implications for the biology of the region and in particular the retention of larvae spawned on the shelf.

The present observations were obtained in support of a multi-disciplinary cruise with multiple objectives and because of sampling compromises are not synoptic but only representative of restricted areas at specific times. Nevertheless, the data set provides new information on the behaviour of the filament system and highlights important questions as to the initiation and decay of filament structures.

CHAPTER

6 Downwelling regime

6.1 Introduction

As we have seen in the previous chapter, a poleward flowing undercurrent is intrinsic to most upwelling systems [*Neshyba et al.*, 1989] and the Galician upwelling system is no exception. Along-slope variability in wind stress forcing or topography can be called upon to explain its presence in the face of upwelling favourable winds [*Wang*, 1997; *Trowbridge et al.*, 1998]. However, the Galician upwelling regime is only present for part of the year (June-October). The rest of the year, a downwelling regime with a surface poleward flow settles in the shelf, and in the absence of upwelling, other forcings drive the slope poleward flow. Northward winds represent a possible mechanism except, as shown in chapter 3, they are highly variable. They are more likely to contribute to the short temporal variability associated with the poleward flow, while an oceanic pressure gradient is responsible for its seasonal onset [*Frouin et al.*, 1990; *Haynes and Barton*, 1990]. Steady-state adjustment of an alongshore oceanic pressure gradient adjacent to a steep continental slope would fail to penetrate the shelf [*Wang*, 1982] as described in terms of the arrested topographic wave model of *Csanady* [1978]. Shelf-ocean adjustment is confined to the slope region and results in a poleward slope-trapped current on eastern boundaries [*Hill et al.*, 1998]. *Huthnance* [1984, 1995] described the JEBAR effect (*joint effect of baroclinicity and relief*), assuming the oceanic sea-level gradient is physically due to the meridional drop in steric height arising from the fall in oceanic temperatures poleward. Zonally oriented density surfaces intersect a meridional sloping boundary and a dynamical adjustment of the density-induced pressure gradient to the bottom slope takes place. The JEBAR effect should apply along the entire eastern boundary but is most relevant upstream of regions where steric height drops markedly. A meridional density gradient is maximum between 39°N and 41°N [*Arhan et al.*, 1994] but weakens/disappears northwards. At 43°N, the slope turns zonally and the JEBAR mechanism no longer forces the poleward flow directly. In the absence of direct forcing and considering frictional effects, *Pingree and LeCann* [1990] showed that the JEBAR induced poleward slope flow decays with a length scale smaller than the northern Spanish coast, and hence propagates along the slope away from the source reaching the French coast of the Bay of Biscay. Temporally varying spatial structures in the California undercurrent have been related to the interaction of the current with the complex topography [*Noble and Ramp*, 2000], but the relevance of this in the Galician region remains to be assessed.

6.2 Cruise Description

The data presented in this chapter were largely collected during 13 October-7 November 1999 cruise on board the R/V *Thalassa* in the Galician region. The cruise was divided into two legs with different objectives. The aim for Leg A (13-20 October) was to sample OMEXII-II S, P, and N reference transects (see chapter 4, Fig. 4.1 for location) during the autumn and study the distribution of physical, biological and chemical properties. This was to enable the building of biogeochemical budgets for input to models of the exchange of material between the continental shelf and the ocean at seasonal scales. The main objective of Leg B (20 October-7 November) was to study the physical structure and biological functioning of a Slope Water Oceanic eDDY (SWODDY) previously identified in SST images. Bad weather and lack of evidence in the hydrography of such structures influenced the decision to continue sampling the poleward flow seen during Leg A at more northern latitudes, hence providing one of the most detailed samplings of the poleward flow around the Galician coast. Nearshore transects and CTD stations occupied during the entire cruise can be seen in Fig. 6.1.

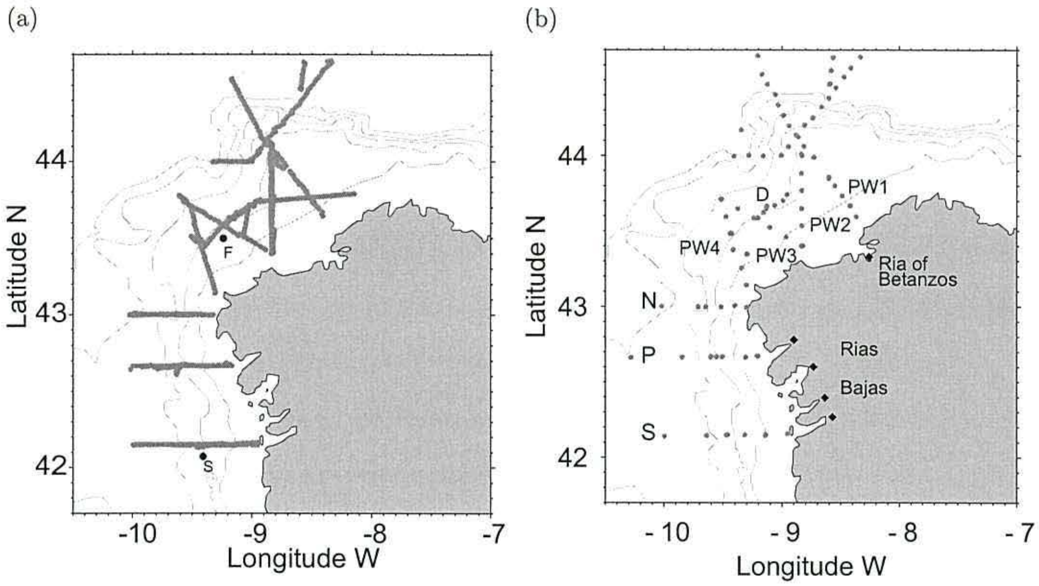

Figure 6.1.: (a) ADCP transects and (b) CTD stations positions visited during the THAL99 cruise (13 October-7 November 1999). Black diamonds mark the fresh water sources along the Galician coast. Buoys S and F are also labelled.

6.3 Data and methods

A total of 120 CTD drops was made with a 24-position Rossette (General Oceanics) sampler coupled to a Neil Brown Systems Mk IIIB CTD with temperature, conductivity, pressure and fluorescence sensors. Pre-cruise calibration of the temperature sensor undertaken by the Unidad Tecnologica Marina (previously Unidad de Gestion de Buques Oceanograficos e Instalaciones Polares) from Barcelona showed it was working to the manufacturer's specifications. The conductivity sensor was calibrated against 42 bottle samples collected during the cruise, encompassing the whole depth range of measurements, with a Guildline Autosal® salinometer giving the calibration equation,

$$S_c = 0.921 \times S_u(\pm 0.03) + 2.81(\pm 1.3) \tag{6.1}$$

with correlation $r^2 = 0.956$, where S_c stands for corrected salinity and S_u for uncorrected salinity. Associated errors at 95% confidence are enclosed in brackets. Casts were made to a specified depth of 500m or the sea bottom if shallower. For information on the Biological and Chemical measurements see *Varela-Rodriguez* [2000b, a]. On several occasions, transects of the top 100m were sampled with a towed undulating CTD, the Aquashuttle Undulating Oceanographic Recorder (UOR) from Chelsea Instruments. The UOR is a multisensor instrument measuring underway conductivity, temperature, pressure, fluorescence and photosynthetically active irradiance (PAR). The depth range sampled depends on the towing speed and the length of the cable. The typical depth range during the cruise was 30-100m at a towing speed of 8kt.

Underway measurements of temperature, salinity and fluorescence were taken every 10min with a SeaBird 21 Thermosalinometer from the continuous water supply from a nominal depth of 5m. Meteorological data were measured with a Vaisala MILOS 500 weather unit and recorded every 10min together with the navigational data.

The *Thalassa* is equipped with two RDI ADCP that were used simultaneously during the cruise. Both the 150Khz broadband (BB) and 75Khz narrowband (NB) performed relatively well in spite of the bad weather conditions encountered during the cruise. The systems were running on two different PC with RDI Transect software. The 150Khz BB ADCP, firmware 5.52, is a four beam transducer, with a beam angle of 20° and a concave configuration. The 75Khz NB ADCP, firmware 1712, had the same configuration, and both presented a misalignment angle of 45° which was accounted for in the software settings. The systems were installed at 6m depth.

The two systems differed not only in their operating frequency but in the way they measure water velocities. Narrowband ADPCs measure frequency shifts of single sound pulses and transform it into velocity estimates through the Doppler Effect. Broadband ADCPs instead measure the phase shift of multiple echoes, i.e. over a broad range of frequencies, taking advantage of the full signal bandwidth available for measuring velocity. Each broadband sound pulse contains many shorter coded pulses and the final velocity value is the average of multiple estimates. The phase ambiguity associated with this technique is resolved by autocorrelation methods. Broadband Doppler phase processing is equivalent mathematically to using the Doppler shift of frequency but employs a method for estimating velocity that results in better accuracy than with narrowband ADCP.

There is an inverse relationship between sound absorption and frequency which translates into a greater penetration of the 75Khz system compare to the 150Khz. The difference is further increased because the BB system has a reduced depth penetration at an equivalent working frequency in favour of greater accuracy in shorter averaging intervals. A summary of the configuration used in the two systems is given in Table 6.1.

	Characteristics of ADCP system setup						
	Cell length	Pulse length	Blanking interval	No of bins	Pings per ensemble	Averaging interval	Pitch & roll compensation
75Khz	16m	16m	16m	50	4	300s	No
150Khz	8m	8m	8m	50	1	300s	No

Table 6.1: Configuration setup for cruise Thal99

The processing of both datasets followed the technique described in Chapter 4 and only a brief assessment of the data quality will be presented. The percentage of good bins processed by both ADCPs (Fig. 6.2) was high during most of the cruise (>80%) except at times of rough weather. Typical depth penetration was 500m for the NB ADCP and 200m for the BB ADCP, on occasions reaching 600m and 250m respectively. The BB ADCP showed worse data quality at times when the ship was sailing against the predominant sea (Fig. 6.2, days 306.5 and 307.5) as it was fixed closer to the prow with respect to the NB ADCP. The shallower bins do not seem to be contaminated as was the case with the R/V *Charles Darwin* cruises, an indication that the problem was caused by suboptimal installation on R/V *Charles Darwin.*

The calibration of both systems was done as described in section 4.3.3 using the water track method. Amplitude and phase estimation was done by averaging 190 and 182 points for the NB and BB ADCP respectively. The amplitude and misalignment angle used in the correction are shown in Table 6.2 together with their standard deviation. The largest associated uncertainties in calibration parameters come from the standard deviation of the phase misalignment angle which could introduce spurious speeds of up to 7cms^{-1} at a highest ship speed of $\sim$5ms^{-1}.

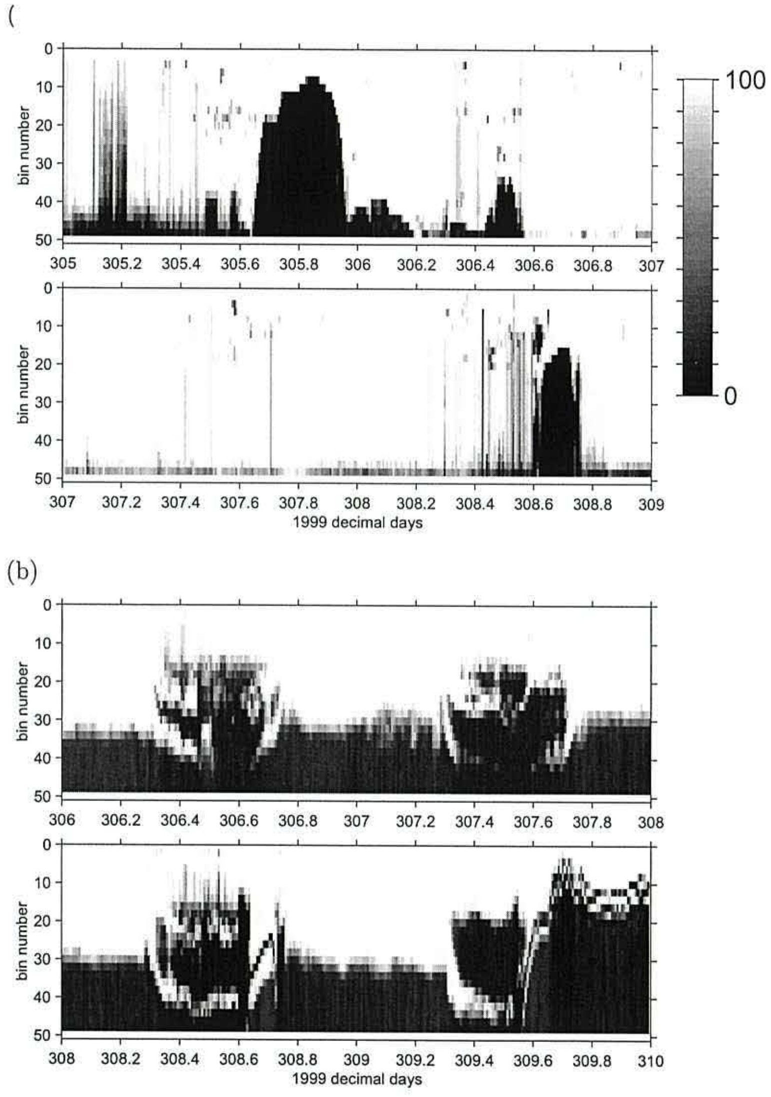

Figure 6.2.: Example of Percentage good pings vs. time and bin number for a) 75Khz NB and b) 150Khz BB ADCPs

	$\beta \pm \sigma$		$\alpha \pm \sigma$	
75 Khz	0.98	± 0.01	0.2	± 0.8
150 Khz	0.99	± 0.01	0.9	± 0.8

Table 6.2: Calibration parameters for THAL99

The comparison between on station and underway of the mean and standard deviation profiles for the Amplitude and Percentage good (PG) show a small degradation of the signal while underway (Fig. 6.3). Similar trends are seen in all other variables checked. The variability generally increased below 500m for the NB ADCP (e.g. PG) and no deeper data while underway are used in the chapter. The variability seen in the BB ADCP increased more rapidly at a shallower depth, 100m, reaching a maximum saturation at 250m, below which depth the PG falls below 80% and no data will be used. Data between 100m and 250m are presented only after careful examination.

The two systems were compared using linear regression on data acquired during a three and a half day drifting experiment (2-5 November) within the poleward flow core. Data in the depth range of 54-70m for the NB were compared to data between 51-75m from the BB for the entire duration of the experiment (Fig. 6.4). In general, the NB measured greater velocities than the BB, by 6% and 13% on the U and V components as shown below,

$$U_{BB} = 0.94\,(\pm 0.03) \times U_{NB} + 0.006\,(\pm 0.004), \tag{6.2}$$

$$V_{BB} = 0.87\,(\pm 0.03) \times V_{BB} + 0.01\,(\pm 0.004), \tag{6.3}$$

with correlations $r^2 = 0.95, 0.92$ respectively. Confidence limits for the coefficients at 95% level of confidence are shown in brackets. Considering the difference in depth resolution and the 2min offset between the two ADCPs, both systems agree well and data from the BB ADCP were used to enhance details of the top 200m of the water column. No attempt was made to correct the NB ADCP data with the calibration as little more information would be gained considering the high smoothing involved with the CTD data.

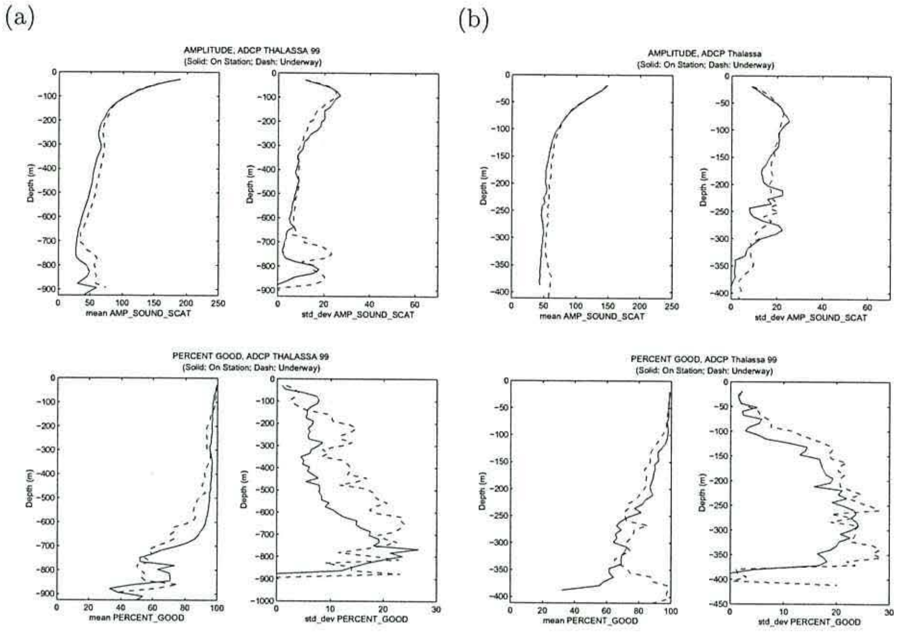

Figure 6.3.: Comparison between underway and on station averaged and standard deviation profiles of Amplitude and Percentage good for a) 75Khz NB and b) 150Khz BB ADCPs

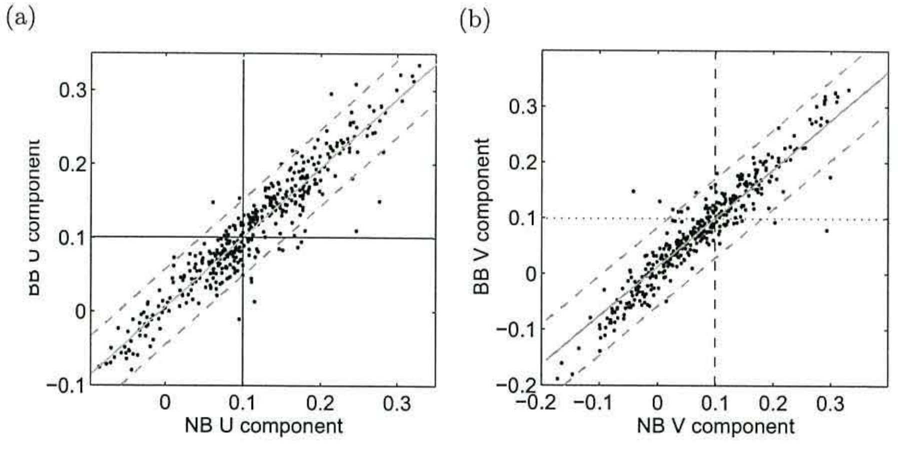

Figure 6.4.: Linear Least-square fit and confidence intervals at 95% between NB and BB ADCP data during the poleward flow drift experiment averaged over a depth range of 54-70m and 51-75m respectively for a) U component and b) V component. Values in ms^{-1}

6.4 Results

6.4.1 Background and evolution

Weekly composites of SST for the cruise area (Fig. 6.5) spanning the entire cruise show the warm anomaly related to the poleward flow starting to develop mid cruise and strengthening towards its end. A general decrease of 1.5°C in SST is apparent in the sequence. A meridional SST gradient of 1°C per 10-40km is present in all images, centred at 42°. During the week starting prior to the cruise, evidence of remnant coastal upwelling can be seen on the west coast and north of Cape Finisterre (Fig. 6.5a). Moderate poleward winds on 14-18 October (see Fig. 6.6a-b) reduced the coastal band of upwelled water and a warm intrusion of SST moved northwards along the 1000m isobath north of 42° (Fig. 6.5b). Winds increased on 19-23 October and the coastal upwelled water disappeared from both coasts (Fig. 6.5c). The warm intrusion (1° warmer than surrounding water on the west coast) became better defined, its core located between the 200m and 1000m isobath on the west coast. The intrusion can be tracked around Cape Finisterre after which it weakened (temperature anomaly of 0.5°C) and moved closer to the coast. A short upwelling favourable wind pulse on 26-27 October and 2-3 November could have been responsible for the narrow band of cold water close to the west coast, however the warm poleward intrusion became better defined, with the 1°C anomaly reaching Cape Finisterre. North of the cape, the intrusion became wider and continued along the coast the following week (not shown) in the face of upwelling favourable winds (Figs. 6.6).

Daily median of hourly winds from buoys S and F from 1 October-30 November are shown in Fig. 6.6a-b (see Fig. 6.1a for their position) and are representative of the larger scale winds measured by the Seawinds instrument on the QuikScat satellite (see Chapter 3). No data from buoy N were available for that period due to failure of the buoy. Maximum upwelling and downwelling favourable winds of 13ms^{-1} were measured at F. The cruise was characterised by weak SE winds until 15 October, becoming stronger ($\sim$ 13ms^{-1}) and more SW and W towards 23 October. Winds were highly variable for the remainder of the cruise with brief pulses alternating

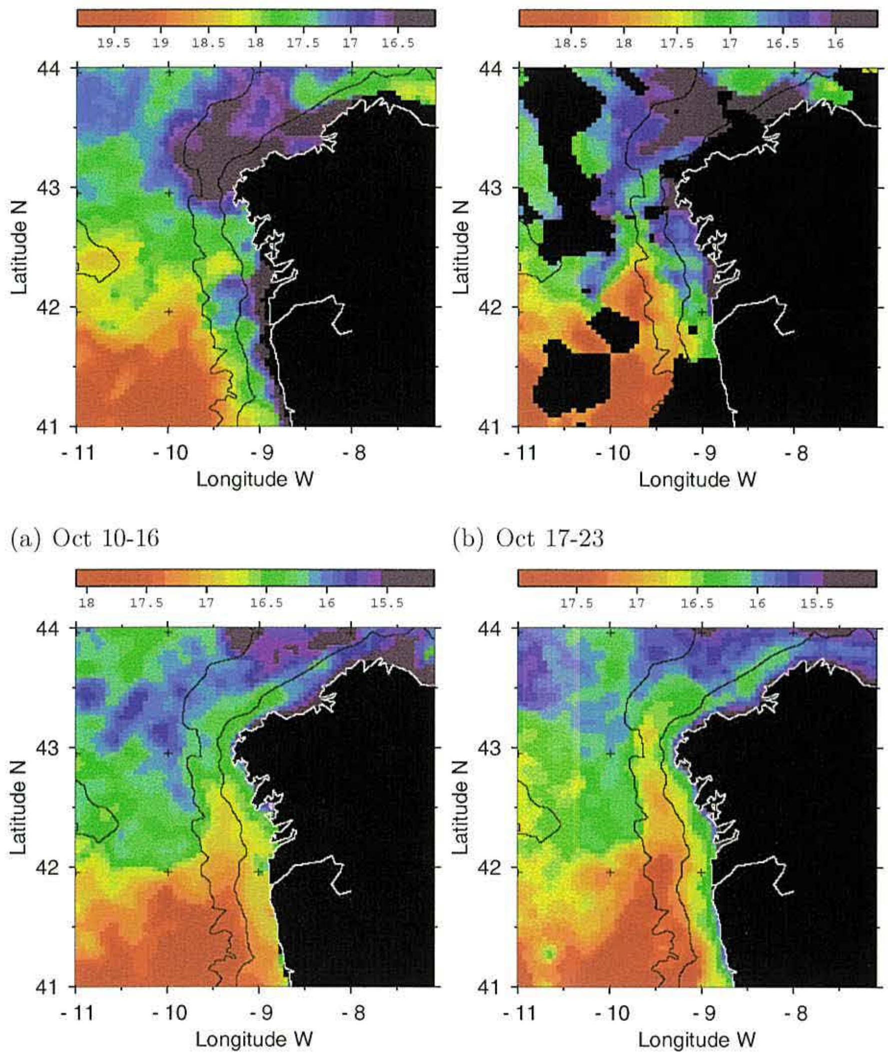

(a) Oct 10-16

(b) Oct 17-23

(c) Oct 24-30

(d) Oct 31- Nov 6

Figure 6.5.: Weekly SST composites during the THAL99 cruise (13 October-7 November 1999). Clouds and land are masked as black.

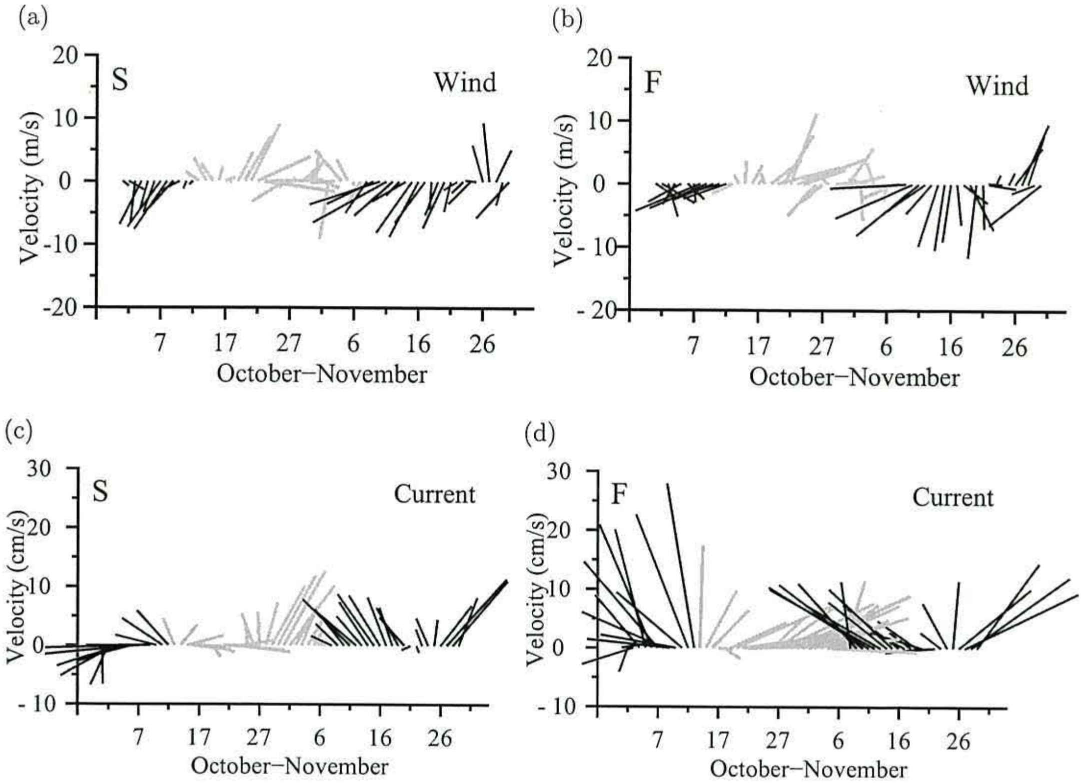

Figure 6.6.: Wind (a-b) and Current (c-d) vectors measured at buoys a,c) S and b,d) F (1 October- 30 November). Light gray corresponds to the cruise period. North is aligned to the positive y axis.

upwelling and downwelling favourable winds. After the cruise, 8-23 November, winds become upwelling favourable.

Subtidal surface currents (Fig. 6.6c-d) were southwards at the beginning of the record at S, rotated clockwise and became poleward during 10 October-7 November, prior to the change in winds. The period included a brief current reversal around 18-19 October, after a weakening of downwelling favourable winds. Although winds changed afterwards to upwelling favourable, currents remained poleward with a small offshore component. At F, currents were larger ($\sim$ 22cms^{-1} on the 29 October compared to $\sim$ 15cms^{-1} at S) but followed the same evolution as at S. The only apparent difference was the earlier onset of poleward currents and near reversal of currents on 8-18 November.

Summarizing, the THAL99 cruise took place during the onset of the winter poleward flow regime at the end of a weak summer upwelling regime (see Chapter 3), when persistent poleward flow started to develop. In the remainder of the chapter, data will be presented in two sections, the west coast sampling from 13-21 October which can be related to the first stages of the poleward flow development seen at the buoys; and the north coast sampling, during which the poleward flow was steadier and stronger and had reached north of Cape Finisterre.

Transect	Instrument	St. Time	End Time	St. Position	End Position
S	CTD	14/10 15:22	15/10 20:07	9° 59-42° 09	8° 57-42° 08
		14/10 15:38	15/10 13:57	9° 59-42° 09	8° 58-42° 08
S	ADCP	15/10 22:12	16/10 02:19	9° 12-42° 09	10° 00-42° 09
		16/10 02:27	16/10 07:07	9° 58-42° 09	9° 8-42° 08
	CTD	16/10 14:56	17/10 14:37	10° 00-42° 40	9° 12-42° 40
P	ADCP	16/10 15:57	17/10 14:17	10° 00-42° 39	9° 14-42° 40
		18/10 02:43	18/10 06:53	9° 57-42° 40	9° 13-42° 40
	CTD	18/10 14:06	19/10 11:41	10° 01-43° 00	9° 18-43° 00
		18/10 15:27	18/10 21:06	9° 59-43° 00	9° 24-43° 00
N	ADCP	18/10 22:08	19/10 01:35	9° 25-43° 00	10° 01-43° 00
		19/10 01:43	19/10 07:23	10° 01-43° 00	9° 24-43° 00
	UOR	18/10 22:45	19/10 01:35	9° 25-43° 00	10° 01-43° 00
	CTD	25/10 9:54	26/10 5:30	8° 22-43° 35	9° 10-44° 32
PW1		21/10 10:25	21/10 23:52	8° 27-43° 34	9° 30-44° 55
	ADCP	22/10 03:12	22/10 14:13	9° 29-44° 54	7° 56-43° 50
		25/10 09:40	26/10 05:58	8° 25-43° 40	9° 10-44° 32
PW2	CTD	31/10 8:12	31/10 22:06	8° 50-44° 00	8° 50-43° 24
	ADCP	31/10 09:39	31/10 22:59	8° 50-44° 01	8° 50-43° 24
		31/10 23:09	01/11 04:46	8° 49-43° 24	8° 50-44° 07
PW3	CTD/ADCP	01/11 11:48	01/11 22:47	8° 49-43° 24	9° 30-43° 42
PW4	CTD/ADCP	02/11 8:17	02/11 19:58	9° 31-43° 42	9° 18-43° 08

Table 6.3: Time, location and instrument of the transects sampled during cruise Thal99.

6.4.2 The west coast

During Leg A, three transects were sampled, S, P and N. They were occupied with CTD stations once, and repeated at least one more time with ADCP and on occasions with the UOR. Details of all transect times, starting and ending points are summarised in Table 6.3. CTD transect plots were built through Barnes interpolation with 10m and 15km scales in the vertical and horizontal respectively, with no extrapolation, i.e. the start and end points of each plot correspond to a CTD cast. We have used distance from the shelf edge, as identified from the ADCP signal, with positive values offshore from the shelf as the horizontal gridding variable. Due to the larger station separation offshore, the interpolation scheme smooths horizontal gradients. Unsmoothed surface salinity and temperature from the Thermosalinometer have been included to help assess the level of smoothing.

CTD section plots of transect S show low surface salinity and temperature values (35.3psu and 17.2°-17.5°C) (Fig. 6.7a-b) extending from nearshore to 13km from the shelf edge. Offshore, surface temperature and salinity values increased to 18.7°C and 35.75psu in a sharp surface layer front of $\sim$5km (Figs. 6.7a-b). The low surface salinity layer nearshore was 50m deep (Figs. 6.7c) with associated high fluorescence levels (Fig. 6.7e) indicative of a freshwater origin. Nonetheless, the slight coastal uplifting of all isolines (salinity, temperature and density) provides evidence of weak coastal upwelling though no isolines break the surface nearshore. The surface front also marked the transition between a surface fluorescence maximum inshore and the subsurface fluorescence maximum centred at 50m offshore (Figs. 6.7e). This deepening of the maximum may be related to the seaward intrusion of offshore warm surface waters, as indicated by buoy S at that time (Fig 6.6c), which have not been in contact with coastal waters. This idea is supported by the association of the offshore subsurface maximum with relatively low salinity values at 40-50m (Fig 6.7c).

A subsurface salinity maximum (>35.9psu) was measured at 65-110m depth, 0-35km off the shelf. It was related to a localised increase in vertical separation of the isotherms (Fig 6.7d). At that level, isopycnals (e.g 27.1 isopycnal) deepened towards

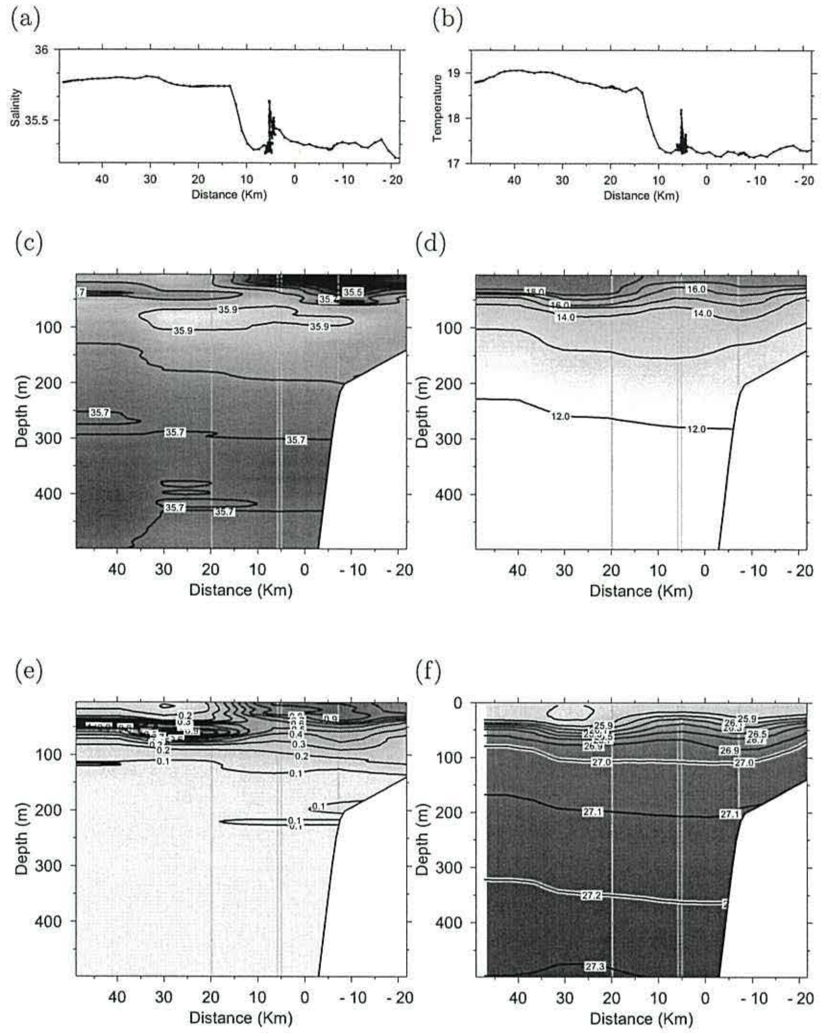

Figure 6.7.: Transect S CTD sections (14-15 October) for a) surface salinity, b)surface temperature, and vertical sections of c) salinity, d) temperature, e) fluorescence and f) density.

the coast, which can indicate geostrophic poleward flow (Fig 6.7f). Below 400m, higher salinity was measured within 30km of the shelf in relation to the northward advection of Mediterranean water. Due to the wide spacing of the stations it is difficult to estimate the offshore limit of the subsurface intrusion although some indication can be gained from the more densely spaced ADCP dataset.

The U and V velocity components were rotated throughout into along and across-shelf components. The choice of along-shelf direction is difficult, particularly in an area of such complex bathymetry. Uncertainties in the along-shelf direction have an

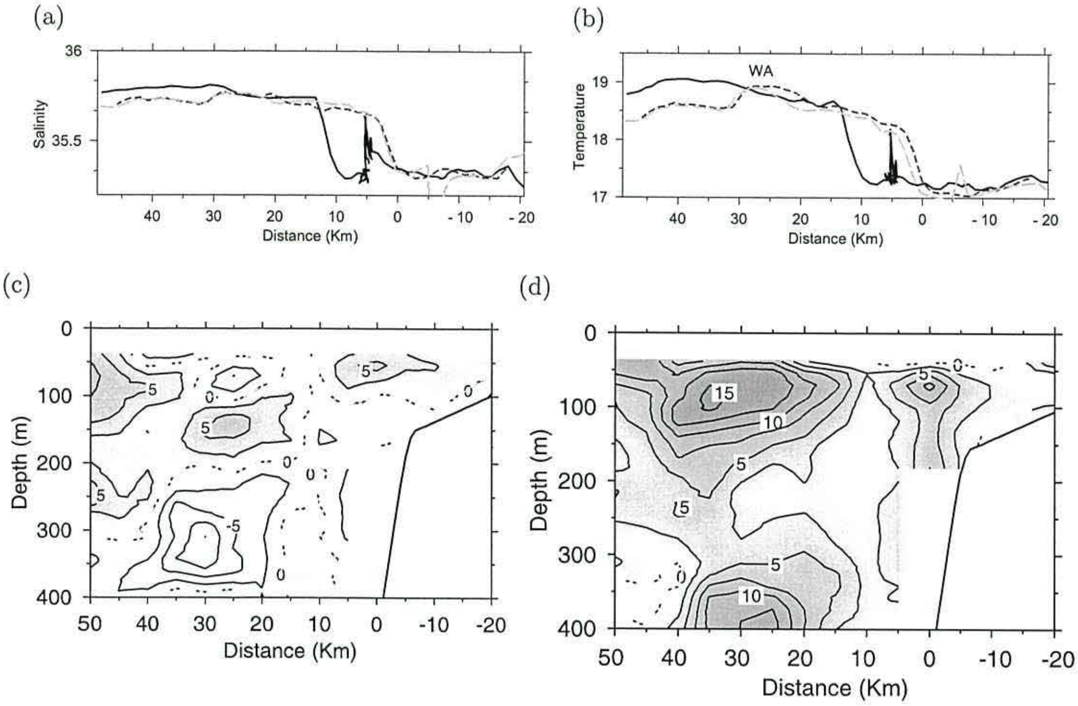

Figure 6.8.: Surface a) salinity and b) temperature coincident with the ADCP sections (lighter dashed line indicates later crossing) for transect S. The developing warm anomaly (WA) is labelled. NB ADCP averaged sections, c) across-shelf component (+ve onshore) and d) along-shelf component (+ve alongshore). The coast local direction is 21.1°E.

important effect on the across-shore component which should be interpreted with caution. Mean sections of the along and across-shelf velocity components (Fig. 6.8) for the three repetitions of transect S (see table 6.3) have been built in an attempt to reduce the tidal signal. More effective and complex methods exist for reducing the tidal signal in shipboard ADCP records [e.g. *Candela et al.*, 1992; *Howarth and Proctor*, 1992; *Münchow*, 2000b] but the availability of repeated sections and the strength of the offshore residual currents in comparison to the tidal flow [$\sim$8cms^{-1}, *Fanjul et al.*, 1997] allowed us to use the simplest method.

During the ADCP repeat surveys, the surface salinity and temperature (Fig. 6.8a-b) showed a shoreward advection of 10km of the frontal region. Also, a surface temperature maximum (temperature anomaly of $\sim$0.5°C)) developed at 20-30km from the shelf edge (WA in Fig. 6.8b). The across-shelf component (Fig. 6.8c) was small and overall onshore, except for a deep offshore flowing core at 200-400m centred at 30km off the slope. The along-shelf component (Fig. 6.8d) revealed two northward

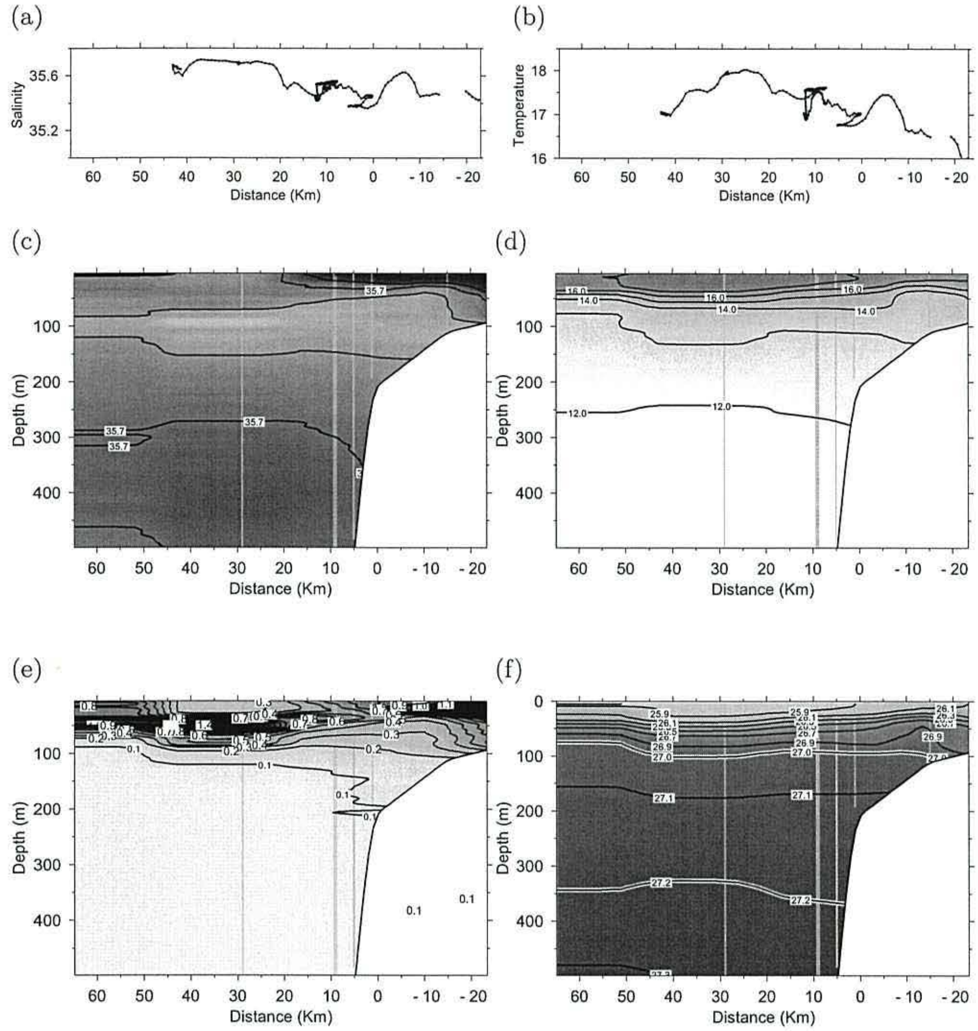

Figure 6.9.: Transect P CTD sections (16-17 October) for a) surface salinity, b)surface temperature, and vertical sections of c) salinity, d) temperature, e) fluorescence and f) density.

cores offshore of the shelf reaching speeds of 15-10cms^{-1}, coincident with minima in the standard deviation (σ < 5cms^{-1} not shown). The shallower, at 50-120m depth, was 10km offshore of the surface temperature maximum at 25km off the shelf (Fig. 6.8b) measured in the last two repetitions of the transect. It also corresponded in position with the interpolated offshore limit of the subsurface salinity maximum in Fig. 6.7c. The deeper core appeared to shift shorewards with respect to the shallower one and may be related to the northward advection of Mediterranean water. A weaker northward flowing core can also be seen on the shelf edge occupying most of the water column.

Transect P (Fig 6.9) showed similar characteristics to transect S. A surface temperature maximum of 18°C was measured 25km off the shelf (Fig 6.9b), 1°C less than transect S. The salinity also reached a maximum of 35.7psu between 20-40km off the shelf edge (Fig 6.9a) but was ~0.1psu less saline than in transect S. The surface thermosalinograph record showed weaker T and S fronts on this section than in transect S, but over the outer shelf small maxima in both T and S were evident. The low salinity layer nearshore was shallower, reached 25m depth, and had higher values than in transect S, reflecting the larger concentration of freshwater sources further south (The Rias Bajas and the Miño river).

The subsurface salinity maximum at 50-150m depth spanned the entire section with a weak local maximum at 30km offshore (Fig 6.9c), where the temperature increased locally (Fig 6.9d). Similar to transect S, the surface fluorescence maximum was deeper underneath the warm tongue intrusion (Fig 6.9e). On the shelf between 10-15km, all isolines showed a local increase in vertical separation below 50m depth at the same time that fluorescence levels increased near the bottom inshore and on the shelf edge (Fig 6.9e). The latter could indicate a bottom Ekman layer associated with poleward flow in the shelf.

Surface temperature and salinity in the two repetitions of transect P (Fig 6.10 a-b) showed a shoreward displacement of the offshore warm intrusion and front similar to Fig 6.8 a-b. In response to the sustained if weak downwelling winds the warm anomaly was better defined with a local maximum temperature around 25km offshore of over 18°C in the first section and slightly cooler in the second section. The narrower warm and salty intrusion on the shelf also moved further inshore, possibly in response to the downwelling winds. The averaged velocity section showed weak onshore velocities (Fig 6.10 c) which agreed with the general shoreward displacement of the surface structures. The alongshore component (Fig 6.10 d) was predominantly poleward both off and on the shelf (>10cms^{-1}) and like transect S, a subsurface maximum of ~20cms^{-1} at 50m depth 30km off the shelf was again associated with the offshore end of the warm intrusion.

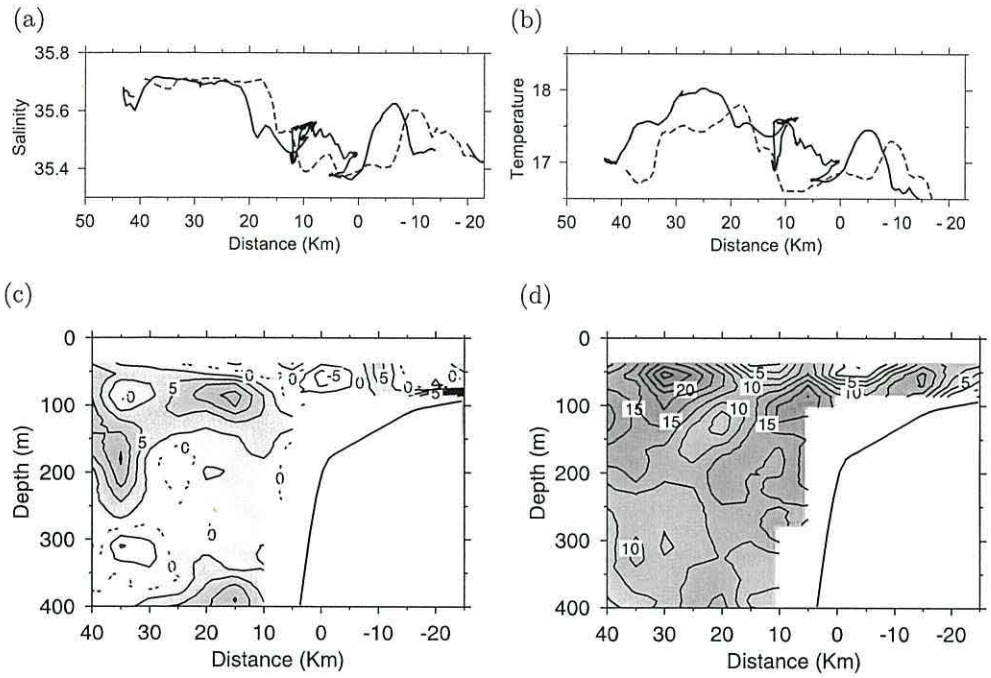

Figure 6.10.: Surface a) salinity and b) temperature coincident with the NB ADCP section averages (lighter dashed line indicates later crossing) for transect P: c) across-shelf component (+ve onshore) and d) along-shelf component (+ve alongshore). The coast local direction is 28.6°W.

Transect N (Fig 6.11) showed similar characteristics to the previous ones: a warm surface intrusion associated with low fluorescence values, a subsurface salinity maximum at 100m off shelf and low salinity waters associated with freshwater runoff on the shelf. The surface signature of the offshore warm and salty intrusion (Fig 6.11a-b) was less well defined than in transect P. The colder and fresher shelf waters form a front at the shelf break similar to transect S albeit not as sharp. Freshwater runoff was present on the shelf forming a thicker (50m) and narrower layer than in more southern transects although it still extended to the shelf edge. As in transect P, the isotherms and isopycnals on the shelf separated vertically between 30-200m (Fig 6.11d,f), and again bottom fluorescence values increased on the shelf edge compared to transect S (Fig 6.11e), suggesting sinking along the shelf bottom. Two cores of subsurface salinity maxima (Fig 6.11b) are clearly discernible, one on the shelf and one offshore. The evolution of the surface salinity and temperature (Fig. 6.12a-b) during subsequent repetitions of transect N showed an enhancement of the warm intrusion temperature signature but little shoreward displacement in

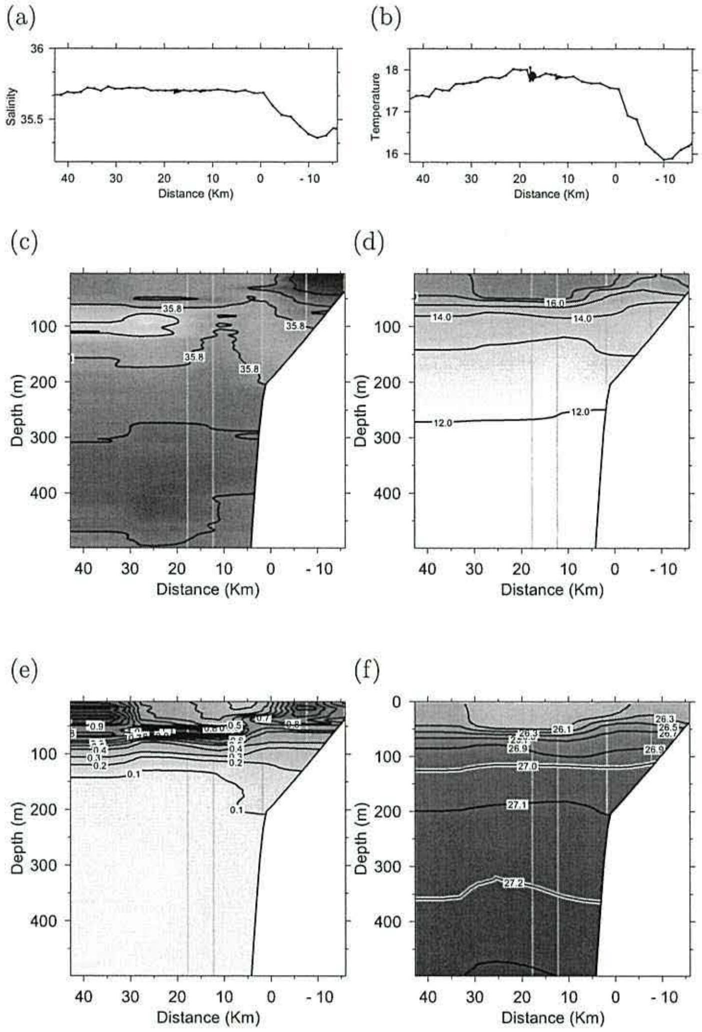

Figure 6.11.: Transect N CTD sections (18-19 October) for a) surface salinity, b)surface temperature, and vertical sections of c) salinity, d) temperature, e) fluorescence and f) density.

contrast with previous transects. The velocity structure of the averaged section showed offshore flow west of 20km (Fig. 6.12c) with negligible associated along shelf component while poleward flow (Fig. 6.12d) was associated with zero or very weak onshore flow. Barotropic poleward flow was measured on the shelf (>15cms^{-1} in both ADCPs), and off the shelf in two cores similar to transect S although they were weaker. The shallower core had peak velocities of ~6-7cms^{-1} extending from the shallower bin to 200m depth at 30km off the shelf. The deeper core had velocities in excess of 7cms^{-1} at 300m depth, 20km off the shelf. Overall maximum velocities were weaker and closer to the shelf break than in transect S.

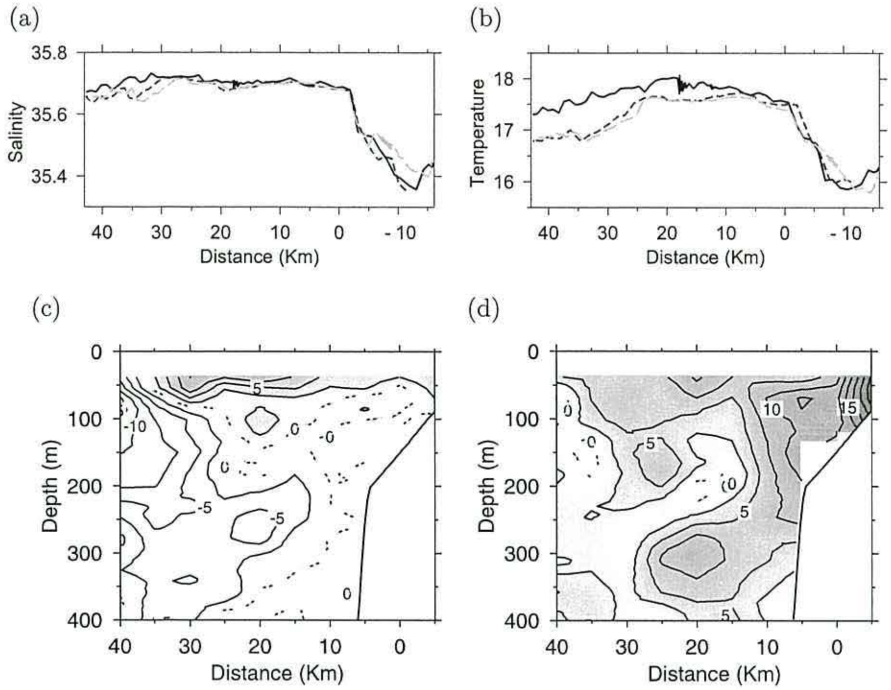

Figure 6.12.: Surface a) salinity and b) temperature coincident with the NB ADCP section averages (lighter line colour indicates later crossing) for transect N: c) across-shelf component (+ve onshore) and d) along-shelf component (+ve alongshore). The coast local direction is 7.1°W.

The second repetition of transect N (Fig. 6.12) with UOR and BB ADCP shows the detailed vertical structure of the warm intrusion (Fig. 6.13). It is worth pointing out the numerous vertical fluctuations at the thermocline (larger than 15m), indicative of the high internal wave activity of the region [*Barton et al.*, 2001]. The intrusion was very shallow affecting mainly the top 50m, and is characterised by a widened thermocline (Fig. 6.13a). The narrow core (~20km) had temperatures in excess of 17.5°C in agreement with the surface records in Fig. 6.12b. The velocity structure in Fig. 6.12b largely reflected northward flow in the thermal anomaly. Maximum speeds in the strongly baroclinic flow were associated with the offshore limit of the intrusion, and was near zero at its nearshore end.

Summary

A surface N-S gradient in temperature was evident from the data between transects S and P. Surface values decreased by 1°C. Similar structures were seen in all three

(a)

(b)

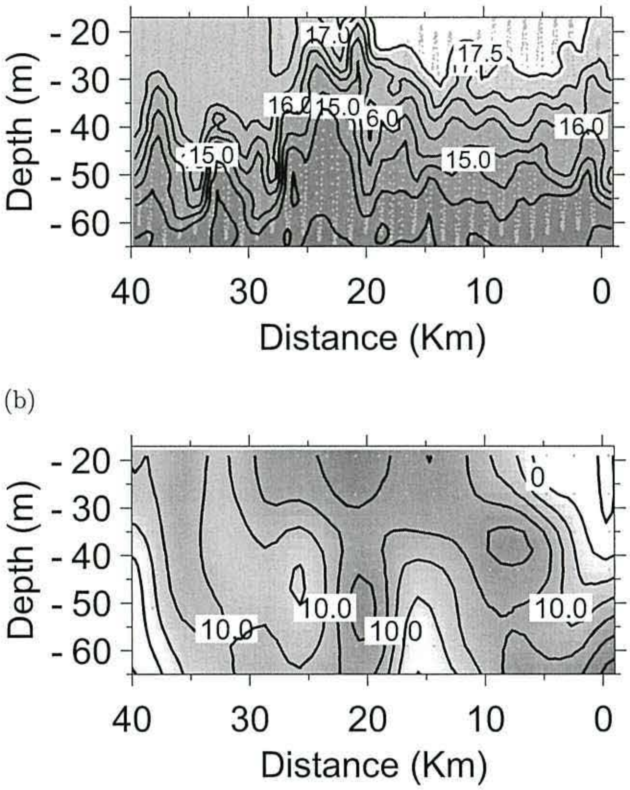

Figure 6.13.: Coincident N section of a) temperature from the UOR and b) along-shelf component (+ve alongshore) from the BB ADCP. The coast local direction is 7.1°W.

transects. Less saline water was encountered over the shelf and was bounded by a strong surface front at the shelf edge. Evidence for upwelling was seen only in the earliest sampled transect S. At deeper levels, isolines separated vertically and an increase in fluorescence along the bottom of the shelf suggested that a bottom Ekman layer associated with poleward flow on the shelf was producing offshore flow down the sloping bottom. A surface warm anomaly with reduced fluorescence levels developed during the cruise, generally inshore of the subsurface salinity maxima. Its western end was associated with a local velocity maximum >10cms^{-1}. The subsurface salinity maximum was invariably present between 20 and 30km offshore of the shelf break at 70-120m depth, although its maximum deepened northwards. Poleward flow was present in all sections both off and on the shelf.

6.4.3 The North Coast

The data presented here were collected between 25 October and 6 November, during a period of variable winds (Fig. 6.6a-b) but strong and steady poleward flow off both the west coast and Cape Finisterre (Fig. 6.6c-d), with surface values >15cms^{-1} at the buoy locations. Underway data in transect PW1 were collected in the north coast on 21 and 22 October but strong swell prevented CTD sampling.

The first CTD sampling of transect PW1 (the easternmost transect in the north coast) on 25-26 October was undertaken before the core of the poleward flow reached the site (Fig 6.5c). The surface values of salinity and temperature (Fig. 6.14a and b) showed no warm anomaly indicative of the poleward intrusion seen in the west coast. A band of low salinity water was measured at -20km inshore of the shelf-break although there was no associated temperature change. However, a surface temperature minimum was located at the shelf break. The subsurface maximum of salinity (Fig. 6.14c) associated with the poleward flow in the west coast was again present in the data although its maximum was weaker (35.8psu instead of 35.9psu in the western coast) and closer to the shelf edge (within 10km) at 100m. The isohalines deepened at the shelf edge, as in previous transects P and N. The salinity maximum (>35.7psu) extended offshore 70km and down to 300m depth. Transects in the west coast did not reach as far offshore and it remains unknown whether a similar distribution, with a clear offshore limit, was present. At the deepest levels (>400m) salinity was relatively high nearshore, but decreased to <35.6psu at 65km offshore. The lowest salinity (<35.3psu) was measured in the near-surface layer above 25-30m, between the shelf-break and 55km offshore. This was probably in response to the brief upwelling favourable winds on 25-26 October and represents offshore advected Ria's water.

The vertical temperature structure (Fig. 6.14d) follows the salinity distribution. Lower temperatures were associated with low salinity at the surface. The subsurface salinity maximum corresponds to locally warmer waters (seen as deepening of the 12°C isotherm) and reduced mixed layer depth in agreement with its southern origin where wind mixing is weaker and near surface stratification stronger. Two cores were

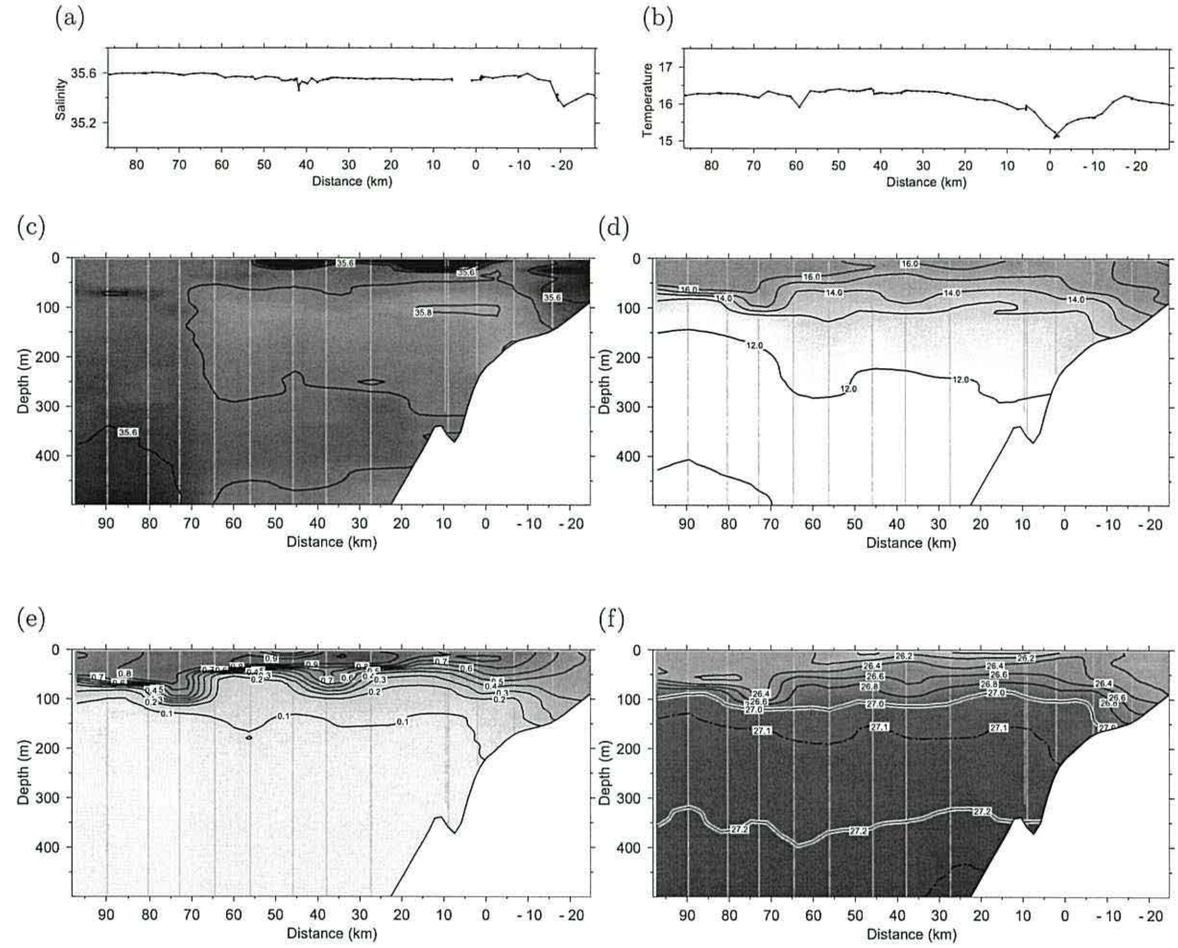

Figure 6.14.: Transect PW1 CTD sections (25-26 October) for a) surface salinity, b)surface temperature, and vertical sections of c) salinity, d) temperature, e) fluorescence and f) density.

apparent in this subsurface warm anomaly at 60 and 10km offshore. The thermocline deepened sharply at the shelf edge reaching the bottom at -15km inshore and a similar vertical gradient was maintained shorewards. At the deepest levels, the offshore low salinity waters were colder than the saltier waters closer to the slope which mark the shallowest levels of Mediterranean water influence.

High surface fluorescence levels (Fig. 6.14e) were measured across the entire section except for the coastal stations inshore of -10km. There, the water was vertically mixed (Fig. 6.14f). No sign of reduced surface fluorescence levels was found in relation to the poleward intrusion in contrast to all west coast sections.

The vertical density distribution (Fig. 6.14f) strongly resembled the temperature structure with deeper mixed layers at either side of the subsurface maximum salinity and steep deepening of the isopycnals at the shelf edge indicative of geostrophic poleward flow.

The evolution of surface salinity and temperature with the measured ADCP sections of PW1 is shown in Fig. 6.15. The weekly composite of SST around the time of the first two crossings (Fig. 6.5b) shows a band of cold water at the location of transect PW1, remnant of previous upwelling events, and indeed a band of cold and salty water was seen in the *in situ* data over the shelf (Fig. 6.15a-b). The coastal band increased in temperature inshore which supports the idea of inactive upwelling. By the third crossing, fresher and warmer water (salinity <35.4psu, temperature >16°C) was established nearshore (20km inshore of the shelf edge). Surface temperature and salinity decreased overall. Changes in the velocity sections (Fig. 6.15c-f) suggest an increase in poleward flow nearshore with flows reaching 30cms^{-1} on the last crossing (Fig. 6.15f). Much of the variability present in the sections (particularly in the across-shore component, but also in the alongshore one) is tidal, but the strength of the flow and its similarities to the hydrography (Fig. 6.14) give support to the presence of a largely barotropic coastal poleward flow.

The next three transects PW2-4, were done consecutively towards Cape Finisterre (Fig. 6.1b) in the presence of downwelling favourable winds (Fig. 6.6). The surface profile consistently displayed uniform salinity offshore ($\sim$ 35.6psu e.g. Fig.6.16a), a weak surface maximum between 10 and 30km off the shelf (Fig. 6.18a), and a minimum of 34.4psu on the shelf (Fig.6.18a). The temperature field was characterised by an across-shore gradient with maximum temperatures nearshore (Figs. 6.16a-6.18a) and no sign of a surface warm anomaly, in contrast to the situation found in the west coast.

The low salinity coastal band (5km inshore of the shelf edge) was vertically homogeneous and extended to the bottom (down to 100m) at the common coastal station in the first two transects (Figs. 6.16-6.17a). It probably came from the three rivers that flow into the Ria of Betanzos (see Fig. 6.1). In transect PW4 it showed lower surface salinity and formed a shallow layer (top 25m). A gradual change in the subsurface salinity maximum was seen in all transects (Figs. 6.16-6.18). As the sections were sampled closer to Cape Finisterre the salinity maximum (delimited by the 35.7psu isohaline) broadened, deepened to 350m depth near the slope, and broached the surface between 5 and 30km off the shelf (Fig. 6.18c). It intersected the bottom 10km either side of the shelf edge. The salinity maximum also increased in value to >35.9psu towards Cape Finisterre becoming shallower from 100m to 65m at 30-20km offshore.

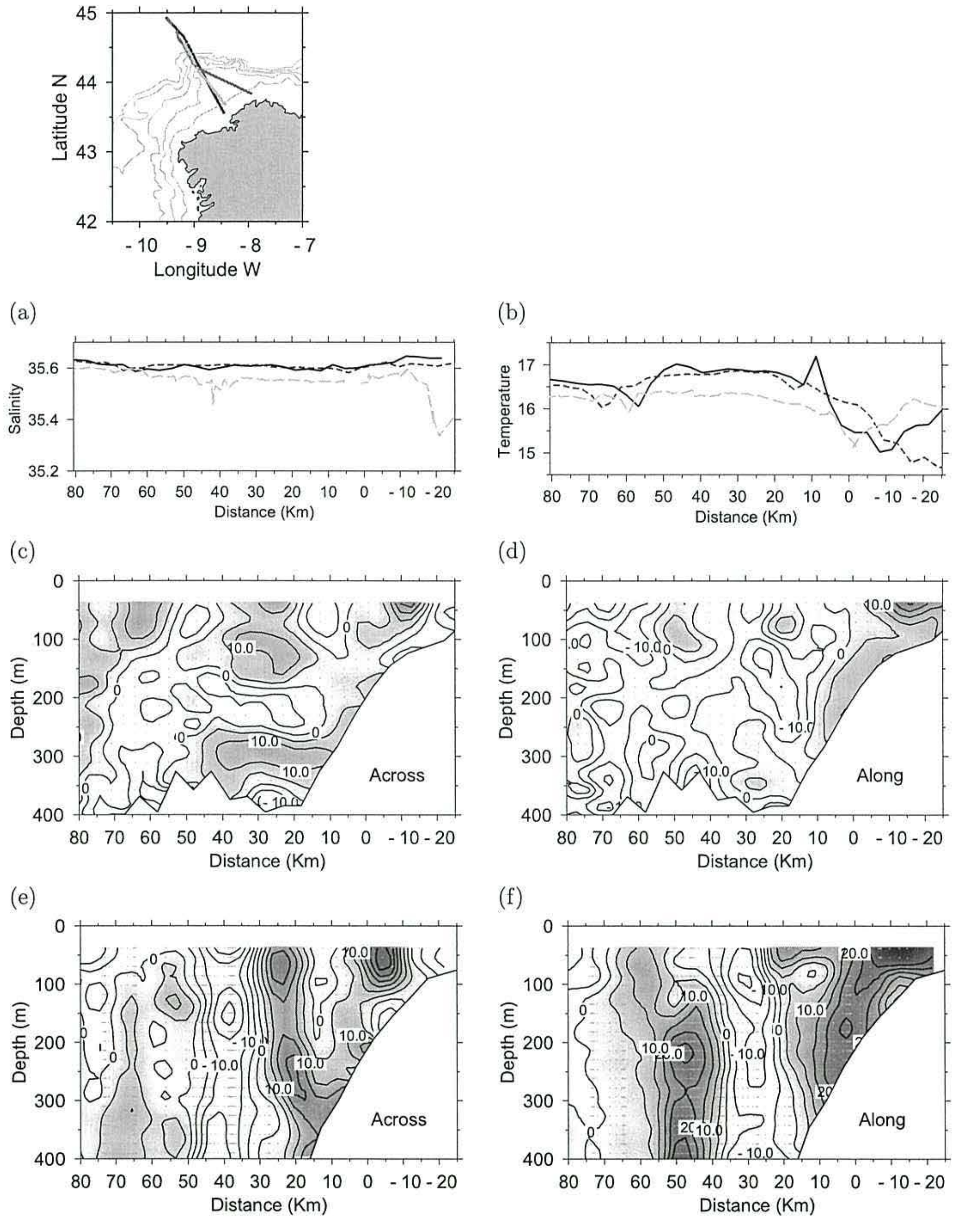

Figure 6.15.: Location of surface realisations of PW1 transect (21-26 October, lighter line colour indicates later crossing) with a) salinity and b) temperature, and first and last vertical sections of rotated velocity components c) along and d) across shelf (21 October), e) along and f) across shelf (25-26 October). The coast local direction is 62°E.

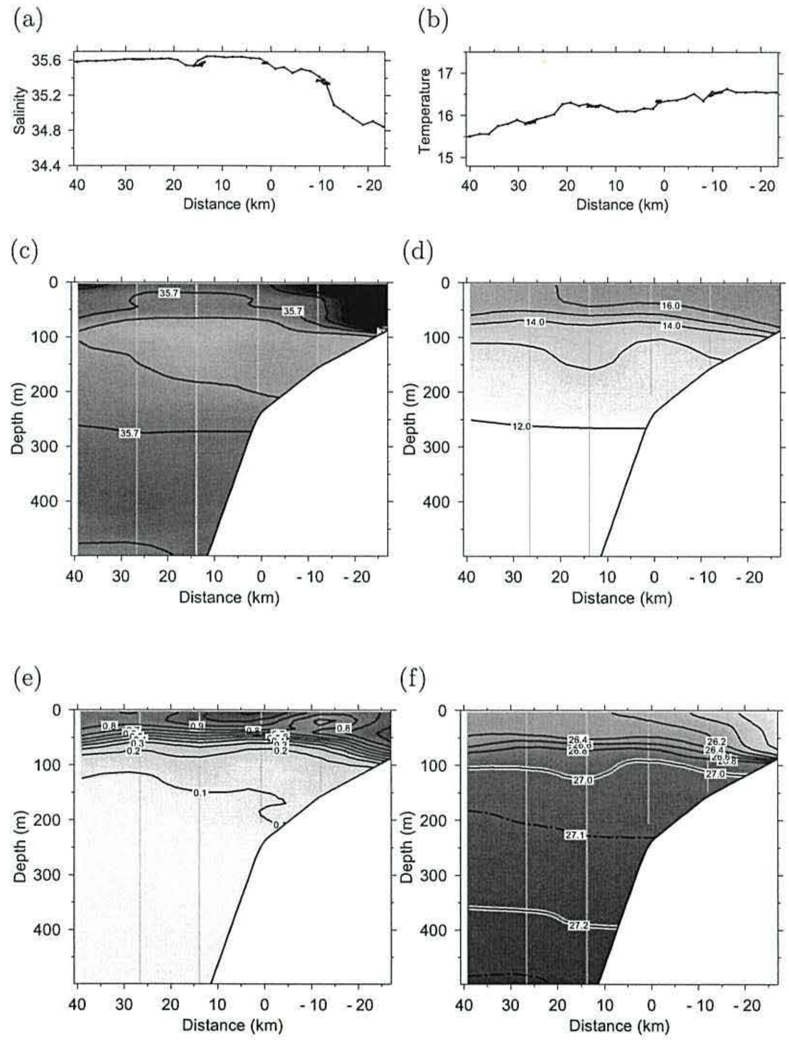

Figure 6.16.: Transect PW2 CTD sections (31 October) for a) surface salinity, b)surface temperature, and vertical sections of c) salinity, d) temperature, e) fluorescence and f) density.

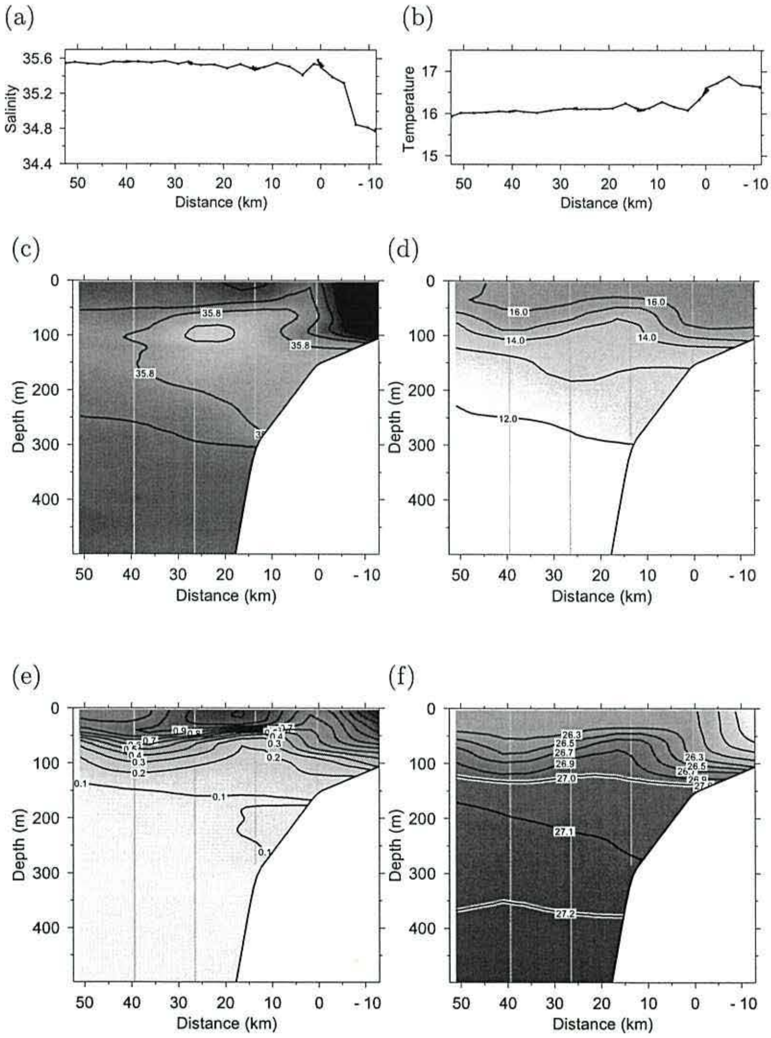

Figure 6.17.: Transect PW3 CTD sections (1 November) for a) surface salinity, b)surface temperature, and vertical sections of c) salinity, d) temperature, e) fluorescence and f) density.

The temperature structure of transects PW2-PW4 showed a weakening of the vertical gradient, seen as wider separation of isotherms associated with the salinity maximum at 20-30km off the shelf (Figs. 6.16d-6.18d). The intrusions were less apparent in the fluorescence distribution. Surface values were relatively high (> 0.7 V) along the entire extension of the sections (Figs. 6.16e-6.18e), but decreased towards Cape Finisterre. A local maximum existed at 10-20km offshore in all sections, in contrast with the west coast transects, and nearshore in PW2 and PW3 (Figs. 6.16e-6.17e). In transects PW3 and PW4, a local minimum existed on the shelf which was more pronounced near Cape Finisterre (Fig. 6.18e). The density distribution (Figs. 6.16f-6.18f) also showed vertical separation of isopycnals at the salinity maximum, particularly in transects PW3 and PW4, and lower density associated with the coastal freshwater band similar to PW1. They all suggested geostrophic poleward flow on the shelf and between 100-300m, at which depth the isopycnals deepened towards the slope (Figs. 6.17-6.18f).

The averaged velocity structure for transects PW2-PW4 (Fig. 6.19) shows fundamental differences with the west coast transects. The across-shelf component (Fig. 6.19a) was offshore weak throughout ($<7.5 cms^{-1}$) except for a weak onshore narrow area on the shelf edge. The along-shelf component lacked the double core structure of the west coast. Instead, coastally trapped along-shelf flow was in the poleward sense at all levels, resembling the area of salinity larger than 35.8 of Fig. 6.17c. Inshore, a strong baroclinic poleward jet ($>30 cms^{-1}$) was associated with the salinity front at the shelf edge.

The last three days of the cruise were dedicated to a short Lagrangian experiment during 3 14:17-6 11:27 November. A buoy drogued at 100m with a cruciform sail was placed at the centre of the poleward flow at 25km offshore coincident with the offshore salinity maximum of transect PW3 (Fig. 6.17c, see Fig. 6.1b for the location of the CTD stations during the drift, D in the graph). The buoy was followed as it covered, approximately, the distance between transects PW3 and PW2. Both ADCP's performed well, yielding data down to their maximum penetration depth, 250m and

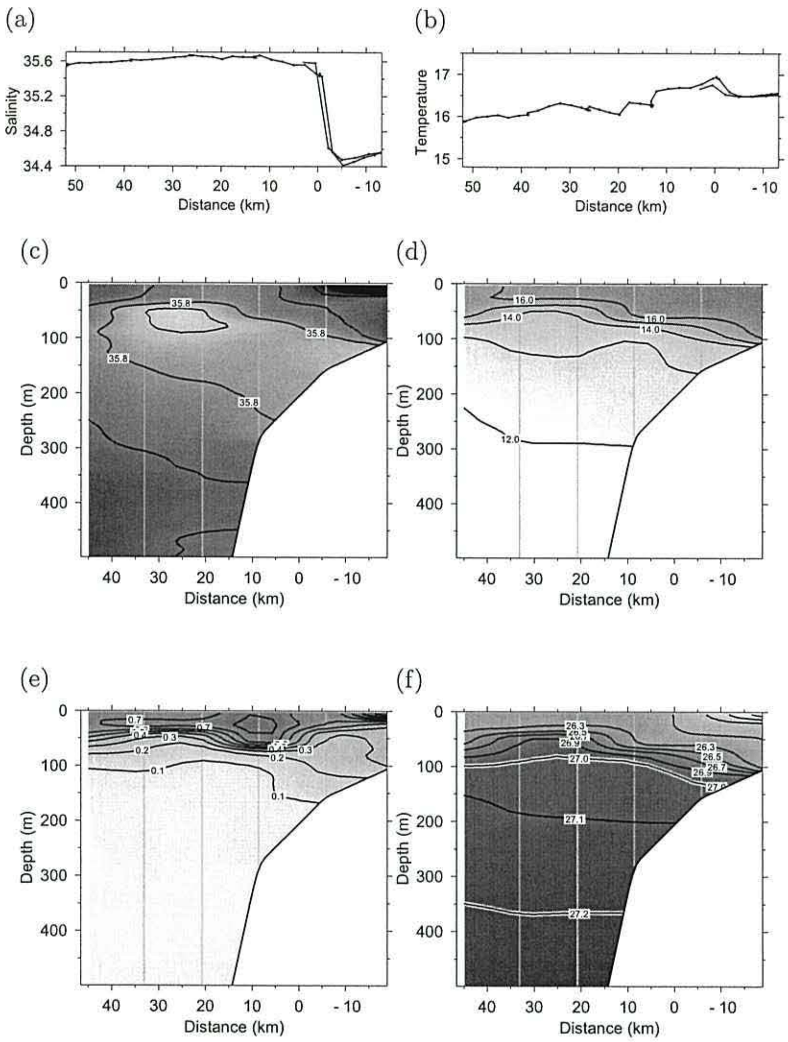

Figure 6.18.: Transect PW4 CTD sections (2 November) for a) surface salinity, b)surface temperature, and vertical sections of c) salinity, d) temperature, e) fluorescence and f) density.

650m for the BB and NB respectively. Mean velocity profiles, rotated to along and across-shelf components, during the drift and temperature and salinity profiles for the first and last CTD casts are shown in figure 6.20. The velocity profiles (Fig. 6.20a) show continuous poleward flow at all depths. Maximum discrepancy between the two instruments at their common depth range was less than 1cms^{-1} at depths of rapid change. The across-shelf component (with values <4cms^{-1} throughout) suggests a three layer structure. The top 200m corresponds to a strongly sheared poleward flow with an offshore tendency (with respect to the large scale shelf-edge orientation on the north coast). Maximum poleward flow (15cms^{-1}) was measured below the

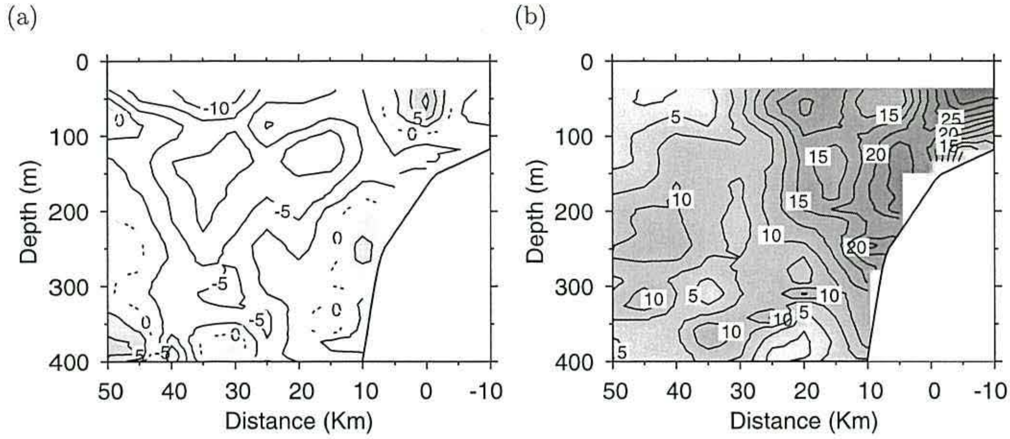

Figure 6.19.: NB ADCP section averages of transects PW2-PW4, a) across-shelf component (+ve onshore) and b) along-shelf component (+ve) alongshore. The coast local direction is 62°E.

thermocline (Fig. 6.20b) at 65m decreasing almost linearly to 8cms^{-1} at 150m. Along-shelf poleward flow with near zero across-shelf component can be seen in the layer between 200m and 400m. The along-shelf component decreased linearly from 9cms^{-1} to 7cms^{-1}. Below that, between 400m and 550m, weak, slightly offshore poleward flow was again present.

The three layer velocity structure is less clear in the temperature and salinity profiles during the drift, showing no obvious correspondence (Fig. 6.20b). The top layer roughly corresponds to the salinity maximum, which thickened towards the end of the drift to reach 150m, where a sharp decrease in salinity (0.08psu) marks its lower limit. The intermediate layer was characterised by a linearly decreasing salinity and temperature layer, which showed no differences at the start and end of the drift. Below 350m, the largest differences between the first and last CTD of the drift were measured, with both salinity and temperature decreasing.

6.4.4 Watermass analysis

T/S characteristics for the cruise from surface to 500m are summarized in Fig. 6.21. Selected casts from offshore positions outside the poleward flow (red and orange) represent the background oceanic conditions. They show an increased proportion

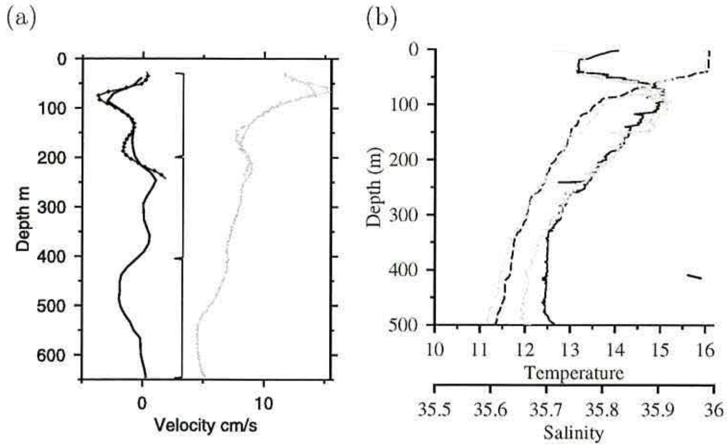

Figure 6.20.: a) Mean profile of along-shore (grey) and across-shore (black) components during the drift experiment on 3 14:17-6 11:27 November for both the BB (circles) and NB (solid) ADCP. The three layers referred to in the text are shown. b) temperature (dashed) and salinity (solid) for the first (black) and last (grey) CTD of the drift.

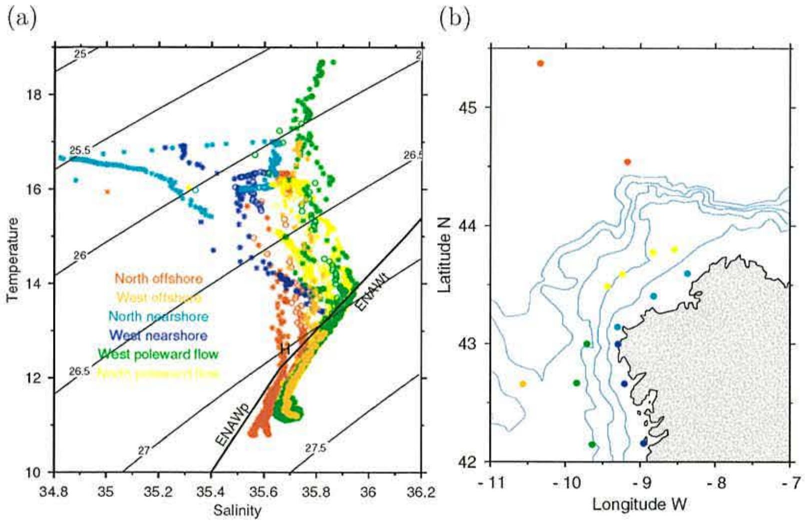

Figure 6.21.: a)T/S diagram between surface and 500m of representative sub-regions (offshore, coastal and poleward flow) encountered during the cruise on the west and north coasts. The regions are color coded as shown in the graph. Circles correspond to the northernmost CTD cast within each group and asterisks to the southernmost. b) Position of CTD casts with the same color code as a).

of $ENAW_P$ with respect to the poleward flow casts (green and yellow) but no consistent differences can be drawn with respect to their latitude or proximity to the slope (the differences between the two northernmost offshore casts (red) were the largest). Above the central water definition lines, salinity was uniform and no sign of subsurface salinity maximum was found. It is worth noting that the central waters T/S relationships were shifted towards higher salinity or lower temperature compared to the ENAW reference line [*Ríos et al.*, 1992]. Similar variability in the region has been linked to decadal changes in the $\mathrm{ENAW_P}$ ventilation conditions [*Pérez et al.*, 1995; *Pollard et al.*, 1996] and evidence suggest that the changes are a large scale phenomenon [*Huthnance et al.*, 2002]. The poleward flow casts had a larger proportion of $\mathrm{ENAW_T}$ as expected from its northward advection and a relatively well defined subsurface salinity maximum on the $\mathrm{ENAW_T}$ definition line. The subsurface salinity maximum shows similar range at both the west and north coasts as expected from the developing stages of the poleward flow regime. On the north coast, higher values were encountered near Cape Finisterre decreasing polewards (eastwards) reflecting the southern source area at this developing stage. Surface T/S characteristics away from strong freshwater influences were very similar among nearshore, offshore and poleward flow stations which clustered between 35.5-35.7psu and 15.5-16.5°C. The nearshore stations (blue and cyan) showed influences of freshwater origin ranging from thin freshwater plumes to vertically mixed shelf-freshwater waters as described in previous sections.

6.5 Discussion

Slope poleward flows are ubiquitous along the entire western European shelf during at least part of the year. Remotely sensed SST [e.g. *Pingree and LeCann*, 1990], Lagrangian [e.g. *Van Aken*, 2002; *Pingree*, 1993] and modelling studies [e.g. *Coelho et al.*, 2002; *New et al.*, 2001], all suggest a continuous flow originating in the Portuguese coast and ending in the Norwegian coast. In the Iberian Peninsula, the poleward slope current has a strong seasonality with maximum flow in winter, reversing to southward flow during the summer [e.g. *Haynes and Barton*, 1990; *Huthnance et al.*, 2002]. North of Spain, seasonal variations in the flow decrease with latitude, with current reversals in February-April as far north as the Porcupine Bank, north of the Celtic Shelf [*Pingree and LeCann*, 1990]; but in the Hebridean Shelf off Scotland, the flow only weakens during the summer and does not reverse [*Souza et al.*, 2001]. Maximum but more variable poleward flow occurs during winter in response to stronger winds.

In this chapter, data from the early stages of the slope current development in autumn have been presented. Favourable winds before the start of the cruise maintained weak upwelling in a nearshore band in the west coast and over a broader area off the north coast, as seen in SST images (Fig. 6.5a). Winds were downwelling favourable during the first half of the cruise and variable during the remainder of the cruise. Downwelling winds are expected to force poleward currents nearshore (see also Chapter 4). *Vitorino et al.* [2002] showed that surface and bottom currents at 41.3°N in mid-shelf were highly correlated to winds, which they lagged by 6h. The expected poleward wind driven currents on the west coast shelf were enhanced by the vertical mixing of the low salinity upper layer in the inner shelf. The increase in vertical mixing is evident in transects S, P and N during the downwelling winds, where the surface layer depth increased from 25m to 50m, and reached 100m in the north coast. There, the thermocline, which occurred between 50m and 80m depth off the shelf, intersected the upper slope topography as a bottom front, inducing poleward geostrophic flow. In response to both direct wind forcing, through momentum transfer and sea level elevation at the coast as a result of onshore Ekman transport associated with the downwelling winds, and the fore-mentioned wind mixing induced geostrophic flow, poleward velocity increased over the shelf during the cruise. Velocity less than 2.5cms^{-1} in the first transect S (Fig. 6.8d), increased to values larger than 25cms^{-1} in the final one (Fig. 6.19d). Similar velocities were found by *Vitorino et al.* [2002], who measured northward velocities of about 20-30cms^{-1} in the northern Portuguese shelf during winter, and *Haynes and Barton* [1990] who measured northward velocities at 100m depth of $\sim$20cms^{-1} at 42.8°N in September 1986.

The SST images at the time of the cruise showed a meridional SST gradient around 42°N which turned northwards at the slope forming a warm tongue that progressed northwards as in *Haynes and Barton* [1990]. The meridional SST gradient near 42°N is a common feature of the early downwelling regime (see for example Fig. 3.3c) and has an associated salinity gradient as shown here. Modelling studies of *Du-*

bert [1998] showed that poleward flowing surface warm intrusions are generated over 10 days during the adjustment of a meridional density gradient to the slope topography in western Iberia. Here similar results are apparent. The meridional SST gradient (Fig 6.5) moved towards the shelf edge in response to downwelling winds, and in five days, it developed a surface warm anomaly that strengthened and progressed northwards during the cruise, serving as a surface tracer for the slope poleward flow. The detailed temperature structure at transect N showed the warm anomaly was restricted to the top 30m and was approximately 20km wide, close to the climatological Rossby radius of deformation calculated as $R' = HN/f$, where H is the thickness of the stratified upper layer, N is the mean Brunt-Väisälä buoyancy frequency for that layer, and f is the Coriolis parameter, [*Chelton et al.*, 1998]. Raw velocity data indicated enhanced poleward flow in its offshore limit to at least 65m depth related to down-sloping isotherms, an indication of geostrophic flow. The warm, low fluorescence surface anomaly was wider in the north coast with the expansion of the poleward flow onto the shelf as discussed previously. No indication of reduced fluorescence was apparent in the *in situ* data for the north coast, which suggests that the initial narrow tongue did not reach further than Cape Finisterre or was mixed by the wind. The SeaWifs image of the region after the cruise (9 November, Fig. 6.22) shows a narrow tongue of low estimated chlorophyll parallel to the west coast slope that failed to round Cape Finisterre. The SST images of the last portion of the cruise showed a narrow warm tongue along the north coast shelf edge and on the shelf rather than on the slope, being advected poleward by wind driven and geostrophic flow described above.

The subsurface salinity maximum near the slope has been used as a slope poleward flow tracer for some time now [e.g. *Frouin et al.*, 1990; *Hill and Mitchelson-Jacob*, 1993; *Souza et al.*, 2001], as it diminishes in value and deepens northwards. The vertical structure of the salinity found during the present cruise resembles the data presented by *Frouin et al.* [1990], where a salinity maximum >35.9psu at 41.8°N, 36km off the shelf decreased to <35.8psu at 55km. The Rossby radius of deformation ranged from 15km to 20km at the time. In the present data, a poleward flow maximum was

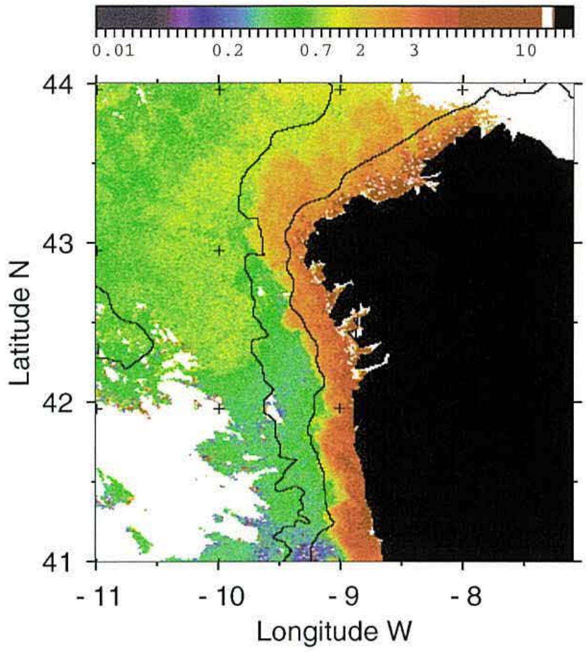

Figure 6.22.: Chlorophyll derived values from Seawifs data for 8 November 1999. A low chlorophyll tongue can be seen parallel to the shelf edge on the west coast of Galicia failing to round Cape Finisterre. Clouds are masked white.

generally associated with the offshore limit of the warm anomaly in the west coast and the subsurface salinity maximum between 50m and 100m depth and 20-30km off the shelf in the north coast. The Rossby radius of deformation ranged from 10-15Km for H=150m, to 25-30Km for H=500m. The latter values agreed with the climatological ones derived by *Chelton et al.* [1998]. The subsurface salinity maximum was better defined in the north coast, when surface current vectors from the buoys showed a steadier poleward current (Fig. 6.6c-d), and was located between 20-30Km off the shelf (see Figs. 6.16c-6.18c) in agreement with the Rossby radius of deformation estimate. A good agreement between the subsurface poleward velocity maximum location and R' was also found by *Pierce et al.* [2000] along the entire mid-latitude eastern boundary of the North Pacific from 34°N to 51°N. Its width was also similar to R'.

The averaging of the sections can not be expected to fully eliminate the oscillatory variability of tides and inertial waves but the agreement between maximum poleward flows in the averaged sections and the mean profile during the 3 and half day's drift

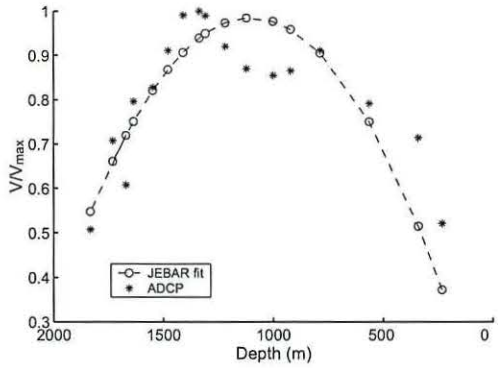

Figure 6.23.: Jebar fit following Eq. 6.5 to the depth-averaged velocity of all sections normalised by the section maximum velocity. No data shallower than 200m is presented. The ADCP data was gridded every 2.5Km and 16m in the horizontal and vertical.

experiment gives support to the results. A least square fit of the drift data to the semidiurnal tide and inertial frequencies gives an indication of the strength of the main oscillatory flows. The amplitude associated with the semidiurnal tide was in the range of 5 to 7cms^{-1} orientated mostly parallel to the shelf while inertial flows were larger (amplitude of 10cms^{-1}) and surface intensified in the top 150m. *Fanjul et al.* [1997] modelled large variability in the tidal currents due to the complex topography of Galicia with the V (or alongshore) component increasing offshore of the capes and the U (or crosshore) increasing in the lee (northward of the cape) thus divergence terms are likely to be large and possibly tidal rectification. The mean along-shore profile during the drift showed poleward flow larger than 5cms^{-1} at all depths and suggests a continuous poleward flow from surface to MIW levels. A subsurface maximum poleward flow was coincident with the subsurface salinity maximum, although it could be a result of the non zero average of the surface intensified inertial currents. Northward advection of warmer and saltier waters from the west coast may explain the increased separation in isotherms at that level during the short drift experiment.

As mentioned in the introduction, JEBAR is a good candidate for forcing the slope current. It was introduced by *Sarkisyan and Ivanov* [1971], who derived a balance between the along-slope density gradient and surface slope in the absence of depth averaged cross-slope transport and friction as,

$$\frac{\partial \eta}{\partial y} = -\frac{1 H \partial \rho}{2 \overline{\rho} \partial y}, \tag{6.4}$$

where η is the surface height, H is depth, and ρ is density with $\overline{\rho}$ being a mean oceanic density reference. Equation 6.4 shows that the along-shore decline is greatest in deep water for a given meridional density gradient. *Huthnance* [1984] followed the argument further by deriving the cross-slope structure of a slope poleward flow forced by the interaction between the along-isobath density gradient and bathymetry along a narrow slope. The depth-averaged along-slope velocity component results from the balance of the longitudinal density gradient, the bottom topography and friction in the form:

$$V(x) = \frac{g}{2k\overline{\rho}} \frac{\partial \rho}{\partial y} h(x)(H - h(x)) \tag{6.5}$$

where V is the along-slope velocity component, k is a bottom drag coefficient, g is the gravitational acceleration, $h(x)$ is the local depth and H is the abyssal depth where the JEBAR tends to zero. Equation 6.5 can be used to diagnose the possibility of JEBAR forcing the poleward flow [*Souza et al.*, 2001]. The least square fit of the depth-averaged velocities from all sections normalised by the sectional maximum against $h(x)(H - h(x))$ (Eq. 6.5) showed a good fit (Fig. 6.23). The data covered the slope from the shelf-edge to 40km offshore. The abyssal depth that optimised the fit was 2100m, which is deeper than the 1100-1600m found by *Souza et al.* [2001]. From Eq. 6.5, a maximum velocity of $\sim$10cms^{-1} between 15-30km offshore, was obtained, which compared well with the measured depth-averaged velocity of $\sim$8cms^{-1}. The gradient term $h/\rho \times \partial\rho/\partial y$ estimated from the least square fit was in the order of $\sim 10^{-7}$ in agreement with results from *Souza et al.* [2001] and *Huthnance* [1984]. Numerical experiments from *Dubert* [1998] showed that a broad density gradient could indeed force a slope poleward flow and identified the JEBAR mechanism as the main forcing.

The presence and maintenance of the meridional density gradient in the western Iberian coast can be related to both the poleward cooling of the sea and features of the large scale circulation in the region. The large scale circulation offshore the Iberian

Peninsula is weak; dominated by the southward flowing Portugal Current ([Chapter 2 *Saunders*, 1982]) and eastward transport along the Portuguese-Spanish Atlantic coast. Eastward transport is more prominent south of 40°N and has been related to an eastward flowing branch of the Azores current [*Käse and Siedler*, 1982; *Pollard and Pu*, 1985] transporting $\mathrm{ENAW_T}$ [*Ríos et al.*, 1992]. At that latitude, both currents converge, helping to maintain and enhance the meridional density front. Evidence for this is somewhat circumstantial. Numerical experiments by *Dubert* [1998] with a broad density gradient similar to the one observed by *Mazé et al.* [1997] failed to reproduce the frontal instabilities and eddies observed in the region by *Vitorino* [1995]. The associated geostrophic depth-integrated eastward transport was estimated by *Mazé et al.* [1997] as 2Sv between 37.2°N and 43°N. The sharper gradient sampled by *Vitorino* [1995], of the order of 100km instead of the 600km measured by *Mazé et al.* [1997], had similar associated eastward transport. *Dubert* [1998] found that the associated eddies provided another mechanism that helped maintain this smaller scale front, also suggested by *Spall* [1997]. The associated transport entrains the poleward slope current and accounts for the increase proportion of $\mathrm{ENAW_T}$ with respect to surrounding waters, also noted by *Frouin et al.* [1990]. Numerical experiments with both the large and small scale meridional density gradients by *Dubert* [1998] produced a slope poleward flow provided the onshore transport was of similar magnitude.

Few transport estimates are available for the slope poleward flow for the Iberian region with a large variability due in part to the different depths and offshore extent of integrations. *Jorge da Silva* [1996] in *Huthnance et al.* [2002] calculated integrated geostrophic transports from the shelf edge to the outer limit of the slope current down to 550dbar which ranged from 5.7Sv at 37.25°N to 4.3 at 43°N. Northward decrease in transport is consistent with topographic steering, including deflection around the Galician Bank [see Fig. 2.1 for location, *Coelho et al.*, 2002]. Mean alongshore transport estimated from the ADCP sections was smaller, 2±0.5Sv, calculated from the shelf edge to 40km offshore and from 35m to 500m depth, possibly related to the early stages of the poleward flow development.

6.6 Conclusions

A combination of *in situ* and remotely sensed data have showed the first stages of development of the slope poleward flow in the Galician region.

- Slope poleward flow can be identified in SST as a warm anomaly effectively acting as a tracer.
- Poleward flow extends onto the shelf and is intensified due to the wind induced sea level slope, mixing of the water column and formation of a bottom front, and direct transfer of momentum. Its associated mean poleward transport was 2±0.5Sv.
- Over the slope, poleward flow structure as depicted from the mean of the sections conform to JEBAR forcing and the order of magnitude of the estimated meridional density gradient agrees with previous data.
- Subsurface maximum poleward flow was associated with the salinity maximum at an off the shelf distance in agreement with the Rossby radius of deformation.
- The salinity maximum was better defined in the north coast at the time of steadier poleward flow reflecting the late stages of its development.
- Poleward flow was continuous to the maximum penetration depth of the ADCP, 650m, and could reach the level of MIW.
- Poleward flow at the MIW level and at the subsurface maximum arise from different dynamical reasons but can form a continuous flow inducing topographic guidance of the surface flow.
- This becomes particularly relevant when the poleward flow reaches Cape Finisterre, where both, continental slope and SST anomaly broaden.

CHAPTER

7 Drifter analysis

7.1 Introduction

While previous chapters provided information about the shelf circulation in small quasi-synoptic time scales, this chapter will focus on the Lagrangian observations of the regional behaviour of mixed-layer drifters. The study of the upper layer circulation with surface mixed-layer drifters has become a very attractive option due to its broad scaling sampling capabilities and low cost. As they inherently average over space and time, they are well suited for measuring the large-scale, low-frequency field that produces the diffusive transport. Nonetheless, drifters are "quasi-Lagrangian" because they can not follow vertical displacements. This becomes particularly relevant in the presence of flow inhomogeneities.

Mixed-layer drifters have been successfully used to track the complex mesoscale circulation associated with Eastern Upwelling Systems [*Brink et al.*, 1991, 2000]. In the California Upwelling System their capability to follow jets associated with upper layer fronts has been demonstrated [e.g. *Swenson et al.*, 1992]. They have also been useful in the study of upper flow dynamics [e.g. *Flament and Armi*, 2000] and even high frequency motions like the upper layer inertial response to wind forcing [*Poulain*, 1990]. Lagrangian statistics from drifters have also proved important in evaluating model performance at large scales [*McClean et al.*, 2002].

The large volume of drifter data collected to date has enabled the development of statistical techniques to estimate horizontal mixing coefficients from drifters [e.g.

Colin de Verdière, 1983; *Davis*, 1985]. These studies have helped characterize the diffusive properties of oceanic regions and to validate the representation of oceanic mixing in numerical models. Estimates have ranged from basin scale studies [e.g. *Fratantoni*, 2001] to more regional studies [*Dever et al.*, 1998; *Poulain*, 2001].

The diffusive properties of the drifters can be related to the scales of motion of the random velocity field [*Swenson and Niiler*, 1996] and can be used to evaluate the predominant mesoscale field that distributes energy, momentum and heat. *Davis* [1985] showed that large open ocean mesoscale eddies (with Lagrangian space and time scales of L$\sim$50-100 km and T$\sim$10 days) displayed larger horizontal diffusivities (K$\sim$ $10^7 cm^2s^{-1}$) than the smaller coastal eddies (L$\sim$30 km, T$\sim$1-2 days and K$\sim$ $10^{4-6} cm^2s^{-1}$).

Previous mixed-layer drifter deployments in the present study area included those described by *Haynes and Barton* [1991] and during the MORENA EU project [*Martins et al.*, 2002]. They focused on the setup and evolution of the winter poleward flow (e.g. Chapter 6) while here, two contrasting seasonal regimes are compared. Other drifter releases in the region have concentrated in the seeding and tracking of swoddies (Slope Water Oceanic Eddies) [*Pingree and LeCann*, 1992a] or have studied deeper levels [*Paillet et al.*, 2002].

A quantitative description of the regional Lagrangian statistics and their seasonal variability within the Galician region is provided by 2 sets of 4 satellite tracked drifters released in the OMEX area in August of 1998 ("summer deployment") and January 1999 ("winter deployment"). The exact deployment date and location are summarised in table 7.1. The total number of drifter days was 822 (478 during the "summer deployment" and 344 for the "winter" one). This is the first time diffusivity estimates have been calculated during the Iberian upwelling regime even if with a limited number of drifters.

	Launch			End of Record			
I.D.	Date	Latitude	Longitude	Date	Latitude	Longitude	Days
10312	12/08/98	41°58.31	9°47.06	05/03/99	38°00.50	12°28.68	205
10313	12/08/98	41°53.83	9°47.29	25/11/98	41°50.34	10°49.20	103
10314	12/08/98	41°53.82	9°52.89	05/12/98	36°59.4	13°29.94	110
10315	12/08/98	41°58.71	9°53.10	13/10/98	40°23.10	12°12.06	60
4010	02/01/99	40°59.97	9°24.86	17/05/99	38°43.50	9°36.90	134
3924	02/01/99	40°59.98	9°27.72	17/05/99	38°00.24	10°48.36	82
4558	02/01/99	41°01.85	9°27.83	08/04/99	39°21.18	9°22.62	95
3923	02/01/99	41°01.91	9°25.37	05/02/99	42°54.36	9°15.66	33

Table 7.1
: Summary of each of the drifters releases. Latitude in degrees North and Longitude in degrees West.

7.2 Data and methods

All drifters deployed for this study carried a Holey-sock drogue at a nominal depth of 15m (Fig 7.1) as described in Chapter 5. The subsurface buoyancy provides decorrelation of the surface float from surface wave induced high frequency motion in the drogue, and allows the satellite transmitter to remain above the surface water. The transmitter was different in the two deployments. In the "summer" release cylindrical Horizon Marine Inc units were used while spherical SERPE-IESM transmitters were used during the "winter" release. Both configurations were tracked through the ARGOS system yielding 6-8 fixes a day (Fig. 7.2). The ARGOS positioning system supplies an accuracy flag divided in 4 classes, 0, 1, 2 and 3. The first class has no upper limit in its accuracy so they were removed from the data. Classes 1, 2 and 3 correspond to accuracies of 1000-350m, 350-150m and less than 150m respectively. Typical examples for one "summer" and one "winter" drifter are presented in Fig 7.2 as 5 day bins histograms. Global average percentages were 39%, 43% and 18% for classes 1, 2 and 3. There were indications of a larger number fixes during the "winter" deployment than the "summer" one probably related to the larger floatability of the SERPE-IESM spherical drifter.

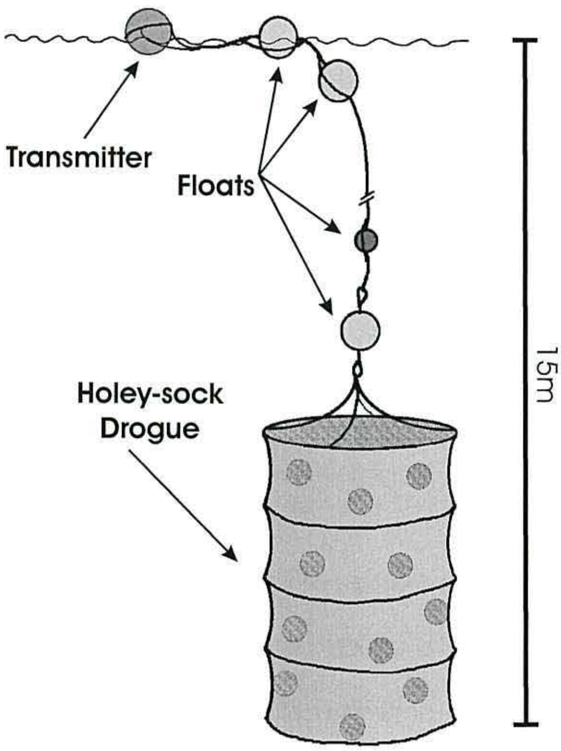

Figure 7.1.: Standard drifter design used in this work. The spherical transmitter corresponds to the SERPE-IESM model.

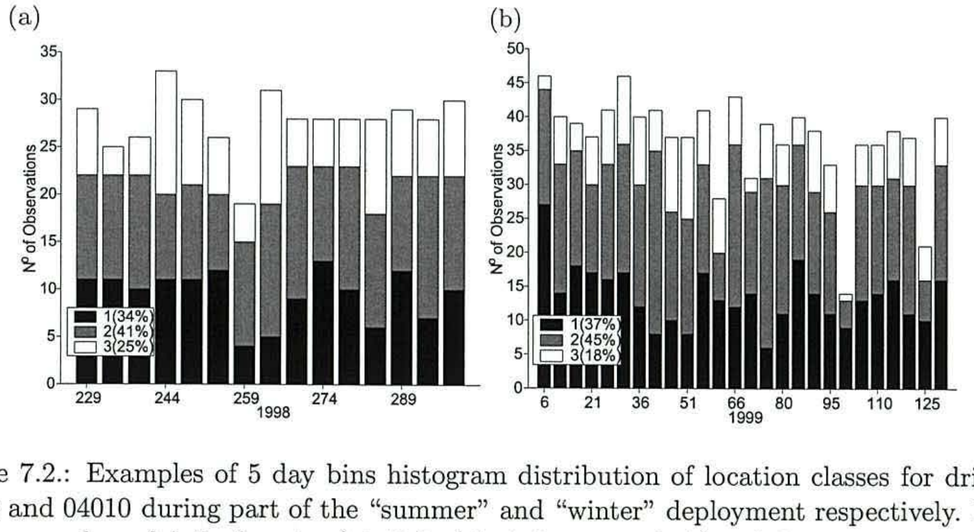

Figure 7.2.: Examples of 5 day bins histogram distribution of location classes for drifters 10312 and 04010 during part of the "summer" and "winter" deployment respectively. Note average number of daily fixes in a) is 5-6 while it increases in b) to 7-8.

All drifters were screened for evidence of drogue loss through a sustained increase in the velocity variance of the raw data similar to *Burrows and Thorpe* [1999] and none were found. In fact, two "winter" drifters (I.D. 3923 and 4558) grounded after 95 and 33 days respectively and both were recovered with the drogue still attached.

All drifter data have been regularly interpolated to 1 hour intervals with a cubic spline (NAG routines E01BAF and E02BBF). Gaps larger than 6 hours were linearly interpolated prior to the use of the cubic spline. Velocity estimates were generated by taking the first derivative of the cubic-spline. The data were then filtered with a 60+1+60 Cosine-Lanczos filter with a half power point at 40hours and subsampled at 6 hours intervals [*Haynes and Barton*, 1991]. This way, the data were efficiently removed of any periodicity with a timescale shorter than 40 hours (tidal and inertial currents, Fig 7.3), hence avoiding aliasing the energy into the low frequency motions that are of primary interest here. Nevertheless, frequency analysis of the drifter data set showed the inertial-band wave energy at this latitude range to be generally low. Complex demodulation of the velocity time series around the inertial frequency yielded amplitudes in the order of 2-5cms^{-1}, smaller than the velocities associated with the structures responsible for the residual flow, such as upwelling front-filaments (20-35cms^{-1}) or the winter poleward flow (15-25cms^{-1}). Similarly, in other regions situated at the same latitude, e.g. in the California Current, the inertial band energy is at least 1 order of magnitude less than the energy of low-frequency motions [*Swenson and Niiler*, 1996].

7.2.1 The Summer deployment

In the summer deployment (Fig 7.4), the four drifters were released on 12 August 1998 in a cluster of 5nm side square in the core of an upwelling filament previously identified from SST images (see Chapter 5). Minimum tracking was 60 days, totaling 420 drifter days (Table 7.1).

The summer period was a good representation of the upwelling system with fully developed filaments and a broad band of upwelled water extending beyond the shelf

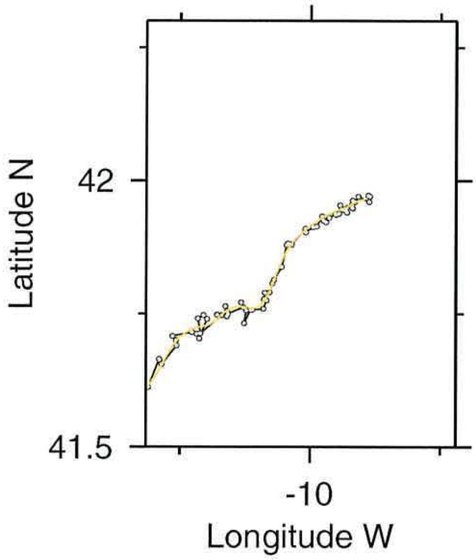

Figure 7.3.: Filtered and raw data of drifter 10312 during the first 10 days of deployment.

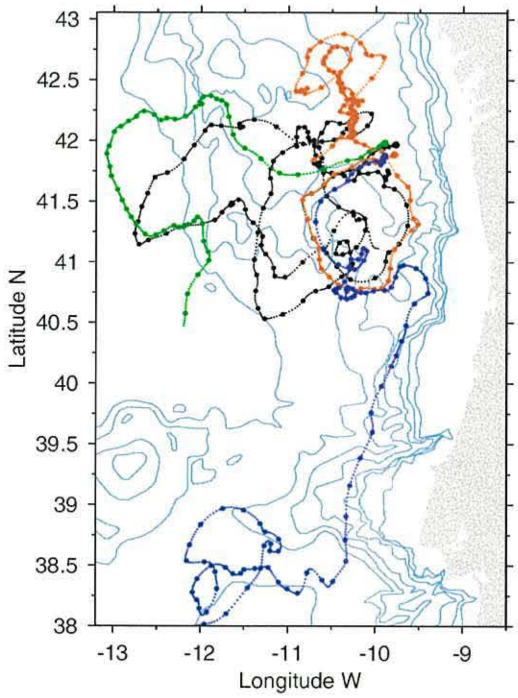

Figure 7.4.: Summer deployment drifter tracks. Solid dots indicate days. The minimum duration of the tracking was 60 days (green drifter). Only data before the end of 1998 are shown corresponding to 420 drifter days.

($\sim$100km from the coast, see Fig. 5.14a). Three filaments were present at the time of the deployment. The 42°N filament is the most persistent one and reappears in the same location every year. The northern most filament at 43°N was growing at the time but faded away shortly after the cruise. The southern 41°N filament was highly variable and underwent shifts in its location that hindered its development. Overall, the drifters responded to the changes of the system, slowing during a period of slack winds and speeding up with increasing winds. Although filaments are expected to be paths for exchange between shelf and open ocean only one drifter traced the offshore extent of the SST signature of the 42°N filament and stayed offshore for 45 days prior to the end of its transmission. The other drifters stayed in the filament core before eventually crossing the filament southern boundary to flow in an eddy like return flow onto the slope with an average velocity of $0.17 \pm 0.07 cms^{-1}$, which is of similar order to the filament velocities. One then moved south along the shelf break at a speed of 0.21 ± 0.08 cms^{-1}. This southward flow was related to the unusual extension of the upwelling season into the autumn months. It left the shelf again near Cape Roca, a well known site of filaments. The other two drifters stayed near their original latitude of release with offshore excursions of $\sim$100km before ending their transmission within 100km of the coast.

In summary, the strongest flows were associated with the offshore filament and the upwelling related slope southward flow. The overall picture for the summer deployment is hence that of a rich mesoscale field which actively links the shelf and the open ocean at a large variety of time scales but with no clear net transport.

7.2.2 Winter deployment

In winter, westerly or southwesterly winds and northward flow at the slope like that described in Chapter 6 are expected but exceptional weather gave conditions similar to summer, therefore upwelling favourable. This situation was the norm rather than the exception for the winter of 1999 as shown by weekly averaged SST images spanning February-May 1999 (Fig 7.5). No sustained poleward flow development was evident in the SST during this period. Instead, a semi-permanent coastal band of upwelled waters was identifiable in the images. The only period of indicated poleward flow occurred during and immediately after the winter deployment.

Overall, the winter deployment, made on 2 January 1999, showed a remarkably different picture from the expected winter circulation. Again the four drifters were released in a cluster of 5nm side square but this time over the slope (1000m depth). Minimum tracking duration was 25 days for the drifter which grounded south of Finisterre. The data amount to 400 drifter days.

The typical poleward flow over the slope described in Chapter 6 was only present during early January (Fig 7.6). The drifters, in the period 2-10 January moved northward following the bathymetry in a warm tongue seen in SST image of 6 January (Fig 7.6). Velocity estimates from the drifter positions give a mean value of 0.27 ± 0.08 m/s similar to the highest ADCP near surface velocity measured during the winter cruise (Chapter 6). Surface isobaric pressure charts for 11 January showed the onset of northerly winds and the drifters ceased their northward motion. The warm slope anomaly structure weakened during January as seen in SST images but was nonetheless present until the end of January. The rest of the winter deployment (Fig 7.7) saw a net southward flow both near and offshore and there was a clear inhibition of the shelf-ocean exchange seen during the summer deployment. This arises from the upwelling favourable winds that have been "typical" of the 1999 winter season. Mean velocity estimates varied between 0.22 and 0.11 m/s. The offshore southward flow is related to the Portugal Current, the easternmost branch of the North Atlantic subtropical gyre, which showed mean velocities of 0.17 ± 0.08 m/s.

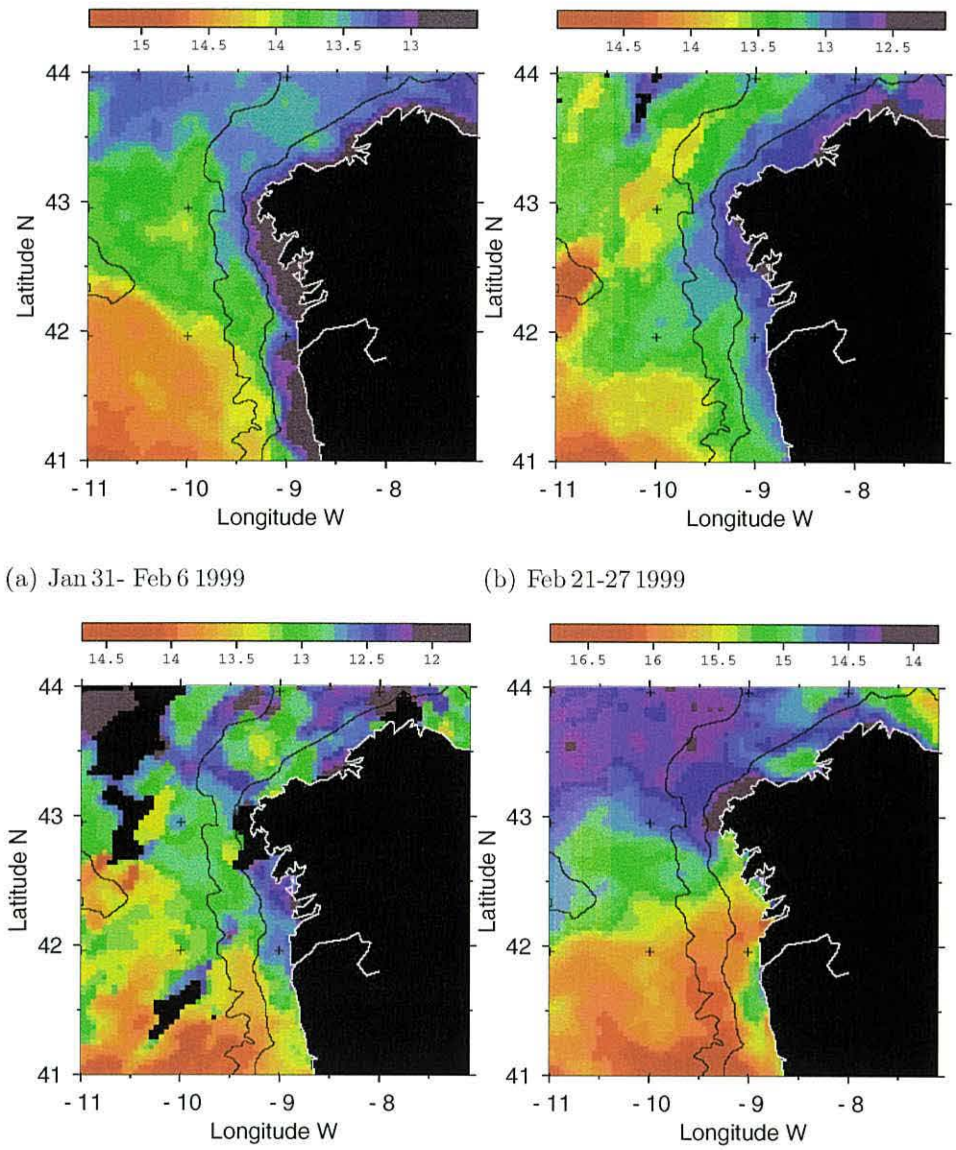

(a) Jan 31- Feb 6 1999

(b) Feb 21-27 1999

(c) Mar 28-Apr 3 1999

(d) May 23-29 1999

Figure 7.5.: Examples of SST during the 1999 winter. Note the absence of the warm tongue indicative of poleward flow along the coast.

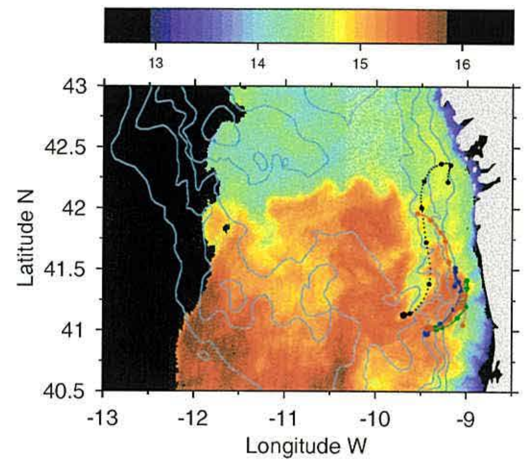

Figure 7.6.: Drifter data for the period 2-10 January 1999 overlaid on the SST image of the 6 January 1999. Dots correspond to the start of each day. Black corresponds to cloud masking.

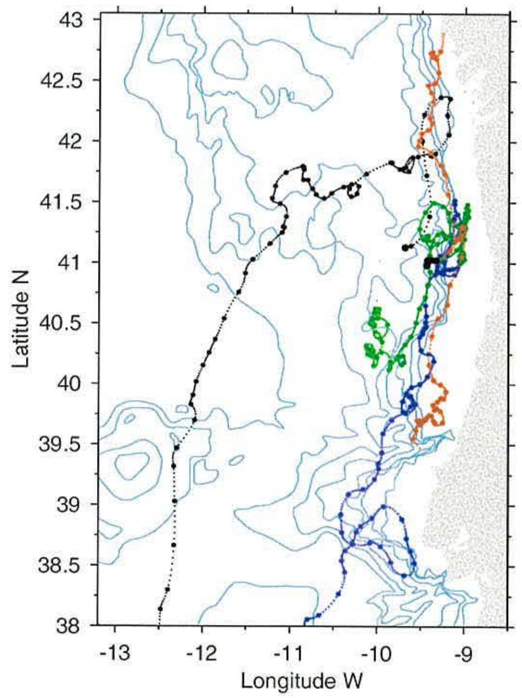

Figure 7.7.: Winter deployment drifter tracks. Solid dots indicate days. Larger black dots indicate deployment location.

7.3 Lagrangian statistics and diffusivity estimates

Lagrangian statistics were calculated for both deployments following the method described in *Davis* [1985] and subsequently used by many authors [e.g. *Haynes and Barton*, 1991; *Salas et al.*, 2001]. Arriving to statistically significant conclusions from Lagrangian measurements requires the separation of the flow into mean and perturbation components. The mean velocities (U,V, see Table 7.2) were obtained for each deployment and subtracted from the calculated values to get the perturbation components (u',v'). To quantify the influence of the perturbation flow on the mean flow we have to determine an eddy diffusivity coefficient (K). To calculate it from Lagrangian statistics it is usual to apply the theory of homogeneous isotropic turbulence following the Taylor's Theorem [*Taylor*, 1921]. A more complex approach was presented in *Davis* [1987] and *Davis* [1991] where the diffusivity is not assumed constant and where the flow homogeneity and infinitesimal eddies constraints (infinitesimal eddies that are no longer related to the mean flow, *i.e.* at the end of the energy cascade) are relaxed. This is basically a generalization to circumstances with mean flow of the single-particle diffusivity introduced by *Taylor* [1921]. However, the limited number of drifters restricted its implementation.

Mean global velocities (Table 7.2) indicated a small southwestward drift during the summer deployment although the values were not significantly different from zero. The winter zonal average was again not different from zero but the meridional component showed a small southward drift as seen in the drifter trajectories.

Characteristic integral space and time scales can be defined from the normalised autocorrelation function $R(\tau)$ of Lagrangian velocity perturbation components u', v' given by

$$R_{ij}(\tau) = \frac{1}{\overline{u_i' u_j'} T} \int_0^T u_i'(t) u_j'(t+\tau) dt, \tag{7.1}$$

T being the length of the time series, the overbar and ensemble average and the subindices i, j correspond to the zonal and meridional components respectively. The Lagrangian integral timescale T_{ii} represents a measure of the time over which a

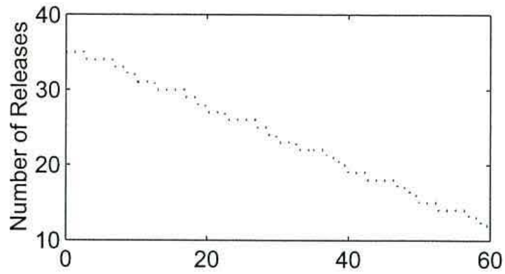

Figure 7.8.: Number of "new drifter" releases for the winter deployment.

particle remembers its path. Its dependence on the autocorrelation function $R(\tau)$, which is usually close to zero for long lags (τ) but often exhibit a systematic trend of oscillations (Fig 7.13), masks the evaluation of Eq 7.2. This is usually solved by time integrating the velocity autocorrelation function $R(\tau)$ to the first zero crossing T_0 giving an upper bounds limit [*Poulain and Niiler*, 1989].

$$T_{ii} = \int_0^{T_0} R_{ii}(\tau)d\tau. \tag{7.2}$$

The equivalent Lagrangian length scale L_{ii} is defined accordingly,

$$L_{ii} = \sqrt{\overline{u_i'^2}} \int_0^{T_0} R_{ii}(\tau)d\tau = \sqrt{\overline{u_i'^2}} T_{ii}. \tag{7.3}$$

The small differences in each deployment between the two components of $T_{ii,jj}$ and $L_{ii,jj}$ (Table 7.2), support the initial isotropic assumption implied in the analysis. Larger Lagrangian time and space scales were obtained from the summer deployment and reflect the larger, energetic features associated with the summer upwelling, as T and L generally increase with the Eddy Kinetic Energy (EKE) of the system [i.e. *Martins et al.*, 2002].

The number of drifters in each deployment (four) is insufficient to arrive at statistically meaningful eddy diffusivity coefficient estimates. Since the data set is assumed to be homogeneous and stationary and the de-correlation time scale is small (maximum 2 days) it is common practise to increase the data set by generating "new drifters" every few T_{ii} [*Colin de Verdière*, 1983](Fig. 7.8). By using a few T_{ii}, the possibility of having unwanted correlations between drifter segments which would corrupt the analysis is reduced. This procedure allocates too much emphasis on the intermediate portions of each trajectory, which is the most frequently sampled by this segmentation process,

	Velocity		Time scale		Length scale		Diffusivity	
	U	V	T_{ii}	T_{jj}	L_{ii}	L_{jj}	K_{ii}	K_{jj}
	cms^{-1}	cms^{-1}	$days$	$days$	km	km	$10^6 cm^2 s^{-1}$	$10^6 cm^2 s^{-1}$
Summer	-1.45	-1.64	2.01	1.68	18.7	20.5	8.7	10.7
Winter	-1.42	-6.08	1.14	1.26	10.2	12.1	1.9	3.3
Global	-0.65	-2.21	1.41	1.57	12.5	15.9	5.2	10.6

Table 7.2
: Summary of bulk Lagrangian statistics for each of the deployments and of all available data, see text for details.

and may constitute a disadvantage given the small number of drifters. However, it is expected that the increase in degrees of freedom compensates for this. For all deployments, drifters were segmented every 10 days. The dispersion of the segmented drifters (Fig 7.9, example from the summer deployment) resembles the dispersion of an instantaneous dye release about its center of gravity, highlighting the diffusive character of the Iberian currents.

According to [*Taylor*, 1921], the single-particle dispersion (displacement variance) is related to the autocorrelation function and the variance of their velocities:

$$\overline{x'^2(t)} = \overline{2u'^2} \int_0^t (t-\tau) R_{ii}(\tau) d\tau, \tag{7.4}$$

where the bar indicates an ensemble average and $x'(t)$ is the displacement of the particle due to u' and $R_{ii}(\tau)$ is the normalised autocorrelation coefficient of the perturbation velocity. Equation 7.4 reaches two asymptotic limits independent of the form of $R(\tau)$:
Initial dispersion, as $t \to 0$, $t < T$,

$$\overline{x'^2} = \overline{u'^2} t^2, \tag{7.5}$$

and Random walk regime for $t \gg T$,

$$\overline{x'^2} = \overline{2u'^2} Tt. \tag{7.6}$$

The Lagrangian diffusivity is then defined as half the rate of change of the dispersion. Equation 7.7 allows diffusivities to be calculated in two ways: by directly evaluating

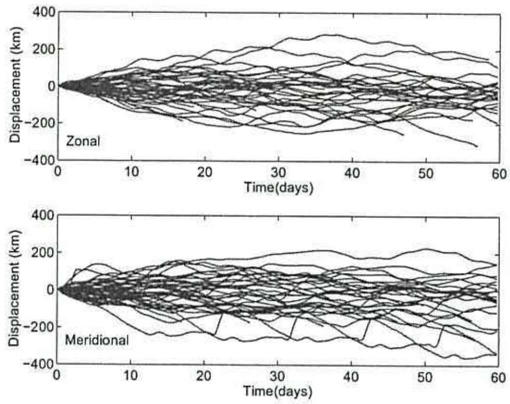

Figure 7.9.: Example of displacement from each of the "new released" drifter segments from a single source. Note the similarity to a diffusive dye plume.

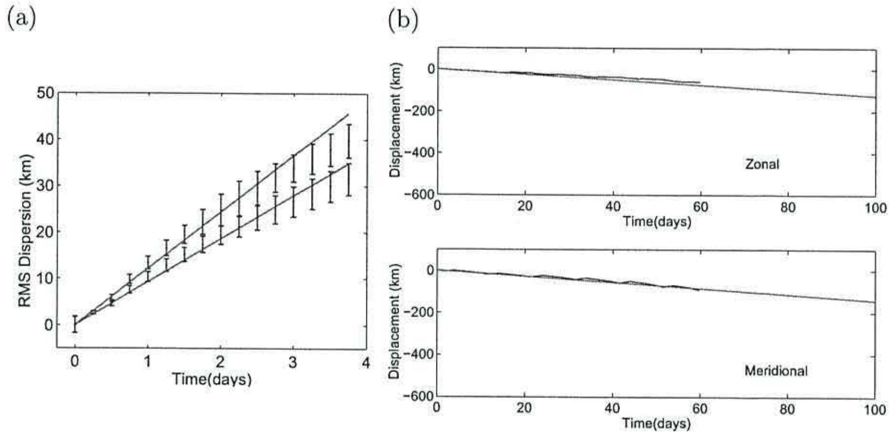

Figure 7.10.: Examples of evaluation based on Taylor assumptions for the summer deployment. a) Initial displacement and b) mean displacement.

the derivative of the left-hand side, and the other by numerical integration of the right-hand side. The result presented here were arrived at through the second method.

$$K_{ii} = \frac{1}{2}\frac{\overline{dx'^2}}{dt} = \overline{u'^2}\int_0^{T_0} R_{ii}(\tau)d\tau = \overline{u'^2}T_{ii}. \tag{7.7}$$

The validity of Taylor's Theorem (and hence our assumptions of homogeneity and stationarity) can be assessed by comparing the data against the theoretical initial dispersion and the final random walk regime. Calculated Taylor's initial dispersion is overlaid on the summer observed root mean square (RMS) dispersion together with error bands (Fig. 7.10a, green for meridional and blue for zonal). Both data agree for the first 2 days hence giving further support to the applicability of Taylor's Theorem in the OMEX region. Similar agreement was found for the winter deployment. Mean displacements of the segmented data (Fig. 7.10b) agree well with the values of the

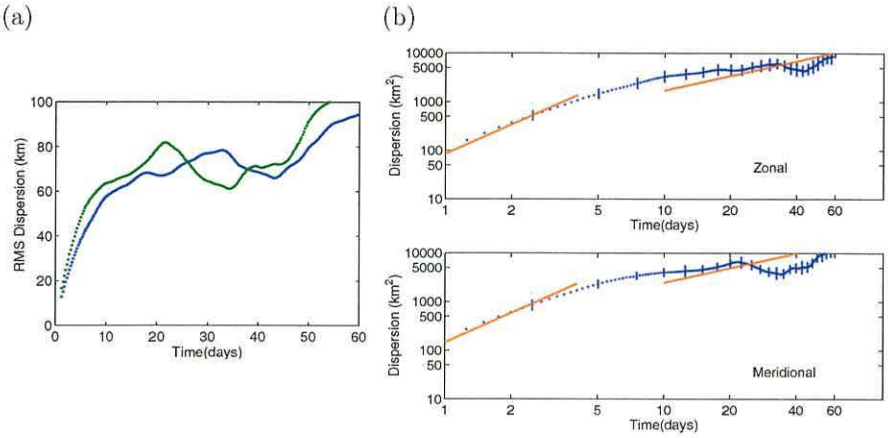

Figure 7.11.: Displacement plots for summer deployment. a) RMS displacement and b) Log-Log zonal (top) and meridional (bottom) dispersion. Symbols represent observations, solid lines represent Taylor's theorem for initial dispersion and random walk regime. Error bars represent 67% confidence.

removed background mean flow which supports our assumption that the flow field can be approximated by the Taylor theorem (example from the summer deployment).

The time evolution of the RMS dispersion of the summer drifters (Fig 7.11a, blue is zonal and green is meridional) shows an rapid increase in dispersion corresponding to the initial Taylor dispersion. After that, dispersion is highly reduced and maintained constant for 30 days reaching the linear random walk regime only in the last part of the record. This behaviour might be characteristic of upwelling-filament areas where the bulk dispersion will largely depend on the time scales under consideration. The log-log plots (Fig. 7.11b) of zonal (top) and meridional (bottom) summer dispersion versus time again shows the agrement with Taylor's theorem of initial dispersion. The Random Walk regime agreement is worse possibly due to the large effect of eddies in the dispersion. Error bars represent 67% confidence limits of the dispersion.

The winter RMS dispersion (Fig 7.12a) is much smaller than in summer with the two regimes (Initial and Random Walk) clearly distinctive. The differences between zonal (green) and meridional (blue) RMS dispersion are more significant due to the more anisotropic diffusive winter regime. The agreement between the Random Walk regime and the observations (Fig 7.12b) is now better. Comparing the drifter's behaviour during summer and winter (Fig. 7.12a-b) one can note that there is a much higher

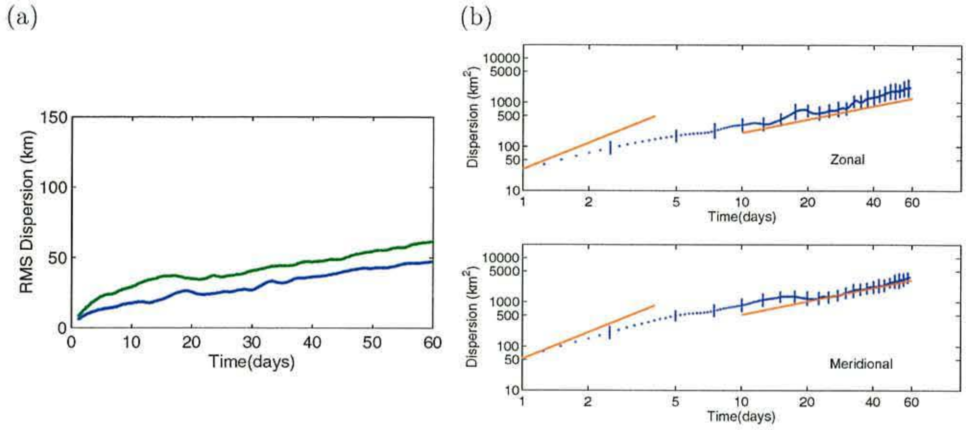

Figure 7.12.: Displacement plots for winter deployment. a) RMS displacement against time and b) Log-Log zonal (top) and meridional (bottom) dispersion. Symbols represent observations, solid lines represent Taylor's theorem for initial dispersion and random walk regime. Error bars represent 67% confidence.

initial dispersion during the summer associated with the large-scale eddy identified in the drifter tracks.

Summer and winter diffusivities and the autocorrelation function for both zonal and meridional components are shown in Fig. 7.13. The final estimate is the average of the diffusivity over the time when it approaches a constant value. They are expected to asymptote at a few T_{ii} and failing to do so manifests the difficulties in estimating K_{ii} from a limited amount of drifter data. Winter diffusivities did indeed approach a constant value in a few T_{ii}, from day 20, giving support to the assumptions of stationary and homogeneity, with averages of $1.9 \times 10^2 \mathrm{m^2s^{-1}}$ and $3.3 \times 10^2 \mathrm{m^2s^{-1}}$ in the zonal and meridional components. Summer diffusivities were much higher and failed to asymptote until day 50 suggesting that the inhomogeneities in the flow were large. Final averages suggest small isotropy with values of $8.7 \times 10^2 \mathrm{m^2s^{-1}}$ (zonal) and $10.7 \times 10^2 \mathrm{m^2s^{-1}}$ (meridional). The number of drifters decrease with time and summer diffusivities should be taken with caution as sampling errors increase. It is worth mentioning the sharp peak in the diffusivity at times smaller than 10 days. This is caused by the presence of the eddy/filament meander as mentioned previously. Similar results were obtained by *Swenson and Niiler* [1996] for drifters deployed in the California Current system in regions where eddies were present.

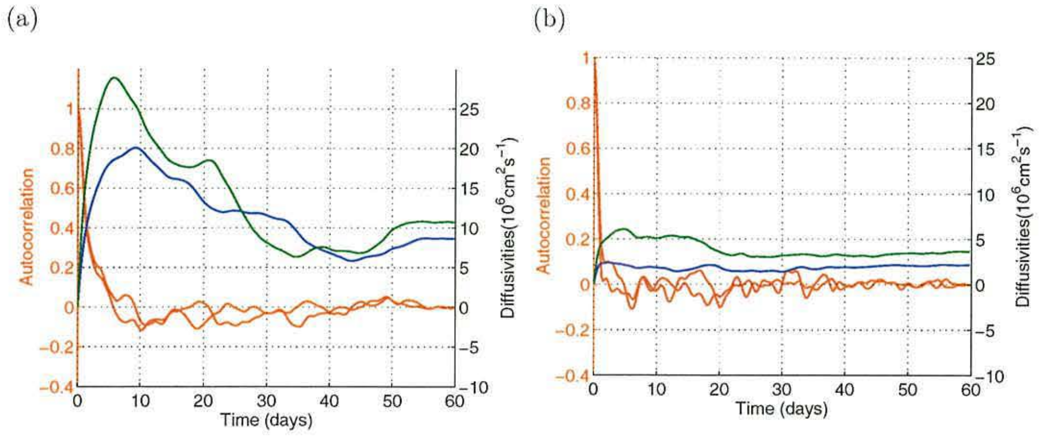

Figure 7.13.: Diffusivity and autocorrelation function with time for the, a) summer and b) winter deployments for both zonal (blue) and meridional (green) components.

The analysis was repeated with all available mixed layer drifters for the region including data from a previous deployment in autumn 1986. During that time the drifters moved northward following the winter poleward slope in contrast with our winter data. A full description of the data can be found in *Haynes and Barton* [1991]. The bulk results show a better agreement with Taylor's theorem (Fig 7.14) due to the larger number of realisations. The number of "pseudo drifters" decreases linearly from 150 to 50 at day 90. The dispersion versus time graph (Fig 7.14a) shows clearly the two regimes. In this final case, differences between zonal and meridional components have increased with respect to the winter and summer values. The Log-Log plots (Fig 7.14b) also show a better agreement between observations and Taylor's theorem than in the separate deployments.

The bulk Lagrangian length scales were 12.5km and 15.9km for the zonal and meridional directions, which lay in between the values for the two seasons. The Lagrangian time scales were 1.41 days (zonal) and 1.57 days (meridional). The diffusivity and autocorrelation function (Fig 7.15) show characteristics from the summer deployment. The diffusivity peaks similarly to the summer deployment and asymptotes around day 50. The final averages were also a compromise between the two seasons with values of $5.2 \times 10^2 m^2 s^{-1}$ (zonal) and $10.6 \times 10^2 m^2 s^{-1}$ (meridional) although they became more anisotropic.

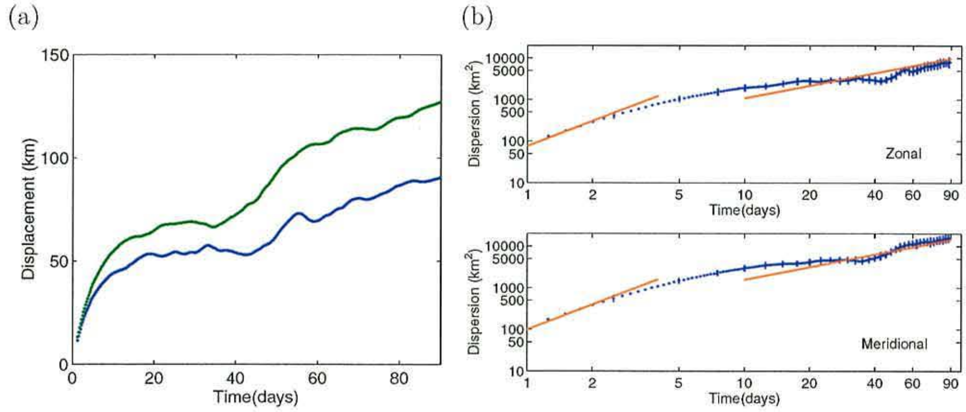

Figure 7.14.: Displacement plots for all available data. a) RMS displacement against time and b) Log-Log zonal (top) and meridional (bottom) dispersion. Symbols represent observations, solid lines represent Taylor's theorem for initial dispersion and random walk regime.

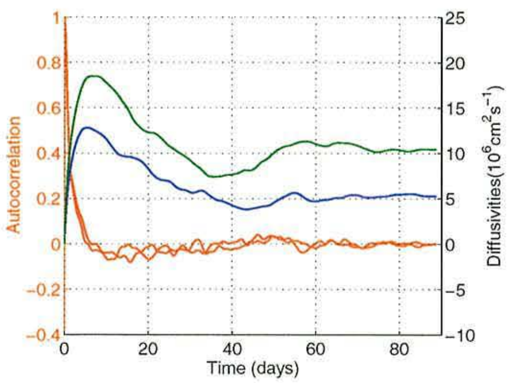

Figure 7.15.: Diffusivity and autocorrelation function with time calculated from all available drifter data for both zonal (blue) and meridional (green) components.

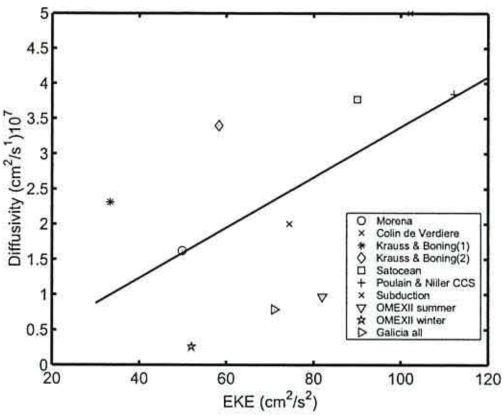

Figure 7.16.: Diffusivity against EKE for the current data and other published data extracted from *Martins et al.*,[2002]. See text for details.

The relationship between estimates of K and the EKE of the system is explored in Figure 7.16. The current data is plotted alongside previously published data extracted from *Martins et al.* [2002, and references therein]. The data includes other upwelling areas like the California Current and oceanic regions like the North Atlantic or Azores regions. As expected a general trend is observed, with regions or seasons of larger EKE having larger K. The current K estimates are the smallest. In our limited dataset a clear increase in EKE and K can be seen from winter to summer which is also supported by the data from *Haynes and Barton* [1991].

7.4 Discussion

This chapter has aimed to quantify the observed variability of summer and winter regimes in terms of the Eddy diffusivity as estimated from drifter data. Although the dataset is small it was shown to conform to Taylor's theorem and the single-particle diffusivity method is expected to be of significance. Validity of the method with this small number of drifters should however be viewed with caution. In order to obtain more reliable estimates, data were searched on August 2000 in the WOCE drifter database but the other deployment documented there (from the MORENA project) did not have public access to the data.

Nonetheless there are limitations and associated errors that should be considered. First of all, our small number of drifters means that the spatial coverage was limited

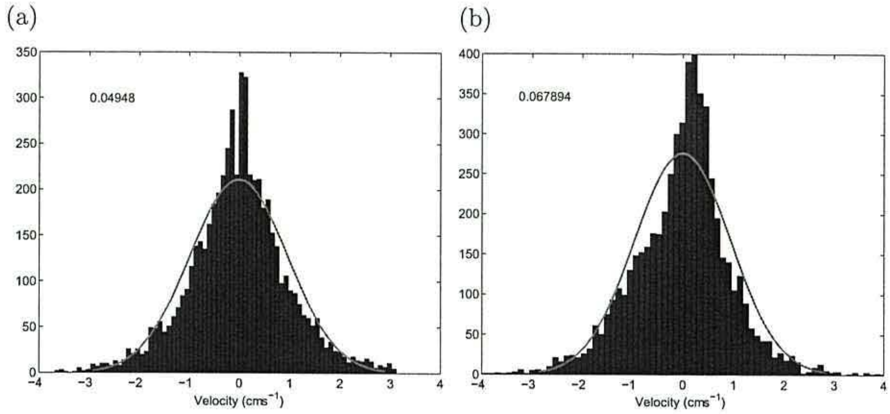

Figure 7.17.: Histograms for the global analysis of velocity departure statistics for the zonal (a) and meridional (b) components normalised by the observed variance. The grey line is the fitted Gaussian distribution. The number in the upper left-hand corner of each figure is the Kolmogorov-Smirnov statistical test value for normal distribution. Values smaller than 0.0179 means the data is normal distributed. Although they are not gaussian distributed at the 95.5% level of confidence, the zonal component is closer to a Gaussian distribution than the meridional one.

and unevenly sampled. This adds an intrinsic bias in K estimates towards high diffusivity areas. This is proportional to the mean gradient of particle concentration, which can be solved by using spatial ensembles of uniform average buoy density for which a much larger and extensive deployment strategy should be used. The velocity departure normalised by the variance should fit a Gaussian distribution for the single-particle method to be applicable. It was found that the distribution of all available data was always marginally different from Gaussian (Fig 7.17), although more so for the meridional component. This could be accounted for by spatial inhomogeneity, particularly during the summer, and the presence of the coast.

Although weather conditions proved to be very similar during the two deployments there are clear differences in drifter behaviour in the summer and winter periods. The activity of upwelling filaments marks the summer surface circulation and they act as an active link between the shelf and open ocean but the associated return flow inhibits a net offshore flow of shelf waters [*Barton et al.*, 2001]. During winter, filaments did not occur, even though upwelling conditions persisted, and shelf waters were isolated from the ocean. During this exceptional winter, there was a net southward transport over the slope contrary to previous evidence of persistent winter poleward flow.

We have found clear differences in the Lagrangian statistics of the two deployments, summer and winter, although they cannot solely be attributed to seasonal differences. The summer drifters stayed mostly offshore away from the constraint of the coast and one expects the regime to be more isotropic [e.g. *Martins et al.*, 2002]. The larger scales of the dominant physical processes (filaments and eddies) caused the diffusivities, Lagrangian length and time scales to be bigger during the summer. The winter drifters stayed mostly close to the coast, which made the diffusivity slightly anisotropic. Also, the physical processes involved were weaker and no signs of eddy formation were seen, which is characteristic of the winter circulation in the Iberian Coastal Transition Zone [*Haynes and Barton*, 1991; *Huthnance et al.*, 2002]. Overall, the diffusivities and Lagrangian scales were smaller. One has to be however careful in interpreting the winter data as dispersion in the slope region in the presence of the slope current is critically dependent on the initial deployment position relative to the slope current [*Burrows and Thorpe*, 1999]. The 1986 deployment of *Haynes and Barton* [1991] was done under typical winter conditions with a well developed poleward flow and evidences of eddy shedding from it. Nevertheless, their values of diffusivity ($3.4 \times 10^2 m^2 s^{-1}$ and $2.5 \times 10^2 m^2 s^{-1}$ for zonal and meridional), Lagrangian length scale (9.2 and 11.2km) and time scale (1.3 and 1.9 days) were similar to our winter deployment. The main discrepancies were found in the zonal values were the eddies acted to increase these scales. *Van Aken* [2002] found larger eddy activity in the Bay of Biscay during the poleward flow regime but the region lacks the summer upwelling regime so comparisons can not be drawn easily. Although slope water eddies are believed to play a significant role in the shelf-ocean exchange during the winter [*Huthnance et al.*, 2002] they are not continuously generated at any location (although there are preferred sites) and export bulk capabilities remain to be assessed.

One of the main difference between the summer and winter deployments is the shape of $K(t)$, which sharply peaks in the summer one as a consequence of the strong eddy like signals in the tracks. Similar results were also observed by *Swenson and Niiler* [1996] induced by relevant spatial inhomogeneity.

7.5 Conclusions

It was expected that there would be a seasonal modulation of the Lagrangian statistics in the Iberian CTZ mainly due to the seasonality of the currents regime. However, the present data lacks sufficient spatial coverage during either season to determine the amount of our temporal variation due to spatial differences and the proportion due to seasonal changes. Nonetheless we can conclude that:

- Clear differences were seen in the drifter behaviour during the two deployments despite the similar atmospheric forcing conditions.
- During the summer, high values of EKE were found, and the characteristic Lagrangian space and time scales were larger than in the winter deployment.
- Diffusivity estimates were also larger during the summer than during the winter deployment suggesting an increased mixing during active upwelling and filament formation.
- Diffusivity estimates compared well with previous estimates in the region but rank in the lower end of estimates in other upwelling areas.
- Inclusion of all available data in the analysis showed a better agreement with Taylor's theorem suggesting that more drifter deployments are needed to accurately describe the diffusivity seasonality in the region.
- Diffusivity estimates from all available data were more anisotropic than individual estimates from each deployment.

Despite its shortcomings, this work is important because of the lack of observations in the area. Hopefully, with more deployments there will be a better estimate of the eddy flux transport in the region during the different regimes.

CHAPTER

8 General discussion and recommendations

8.1 Introduction

The principal objective of this thesis is to characterise the Galician shelf response to varying seasonal forcing, in particular to identify the typical spatial and temporal variability of wind and its effect on the shelf circulation. Through a set of observations including satellite data (scatterometer, AVHRR, SeaWIFS and drifters), cruise data (CTD, ADCP, turbulence probe) and mooring data (wind and surface currents) the complex shelf circulation and its response to large scale forcing has been explored. Many of the observations, although limited in their spatial and temporal coverage, are novel in an area where systematic sampling has been sparse. In Chapter 3, for the first time, the spatial and highly temporal variability of the wind has been unequivocally shown and indirect evidence of its effect, through SST were presented. Results from Chapter 3 were extrapolated to aid interpretation of SST data in the absence of direct spatial wind measurements. In subsequent chapters, examples of the spring transition, upwelling season and autumn transition/downwelling stage were presented covering the contrasting shelf environments previously identified for the Galician CTZ. Chapter 7 provided an integrated quantitative view of the Lagrangian differences between the upwelling and downwelling regime.

8.2 Shelf classification

The gently sloping shelf around Galicia extends, on average, 40km seawards either side of Cape Finisterre (with a minimum at the cape of 20km), constituting a narrow shelf. Even in the absence of filament formation, the upwelling front extends beyond the shelf break into waters >1000m (Chapter 3). This is expected during sustained favourable upwelling winds in a wide shelf, or for a narrow shelf with intermittent upwelling winds, as in Galicia. The front's offshore position indicates weak topographic control, as the shelf break would anchor the upwelling front there, in contrast with the stronger link reported by *Fiúza* [1996] and *Peliz et al.* [2002] in the wider Portuguese shelf south of 41°N (Figs 2.1 and 2.7c). There, the upwelling front resembles the geometry of the bottom topography. Upwelling areas often have associated poleward undercurrents [*Neshyba et al.*, 1989; *Barton*, 1990] which are located off-shelf in narrow shelves. This is the case in the Galician region, where the poleward flowing Portugal Coastal Under Current (PCUC) is located on the slope during strong upwelling wind episodes (Chapters 4-5). The shelf can be expected to function like a shallow one, with surface and bottom Ekman layers occupying the entire water column in a two layer circulation [*Garvine*, 1971; *Hill et al.*, 1998]. It is only during wind relaxations (Chapter 5) that the poleward undercurrent occupies the shelf.

The narrow shelf width means there is a strong interaction between shelf circulation, circulation inside the Rias and wind forcing. Previous authors have acknowledged this for the Rias Bajas [e.g. *Gomez-Gesteira et al.*, 2001; *Prego et al.*, 2001; *Sordo et al.*, 2001] and they must be considered an integral part of the shelf as they respond to the same forcings. Upwelling and downwelling winds strongly influence the circulation inside the Rias, enhancing or reducing their flushing time throughout the year, even during maximum river runoff in autumn and winter [*Álvarez-Salgado et al.*, 2000]. During the summer the river discharge is minimal, but upwelling takes place inside the Rias where upwelled water undergoes warming, freshening and nutrient utilisation. The effect of outwelling from the Rias on shelf circulation is greatest in the presence of the PCC (Chapter 4), as the freshwater plume can reach the shelf break and interact with it. Enhanced stratification on the shelf could potentially delay the outcropping of isothermals.

8.3 Variability

It has been shown that the upwelling region of Galicia is a highly variable system. Two main interconnected sources of variability identified in the present work are 1) the irregular coastline and shelf, notably at Cape Finisterre, and 2) the strong spatial and temporal variability of wind forcing. Both aspects affect the development and evolution of the upwelling regime (Chapter 3) as also shown for the Oregon coast by *Barth et al.* [2000]; *Samelson et al.* [2002] and the downwelling regime (Chapter 7) [e.g. *Dubert*, 1998]. Small time scales were consistently obtained from Lagrangian observations and large scale winds suggesting a very dynamic region. Despite its complexity, the mesoscale wind variability can be reduced to a finite number of spatial patterns which, to a certain extent, explain the Galician shelf response (Chapter 3). One quarter of the wind spatial variability rests in increasingly complex spatial patterns, while the reminder corresponds to a coherent wind. The seasonality of wind forcing is masked by upwelling/downwelling events throughout the year, as also noted in previous studies [*Álvarez-Salgado et al.*, 2003]. However, the system response shows a clearer seasonality with upwelling during summer and downwelling during winter mediated by a meridional density gradient; this seasonality is determined by more consistent and frequent upwelling winds during summer. However, the intermittency of upwelling winds (Time scales of 14 days, Chapter 3) produce a contouring broad upwelling front (Chapter 5, Fig 5.8) [*Brink*, 1983] rather than the sharp one as measured south in the broader Portuguese shelf [*Peliz et al.*, 2002]. Each upwelling pulse generates a new front that is advected offshore and modified by surface heating and freshwater mixing. Further south, along the Portuguese coast, the wind is expected to be stronger and less variable, similar to Oregon-California as a result of the continental mass and coastal guidance. Nonetheless, large interannual differences in the upwelling and downwelling regimes are related to the wind [*Huthnance et al.*, 2002]. Unusual predominance of PUNC over PUWC patterns restrict filament development on the west coast while enhancing the Cape Finisterre filament, as was the case in 1999 (Chapter 3). Integrated values of monthly upwelling indices for the west coast (Vigo region, as in Chapter 4) showed smaller values in 1999 (119

m^3s^{-1}per100m) compared to 1998 (273 m^3s^{-1}per100m) when west coast filaments fully developed (Chapter 5), which agrees with the expected differences between PUNC and PUWC years. Similarly, predominance of PUWC patterns over DOWN patterns during the winter of 1999 precluded the development of the poleward flow over the slope (Chapter 7).

Rather than long upwelling index integrals (i.e. over the summer months), *Austin and Barth* [2002] found that a finite integration between 5-12 days best explained the upwelling intensity, measured as the displacement from horizontal (outcropping) of the permanent pycnocline. If this holds for the Galician region given the similarities in wind forcing, the characteristic wind time scale of 14 days would suffice to maintain an active and productive upwelling. *Austin and Barth* [2002] also found that a wind relaxation of 5-12 days produced a dynamical relaxation stage, i.e. the pycnocline relaxed but still produced a southward geostrophically balanced jet. The relaxation process can be driven by alongshore pressure gradients created during upwelling events [*Send et al.*, 1987] or alongshore variations in wind stress [*McCreary et al.*, 1987] among other mechanisms. Alongshore variations in upwelling conditions may lead to alongshore transport divergence and hence regions of high or low pressure, and the opposing pressure gradients drive alongshore poleward flow. This alongshore flow, in turn, drives transport in the bottom Ekman layer counter to that in the bottom Ekman layer during the wind event which would restore the density structure to a more horizontal position. *Samelson et al.* [2002], in their study of wind scatterometer data off the coast of Oregon, showed a systematic increase of southward wind stress by a factor of 3-4 along the Oregon coast. Whether such variation can be expected off the Iberian coast remains to be assessed, although some indication of this is seen in the median of wind during the summer 1999 and 2000 in Fig 3.2, and in the reconstructed wind patterns (Fig 3.9). Nonetheless, the latitudinal variation in upwelled watermass characteristics can also induce alongshore pressure gradients. The latitudinal density variation in upwelled waters shown in Chapter 2 (Fig 2.11) represents 1kgm^{-3} change in 500km, a gradient of $\sim 10^{-6}kgm^{-3}$ per m, sufficient to drive a poleward flow (Chapter 6). This could account for the existence of the PCUC seen during the relaxation event in Chapter 5.

With no clear seasonal wind changes in the scatterometer data, the transitional periods between downwelling and upwelling regimes are difficult to examine. Monthly upwelling indeces (Chapter 5) suggest a long spring transition (April to June) from the downwelling to upwelling regime for the 1986-1998 record, due to high wind variability. During those months, co-existence of the PCC and coastal upwelling is possible (Chapter 4). However, upwelling relaxations or downwelling winds quickly suppress the coastal upwelling (e.g. Chapter 3). These early upwelling events are eroded faster because the upwelled water does not provide a strong upwelling front or sea level declining onshore in response to high density water. The compensatory onshore flow originates from above the bottom Ekman layer of the poleward flow with watermass characteristics similar to the surface water. Upwelling is not permanently established until the poleward flow shuts down or is pushed offshore.

Interannual and seasonal variability of the large scale circulation influences the development of the poleward flow. The seasonal signal in the Sea Level Anomaly (SLA), determined from altimetry data for 1992-1998, is large offshore the Iberian peninsula [*Efthymiadis et al.*, 2002], and is related to changes in the upper-ocean heat content. The authors found maximum negative SLA during autumn and winter, enhancing the southward flowing Portugal Current, in part responsible for the maintenance and intensification of the meridional density gradient off Iberia that drives the PCC. *Martins et al.* [2002] have shown a seasonal increase in altimetry derived Eddy Kinetic Energy (EKE) from autumn, with a maximum in winter, and decreasing towards the summer in the region of the Portugal Current for 1992-1999. The increase is partly related to the higher number of eddies associated with the meridional density front. Both SLA and EKE seasonal trends are related; the enforcement of the Portugal current sharpens the front, which allows for eddy formation, which at times, could help maintain and enhance the front as discussed by *Dubert* [1998]. Both mechanisms reinforce the slope poleward flow but also cause pulses as eddies could modulate the impingement of the front on the slope.

Interannual variability was seen in both EKE [*Martins et al.*, 2002] and SLA [*Efthymiadis et al.*, 2002] off Iberia. The dominant interannual basin scale variability during winter over the North Atlantic is the North Atlantic Oscillation (NAO) [*Rogers*, 1985]. The NAO index is defined as the normalised sea-level pressure difference between the Azores and Iceland [*Jones et al.*, 1997] and it is associated with changes in the strength and direction of winter westerly winds over the North Atlantic and northwest Europe. Winter negative NAO values correspond to stronger westerly winds on the subtropical North Atlantic. It is not surprising then that interannual variations matching the NAO index are more dominant north of 34°N [*Efthymiadis et al.*, 2002] and are greater during winter related to wind-induced net heat loss. *Garcia-Soto et al.* [2002] studied the relationship between the NAO index and the presence of the PCC along the Bay of Biscay and found a good relationship between winter negative NAO index and strong poleward flow development. *Efthymiadis et al.* [2002] found the largest SLA fall during 1995/96, which corresponded to strong poleward flow development year [*Garcia-Soto et al.*, 2002; *Pingree et al.*, 1999]. 1999 was a year of positive NAO index which relates to weak downwelling/upwelling winds during winter off Iberia and the PCC failed to develop (Chapter 7).

The year-round presence of a poleward flow in the Galician CTZ has been suggested previously, switching from winter surface flow (Chapter 6) to an undercurrent during the summer upwelling (Chapter 5), but direct observational evidence is sparse [*Barton*, 1990]. Here, two different forcing mechanisms are proposed for the PCC and the undercurrent. Adjustment of the meridional oceanic density gradient to slope-shelf topography drives the PCC, while the undercurrent is forced by an alongshore pressure gradient induced by latitudinal variation of watermass characteristics of the upwelled water.

8.4 Seasonality

A schematic of the expected upper layer seasonal circulation in the Galician shelf is proposed in Fig 8.1. Transport estimates that were resolved during the different

Upwelling	Spring transition		Downwelling
Filament	Offshore Poleward flow	Nearshore equatorward flow	Slope Poleward flow
0.5Sv	0.39 ± 0.15Sv	−0.46 ± 0.22Sv	2.0 ± 0.5Sv

Table 8.1: Resolved transport estimates during the different cruises.

cruises are shown in Table 8.1.

8.4.1 The downwelling or poleward flow regime

The poleward flowing PCC develops during late autumn and early winter as the meridional density gradient strengthens. The current develops into typical narrow tongue-like structure off Galicia, broadening north of Cape Finisterre (Fig 8.1a). The shelf is effectively isolated from the ocean due to the shelf-edge front (Chapter 6) although some exchange occurs in the form of a bottom Ekman layer. Finally it reaches a mature/turbulent stage with eddies pitching off, albeit with limited export capabilities [*Huthnance et al.*, 2002]. In this respect, horizontal diffusivities were smaller when compared to estimates during the upwelling regime (Chapter 7). Cape Finisterre and Cape Ortegal have been suggested as the possible origin of both SWODDIES [*Pingree and LeCann*, 1992a] and MEDDIES [*Paillet et al.*, 2002]. The PCC transports $ENAW_T$ northward and its chemical signature changes downstream. In particular, off Iberia, the mixing between the PC and the PCC accounts for the northward indirect ventilation (increase in oxygen and decrease of nutrients) of $ENAW_T$ by the $ENAW_P$ transported in the PC [*Pérez et al.*, 2001]. The distinctive biogeochemical signature of the PCC has a large impact on the biology of the shelf [*Álvarez-Salgado et al.*, 2003], affecting the timing of the autumn and spring bloom, the phytoplankton assemblages and the carbon export between the shelf and the ocean.

8.4.2 The transition between downwelling to upwelling regime

The weakening of the meridional density gradients initiates decay of the poleward slope current. The PCC was still present in June 1997 prior to the onset of coastal

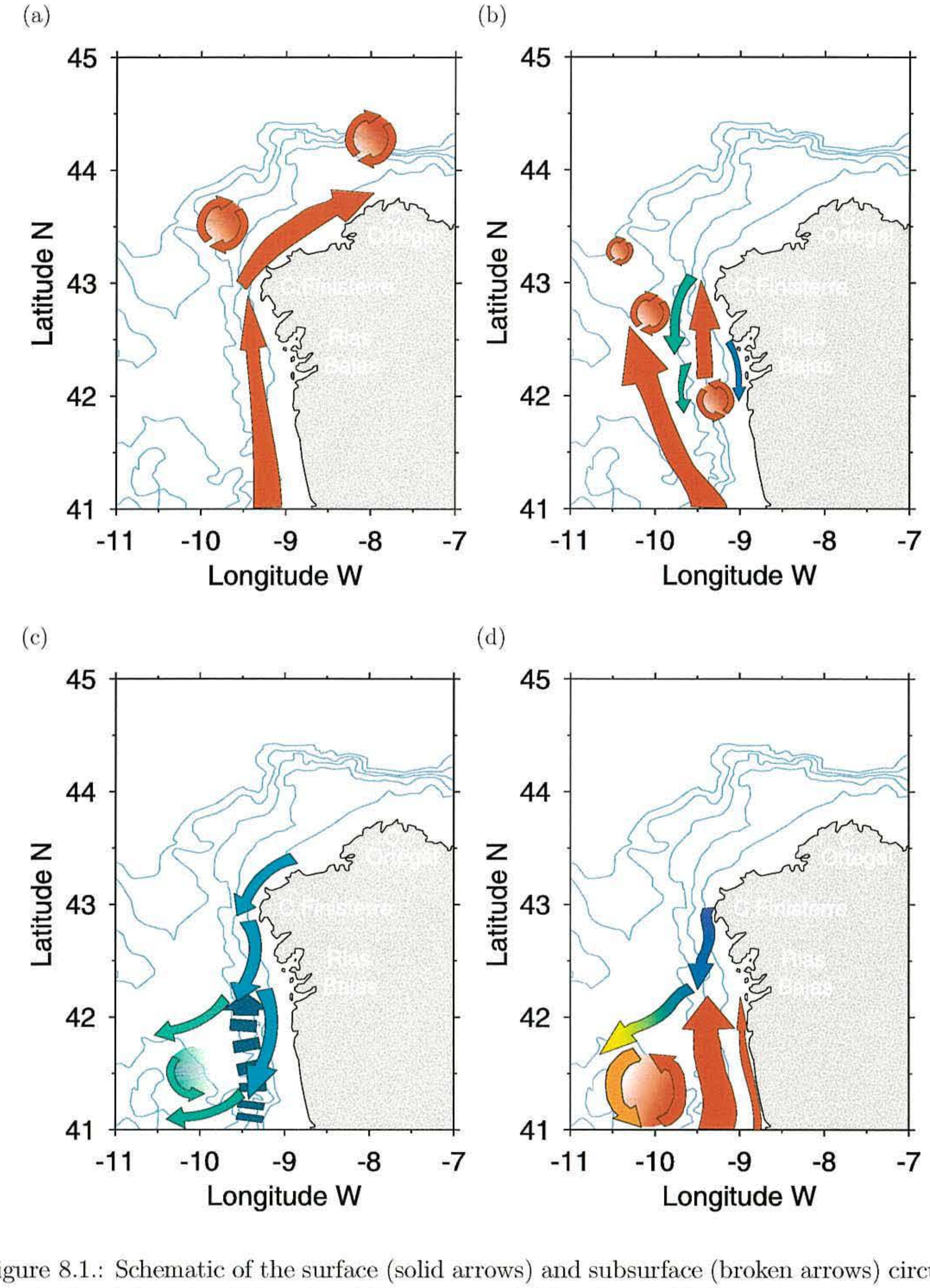

Figure 8.1.: Schematic of the surface (solid arrows) and subsurface (broken arrows) circulation during (a) winter, (b) spring, (c) summer and (d) autumn. Red corresponds to warmer temperatures and green/blue to cooler ones, ic. text for details.

upwelling (Chapter 4). The warm tongue broadens, and the organised flow of the poleward current breaks down as eddies are generated and the flow branches into separate streams, one along the shelf break and one along the outer slope. At this late stage, the PCC is better established offshore than on the slope (Fig 8.1b). A portion of the PCC is still depicted on the slope south of Cape Finisterre as the main detachment point is off the Rias Bajas. The upwelling winds quickly establish a southward flowing jet nearshore while a second southward flow separates the two PCC branches. A similar southward flow intrusion separating general northward flow was also measured by *Relvas de Almeida* [1999] at the end of the upwelling season near Cape Saõ Vicente, south of Portugal. The author related it to a remnant of the coastal upwelling front. In our case, the upwelling regime had not been established yet and it is more likely the result of advection of colder oceanic water from off Cape Finisterre by the two eddies seen in the velocity data (Chapter 4, Figs 4.14- 4.16).

8.4.3 The upwelling regime

During the upwelling regime, the upper column structure becomes dominated by coastal upwelling and filaments and the poleward flow is restricted to deeper levels (Fig 8.1c). As discussed previously, there is strong interannual variability during the upwelling regime characterised by either presence/absence of filaments on the west coast or whether the main filament is at Cape Finisterre or at 42°N latitude. Nonetheless, coastal upwelling was present in all years studied here. This supports the idea of growing instabilities associated with the upwelling front [*Haynes et al.*, 1993; *Roed and Shi*, 1999]. An eddy field would generate filaments whenever an upwelling front is present. Figure 8.1c shows a schematic of the mature stage of west coast upwelling. Up to two filaments may be present at this stage, one rooted at 42°N and another one at 41°N. The latter was more intermittent and can shift its position northward and merge with the 42°N one (Chapter 5). Although weak, upwelling can still be seen north of Cape Finisterre. Detailed *in situ* sampling of the 42°N filament revealed a very shallow structure which might either be representative of a decaying structure, or typical of the Galician upwelling regime. The export capabilities of the filament were small (Chapter 5), not only due to its relatively weak offshore transport, but also due to the filament return flow. Although diffusive transport was enhanced during the summer upwelling regime it was still small compared to other upwelling areas (Chapter 7).

8.4.4 The transition between upwelling to downwelling regime

Towards the end of the upwelling regime, when the upwelling winds start to weaken, the poleward flow reoccupies the upper slope (Chapter 6,Fig 8.1d). The meridional density gradient strengthens, possibly through the seasonal intensification of the Portugal current, and the poleward flow surfaces again. If filaments are still present, their offshore end is broad, badly defined and bends southward describing a short lived eddy like closed circulation (Chapter 5). The slope poleward flow eventually cuts their water supply as it progresses northward and they slowly mix away.

The Coastal Countercurrent, briefly discussed in Chapter 5 is clearly visible in years of high filament activity. Similar nearshore poleward flows have been reported off the south Iberian Peninsula [*Relvas and Barton*, 2002], and the California Current System [e.g. *Send et al.*, 1987]. In the Iberian Peninsula the authors related it to a strong sea surface slope induced by the general eastward drift entering the Gulf of Cadiz, and subsequent cyclonic recirculation along southern Portugal. However, the propagation of such pressure gradient northward along the Iberian Atlantic coast is yet to be established. In the California System nearshore poleward flows have been related to poleward pressure gradients caused by cape induced wind-curl and subsequent wind relaxation events [*Wang*, 1997]. In this case, there is no major cape associated with the poleward coastal current and the alongshore variability may originate from the filaments and/or freshwater plume dynamics [e.g. *Peliz et al.*, 2002] and drive the shelf poleward flow during upwelling relaxations.

8.5 Future work

Although there have been various significant efforts to observe facets of the Galician or Iberian upwelling over the years e.g. recently MORENA, OMEX II, there has never been a systematic effort to monitor its year-round physical development with simultaneous hydrographic, current and meteorological observations on the scale of the California Current programs like CTZ or CalCOFI. The gradualist approach, while illuminating many aspects of the system, has left many basic questions like the 3-D structure, the spin up and spin down of upwelling, and the importance of alongshore propagating upwelling signals, unanswered. The latest oil spill by the tanker Prestige in Galicia has highlighted the need for further understanding of the oceanography of the region.

The present study has focused on the Galician shelf, however, the Iberian upwelling system encompasses the entire Portugal shelf and subsequent studies should address the connection and feed back mechanisms over the whole system. For example, the large scale wind field and its temporal variability needs to be characterised including any spatial trends as found in the California-Oregon coast and possible remote forcing signals. Alongshore pressure gradients have been speculated to explain some of the observed dynamics but no publicly available coastal pressure data could be found for the region Lisbon-Finisterre. Such data would undoubtedly help resolve some unanswered questions like the existence of alongshore propagating signals and the forcing of the PCUC and coastal countercurrent during wind relaxation.

On a more regional scale, intensive and extensive sampling of responses to north/west coast upwelling should resolve its effect on system evolution. The local influence of the prominent Finisterre filament has been speculated but detailed studies of small scale shelf circulation and the wind distribution around the Cape will help understand and quantify its effect. Such detailed studies could also address the open questions regarding the response of the Rias circulation to both wind and shelf circulation, and their possible feedback mechanisms.

The results from the *in situ* survey of the 42°N filament were quite surprising and further detailed sampling of the 3-D filament structure are needed in order to provide a more accurate description of its dynamics and assess the relevance of the results presented here. Evidence pointing at the year-round presence of a poleward undercurrent have been presented but future efforts should be directed at the forcing mechanisms particularly during the upwelling regime. Current knowledge regarding the dynamics and driving forces of the poleward coastal countercurrent are scarce and given its economic impact (e.g. its relation to HAB events in the Rias Bajas, one of the world largest producer of mussels), its study is of principal importance.

The poleward winter flow (PCC) has received a good deal of attention in the last decade but mostly from remote sensing and only a handful of studies have surveyed the feature *in situ*. A more intensive study of the poleward flow, looking at large scale circulation variability, its dependency on wind forcing, and modelling and *in situ* regional studies should unequivocally show the main source of variability and quantify the effect of wind forcing in precluding its year-round presence.

The role of Coastal Trapped Waves (CTW) in the system's evolution and other high frequency sub-inertial signals have never been investigated in the region. In fact, no attempts have been made to determine the existence of CTW here although they could be of importance given the large wind variability. *Huthnance et al.* [2002] reported that 4-6 day wind stress fluctuations excited a second-mode CTW with 4-6 day current fluctuations which corresponded to a phase speed of $2.2 ms^{-1}$.

The prominent location of the Galician region in relation to marine traffic and its dangerous waters (there have been more oil spills in the last 30 years here than in any other European area) requires efforts to be directed towards an operational oceanography strategy. For it to be successful, data are needed to validate models and design measurement networks to maximise resources.

Many of these questions could partially be tackled from a modelling approach. However, existing modelling efforts on the region have been restricted to climatological experiments and idealised topography. The relevance shown here of the complex topography and short time variability highlights the requirement for better and more realistic topography, coast and wind forcing.

APPENDIX

A.1 Processing of FLY data

A more thorough description of the processing of the FLY data can be found in *Inall* [1998].

The free falling FLY (Fast, Light, Yo-Yo) IV profiler was built by Chris Mackay of Systech Instruments. The instrument is equipped with two fast response airfoil shear sensors made of a small piezoceramic bimorph plate that responds to shear strain by generating a voltage. The sensor is able to detect shears between 0 and $4s^{-1}$ with a precision of $\pm5\%$ and a response length of 0.01-0.02m [*Dewey et al.*, 1987] measuring at 280Hz. Two shear sensors operate in the instrument giving one replica of energy dissipation.

Further to the shear, the instrument also measures differential temperature at 140Hz, and conductivity, temperature, tilt, and pressure at 20Hz, the so called slow response sensors.

The probe is operated by dropping it from the stern of a slowly moving ship ($\sim0.25ms^{-1}$) and letting it free fall, the data relayed on board through a Kevlar Multi-Conductor cable. While it falls with a constant velocity W (normally attained within 10-20m of the surface), it experiences a sideways lift force, F, due to the horizontal component of the turbulent velocity fluctuations, u, which is given by

[*Crawford*, 1976]

$$F = \frac{1}{2}\rho\tilde{W}^2 A sin2\phi \tag{A.1}$$

where $\tilde{W}^2 = W^2 + u^2$ is the apparent velocity past the probe; A is the effective cross-sectional area of the probe; ρ is the density of seawater; and $\phi = tan^{-}1\frac{u}{W}$ is the angle of $\tilde{W}$ to the probe. With small ϕ (<5°), the instantaneous shear is given by

$$\frac{\partial u}{\partial z} = \frac{1}{CW^2}\frac{\partial \varsigma}{\partial t} \tag{A.2}$$

where C is a calibration constant and ς (proportional to F) is the output voltage from the sensor. To arrive at the shear estimates, the fall velocity needs to be generated at 240Hz, which is done by fitting a third order polynomial to the pressure record and calculating its first derivative.

The dissipation rate per unit volume, ϵ, is calculated from the variance of the shear time series

$$\epsilon = 7.5\nu\overline{\left(\frac{\partial u}{\partial z}\right)^2} \tag{A.3}$$

where $\nu = 1.049 \times 10^{-}6\text{m}^2\text{s}^{-1}$ is the kinematic viscosity of seawater.

The variance is obtained by integrating the power spectrum of the shear time series. Subsets of the time series of size N=1024 were used in the main water column resulting in ~2m blocks, while near the bed, smaller segments were used. The segments overlapped by N/2 and each were detrended, multiplied by an N point Hanning cosine window and its power spectral density calculated through the Welch's method as

$$P(f) = \frac{2\Delta t X(f)^2 V}{N} \tag{A.4}$$

where $2\Delta t$ is the inverse Nyquist frequency, V the variance lost by applying a cosine window to the series subset, and $X(f)$ the first N/2 values of the N point Fast Fourier Transform of the subset. Further corrections are then applied to account for the decrease in probe sensitivity to frequencies higher than 45Hz [*Inall*, 1998]. Finally, ϵ is obtained by integrating $P(f)$ between 1.5Hz and 55Hz.

The conductivity and temperature sensors were compared and calibrated against simultaneous CTD casts during the CD114 cruise. A linear correction was found and applied to the conductivity data as

$$CTDc = 1.127 \times FLYc - 6.4595 (R^2 = 0.987) \tag{A.5}$$

where CTDc is the conductivity from the CTD and FLYc the conductivity from the FLY instrument. The temperature data were found to be in agreement with the CTD data and no correction was applied.

Bibliography

Adams, J. K., and U. T. Buchwald, The generation of continental shelf waves, *Journal of Fluid Mechanics*, *35*, 815–826, 1969.

Akima, H., Rectangular-grid-data surface fitting that has the accuracy of a bicubic polynomial, *ACM transactions on Mathematical Software*, *22*, 357–361, 1996.

Allen, J. S., Models of wind-driven currents on the continental shelf, *Annual Review of Fluid Mechanics*, *12*, 389–433, 1980.

Allen, J. S., P. A. Newberger, and J. Federiuk, Upwelling circulation on the Oregon continental shelf. part I: Respons to idealized forcing, *Journal of Physical Oceanography*, *25*, 1843–1866, 1995.

Álvarez-Salgado, X. A., J. Gago, B. M. Míguez, M. Gilcoto, and F. F. Pérez, Surface water of the NW Iberian margin: upwelling on the shelf versus outwelling of upwelled waters from the Rias Baixas, *Estuarine, Coastal and Shelf Science*, *51*, 821–837, 2000.

Álvarez-Salgado, X. A., F. G. Figueiras, F. F. Pérez, S. Groom, E. Nogueira, A. V. Borges, L. Chou, G. C. Castro, G. Moncoiffé, A. F. Rios, A. E. J. Miller, M. Frankignoulle, G. Savidge, and R. Wollast, The portugal coastal counter current off NW spain: new insights on its biogeochemical variability, *Progress in Oceanography*, *56*, 281–321, 2003.

Ambar, I., and A. F. G. Fiúza, Some features of the Portugal current system: A poleward slope undercurrent, an upwelling-related summer southward flow and autunm-winter poleward coastal surface current, in *Proceedings of the 2^{nd} International Conference on Air-Sea Interaction, Meteorology and Oceanography of the Coastal Zone*, edited by K. Katsaros, A. Fiúza, and I. Ambar, p. 311, American Meteorology Society, 1994.

Ambar, I., and M. R. Howe, Observations of the Mediterranean outflow -I. mixing in the Mediterranean outflow, *Deep-Sea Research*, *26*, 535–554, 1979.

Ambar, I. J., Seis meses de mediçoes de correntes, temperaturas, e salinidades na vertente continental ao largo da costa Alentejana, *Tech. Rep. 1/84*, Grupo de Oceanograpfia, Universidade de Lisboa, 1984.

Ambar, I. J., Seis meses de mediçoes de correntes, temperaturas e salinidades na vertente continental ao largo da costa Alentejana, *Tech. Rep. 1/85*, Grupo de Oceanografia, Universidad de Lisboa, 1985.

Andrews, W. R. H., and L. Hutchings, Upwelling in the southern Benguela current, *Progress in Oceanography*, *9*, 81, 1980.

Arhan, M., A. C. D. Verdière, and L. Mémery, The eastern boundary of the subtropical North Atlantic, *Journal of Physical Oceanography*, *24*, 1295–1316, 1994.

Armi, L., and W. Zenk, Large lenses of highly saline Mediterranean Water, *Journal of Physical Oceanography*, *14*, 1560–1576, 1984.

Atkinson, L. P., K. H. Brink, R. E. Davis, B. H. Jones, T. Paluszkiewicz, and D. W. Stuart, Mesoscale variability in the vicinity of Points Conception and Arguello during april-may 1983: The OPUS 1983 experiment, *Journal of Geophysical Research, 91*, 12,899–12,918, 1986.

Austin, J. A., and J. A. Barth, Variations in the position of the upwelling front on the oregon shelf, *Journal of Geophysical Research, 107(C11)*, 3180,doi:10.1029/2001JC000858, 2002.

Bakun, A., Coastal upwelling indices, west coast of North America, 1946-1971, *Tech. Rep. NMFS SSRF-671*, NOAA, 1973.

Bakun, A., and C. S. Nelson, The seasonal cycle of wind stress curl in subtropical eastern boundary current regions, *Journal of Physical Oceanography*, *21*, 1815–1834, 1991.

Barnes, S. L., Applications of the Barnes objective analysis sheme, part III: Tuning for minimum error, *Journal of Atmospheric and Oceanic Technology*, *11*, 1459–1470, 1994.

Barth, A., Short-wavelength instabilities on coastal jets and fronts, *Journal of Geophysical Research*, *99*, 16,095–16,115, 1994.

Barth, J. A., and K. H. Brink, Shipboard acoustic doppler velocity observations near Point Conception: Spring 1983, *Journal of Geophysical Research*, *92*, 3925–3943, 1987.

Barth, J. A., S. D. Pierce, and R. L. Smith, A separating coastal upwelling jet at Cape Blanco, Oregon and its connection to the California current system, *Deep-Sea Res. Part II-Top. Stud. Oceanogr.*, *47*, 783–810, 2000.

Barton, E. D., The poleward undercurrent on the eastern boundary of the subtropical North Atlantic, in *Poleward Eastern Boundary Currents*, edited by S. Neshyba, C. N. K. Mooers, and R. L. Smith, pp. 82–95, Springer-Verlag, New Yotk, 1990.

Barton, E. D., J. Arístegui, P. Tett, M. Cánton, J. García-Braun, S. Hernández-León, L. Nykjaer, C. Almeida, J. Almunia, S. Ballesteros, G. Basterretxea, J. Escánez, L. García-Weill, A. Hernández-Guerra, F. López-Laatzen, R. Molina, M. F. Montero, E. Navarro-Pérez, J. M. Rodríguez, K. V. Lenning, H. Vélez, and K. Wild, The transition zone of the Canary Current Upwelling Region, *Progress in Oceanography*, *41*, 455–504, 1998.

Barton, E. D., M. E. Inall, T. J. Sherwin, and R. Torres, Vertical structure, turbulent mixing and fluxes during lagrangian observations of an upwelling filament system off northwest Iberia, *Progress in Oceanography*, *51*, 249–268, 2001.

Barton, E. D., R. Haynes, and R. Torres, Water mass variability and structure along the Atlantic coast of the Iberian Peninsula, *In preparation*, 2002.

Batteen, M. L., Poleward flows along eastern ocean boundaries, in *Model Simulations of a Coastal Jet and Undercurrent in the Presence of Eddies and Jets in the California Current System*, edited by S. J. Neshyba, C. N. K. Mooers, R. L. Smith, and R. T. Barber, p. 374, Springer-Verlag, New York, 1989.

Batteen, M. L., Wind-forced modelling studeis of currents, meanders and eddies in the California current system, *Journal of Geophysical Research*, *102*, 985–1010, 1997.

Batteen, M. L., C. L. L. D. Costa, and C. S. Nelson, A numerical study of wind stress curl effects on eddies and filaments off the northwest coast of the Iberian Peninsula, *Journal of Marine Systems*, *3*, 249–266, 1992.

Blanton, J. O., L. P. Atkinson, F. Castillejo, and A. L. Montero, Coastal upwelling of the Rías Bajas, Galicia, northwest Spain, i; hydrographic studies, *Rapp. P. V. Réun. Cons. int. Explor. Mer.*, *183*, 179–190, 1984.

Blanton, J. O., K. R. Tenore, F. Castillejo, L. P. Atkinson, F. B. Schwing, and A. Lavin, The relationship of upwelling to mussel production in the rias on the western coast of Spain, *J. Mar. Res.*, *45*, 497–511, 1987.

Bower, A. S., L. Armi, and I. Ambar, Lagrangian observations of Meddy formation during a Mediterranean undercurrent seeding experiment, *Journal of Physical Oceanography*, *27*, 2545–2575, 1997.

Brainerd, K. E., and M. C. Gregg, Surface mixed layer and mixing layer depths, *Deep-Sea Research I*, *42*, 1521–1543, 1995.

Brink, H. H., R. C. Beardsley, P. P. Niiler, M. Abbott, A. Huyer, S. Ramp, T. Stanton, and D. Stuart, Statistical properties of near-surface flow in the California current coastal transition zone, *Journal of Geophysical Research*, *96*, 14,693–14,706, 1991.

Brink, K., and T. J. Cowles, The coastal transition zone program, *Journal of Geophysical Research*, *96*, 14,367–14,647, 1991.

Brink, K. H., The near-surface dynamics of coastal upwelling, *Progress in Oceanography*, *12*, 223–257, 1983.

Brink, K. H., Coastal-trapped waves and wind-driven currents over the continental shelf, *Annual Review of Fluid Mechanics*, *23*, 389–412, 1991.

Brink, K. H., Wind-driven currents over the continental shelf, in *The Sea*, edited by K. Brink and A. Robinson, John Wiley & Sons, Inc., 1998.

Brink, K. H., D. C. Chapman, and J. G. R. Halliwell, A stochastic model for wind-driven currents over a continental shelf, *Journal of Geophysical Research*, *92*, 1783–1797, 1987.

Brink, K. H., R. C. Beardsley, J. Paduan, R. Limeburner, M. Caruso, and J. G. Sires, A view of the 1993-1994 California current based on surface drifters, floats, and remotely sensed data, *J. Geophys. Res.-Oceans*, *105*, 8575–8604, 2000.

Burrows, M., and S. A. Thorpe, Drifter observations of the Hebrides slope current and nearby circulation patterns, *Annales Geophysicae. Atmospheres, Hydrospheres, and Space Sciences*, *17*, 280–302, 1999.

Candela, J., R. C. Beardsley, and R. Limeburner, Separation of tidal and subtidal currents in ship-mounted acoustic doppler current profiler observations, *Journal of Geophysical Research*, *97*, 769–788, 1992.

Carter, E. F., and A. R. Robinson, Analysis models for the estimation of oceanic fields, *Journal of Atmospheric and Oceanic Technology*, *4*, 49–74, 1987.

Castro, C. G., F. F. Pérez, X. A. Alvarez-Salgado, G. Rosón, and A. F. Ríos, Hydrography conditions associated with the relaxation of a upwelling event off the Galician coast (NW Spain), *Journal of Geophysical Research*, *99*, 5135–5147, 1994.

Castro, C. G., X. A. Alvarez-Salgado, F. G. Figuerias, F. F. Perez, and F. Fraga, Transient hydrographic and chemical conditions affecting microplankton populations in the coastal transition zone of the iberian upwelling system (NW Spain) in September 1986, *Journal of Marine Research*, *55*, 321–352, 1997.

Castro, C. G., F. F. Pérez, X. A. Álvarez-Salgado, and F. Fraga, Coupling between the thermohaline, chemical and biological fields during two constrasting upwelling events off the NW Iberian Peninsula, *Continental Shelf Research*, *20*, 189–210, 2000.

Chelton, D. B., R. A. deSzoeke, M. G. Schlax, K. El Naggar, and N. Siwertz, Geographical variability of the first-baroclinic Rossby radius of deformation, *Journal of Physical Oceanography*, *28*, 433–460, 1998.

Chen, D., and D. P. Wang, Simulating the time-variable coastal upwelling during CODE 2, *Journal of Marine Research*, *48*, 335–358, 1990.

Clarke, R. A., H. W. Hill, R. F. Reiniger, and B. A. Warren, Current system south and east of the Grand Banks of Newfoundland, *Journal of Physical Oceanography*, *10*, 25–65, 1980.

Coelho, H. S., R. J. J. Neves, M. White, P. C. Leitão, and A. J. Santos, A model for ocean circulation on the Iberian coast, *Journal of Marine Systems*, *32*, 153–179, 2002.

Colin de Verdière, A., Lagrangian eddy statistics from the surface drifters in the eastern north Atlantic, *Journal of Marine Research*, *41*, 375–398, 1983.

Condie, S. A., Formation and stability of shelf-break fronts, *Journal of Geophysical Research*, *98*, 12,405–12,416, 1993.

Crawford, W. R., Turbulent energy dissipation in the Atlantic equatorial undercurrent, Ph.D. thesis, University of British Columbia, 1976.

Crépon, M., and C. Richez, Transient upwelling generated by two-dimensional atmospheric forcing and variability in the coastline, *Journal of Physical Oceanography*, *12*, 1437–1457, 1982.

Crepon, M., C. Richez, and M. Chartier, Effects of coastline geometry on upwellings, *Journal of Physical Oceanography*, *14*, 1365–1382, 1984.

Csanady, G. T., The arrested topographic wave, *Journal of Physical Oceanography*, *8*, 47–62, 1978.

Cummins, P. F., and G. K. Vallis, Algorithm 732: Solvers for self-adjoint elliptic problem in irregular two-dimensional domains, *ACM Transactions Mathematical Software*, *20*, 247–261, 1994.

Dale, A. C., and J. A. Barth, The hydraulics of an evolving upwelling jet flowing around a cape, *Journal of Physical Oceanography*, *31*, 226–243, 2001.

Dalu, G. A., and R. A. Pielke, An analytical study of the frictional response of coastal currents and upwelling to wind stress, *Journal of Geophysical Research*, *95*, 1523–1536, 1990.

Daniault, N., J. P. Mazé, and M. Arhan, Circulation and mixing of the Mediterranean water west of the Iberian Peninsula, *Deep-Sea Research I*, *41*, 1285–1714, 1994.

Davies, R. E., Predictability of sea surface temperature and sea level pressure anomalies over the North Pacific ocean, *Journal of Physical Oceanography*, *6*, 249–266, 1976.

Davis, R. E., Drifter observations of coastal surface currents during CODE: The statistical and dynamical views, *Journal of Geophysical Research*, *90*, 4756–4772, 1985.

Davis, R. E., Modeling eddy transport of passive tracers, *Journal of Marine Research*, *45*, 635–666, 1987.

Davis, R. E., Observing the general circulation with floats, *Deep-Sea Research I*, *38, suppl. 1*, S531–S571, 1991.

De Szoeke, R. A., and J. G. Richman, On wind-driven mixed layers with strong horizontal gradients - a theory with application to coastal upwelling, *Journal of Physical Oceanography*, *14*, 364–377, 1984.

Denbo, D. W., and J. S. Allen, Large-scale response to atmospheric forcing of shelf currents and coastal sea level off the west coast of North America: May-July 1981 and 1982, *Journal of Geophysical Research*, *92*, 1757–1782, 1987.

Dever, E. P., M. C. Hendershott, and C. D. Winant, Statistical aspects of surface drifter observations of circulation in the Santa Barbara channel, *Journal of Geophysical Research*, *103*, 24,781–24,797, 1998.

Dewey, R. K., W. R. Crawford, A. E. Gargett, and N. S. Oakey, A microstructure instrument for profiling oceanic turbulence in coastal bottom boundary layers, *Journal of Atmospheric and Oceanic Technology*, *4*, 288–297, 1987.

Dewey, R. K., J. N. Moum, C. A. Paulson, D. R. Caldwell, and S. D. Pierce, Structure and dynamics of a coastal filament, *Journal of Geophysical Research*, *96*, 14,885–14,908, 1991.

Dewey, R. K., J. N. Moum, and D. R. Caldwell, Microstructure activity within a minifilament in the coastal transition zone, *Journal of Geophysical Research*, *98*, 14,457–14,470, 1993.

Dietrich, G., K. Kalle, W. Krauss, and G. Sielder, *General Oceanography*, John Wiley, New York, 1975.

Doval, M. D., E. Nogueira, and F. F. Pérez, Spatio-temporal variability of the thermohaline and biogeochemical properties and dissolved organic carbon in a coastal embayment affected by upwelling: the Ría de Vigo (NW Spain), *Journal of Marine Systems*, *14*, 135–150, 1998.

Dubert, J., Dynamique du système de courants vers le pôle au voisinage de la pente continentale à l'Ouest et au nord de la péninsule Ibérique, Ph.D. thesis, Université de Bretagne Occidentale, France, 1998.

Efthymiadis, D., F. Hernandez, and P.-Y. L. Traon, Large-scale sea-level variations and associated atmospheric forcing in the subtropical north-east atlantic ocean, *Deep-Sea Research II*, *49*, 3957–3981, 2002.

Enriquez, A. G., and C. A. Friehe, Effects of wind stress and wind stress curl variability on coastal upwelling, *Journal of Physical Oceanography*, *25*, 1651–1671, 1995.

Fanjul, E. A., B. P. Gómez, and I. R. Sánchez-Arévalo, A description of the tides in the eastern North Atlantic, *Progress in Oceanography*, *40*, 217–244, 1997.

Firing, E., J. Ranada, and P. Caldwell, *Processing ADCP Data with the CODAS Software System Version 3.1, User's Manual*, University of Hawaii, 1995.

Fiúza, A. F. G., Upwelling patterns off Portugal, in *Coastal Upwelling: Its Sediment Record, Part A*, edited by E. Suess and J. Thiede, p. 604, Plenum Press, New York, 1983.

Fiúza, A. F. G., Hidrologia e dinamica das aguas costeiras de Portugal, Ph.D. thesis, University of Lisbom, Portugal, 1984.

Fiúza, A. F. G., Final report of the MORENA project, 1993-1996, 1996.

Fiúza, A. F. G., and D. Halpern, Hydrographic observations of the Canary Current between 21n and 25.5n during March-April 1974, *Rapp. Proc. -Verb. Rwun.*, p. 180pp, 1982.

Fiúza, A. F. G., M. E. de Macedo, and M. R. Guerreiro, Climatological space and time variation of the Portuguese coastal upwelling, *Oceanologica Acta*, *5*, 31–40, 1982.

Fiúza, A. F. G., J. H. Dias, and . Alonso, Long-term current measurements on the west Iberian margin, *Tech. Rep. 36*, MORENA Scientific and Technical Report, 1996.

Fiúza, A. F. G., M. Hamann, I. Ambar, G. D. González, and J. M. Cabanas, Water masses and their circulation in the western Iberian coastal ocean during may 1993, *Deep-Sea Research I*, *45*, 1127–1160, 1998.

Flagg, C. N., and S. L. Smith, On the use of the acoustic doppler current profiler to measure zooplankton abundance, *Deep-Sea Research I*, *36*, 455–474, 1989.

Flament, P., and L. Armi, The shear, convergence, and thermohaline structure of a front, *Journal of Physical Oceanography*, *30*, 51–66, 2000.

Flament, P., L. Armi, and L. Washburn, The evolving structure of an upwelling filament, *Journal of Geophysical Research*, *90*, 11,765–11,778, 1985.

Flament, P., L. Armi, and L. Washburn, Mesoscale variability off California as seen by the GEOSAT altimeter, in *IGARSS'89*, pp. 1063–1068, 1989.

Fraga, F., C. Mourino, and M. Manriquez, Las masas de agua en la costa de Galicia: Junio-Octubre, *Tech. Rep. 10*, Resultados Expediciones Cientificas, 1982.

Fratantoni, D. M., North Atlantic surface circulation during the 1990's observed with satellite-tracked drifters, *J. Geophys. Res.-Oceans*, *106*, 22,067–22,093, 2001.

Frouin, R., A. Fiúza, I. Ambar, and T. J. Boyd, Observations of a poleward surface current off the coasts of Portugal and Spain during the winter, *Journal of Geophysical Research*, *95*, 679–691, 1990.

Garcia-Soto, C., R. D. Pingree, and L. Valdés, Navidad development in the southern bay of biscay: Climate change and swoddy structure from remote sensing and in situ measurements, *Journal of Geophysical Research*, *107(C8)*, doi:10.1029/2001JC001012, 2002.

Garvine, R. W., A simple model of coastal upwelling dynamics, *Journal of Physical Oceanography*, *1*, 69–179, 1971.

Godin, G., The analysis of tides and currents., in *Tidal Hydrodynamics*, edited by B. B. Parker, pp. 675–709, John Wiley & Sons, New York, 1991.

Gomez-Gesteira, M., M. deCastro, R. Prego, and V. Perez-Villar, An unusual two layered tidal circulation induced by stratification and wind in the Ria of Pontevedra (NW Spain), *Estuar. Coast. Shelf Sci.*, *52*, 555–563, 2001.

Hamann, M., A. F. G. Fiúza, and I. Ambar, Seasonal variability of the hrydrology and geostrophic circulation on the Iberian Atlantic continental margin, *Tech. Rep. 34*, MORENA Scientific and Technical Report, 1996.

Hawkins, H. F., and S. L. Rosenthal, On the computation of streamfunctions from the wind field, *Monthly Weather Review*, *93*, 245–252, 1965.

Haynes, R., and E. D. Barton, A poleward flow along the Atlantic coast of the Iberian Peninsula, *Journal of Geophysical Research*, *95*, 11,425–11,141, 1990.

Haynes, R., and E. D. Barton, Lagrangian observations in the Iberian coastal transition zone, *Journal of Geophysical Research*, *96*, 14,731–14,741, 1991.

Haynes, R., E. D. Barton, and I. Pilling, Development, persistence and variability of upwelling filaments off the Atlantic coast of the Iberian peninsula, *Journal of Geophysical Research*, *98*, 22,681–22,692, 1993.

He, R., and R. H. Weisberg, West Florida shelf circulation and temperature budget for the 1999 spring transition, *Continental Shelf Research*, *22*, 719–748, 2002.

Helland-Hunsen, B., and F. Nansen, The eastern north Atlantic, *Geofysiske Publikasjoner*, *4*, 1–76, 1926.

Hill, A. E., and E. G. Mitchelson-Jacob, Observations of a poleward-flowing saline core on the continental-slope west of Scotland, *Deep-Sea Res. Part I-Oceanogr. Res. Pap.*, *40*, 1521–1527, 1993.

Hill, A. E., B. M. Hickey, F. A. Shillington, P. T. Strub, K. H. Brink, E. D. Barton, and A. C. Thomas, Eastern ocean boundaries coastal segment (e), in *The Sea, Vol. 11*, edited by K. H. Brink and A. R. Robinson, pp. 29–67, John Wiley & Sons, Inc, 1998.

Howarth, M. J., and R. Proctor, Ship ADCP measurements and tidal models of the North Sea, *Continental Shelf Research*, *12*, 601–623, 1992.

Huthnance, J. M., Waves and currents near the continental shelf edge, *Progress in Oceanography*, *10*, 193–226, 1981.

Huthnance, J. M., Slope currents and "JEBAR", *Journal of Physical Oceanography*, *14*, 795–810, 1984.

Huthnance, J. M., Circulation, exchange and water masses at the ocean margin: The role of physical processes at the shelf edge, *Progress in Oceanography*, *35*, 353–431, 1995.

Huthnance, J. M., L. A. Mysak, and D. P. Wang, Coastal trapped waves, in *Baroclinic Processes on Continental Shelves*, edited by C. N. K. Mooers, pp. 1–18, AGU, Washington D. C., 1986.

Huthnance, J. M., H. M. Van Aken, M. White, E. D. Barton, B. LeCann, E. F. Coelho, E. A. Fanjul, P. Miller, and J. Vitorino, Ocean margin exchange- water flux estimates, *Journal of Marine Systems*, *32*, 107–137, 2002.

Huyer, A., A comparison of upwelling events in 2 locations: Oregon and northwest Africa, *Journal of Marine Research*, *34*, 531–546, 1976.

Huyer, A., Coastal upwelling in the California current system, *Prog. Oceanogr.*, *12*, 259–284, 1983.

Inall, M. E., SPIDER, software to process and image dissipated energy rates, *Tech. Rep. U98-7*, Unit for Coastal and Estuarine Studies, University of Wales, Bangor, 1998.

Joint, I., M. Inall, R. Torres, F. G. Figueiras, X. A. Álvarez-Salgado, A. P. Rees, and E. M. S. Woodward, Two lagrangian experiments in the Iberian upwelling system: Tracking an upwelling event and an off-shore filament, *Progress in Oceanography*, *51*, 221–248, 2001.

Jones, P. D., T. Jonsson, and D. Wheeler, Extension to the north atlantic oscillation using early instrumental pressure observations from gibraltar and southwest iceland, *International Journal of Climatology*, *17*, 1433–1450, 1997.

Jorge da Silva, A., The slope current off the west Iberian coast in autumn, *ICES C.M., 1996/S:35*, 1996.

Käse, R. H., and G. Siedler, Meandering of the subtropical front southeast of the azores, *Nature*, *300*, 245–246, 1982.

Kase, R. H., A. Beckmann, and H. H. Hinrichsen, Observational evidence of salt lense formation in the Iberian peninsula, *Journal of Geophysical Research*, *94*, 4905–4912, 1989.

Kelly, K. A., Comment on " empirical orthogonal function analysis of advanced very high resolution radiometer surface temperature patterns in Santa Barbara channel " by G.S.E. Lagerloef and R.L. Bernstein, *Journal of Geophysical Research*, *93*, 15,753–15,754, 1988.

Koch, S. E., M. DesJardins, and P. J. Kocin, An interactive Barnes objective map analysis scheme for use with satellite and conventional data, *J. Climate Appl. Met.*, *22*, 1487–1503, 1983.

Kosro, P. M., Shipboard acoustic current profiling during the coastal ocean dynamics experiment., Ph.D. thesis, UCSD, University of California, La Jolla, Ca., 1985.

Kosro, P. M., and A. Huyer, CTD and velocity surveys of seaward jets off northern California, July 1981 and 1982, *Journal of Geophysical Research*, *91*, 7680–7690, 1986.

Kosro, P. M., A. Huyer, S. R. Ramp, R. L. Smith, F. P. Chavez, T. J. Cowles, M. R. Abbott, P. T. Strub, R. T. Barber, P. Jessen, and L. F. Small, The structure of the transition zone between coastal waters and the open ocean off northern California, winter and spring 1987, *Journal of Geophysical Research*, *96*, 14,707–14,730, 1991.

Kundu, P. K., and J. S. Allen, Some three-dimensional characteristics of low-frequency current fluctuations near the Oregon coast, *Journal of Physical Oceanography*, *6*, 181–199, 1976.

Lentz, S. J., The surface boundary layer in coastal upwelling regions, *Journal of Physical Oceanography*, *22*, 1517–1539, 1992.

Levitus, S., M. E. Conkright, J. L. Reid, R. G. Najiar, and A. Mantyla, Nitrate, phosphate and silicate distributions in the world oceans, *Progress in Oceanography*, *31*, 25–273, 1993.

Lynn, R. J., and J. J. Simpson, The California current system: The seasonal variability of its physical characteristics, *Journal of Geophysical Research*, *92*, 12,947–12,966, 1987.

Martins, C. S., M. Hamann, and A. F. G. Fiúza, Surface circulation in the eastern North Atlantic, from drifters and altimetry, *Journal of Geophysical Research*, *107*, 3217,doi:10.1029/2000JC000345, 2002.

Mazé, J. P., M. Arhan, and H. Mercier, Volume budget of the eastern boundary layer off the Iberian peninsula, *Deep-Sea Research I*, *44*, 1543–1574, 1997.

McClain, C. R., S. Chao, L. P. Atkinson, J. O. Blanton, and F. de Castillejo, Wind-driven upwelling in the vecinity of cape finisterre, Spain, *Journal of Geophysical Research*, *91*, 8470–8486, 1986.

McClean, J. L., P. M. Poulain, J. W. Pelton, and M. E. Maltrud, Eulerian and lagrangian statistics from surface drifters and a high-resolution POP simulation in the north Atlantic, *J. Phys. Oceanogr.*, *32*, 2472–2491, 2002.

McCreary, J. P., P. K. Kundu, and S. Chao, On the dynamics of the californian current system, *Journal of Marine Research*, *45*, 1–32, 1987.

McCreary, J. P., Y. Fukamachi, and P. K. Kundu, A numerical investigation of jets and eddies near an eastern ocean boundary, *Journal of Geophysical Research*, *96*, 2515–2534, 1991.

Meincke, J., G. Siedler, and W. Zenk, Some current observations near the continental slope off Portugal, *Meteor Forschung Ergebnisse, A*, *16*, 15–22, 1975.

Mendes de Sousa, M. F. M., Processos de mesoescala ao largo da costa portuguesa utilizando dados de satélite e obervaçoes *in situ*, Ph.D. thesis, University of Lisbom, Portugal, 1995.

Merrifield, M. A., and C. D. Winant, Shelf circulation in the gulf of California: A description of the variability, *Journal of Geophysical Research*, *94*, 18,133–18,160, 1989.

Miller, P. I., S. B. Groom, A. McManus, J. Selley, and N. Mironnet, Panorama: A semi-automated AVHRR, and CZCS system for observation of coastal and ocean processes, in *Proceedings of the Remote Sensing Society, Reading, September 1997*, pp. 539–544, 1997.

Mittelstaedt, E., The upwelling area off northwest africa - a description of phenomena related to coastal upwelling, *Progress in Oceanography*, *12*, 307–331, 1983.

Mittelstaedt, E., The ocean boundary along the northwest african coast: Circulation and oceanographic properties at the sea surface, *Progress in Oceanography*, *26*, 307–355, 1991.

Mittelstaedt, E., D. Pillsbury, and R. L. Smith, Flow patterns in the northwest african upwelling area, *Deutsch Hydrographische Zeitschrift*, *28*, 146–167, 1975.

Moum, J. M., D. R. Caldwell, and P. J. Stabeno, Mixing and intrusions in a rotating cold-core feature off cape blanco, oregon, *Journal of Physical Oceanography*, *18*, 823–833, 1988.

Moum, J. N., D. J. Carlson, and T. J. Cowles, Sea slicks and surface strain, *Deep-Sea Research I*, *37*, 767–775, 1990.

Münchow, A., Wind stress curl forcing of the coastal ocean near Point Conception, California, *Journal of Physical Oceanography*, *30*, 1265–1280, 2000a.

Münchow, A., Detiding three-dimensional velocity survey data in coastal waters, *Journal of Atmospheric and Oceanic Technology*, *17*, 736–749, 2000b.

Narimousa, S., and T. Maxworthy, Application of a laboratory model to the interpretation of satellite and field observations of coastal upwelling, *Dynamics of Atmosphares and Oceans*, *13*, 1–46, 1989.

Neshyba, S. J., C. N. K. Mooers, R. L. Smith, and R. T. Barber, *Poleward flows along eastern boundaries*, Springer-Verlag, New York, 1989.

New, A. L., Factors affecting the quality of shipboard acoustic doppler current profiler data, *Deep-Sea Research*, *39*, 1985–1996, 1992.

New, A. L., S. Barnard, P. Herrmann, and J. M. Molines, On the origin and pathway of the saline inflow to the Nordic seas: insights from models, *Prog. Oceanogr.*, *48*, 255–287, 2001.

Niiler, P. P., On the ekman divergence in an oceanic jet, *Journal of Geophysical Research*, *74*, 7048–7052, 1969.

Niiler, P. P., A. S. sybrandy, K. Bi, P. M. Poulain, and D. Bitterman, Measurement of the water-following capability of holey sock and tristar drifters, *Deep-Sea Research I*, *42*, 1951–1964, 1995.

Noble, M. A., and S. T. Ramp, Subtidal currents over the central California slope: evidence for offshore veering of the undercurrent and for direct, wind-driven slope currents, *Deep-Sea Research I*, *47*, 871–906, 2000.

Nogueira, E., Análisis y modelado de la variabilidad temporal de las características hidrográficas en la ría de vigo, Ph.D. thesis, University of Vigo, 1998.

Nogueira, E., X. A. Alvárez-Salgado, F. F. Pérez, and G. Casas, Geostrophic wind-stress patterns in the NW Iberian upwelling system. a time series approach, in *3rd EU Conference. Exchange Processes at the Continent/Ocean Margins in the North Atlantic*, Vigo, 1997.

North, G. R., T. L. Bell, R. F. Cahalan, and F. J. Moeng, Sampling errors in the estimation of empirical orthogonal functions, *Monthly Weather Review*, *110*, 699–706, 1982.

Nykjaer, L., and L. Vancamp, Seasonal and interannual variability of coastal upwelling along northwest africa and Portugal from 1981 to 1991, *Journal of Geophysical Research*, *99*, 14,197–14,207, 1994.

Osborn, T. R., Estimates of the local rate of vertical difusion from dissipation measurements, *Journal of Physical Oceanography*, *10*, 83–89, 1980.

Paillet, J., B. LeCann, X. Carton, Y. Morel, and A. Serpette, Dynamics and evolution of a northern MEDDY, *Journal of Physical Oceanography*, *32*, 55–79, 2002.

Pedlosky, J., *Geophysical Fluid Dynamics*, Springer-Verlag, New York, 1987.

Peliz, A., T. L. Rosa, A. M. P. Santos, and J. L. Pissarra, Fronts, jets and counter flows in the western Iberian upwelling system, *Journal of Marine Systems*, *35*, 61–77, 2002.

Peliz, A. J., and A. F. G. Fiúza, Temporal and spatial variability of CZCS-derived phytoplankton pigment concentrations off the western Iberian peninsula, *International Journal of Remote Sensing*, p. ?, 1996.

Pérez, F. F., A. F. Ríos, B. A. King, and R. T. Pollard, Decadal changes of the θ-s relationship of the Eastern North Atlantic Central Water, *Deep-Sea Research I*, *42*, 1849–1864, 1995.

Pérez, F. F., C. G. Castro, X. A. Álvarez-Salgado, and A. F. Ríos, Coupling between the Iberian basin-scale circulation and the Portugal boundary current system: a chemical study, *Deep-Sea Research I*, *48*, 1519–1533, 2001.

Pierce, S. D., R. L. Smith, P. M. Kosro, J. A. Barth, and C. D. Wilson, Continuity of the poleward undercurrent along the eastern boundary of the mid-latitude north pacific, *Deep-Sea Res. Part II-Top. Stud. Oceanogr.*, *47*, 811–829, 2000.

Pingree, R. D., Flow of surface waters to the west of the british isles and in the bay of biscay, *Deep-Sea Research I*, *40*, 369–388, 1993.

Pingree, R. D., Winter warming in the southern bay of biscay and lagrangian eddy kinematics from a deep-drogued argos buoy, *Journal of the Marine Biological Association of the U. K.*, *74*, 107–128, 1994.

Pingree, R. D., and B. LeCann, Structure, strength and seasonality of the slope currents in the bay of biscay region, *Journal of the Marine Biological Association of the U. K.*, *70*, 857–885, 1990.

Pingree, R. D., and B. LeCann, Anicyclonic eddy x91 in the southern bay of biscay, may 1991 to february 1992, *Journal of Geophysical Research*, *97*, 14,353–15,367, 1992a.

Pingree, R. D., and B. LeCann, Three anticyclonic slope water oceanic eDDIES (SWODDIES) in the southern bay of biscay in 1990, *Deep-Sea Research I*, *39*, 1147–1175, 1992b.

Pingree, R. D., and B. LeCann, A shallow meddy (smeddy) from the secondary mediterannean salinity maximum, *Journal of Geophysical Research*, *98*, 20,169–20,185, 1993.

Pingree, R. D., B. Sinha, and C. R. Griffiths, Seasonality of the european slope current (goban spur) and ocean margin exchange, *Cont. Shelf Res.*, *19*, 929–975, 1999.

Pollard, R., and J. Read, A method for calibrating ship mounted acoustic doppler profilers and the limitations of gyro compasses, *Journal of Atmospheric and Oceanic Technology*, *6*, 859–865, 1989.

Pollard, R. T., and S. Pu, Structure and circulation of the upper Atlantic ocean northeast of the Azores, *Progress in Oceanography*, *14*, 443–462, 1985.

Pollard, R. T., M. J. Griffiths, S. A. Cunningham, J. F. Read, F. F. Pérez, and A. F. Ríos, Vivaldi 1991 - A study of the formation, circulation and ventilation of Eastern North Atlantic Central Water., *Progress in Oceanography*, *37*, 167–192, 1996.

Poulain, P. M., Near-inertial and diurnal motions in the trajectories of mixed layer drifters, *Journal of Marine Research*, *48*, 793–823, 1990.

Poulain, P. M., Adriatic sea surface circulation as derived from drifter data between 1990 and 1999, *J. Mar. Syst.*, *29*, 3–32, 2001.

Poulain, P. M., and P. P. Niiler, Statistical analysis of the surface circulation in the California Current System using satellite-tracked drifters, *Journal of Physical Oceanography*, *19*, 1588–1603, 1989.

Prego, R., A. W. Dale, M. deCastro, M. Gómez-Gesteira, J. J. Taboada, P. Montero, M. R. Villareal, and V. Pérez-Villar, Hydrography of the pontevedra ria: Intra-annual spatial and temporal variability in a galician coastal system (NW Spain), *Journal of Geophysical Research*, *106*, 19,845–19,857, 2001.

Press, W. H., S. A. Teulosky, W. T. Vetterling, and B. P. Flannery, *Numerical Recipes (2nd Ed.)*, Cambridge University Press, 1992.

RD Instruments, Calculating absolute backscatter in narrowband ADCPs, *Tech. Rep. FST-003*, San Diego, California, 1998.

Relvas, P., and E. D. Barton, Mesoscale patterns in the Cape São Vicente (Iberian Peninsula) upwelling region, *Journal of Geophysical Research*, *107(C10)*, doi:10.1029/2000JC000456, 2002.

Relvas de Almeida, P. J., Dynamics of the cape saõ vicente upwelling region observed from sea, land and space, Ph.D. thesis, University of Wales, Bangor, 1999.

Ríos, A. F., F. F. Pérez, and F. Fraga, Water masses in upper and middle north Atlantic ocean east of the Azores, *Deep-Sea Research I*, *39*, 645–658, 1992.

Røed, L. P., Modelling mesoscale features in the ocean, in *Waves and Nonlinear Processes in Hydrodynamics*, edited by J. Grue, B. Gjevik, and J. E. Weber, pp. 383–396, Kluwer Academic Publications, 1996.

Roed, L. P., and X. B. Shi, A numerical study of the dynamics and energetics of cool filaments, jets, and eddies off the Iberian peninsula, *Journal of Geophysical Research*, *104*, 29,817–29,841, 1999.

Rogers, J. C., Atmospheric circulation changes associated with the warming over the northern atlantic in the 1920s, *Journal of Climate and Applied Meteorology*, *24*, 1303–1310, 1985.

Rosenfeld, L. K., F. B. Schwing, N. Garfield, and D. E. Tracy, Bifurcated flow from an upwelling center: A cold water source for Monterey Bay, *Continental Shelf Research*, *14*, 931–964, 1994.

Salas, J., E. García-Ladona, and J. Font, Statistical analysis of the surface circulation in the Algerian current using lagrangian buoys, *Journal of Marine Systems*, *29*, 69–85, 2001.

Samelson, R., P. Barbour, J. Barth, S. Bielli, T. Boyd, D. Chelton, P. Kosro, M. Levine, and E. Skyllingstad, Wind stress forcing of the oregon coastal ocean during the 1999 upwelling season, *Journal of Geophysical Research*, *107*, 2.1–2.8, 2002.

Sarkisyan, A. S., and V. F. Ivanov, The combined effect of baroclinicity and bottom relief as an important factor in the dynamics of ocean currents, *Izv. Acad. Sci. USSR, Atmos. Oceanic Phys. (AGU translation)*, pp. 173–188, 1971.

Saunders, P. M., Circulation in the eastern north Atlantic, *Journal of Marine Research*, *40*, 641–657, 1982.

Sena, C., Surface currents in the Iberian Atlantic as observed with drifters, *Tech. Rep. 32*, MORENA Scientific and Technical Report, 1996.

Send, U., R. C. Beardsley, and C. D. Winant, Relaxation from upwelling in the coastal ocean dynamics experiment, *J. Geophys. Res.-Oceans*, *92*, 1683–1698, 1987.

Shearman, R. K., J. A. Barth, and P. M. Kosro, Diagnosis of the three-dimensional circulation associated with mesoscale motion in the California current, *Journal of Physical Oceanography*, *29*, 651–670, 1999.

Smith, R. L., A comparison of the structure and variability of the flow field in three coastal upwelling regions: Oregon, northwest Africa and Peru, in *Coastal Upwelling*, edited by F. A. Richards, pp. 107–118, American Geophysical Union, 1981.

Smyth, T., P. Miller, S. B. Groom, and S. J. Lavender, Remote sensing of physics and biology of lagrangian experiments at the Iberian margin, *Progress in Oceanography*, *51*, 296–281, 2001.

Sordo, I., E. D. Barton, J. M. Cotos, and Y. Pazos, An inshore poleward current in the NW of the Iberian peninsula detected from satellite images, and its relation with *g. catenatum* and *d. acuminata* blooms in the Galician Rias, *Estuarine, Coastal and Shelf Science*, *53*, 787–799, 2001.

Sousa, F. M., Determinaçao da temperatura da superfície do mar com satélites. uma aplicação ao oceano costeiro de Portugal, 1986.

Sousa, F. M., and A. Bricaud, Satellite-derived phytoplankton pigment structures in the Portuguese upwelling area, *Journal of Geophysical Research*, *97*, 11,343–11,356, 1992.

Souza, A. J., J. H. Simpson, M. Harikrishnan, and J. Malarkey, Flow structure and seasonality in the Hebridean slope current, *Oceanol. Acta*, *24*, S63–S76, 2001.

Spall, M. A., Baroclinic jets in confluent flow, *Journal of Physical Oceanography*, *27*, 1054–1071, 1997.

Stramma, L., Geostrophic transport in the warm water sphere of the eastern sub-tropical north-Atlantic, *Journal of Marine Research*, *42*, 537–558, 1984.

Strub, T. P., P. M. Kosro, and A. Huyer, The nature of the cold filaments in the California current system, *Journal of Geophysical Research*, *96*, 14,743–14,768, 1991.

Suginohara, N., Onset of coastall upwelling in a two layer ocean by wind-stress with longshore variation, *Journal of the Oceanographical Society of Japan*, *30*, 23–33, 1974.

Suginohara, N., Coastal upwelling: Onshore-offshore circulation, equatorial coastal jet and poleward undercurrent over a continental shelf-slope, *Journal of Physical Oceanography*, *12*, 272–284, 1982.

Swenson, M. S., and P. P. Niiler, Statistical analysis of the surface circulation of the California current, *Journal of Geophysical Research*, *101*, 22,631–22,645, 1996.

Swenson, M. S., P. P. Niiler, K. H. Brink, and M. R. Abbott, Drifter observations of a cold filament off Point Arena, California, in July 1988, *Journal of Geophysical Research*, *97*, 3593–3610, 1992.

Sy, A., Investigation of large-scale circulation patterns in the central north Atlantic: The north Atlantic current, the Azores current and the Mediterranean water plume in the area of the mid-Atlantic ridge, *Deep-Sea Research I*, *35(3)*, 383–413, 1988.

Taylor, G. I., Diffusion by continous movements, *Proceedings of the London Mathematical Sciety*, *20*, 196–212, 1921.

Tokmakian, R. T., and P. G. Challenor, Observations in the Canary basin and the Azores frontal region using geosat data, *Journal of Geophysical Research*, *98*, 4761–4773, 1993.

Torres, R., and E. D. Barton, Charles darwin CD114 cruise report: Acoustic doppler current fields, *Tech. rep.*, University of Wales, Bangor, 1999.

Trowbridge, J. H., D. C. Chapman, and J. Candela, Topographic effects, straits and the bottom boundary layer, in *The Sea, Vol. 10*, edited by K. H. Brink and A. R. Robinson, pp. 63–88, John Wiley & Sons, Inc., 1998.

Van Aken, H. M., Surface currents in the Bay of Biscay as observed with drifters between 1995 and 1999, *Deep-Sea Res. Part I-Oceanogr. Res. Pap.*, *49*, 1071–1086, 2002.

Varela-Rodriguez, M., Thalassa cruise report: GIGOVI-1099, *Tech. rep.*, Instituto Español de Oceanografía, 2000a.

Varela-Rodriguez, M., Thalassa cruise report: OMEX-1099, *Tech. rep.*, Instituto Español de Oceanografía, 2000b.

Vitorino, J., A. Oliveira, J. M. Jouanneau, and T. Drago, Winter dynamics on the northern Portuguese shelf. part 1: physical processes, *Progress in Oceanography*, *52*, 129–153, 2002.

Vitorino, J. P. N., Resultados do cruceiro CECIR XVII, *Tech. rep.*, Instituto Hidrográfico de Portugal, 1995.

Wang, D. P., Effects of continental slope on mean shelf circulation, *Journal of Physical Oceanography*, *12*, 1524–1526, 1982.

Wang, D. P., Effects of small-scale wind on coastal upwelling with application to point conception, *Journal of Geophysical Research*, *102*, 15,555–15,566, 1997.

Washburn, L., and L. Armi, Observations of frontal instabilities on an upwelling filament, *Journal of Physical Oceanography*, *18*, 1075–1092, 1988.

Washburn, L., D. Kadko, B. H. Jones, T. Hayward, P. M. Kosro, T. P. Santon, S. Ramp, and T. J. Cowles, Water mass subduction and the transport of phytoplankton in a coastal upwelling system, *Journal of Geophysical Research*, *96*, 14,927–14,946, 1991.

Winant, C. D., R. C. Beardsley, and R. E. Davis, Moored wind, temperature and current observations made during coastal ocean dynamics experiment 1 and 2 over the northern California continental shelf and upper slope, *Journal of Geophysical Research*, *92*, 1569–1604, 1987.

Winant, C. D., C. E. Dorman, C. A. Frehe, and R. C. Beardsley, The marine layer off northern California: An example of supercritical channel flow, *Journal of Atmospheric Science*, *45*, 3588–3605, 1988.

Wooster, W. S., A. Bakun, and D. R. Mclain, The seasonal upwelling cycle along the eastern boundary of the north Atlantic, *Journal of Marine Research*, *34*, 131–141, 1976.

Zenk, W., and L. Armi, The complex spreading pattern of Mediterranean water off the Portuguese continental slope, *Deep-Sea Research I*, *37*, 1805–1823, 1990.

Zimmerman, R. A., and D. C. Biggs, Patterns of distribution of sound-scattering zooplankton in warm- and cold-core eddies in the Gulf of Mexico, from a narrowband Acoustic Doppler Current Profiler survey, *Journal of Geophysical Research*, *104*, 5251–5262, 1999.

List of figures